

CHARACTERISTICS OF A MULTIPOLE VOLUME H^- PLASMA

JEREMY DAVID JOHNSON

Doctor of Philosophy

THE UNIVERSITY OF ASTON IN BIRMINGHAM

October 1987

This copy of the thesis has been supplied on condition that anyone who consults it is understood to recognize that its copyright rests with its author and that no quotation from the thesis and no information derived from it may be published without the author's prior, written consent.

The University of Aston in Birmingham

CHARACTERISTICS OF A MULTIPOLE VOLUME H^- PLASMA

Jeremy David Johnson

Doctor of Philosophy

October 1987

SUMMARY

An experimental study of a filtered magnetic-multipole ion source has been carried out, in order to examine the characteristics of a plasma in which negative hydrogen ions are formed by volume processes. The ultimate object was to aid in understanding the mechanisms of volume H^- production, so enabling the output of this type of device to be optimised for use in the fusion programme. The study entailed the design and construction of one such source, and diagnostic systems for both this and another.

A major portion of the results were obtained using planar Langmuir probes. To facilitate the use of these, a computer based control and analysis system was built. Empirical corrections were obtained for both electron screening by a magnetic field and ion sheath expansion, and justified theoretically. An attempt was also made to construct a mass spectrometer small enough to use within the source.

Using the probes, a detailed spatial and parametric survey of particle densities and energies within the filtered multipole plasma was performed. The results are shown mostly to fit simple models of plasma production and loss. The H^- density and fraction were obtained from the same dataset, and compared with data acquired using beam extraction. The results are discussed in relation to models of volume H^- production in a multipole source, based on both atomic and plasma processes. A balance of atomic processes predicted H^- ion densities within 20% of those measured experimentally. The spatial survey located a maximum of H^- density at the peak of the filter field, confirmed by beam-extraction data, which may be explained by the atomic balance. The parametric variation of H^- density was compared with an appropriate parametric model. This was successful, agreement being obtained from both sources.

KEYS: H^-
VOLUME H^- PRODUCTION
MULTIPOLE ION SOURCE
NEGATIVE ION SOURCE
LANGMUIR PROBES

DEDICATION

HILDA ANNE JOHNSON

for teaching me to ask why

SHEILA JAYANT BHATT

for helping me understand the answers

ACKNOWLEDGEMENTS

Having finally reached this point, I would like to mention the help that has been given to me by a large number of generous and thoughtful people along the way. I owe them much, and I am glad to finally have the opportunity to thank them all.

First of all, I should like to thank those who have guided me through the study, my supervisors, for their advice and their confidence in me. At Culham laboratory, Dr. Andrew Holmes, who lent me his knowledge of both plasma physics and the world of research, and persevered in teaching me how to use it. At Aston University, Dr. Keith Fitch, who believed I was capable and started me down this road, and Dr. Dennis Crumpton, who has had the unenviable task of making sure I reached the end of it, and whose guidance has achieved exactly that. I would especially like to wish Keith well in his retirement.

I would also like to thank the physicists at Culham for their help and advice: Dr. Mark Nightingale, along with Dr. Holmes my co-collaborator in the high-voltage experiments, for his sound advice and concern, Dr. Leslie Lea for the many hours he spent talking with me about Langmuir probes, and Dr. Roy McAdams, for discussing H^- heating and survival with me.

I have been fortunate enough to have the chance of talking about the habits and feeding of H^- ions with some of the most respected scientists working internationally in this field. Of these I only have room to thank a very few by name:

Dr. Mike Hopkins and Dr. Bill Graham for listening, Dr. Paul Allison for discussing sources with me, and Dr. Martha Bacal for her generous hospitality at the Palaiseau workshops.

Constructing the apparatus used in the study would have been impossible without the practical help of a host of people: Allan Newman, George Naylor and Jack Bircham deserve my thanks for helping with this, and providing many a rapid fix to a knotty problem. John Hancock helped me many times, skillfully manufacturing numerous odd devices at short notice. Ken Astley deserves special thanks for his continual assistance with the electronics. Frank Watters and his team in the workshops helped me on many occasions with the construction of equipment, for which I am grateful. I owe Ron White a special debt for the dozens of times he came up with an ace to help me out of a hole, generally last thing on a Friday!

Preparation of the thesis has been made possible by the help of many people: Sheila Bhatt has been generally indispensable! I am also indebted to Jim Fieret and John Allen, who have both provided assistance and equipment at considerable inconvenience to themselves.

Many more people deserve to be named here, and to them I must apologize profusely, plead lack of space and say thanks to you all!. Finally, I would like to thank all those people who have struggled to teach me over the years, sometimes in the face of severe adversity. Your efforts were not entirely wasted!

CONTENTS

	Page
TITLE PAGE	1
SUMMARY	2
DEDICATION	3
ACKNOWLEDGEMENTS	4
CONTENTS	6
LIST OF FIGURES	10
CHAPTER 1. <u>Introduction</u>	16
1.1 The requirement for negative hydrogen ions	16
1.2 Development of H^- ion sources	21
1.3 Objectives of the study and structure of thesis	25
CHAPTER 2. <u>Modelling an H^- producing plasma</u>	27
2.1 Ionization in multipole sources.	27
2.2 Formation of H^- ions in the plasma volume	35
2.3 Parametric dependence of an H^- generating plasma	53
CHAPTER 3. <u>Construction and operation of the sources</u>	58
3.1 Generic design of the multipole H^- sources	58
3.2 The fixed-filter source and beamline	61
3.2.1 The ion source and accelerator	62
3.2.2 The beamline	69
3.2.3 The vacuum system	69
3.2.4 The power supply and extraction systems	71
3.2.5 Diagnostic systems	73

3.3	The variable-filter source.	75
3.3.1	The ion source	75
3.3.2	The vacuum system	81
3.3.3	The power supplies	84
3.4	Operation of a filament driven multipole source	84
CHAPTER 4. <u>Diagnostic probes</u>		90
4.1	Langmuir probes	92
4.1.1	Theoretical considerations	92
4.1.1.1	Basic planar probe theory	92
4.1.1.2	Ion saturation sheath - expansion	93
4.1.1.3	Electron screening by the filter field	103
4.1.1.4	Measurement of N_{-} using Langmuir probes	121
4.1.1.5	Summary of Langmuir probe theories	133
4.1.2	Practical use of Langmuir probes	135
4.1.2.1	Design and construction of planar probes	135
4.1.2.2	The LPA computer - based probe system	140
4.2	The mass analyser probe	148
4.2.1	Principle of operation	148
4.2.2	Design and construction	151
4.2.3	Use of the probe	156
CHAPTER 5. <u>Experimental procedure and results</u>		159
5.1	Measurements of basic plasma parameters	160
5.1.1	Spatial variation	160
5.1.1.1	Axial variation	160
5.1.1.2	Transverse variation	169
5.1.1.3	Summary	176

5.1.2	Arc parameter variation	178
5.1.2.1	Arc current variation	180
5.1.2.1	Arc voltage variation	186
5.1.2.1	Pressure variation	191
5.1.2.1	Filter field intensity variation	195
5.1.2.1	Summary	200
5.1.3	Bias variation	205
5.2	Measurements of H^- density	216
5.2.1	Using probe ratio	216
5.2.1.1	Spatial variation	217
5.2.1.2	Arc parameter variation	225
5.2.1.3	Bias variation	234
5.2.2	Using beam extraction	237
5.2.2.1	Spatial variation	240
5.2.2.2	Arc parameter variation	241
5.2.2.3	Bias variation	248
5.3	Results from the mass analyser probe	250
5.3.1	Tests on the extraction system	250
5.3.2	Test spectra	252
5.3.3	Summary	258
CHAPTER 6.	<u>Discussion</u>	260
6.1	Plasma parameters	260
6.1.1	Spatial dependence	260
6.1.2	Parametric dependence	264
6.1.3	Bias dependence	280

6.2 Negative ions	283
6.2.1 Numerical estimate	283
6.2.2 Spatial dependence	284
6.2.3 Parametric and bias dependence	289
CHAPTER 7. <u>Conclusions</u>	295
7.1 Plasma parameters	295
7.2 Negative ions	297
7.3 General comments and suggestions	299
APPENDIX A. Langmuir probe theory	303
APPENDIX B. Computer based probe system	318
APPENDIX C. Atomic process data for volume H^- production	329
APPENDIX D. Uncertainty in probe measurements of N_-	334
APPENDIX E. Symbology	340
REFERENCES	343

LIST OF FIGURES

1.1.1	A possible negative - ion based NBI system	20
2.1.1	Schematic of a multipole H^- ion source	29
2.2.1	Atomic processes and data used in the model	50
3.1.1	Multipole magnet configurations	59
3.1.2	Types of magnetic filter	60
3.2.1	Schematic of fixed filter source and accelerator	63
3.2.2	Axial variation of filter field	64
3.2.3	Schematic of the electron control magnets	66
3.2.4	Schematic of the beamline and diagnostics	67
3.2.5	The fixed-filter source assembly	68
3.2.6	Schematic of the vacuum system	70
3.2.7	Schematic of the power supplies	72
3.3.1	Schematic of the variable filter source	76
3.3.2	Axial variation of filter field intensity	79
3.3.3	Location of features in the variable source	79
3.3.4	The variable - filter source assembly	80
3.3.5	Schematic of the vacuum system	82
3.3.6	Schematic of the power supplies	83
3.4.1	Contamination of the source backplate	86
3.4.2	Erosion of tantalum filaments by the arc	87
3.4.3	The variable - filter source in operation	89

4.1.1	Experimental arrangement, sheath expansion study	95
4.1.2	Typical probe traces obtained in expansion study	96
4.1.3	Variation of index of expansion with Iarc	97
4.1.4	Variation of index of expansion with pressure	97
4.1.5	Geometry of planar probe sheath expansion	101
4.1.6	Variation of R with field intensity in helium	105
4.1.7	Variation of Ne and N+ with field intensity	105
4.1.8	Variation of R - B curve with pressure	107
4.1.9	Variation of R - B curve with arc current	107
4.1.10	Variation of R - B curve with pressure	108
4.1.11	Variation of R - B curve with arc current	108
4.1.12	Universal curve for ratio attenuation	111
4.1.13	Probe area distorted by a parallel field	117
4.1.14	$R_c - F_r$ curve for Doucet theory	127
4.1.15	$R_c - F_r$ curves for Lea theory - Boltzmann model	127
4.1.16	$R_c - F_r$ curves for Lea theory - Local model	131
4.1.17	Effect of high T_- on Lea theory curves	131
4.1.18	The mobile probe, with inset showing probe head	136
4.1.19	Type 1. fixed probe	138
4.1.20	Type 2. fixed probe	139
4.1.21	Probe circuit for the LPA system	142
4.1.22	Flowchart of LPA data analysis and acquisition	145
4.2.1	Schematic of the mass analyser probe	149
4.2.2	Practical design of the mass analyser probe	152
4.2.3	Mass analyser probe detector head components	154
4.2.4	Mass analyser probe assembled onto shaft	155
4.2.5	Schematic of MAP control circuit	157

5.1.1	Axial variation of plasma density	162
5.1.2	Axial variation of thermal electron temperature	162
5.1.3	Axial variation of bulk energy density	164
5.1.4	Axial variation of primary electron density	164
5.1.5	Axial variation of primary electron temperature	166
5.1.6	Axial variation of primary energy density	166
5.1.7	Axial variation of plasma potential	168
5.1.8	Radial variation of plasma density	170
5.1.9	Radial variation of thermal electron temperature	170
5.1.10	Radial variation of bulk energy density	171
5.1.11	Radial variation of $N_+ T_e$ for two arc voltages	171
5.1.12	Radial variation of primary electron density	173
5.1.13	Radial variation of primary electron temperature	173
5.1.14	Radial variation of primary energy density	174
5.1.15	Radial variation of plasma potential	174
5.1.16	Variation of plasma density with arc current	181
5.1.17	Variation of thermal electron temp. with Iarc	181
5.1.18	Variation of bulk energy density with arc current	182
5.1.19	Var. of $N_+ T_e$ with Iarc in the fixed-filter source	182
5.1.20	Variation of primary electron density with Iarc	184
5.1.21	Variation of primary electron temp. with Iarc	184
5.1.22	Variation of plasma potential with arc current	185
5.1.23	Variation of plasma density with arc voltage	185
5.1.24	Variation of thermal electron temp. with Varc	187
5.1.25	Variation of primary electron density with Varc	187
5.1.26	Inverse variation of N_p with Varc at 4 pressures	189
5.1.27	Variation of primary electron temp. with Varc	189

5.1.28	Variation of primary energy density with Varc	190
5.1.29	Variation of plasma potential with arc voltage	190
5.1.30	Variation of plasma density with pressure	192
5.1.31	Variation of thermal electron temp. with pressure	192
5.1.32	Variation of primary electron density with pres.	193
5.1.33	N_p / pressure dependence at four arc voltages	193
5.1.34	Variation of primary electron temp. with pressure	194
5.1.35	Variation of plasma potential with pressure	194
5.1.36	Variation of plasma density with B	196
5.1.37	Variation of thermal electron temperature with B	196
5.1.38	Variation of primary density with B	198
5.1.39	Variation of primary electron temperature with B	198
5.1.40	Variation of plasma potential with B	199
5.1.41	Discharge noise induced by positive BFE bias	206
5.1.42	Variation of plasma density with bias voltage	207
5.1.43	Variation of thermal electron temp. with Vbias	207
5.1.44	Variation of primary electron density with Vbias	209
5.1.45	Variation of primary electron density with Vbias	209
5.1.46	Variation of primary electron temp. with Vbias	210
5.1.47	Variation of plasma potential with Vbias	210
5.1.48	Axial Variation of N_+ as a function of Vbias	212
5.1.49	Axial variation of T_e as a function of Vbias	212
5.1.50	Axial variation of V_p as a function of Vbias	213
5.2.1	Axial variation of I_-/I_+ - uncorrected	218
5.2.2	Axial variation of I_-/I_+ ($=R_c$) - corrected	218
5.2.3	Axial variation of H^- ion fraction	219
5.2.4	Axial variation of H^- ion density	219

5.2.5	Radial variation of probe ratio	221
5.2.6	Radial variation of H^- ion fraction	221
5.2.7	Radial variation of H^- ion density	222
5.2.8	Variation of probe ratio with arc current	226
5.2.9	Variation of H^- ion fraction with arc current	226
5.2.10	Variation of H^- ion density with arc current	227
5.2.11	Variation of probe ratio with arc voltage	227
5.2.12	Variation of H^- ion fraction with arc voltage	228
5.2.13	Variation of H^- ion density with arc voltage	228
5.2.14	Variation of probe ratio with pressure	230
5.2.15	Variation of H^- fraction with pressure	230
5.2.16	Variation of H^- ion density with pressure	231
5.2.17	Variation of probe ratio with filter intensity	231
5.2.18	Variation of H^- ion fraction with filter intens.	232
5.2.19	Variation of H^- ion density with filter intensity	232
5.2.20	Variation of probe ratio with bias voltage	235
5.2.21	Variation of H^- ion fraction with bias voltage	235
5.2.22	Variation of H^- ion density with bias voltage	236
5.2.23	Mass analysis of the extracted beam	238
5.2.24	Variation of extracted J_- with I_{arc}	242
5.2.25	Variation of extracted electron current with I_{arc}	242
5.2.26	Variation of extracted J_- with V_{arc}	243
5.2.27	Variation of extracted electron current with V_{arc}	243
5.2.28	Variation of extracted J_- with pressure	245
5.2.29	Variation of extracted electron current with pres	245
5.2.30	Variation of extracted J_- with B	246
5.2.31	Variation of extracted electron current with B	246

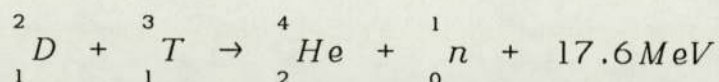
5.2.32	Variation of I_- and I_e with bias voltage	249
5.3.1	Faraday cup current var. with extraction voltage	251
5.3.2	MAP spectra from varying the extraction voltage	253
5.3.3	MAP spectra from two regions	254
5.3.4	MAP spectra from varying the filter intensity	256
5.3.5	MAP spectra from varying the pressure	257
6.1.1	Exponential attenuation of $N_+ T_e$ with distance	262
6.1.2	Primary electron fraction as a function of I_{arc}	265
6.1.3	Primary electron fraction as a function of pres.	265
6.1.4	Inverse dependence of $\ln(N_p)$ on $\ln(T_p)$	268
6.1.5	Effects of inelastic energy loss on T_p vs. V_{arc}	268
6.1.6	Saturation of $N_+ T_e$ with V_{arc} at many pressures	275
A.1.1	A typical planar Langmuir probe characteristic	306
B.1.1	ISO 100 optoisolator circuit	321
B.2.1	Overall structure of the LPA system	323
D.1.1	Effect of variation in T_- on $R_c - F_r$ curve	336
D.1.2	Effect of variation in T_+ on $R_c - F_r$ curve	336
D.1.3	Effect of variation in M_+ on $R_c - F_r$ curve	338

CHAPTER 1

Introduction

1.1 The requirement for negative hydrogen ion sources

In order to produce useful amounts of power from the thermonuclear fusion reaction



a plasma conforming to the Lawson criteria [1] must be generated in a confinement device which allows extraction of the energy produced. Much of the international research into fusion power is centered on the Tokamak, a magnetic plasma confinement device with a toroidal configuration. Designs for prototype reactors based on this rely initially on ohmic heating of the plasma, followed by adiabatic compression with both external and self-generated magnetic fields to further raise the density and temperature. The efficiency of these processes falls as the density and temperature increase. To reach reactor conditions, therefore, additional forms of heating are required [2].

One of the most promising of these is the injection of beams of high-energy neutrals through the confinement fields into the plasma, where their energy is effectively transferred to the plasma by several means. Collisional ionization of the neutrals allows their confinement by the

magnetic fields. Collisions between plasma ions and neutrals can provide an impact energy high enough to initiate fusion directly, offering the possibility of neutral injection being used for thermonuclear "ignition" and thereby reducing the high plasma-ion energy required for fusion initiated by plasma-ion collisions alone. Charge-exchange between plasma ions and neutrals permits the velocity of the resulting confined ions to be selected using the beam energy. The use of the momentum of the fast neutrals to provide a non-inductive current drive has been proposed [3], but the existence of a "back-current" of electrons opposing the injected current may cause this scheme to become inefficient at high densities [4]. One disadvantage of additional heating is the reduction of confinement time, thought to be due to perturbation of the plasma boundary [5]. This occurs for both of the principal additional heating schemes; neutral beam injection and ICRF (radio-frequency) heating. Recent results from JET [6] show that at injected power inputs of 8 MW this effect can halve the energy confinement time. The rate of reduction, however, appears to fall rapidly and possibly saturates at higher injected power levels. Other results suggest that in the case of beam-heating the effect may be alleviated by altering the confinement field geometry to obtain a sharp plasma boundary ("H-mode" operation), and modifications [7] to JET are intended to test this. ICRF heating appears to introduce impurities into the torus, and also suffers from power reflection at the plasma boundary,

making H-mode operation difficult.

The aim of the injection system is to ensure that the maximum energy deposition occurs in the core of the plasma toroid, and that the heating of the vessel wall by the beam, known as "shine-through", is kept to a minimum. Penetration of the beam into the plasma target depends on the plasma density, which thus determines the beam injection energy. However, injection alters the plasma density, requiring the energy to be varied during a Tokamak pulse to ensure deposition of energy in the core. The denser plasmas expected for future experiments and prototype reactors [8] require neutral injection beams with much higher energies than present systems, ranging from several hundred keV into the MeV range. These must be capable of delivering tens of MW of power into the plasma core, whilst avoiding unwanted wall heating.

Present neutral injection beams are formed by the electrostatic acceleration of positive hydrogen ions to several tens of keV followed by neutralization by charge exchange in a gas cell. This system has two disadvantages; Firstly the cross-section for proton neutralization by electron capture drops rapidly at energies >100 keV. Secondly, positive ion sources generate molecular H_2^+ and H_3^+ ions in addition to protons. An accelerated beam containing these will have a range of lower energies, making targeting of the plasma core difficult. The latter problem has been much improved by the use of multipole ion-sources with

modified magnetic fields [9-11], although the relative importance of the molecular ions increases with energy because their neutralization efficiency falls more slowly. However, the former effectively rules out positive-ion based systems for high-energy applications.

Negative hydrogen (and deuterium) ions suffer from neither of these problems. Only the atomic form of H^- is stable, yielding a monoenergetic beam. The extra electron is bound only weakly to the hydrogen atom, and the cross-section for neutralization by stripping is large even at the highest energies proposed. The electron may be stripped more efficiently by alternative means, such as a plasma target; if light of the correct frequency is used to photodetach the electrons, the neutralization fraction may be made close to unity. In addition, the use of negative ions confers other advantages. A negative ion beam transported through a low-density gas (e.g. a drift-space) suffers stripping and positive ion formation. Electrons and positive ions leave the beam, electrons more rapidly than ions, forming a local positive potential well. This results in electrostatic contraction and "self-focussing" of the beam, an effect which appears to increase with beam energy [12]. This effect allows high-energy negative ion beamlines to be made very long, enabling the beam-generation apparatus to be situated outside the primary reactor shielding, so greatly easing maintenance. The small diameter and low divergence of the beam reduces the necessary neutralizer sizes and allows the

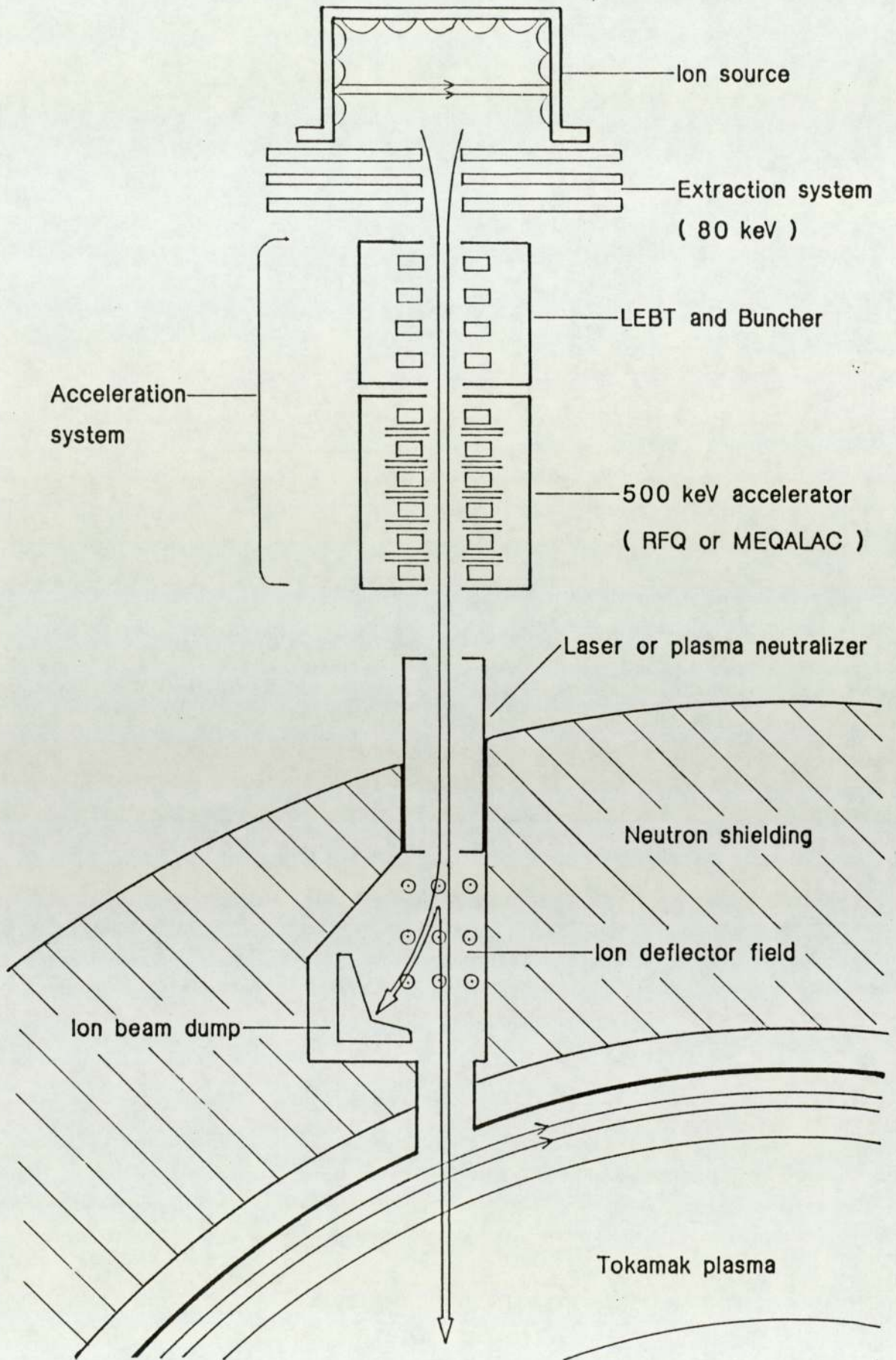


Figure 1.1.1 Schematic of a possible negative ion based NBI system

use of smaller ports and tangential injection [13]. The same properties also allow the use of alternative high-energy accelerators such as radio-frequency quadrupoles and "meqalac" devices, which offer significant safety advantages over electrostatic plate systems but which would be difficult to construct for large-diameter beams. Negative ions thus appear the obvious choice for high-energy NBI systems, such as the one shown schematically in figure (1.1.1). Such systems, however, require suitable H^- sources, and it is in the generation of H^- ions that the problems arise.

1.2 Development of H^- ion sources

Negative hydrogen ions are basically fragile, and hard to produce in quantity in conditions allowing their survival. Historically, H^- ion sources have been capable of generating a few A of ions, principally for particle accelerators and cross-section studies. Three methods are presently available for generating H^- ions: double charge-exchange of proton beams by dual electron capture in an alkali metal vapour, "surface-conversion" sources employing caesium as an intermediary, and volume production sources, where H^- is generated in the plasma volume. Much work has been done on double charge-exchange systems [14,15], the generation of multi-ampere beams at several tens of keV being reported [16,17]. However, this scheme suffers from several disadvantages; the initial low-energy positive ion beam suffers from space-charge neutralization before the second

electron is captured, leading to a divergent beam. Low-energy extraction limits the available proton current. The presence of metal vapour in the system leads to high-voltage breakdown and introduces impurities into the Tokamak.

The latter problem is shared to some extent by caesium-based surface-conversion sources. The increase in negative ion yield with the introduction of caesium vapour into a hydrogen discharge was first noted by Bel'chenko [18], and allowed Prelec et al [19] to treble the extracted H^- current from their device. Further work by Leung and Ehlers [20-22] resulted in the development of a large-volume device containing a caesiated "converter" electrode biased negative to the plasma. Negative ions produced on the surface by ion and neutral bombardment were repelled from the converter, and due to the concave shape "self-extracted" through a plane magnetic field. This arrangement proved capable of producing H^- currents of $\sim 1A$. However, the variation in the velocity with which the negative ions left the converter caused the self-extracted beam to be strongly divergent. These penalties, together with the additional power requirement of the converter electrode and the problems of erosion of the caesium monolayer on the converter, render the use of surface-conversion sources for high-energy systems unlikely.

Prior to this, many experimenters had reported the extraction of small currents (up to 6 mA) of negative ions apparently produced in the plasma volume of a number of

different devices. These early experiments, reviewed by several authors [15,19,23,77], offered the possibility of ion sources free of metallic impurities. The increase in H^- density obtained by caesiating the source surfaces was so large, however, that it was suggested that all H^- ions were produced by some type of surface interaction. Ehlers et al. [22] and Bacal [23] were later to demonstrate that this was not so; two definite populations of negative ions with differing energies existed in the presence of caesium, corresponding to the plasma and converter potentials. Even at the highest level of caesium input, the "volume" peak comprised 25% of the H^- density. Thus even in a surface conversion source, volume production accounted for a significant proportion of the H^- ions generated.

In 1973, Limpaecher & MacKenzie [24] developed a device consisting of a vacuum vessel surrounded by a multi-polar array of permanent magnets. This was capable of confining a large volume of quiescent plasma of a relatively high density ($\sim 10^{12} \text{ cm}^{-3}$). The possibilities for ion-production were quickly realized, initially for positive ions [25,26]. Further experimentation [9-11] revealed that alteration of the magnetic field geometry to provide a "magnetic filter" separating the ionizing electrons from the extracted plasma could affect the ratio of positive ion species, of much use to positive ion injection sources.

In 1976 Bacal et al [27] noted unexpectedly high H^- ion fractions in the centre of a multipole discharge. Advanced

laser diagnostics [28,29] were developed to study the physics behind this, enabling Bacal et al [28] to establish volume H^- production as a fact. Discovery of these high volume H^- densities prompted experiments elsewhere; at Culham laboratory [30,31] results indicating the presence of negative ions in the volume of a small positive ion source were obtained. Both theoretical studies [52,56] and experimental results [23] indicated that volume H^- ions were produced in a two-stage process via. an excited molecular state of hydrogen, requiring regions of both fast and slow electrons. The magnetic filter employed to alter species ratio was introduced to provide these [32-34] and yielded an increase in H^- current and a corresponding fall in extracted electron current, the latter aided by a bias potential applied to the extraction aperture. This configuration has been utilized by several experimenters recently to produce volume H^- sources of ever-increasing yield [35-37], using various optimization schemes [38-41]. The principle of a two-region multipole discharge has recently been applied to the construction of a microwave-driven volume H^- source [42].

The highest yield so far reported from a volume source has been obtained in experiments at Culham laboratory [43] using a JET-type positive ion source modified to optimize H^- production. H^- current densities of 57 mA cm^{-2} have been obtained, allowing 134mA of H^- ions to be extracted, accelerated to 100keV and focussed onto a target. The discharge currents required for this are large ($\sim 1000A$), but

the beam obtained is free of impurities and has a very low divergence.

1.3 Objectives of the study and structure of the thesis

In the above discussion, the importance of magnetically-filtered multipole ion sources for the volume production of H^- ions is illustrated. At present, these appear to offer the best hope of developing a useful high-current H^- ion source. To allow optimization of the extracted current density and ion/electron ratio, it is important to understand in some detail the processes by which H^- ions are formed in such a source. Despite much experimental and theoretical effort, these processes remain only partially explained. The presence of the filter field, which appears crucial to the efficient production of H^- ions, imposes a strong spatial variation on the basic plasma in the source. This must also affect the spatial variation of H^- , and comparison of the two may yield information about the dominant H^- production and loss processes. Extraction of ions and electrons from the source samples only that plasma immediately adjacent to the extraction aperture, and the properties of this sample may be distorted by the extraction process. Thus studies of the extracted H^- current density, whilst essential, may miss some clues to the H^- production mechanisms. The object of this study was to investigate the plasma within a filtered magnetic multipole source, and obtain spatially resolved data on the variation of plasma

parameters and ion densities with the alterable arc conditions. Analysis of this, and comparison with the behavior of the extracted H^- current density should yield data on the effects of source operation and in particular magnetic field geometry. Comparison of this data with models of the atomic and plasma physics governing H^- production and loss will help in the development of a comprehensive theoretical picture of a volume H^- source.

The development of models of a multipole H^- source is discussed in chapter 2. Past and contemporary theoretical work on H^- production is described, and adapted for use in this study. The results are used to make an estimate of the H^- ion density expected in one of the sources used. Chapter 3 describes the design and construction of the sources examined in this investigation, and their support systems. Chapter 4 discusses the design, construction and testing of the diagnostic probes used to study the plasma, and the development of a suitable theory to interpret their output. The main experimental results are presented in chapter 5, with detailed discussion and comparison with theoretical models appearing in chapter 6.

CHAPTER 2

Modelling the H^- producing plasma

A model of the plasma in an H^- ion source must consider both the atomic processes creating and destroying H^- ions and the plasma physics of the ion source itself. Simple models of the ionization processes occurring in multipole positive ion sources have been successful in predicting much of their observed behavior, and provide a good basis from which to start modelling a multipole H^- source. A brief resume of these is provided in section 2.1. The relative importance of the different atomic processes involving H^- has often been debated, and a prerequisite of modelling the H^- generating plasma is to determine which of these are dominant. Section 2.2 starts with a short synopsis of past work in this area before considering the atomic processes in detail. The two aspects of the problem are combined in section 2.3 to produce a parametric model of H^- production in a multipole source.

2.1 Ionization in multipole sources

2.1.1 The magnetic multipole ion source

A magnetic multipole ion source consists essentially of a vacuum vessel surrounded by an array of magnets, which form a short range multi-polar field that lines the interior of the source. This field restricts the flow of plasma to the walls, raising the density and reducing plasma noise. Some

means of injecting energy into the source to form the plasma is necessary. The most common is that of an arc discharge from thermionically heated filament cathodes, although a microwave-driven H^- ion source has recently been successfully constructed [42]. Both devices in this study employed filament discharges.

In operation, gas is fed into the source and ionized by impact with fast electrons emitted from the filaments, which may have energies of up to the injection potential. Typically, a fast electron has an energy of several 10's of eV. The short-range multipole field, typically several kilogauss, serves to deflect the fast-moving ionizing electrons away from the anode surface and back into the discharge. These electrons are therefore lost only to the small areas of anode in the cusps between the fieldlines, thus increasing the chances of an electron ionizing a molecule. Since the electron flux to the wall is reduced, the ion current is also reduced and the plasma density for a given energy input is thus increased. It has proved convenient for modelling to assume that the fast electrons form a distinct group with their own separate thermodynamic equilibrium and temperature; these are known as primary electrons. The discharge is thus considered to have two separate Maxwellian electron populations, a situation for which there is considerable experimental evidence.

The distinguishing feature of a multipole H^- ion source is the presence of a magnetic "filter" field. This divides

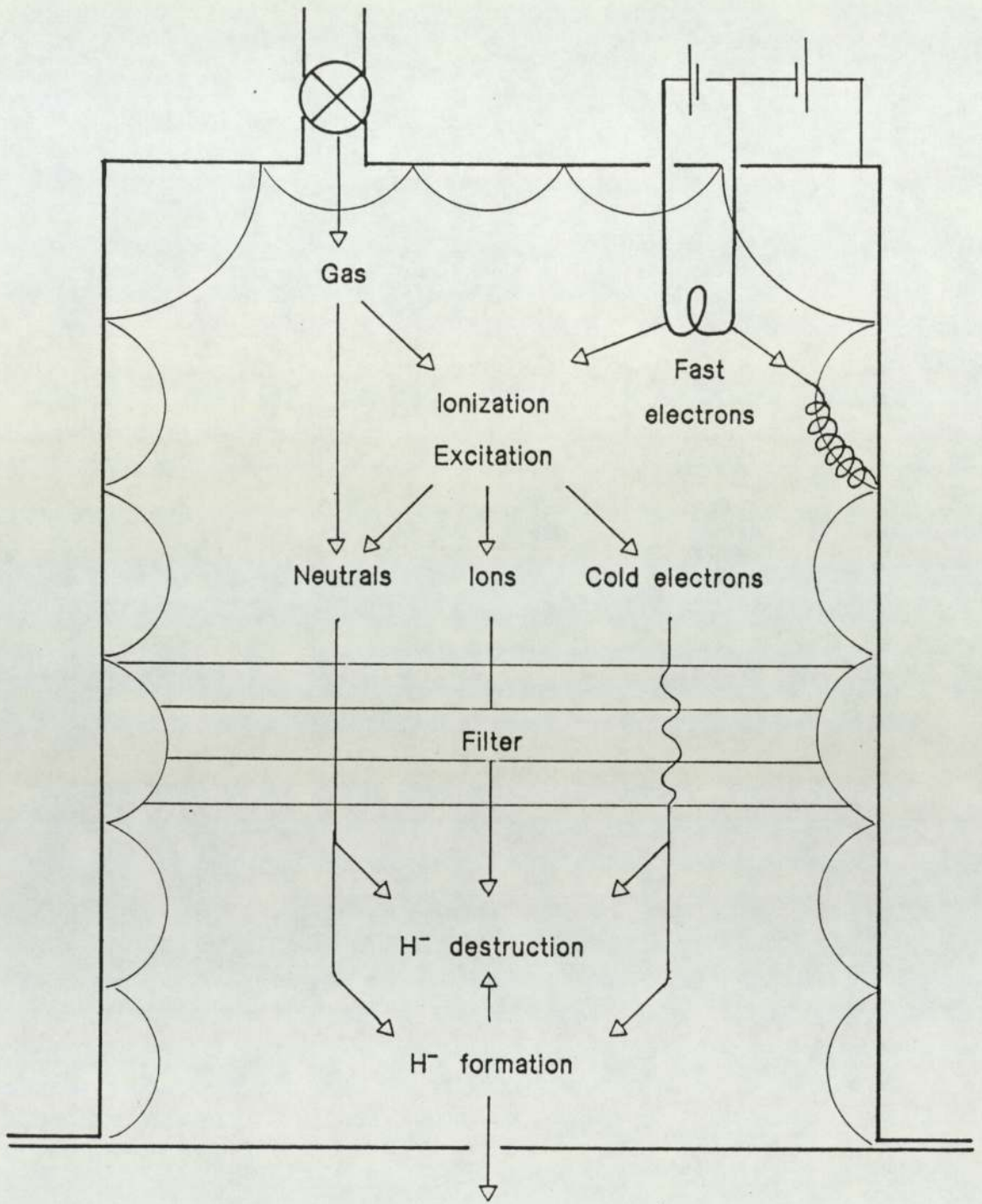


Figure 2.1.1 Schematic diagram of a multipole H⁻ ion source

the region where plasma is generated (the "driver" region) from the region where H^- ions are extracted (the "extraction" region). The geometry differs between sources, but the aim in all cases is the same; to separate the fast ionizing electrons from the fragile H^- ions, and provide a source of electrons "cold" enough to efficiently use the atomic reaction paths outlined in section 2.2. The filter traps electrons into orbiting the fieldlines, from where they may be released by collisions. Colder electrons are more collisional and thus preferentially transmitted through the filter by a random-walk diffusion process. A schematic diagram of a multipole H^- ion source is shown in figure (2.1.1). The interior of one of the sources built for this study may be seen in figure (3.4.3), with the source in operation. The plasma is mainly visible around the filament. The confinement of the plasma by the multipole field may also be seen at the source walls.

2.1.2 Modelling the basic multipole discharge

Simple models based on the balance between the production and loss of charged particles in unfiltered multipole sources have been generated by several workers. Limpaecher and MacKenzie [24] used this approach in characterizing the first multipole source. That of Green et al [26] has been continually successful in predicting the behavior of positive ion sources, and has been used as a basis for many other models. Hopkins and Graham [44] have

recently developed a model of the driver region of a negative ion source which incorporates the work of Hershkowitz et al [45,46] on the leakage of particles through the multipole cusps. The latter have shown that the cusp width varies according to the type of particle; primary electron loss is determined by the primary Larmor radius, thermal electrons encounter a wider cusp determined by a multiple of the hybrid (ion and thermal electron) Larmor radius, and ions a still wider one, of width somewhere between the hybrid and ion radii. Since plasma is thought to be generated mainly in the driver region, many of the parametric dependencies of an H^- source should originate there.

Primary electrons are responsible for the initial ionization of the gas, so a model of the discharge must first consider their equilibrium. Primaries enter the discharge by emission from the filament and acceleration across the space charge sheath surrounding it. They may be lost to the discharge by two methods; collisional scattering below the energy at which the second Maxwellian group hypothesis applies, or loss to the anode. Neutral gas collisions have generally been assumed the dominant scattering mechanism in the relatively low-density multipole plasma. Loss to the anode is affected by the presence of confinement magnets. From Green's work [26] then, the particle balance for primary electrons is given by

$$\frac{I_{arc}}{eVN_p} = N_o \langle ILP \rangle + \frac{1}{\tau_p} \quad \dots(2.1.1)$$

All expressions are as defined in the symbology (appendix E). Here, τ_p represents the confinement time of primary electrons before they are lost to the anode wall. Geometrically, this is given by

$$\tau_p = \frac{4V}{A\bar{v}_p}$$

where V is the plasma volume and A is the effective anode area. In the case of a multipole confinement field with total cusp length L , this becomes [45],

$$\tau_p = \frac{4V}{2r_p L \bar{v}_p} \quad \dots(2.1.2)$$

for a primary Larmor radius r_p . The positive ion particle balance is given by

$$\frac{I_+}{eV} = N_o N_p \langle ION \rangle = \frac{N_+}{\tau_+} \quad \dots(2.1.3)$$

Here, I_+ represents the total ion current to the anode, and

τ_+ is the corresponding positive ion confinement time. The ion flux to the walls is non-random due to the positive plasma potential, so in the case of a multipole field this flux is given by

$$\tau_+ = \frac{V}{C_s r_+ L} \quad \dots(2.1.4)$$

where C_s is the positive ion velocity, given in most cases by the "sound speed". Dividing (2.1.1) by (2.1.3) gives the relation

$$\frac{I_{arc}}{I_+} = \frac{\langle ILP \rangle}{\langle ION \rangle} + \frac{1}{N_o \langle ION \rangle \tau_+} \quad \dots(2.1.5)$$

This does not explicitly deal with the presence of the confinement magnets, but gives good agreement with data from multipole sources. The effects of the confinement field have been considered in [44] for the case of an well-confined driver plasma, by the use of a "source efficiency" factor E. This is defined as $E = VB/L$, where B is the confinement field intensity. If the primary electron temperature may be expressed as a fraction ϕ_1 of the discharge voltage, the primary and ion confinement times can then be expressed in

terms of E and Varc:

$$\tau_p = \alpha_1 E \phi_1 V_{arc}^{-1} \quad \dots(2.1.6)$$

$$\tau_+ = \alpha_2 E T_e^{-1} \quad \dots(2.1.7)$$

Where α_1 and α_2 are constants determined by the units of E. This allows (2.1.1) and (2.1.3) to be combined to yield an expression for the plasma density

$$N_+ = \frac{N_o \langle ION \rangle \alpha_2 E I_{arc}}{e V T_e [V_{arc} (\alpha_1 E \phi_1)^{-1} + N_o \langle ILP \rangle]} \quad \dots(2.1.8)$$

yielding a pressure scaling showing two regimes; an initial pressure dependence followed by a saturation plateau. This has been shown by it's authors to give good agreement with experimental data obtained from the driver region of a multipole H^- source similar to the fixed-filter device described in chapter 3.2

2.2 Formation of H^- ions in the plasma volume

Attempts to identify the atomic reactions responsible for the formation of negative hydrogen ions in the plasma volume have been numerous. Early attempts to model H^- production in Penning discharges pointed to dissociative attachment to neutrals of slow [47] or fast [48] electrons. In 1973, Prelec & Sluyters [19] reviewed theories of H^- ion production in duoplasmatron and PIG sources observed to produce significant quantities of the ion. They reached the conclusion that H^- ions were formed by polar dissociation of neutral molecules by fast electrons in the periphery of the discharge, where the fractional density of neutrals was highest. The discrepancy between calculated and measured J_- was attributed to difficulties in experimental technique.

Experimental work in the mid 1970's by Kuchinskii [49] and others [50] suggested that H^- formation could occur in a two-stage process, by dissociative attachment of slow electrons to neutrals vibrationally excited in collisions with fast electrons. This reaction proceeds via the intermediate unstable molecular ion H_2^- , the breakup of this producing either H^- and neutral hydrogen or the original components of the ion ("autodetachment"). Evidence in support of this came in 1978 from Allen and Wong [51], who demonstrated a "marked dependence" of the dissociative attachment cross section on the initial vibrational state of the neutral molecule. Bacal [27] measured fractional H^- densities in a low-density multipole plasma and obtained

values approaching 50%, noting also a non-linear dependence of this on plasma density. This also suggested that the principal source of H^- ions was via a two-stage process. Theoretical calculations by Bardsley and Wadehra [52,53] supported this idea, the calculated cross-section for dissociative attachment to $H_2(v)$ showing an increase of a factor of 10,000 as the vibrational level increased from $v=0$ to $v=4$. The greatest increase in H^- production would be in the range $6 \leq v \leq 9$, as the probability of autodetachment increases beyond this. However, measurements of the population density of the first four vibrational levels using an optical technique called CARS [54,55] shows a rapid fall with vibrational level. The existence of a sufficiently high population density in the required range thus requires a suitably-placed high plateau in the distribution, although theoretical calculations [56] appear to support this idea.

An alternative candidate for the target of dissociative attachment is the hydrogen molecule in the metastable electronic state $c^3\pi_\mu$. This has been considered in the past several times [23,57], but rejected as the cross section is low, and the lifetime of the state is reduced efficiently by collisions. However, recent measurements of the population of the lower excited levels using resonant multiphoton ionization [59] indicate an increase in the population of the lower levels with arc current. If this increase is reflected in the higher levels, it may offset the negative factors sufficiently for dissociative attachment to $H_2c^3\pi_\mu$ to

become a significant factor in the high-current devices proposed for neutral beam generation. Little is known, however, of the ro-vibrational structure which is superimposed on the electronic state and the effects this has on the dissociative attachment cross-section. In addition, this species may also lead to the formation of $H_2(v)$ in the required vibrational range via a poorly-understood process involving wall collisions.

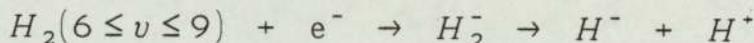
The development of a model for H^- ion production requires firstly that all the possible formation and destruction reactions be surveyed, along with those of intermediaries, for the prevailing conditions. The relevant rates are then examined, and those of the principal reactions summed to obtain a production and loss balance. This survey has been carried out several times for the plasma conditions prevalent in a filtered magnetic multipole source of this size [23,42,56-58] and to perform yet another full survey of all the processes capable of generating H^- and intermediaries would serve no useful purpose. The highest rate processes from the existing surveys have been considered, together with any more recent data available. These are briefly discussed below. A more comprehensive list of processes is present in appendix C, together with cross-sections and references, should this be required. The processes considered important are identified and summarized in figure (2.2.1). The production and loss balance so derived is then used to obtain a numerical estimate of the H^- ion density expected in the

variable-filter source.

2.2.1 Negative ion formation and destruction

2.2.1.1 Formation

The principal H^- formation process is commonly thought to be dissociative attachment to vibrationally-excited molecular hydrogen



cross sections and attachment rates have been calculated by Bardsley and Wadehra [52,53] for the first 9 levels of v . Summed over $6 \leq v \leq 9$, these yield $\sigma = 3 \times 10^{-16} \text{ cm}^2$ and a rate $\langle DA \rangle$ of $1 \times 10^{-8} \text{ cm}^3 \text{ s}^{-1}$ in the extraction region ($T_e \sim 0.4 \text{ eV}$), and $1 \times 10^{-8} \text{ cm}^3 \text{ s}^{-1}$ in the driver region ($T_e \sim 2 \text{ eV}$).

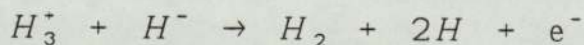
Cross sections for attachment to the metastable electronic state $H_2c^3\pi_u$ have been measured by Botcher and Buckley [60], σ being of the order of 10^{-18} cm^2 for low energies. Reaction rates are $10^{-11} \text{ cm}^3 \text{ s}^{-1}$ for the extraction region and $10^{-9} \text{ cm}^3 \text{ s}^{-1}$ in the driver, orders of magnitude lower than the corresponding dissociative attachment rates for vibrationally excited hydrogen.

Dissociative recombination of electrons with positive ions has been studied extensively by Peart and Dolder [61,63]. The reaction with H_2^+ has a rate of $8 \times 10^{-11} \text{ cm}^3 \text{ s}^{-1}$ at 0.4 eV and $\sim 10^{-10} \text{ cm}^3 \text{ s}^{-1}$ at 2 eV. Measured σ values for

the H_3^+ reaction are of the order of 10^{-19} cm^2 at 2eV and $<10^{-20} \text{ cm}^2$ at low energy, yielding reaction rates of $10^{-12} \text{ cm}^3 \text{ s}^{-1}$ in the driver region, even lower in the extraction region. In addition, maximum ion densities (mostly H_3^+) are ~ 100 times lower than the corresponding neutral density. It therefore appears that dissociative attachment to H^- is the dominant reaction in both regions of the source.

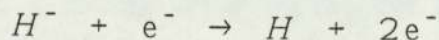
2.2.1.2 Destruction

The most obvious destruction mechanism is mutual neutralization, in this case with H_3^+



Cross sections for the corresponding H^+ process have been measured by Moseley et al [64], and developed into an approximate scaling equation giving the rate coefficient values for variable ionic mass and velocity by Hickman [65]. Using the latter, rates for $\langle MN \rangle$ of $4 \times 10^{-8} \text{ cm}^3 \text{ s}^{-1}$ and $9 \times 10^{-8} \text{ cm}^3 \text{ s}^{-1}$ are obtained for the driver and extraction regions respectively.

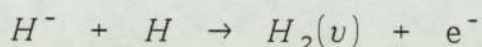
The cross section for H^- detachment by electronic collisions



has been measured by Walton et al [66]. Data is unavailable

below the 3eV value of $5 \times 10^{-16} \text{ cm}^2$, but is probably of the order of $1 \times 10^{-17} \text{ cm}^2$ at 0.4eV. This yields rates for $\langle \text{ED} \rangle$ of $8 \times 10^{-8} \text{ cm}^2 \text{ s}^{-1}$ and $3 \times 10^{-9} \text{ cm}^2 \text{ s}^{-1}$ for the driver and extraction regions. In the case of primary electrons ($T_p \sim 20\text{eV}$) the rate rises to $10^{-6} \text{ cm}^3 \text{ s}^{-1}$. This process is hence of little import in the extraction region, but becomes very significant in the driver, especially when the primary density is high.

Rate coefficients for the associative detachment reaction with atomic hydrogen



have been calculated by Dalgarno and Browne [67], giving values for $\langle \text{AD} \rangle$ of $1.3 \times 10^{-9} \text{ cm}^3 \text{ s}^{-1}$ at low energy ($T_e < 1\text{eV}$). This is small compared to mutual neutralization. However, since neutrals are involved, a high atomic neutral density may offset this. Recent measurements of the atomic hydrogen fraction [69] in the Culham small source have shown that at arc currents of 25A $\sim 2\%$ of the neutral hydrogen may be dissociated, and the fraction increases as a linear function of I_{arc} . This is less important for the low currents used here, but might be thought to have serious implications for higher density devices. However, data obtained from the 1000 ampere discharge in the large Culham multipole [43], where Nightingale's results would indicate high dissociation, indicates that even at these extreme values, loss by mutual

neutralization is still dominant. It is possible that the H_3^+ channels discussed in 2.2.2 below have an important role in H_0 production, not occurring in the H^+ - dominated large source. In addition, Bacal [23] notes that a proportion of $H_2(v)$ molecules created by this process will be in a vibrational level suitable for dissociative attachment, possibly mitigating any losses. Hiskes and Karo [68] have studied other effects of atomic hydrogen on an H^- - generating plasma, and suggest that H_0 may affect the density of vibrationally excited hydrogen.

The loss of negative ions to the wall is governed by the mean free path of H^- , together with electrostatic trapping of the ions by a positive plasma potential. Both of these are controlled by the negative ion temperature, the former by the H^- velocity and the latter by the Boltzmann factor relative to the local plasma potential. Considering the wall-loss first, in the extraction region of the variable-filter source the large unshielded BFE will dominate over loss to any magnetically-screened regions of wall. Assuming the negative ions have a random velocity, the negative-ion confinement time will be given by

$$\tau_- = \frac{4V}{A\bar{v}_-} = \frac{4\pi Z^2 h}{\pi Z^2 \bar{v}_-} = \frac{4h}{\bar{v}_-}$$

where z and h are respectively the radius and height of the extraction region. For a height of 16cm, this yields a

confinement time of

$$\tau_- = \frac{4.1 \times 10^{-5}}{\sqrt{T_-}}$$

The total wall loss rate is then given by

$$\langle W_{ALL_-} \rangle = \frac{e^{-\left(\frac{V_p}{T_-}\right)}}{\tau_-} = 2.4 \times 10^4 \sqrt{T_-} e^{-\left(\frac{V_p}{T_-}\right)} \dots(2.2.1)$$

If the negative ion temperature is low (eg 0.2eV) and the plasma potential is of the order of +1v or greater, the wall loss will be small in comparison to the loss due to mutual neutralization. However, should T_- become large or V_p fall, wall losses will rapidly become important. Recent data obtained from beam-emittance measurements of T_- at Culham [102] has suggested that it may reach values as high as 1eV, indicating that for low V_p , wall losses may indeed be important. Should the plasma potential ever become negative, wall losses of H^- would dominate completely. Bacal [23] suggests that wall losses may be dominant at lower plasma densities in some multipole sources.

2.2.1.3 Summary

H^- production is assumed to occur from dissociative attachment to $H_2(v)$. H^- destruction is assumed to be governed by mutual neutralization and possibly wall losses. In the driver region electron detachment may become a significant loss process, as may associative detachment in

the extraction region. The H^- particle balance is therefore given by

$$N_e N_v = N_+ N_- \langle MN \rangle + N_e N_- \langle ED \rangle + N_H N_- \langle AD \rangle + G N_- \sqrt{T_-} e^{-\left(\frac{v_p}{T_-}\right)} \dots (2.2.2)$$

where G has a value of 2.4×10^4 (eV) s^{-1} for \bar{v}_- in $cm s^{-1}$.

Note that the that the rates for H^- formation are similar both in the driver and extraction regions. However, the $\langle ED \rangle$ rate is greater in the driver by nearly two orders of magnitude, effectively restricting H^- generation to the extraction region.

2.2.2 Formation and destruction of $H_2(v)$

From section (2.1.1), it may be seen that the large dissociative attachment cross section has shifted the dependence of the H^- density to some extent onto the processes populating and depopulating the vibrational levels; these are multifarious, and little data is available for many of them.

2.2.2.1 Formation

The reaction thought to be mainly responsible for populating the high lying states useful for H^- production is known as E-V singlet excitation. In this process, a single collision of a fast electron ($T_p \sim 20$ eV) with a hydrogen molecule leads to an electronically-excited intermediary, decaying

with the emission of a photon to (electronic) groundstate H_2 .



Cross sections for excitation and radiative decay to the different levels have been calculated by Hiskes [70], and yield a value for σ of $\sim 2 \times 10^{-17} \text{ cm}^2$ summed over $6 \leq v \leq 9$. This gives a rate coefficient $\langle E-V \rangle$ of $4 \times 10^{-9} \text{ cm}^3 \text{ s}^{-1}$ in the driver region.

Excitation can occur in a "stepwise" manner as a series of relatively low energy ($T_e \sim 1 \text{ eV}$) impacts, each causing a single level jump in v . Hiskes et al [57] note that the rates for this are relatively small, but increase with density and temperature. They are not relevant here, as they mainly populate the lower vibrational states.

Several different reaction paths leading to $H_2(v)$ are possible from the ground and vibrationally excited states of the H_3^+ ion, including dissociative recombination and proton transfer. These have been considered in some detail by Trow [42]. Due to still-existing gaps in the available data, constants representing unknown fractions of high-level excitation were included. Trow concluded that under extraction-region conditions only, the proton transfer reaction was important, being capable of doubling the total $H_2(v)$ density in the extraction region. However, due to the geometry of his source, the $H_2(v)$ flux from the driver region was small compared to that available from a "traditional"

filtered magnetic multipole, where the driver region feeds a large area over a short drift space. Hence these H_3^+ channels must here be considered negligible in comparison with the $H_2(v)$ feed from the driver.

The mutual neutralization processes for H^- discussed in 2.1.1 will produce $H_2(v)$ molecules, 10% of which Hiskes et al [57] estimate will be in the useful vibrational levels. However, due to the low H^- density the best estimates for the reaction rate are of the order of the dissociative recombination reactions discussed above. Again, these processes are excluded.

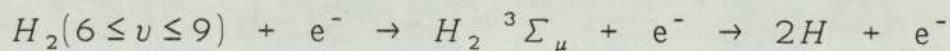
$H_2(v)$ production may occur during wall collisions, through neutralization of positive ions by Auger electrons emitted from the anode surface [71]. Hiskes et al [72,73] estimate that for sources where the positive ions are predominantly H^+ , the surface contribution can double the expected H^- yield. Obviously, this cannot be applied in the H_3^+ dominated conditions here, but similar reactions may occur for H_3^+ . Unfortunately, no data at all is available for these channels.

Finally, Hiskes and Karo [74] suggest that $H_2(v)$ may be produced in very low density ($N_e = 10^9 \text{ cm}^{-3}$) discharges by Auger de-excitation of the metastable electronic $H_2 c^3 \pi_u$ molecule in wall collisions. However, as previously mentioned, the metastable state is destroyed easily by electron collision, and thus at normal multipole densities this reaction will not be important.

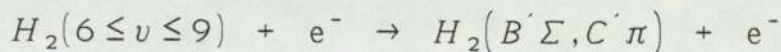
2.2.2.2 Destruction

$H_2(v)$ molecules are lost to H^- production through collisions with ions, neutrals and the walls translating vibrational internal energy into rotational and translational energy [56], and hence de-exciting them. In addition, primary collisions may excite a $6 \leq v \leq 9$ molecule past the useful range into the autodetachment regime, an electronic state or possibly into dissociation or ionization. Finally, the dissociative attachment process itself provides a loss mechanism.

The primary electron de-excitation of $H_2(v)$ may occur through several channels. That through the triplet state $H_2^3 \Sigma_\mu$ leads to dissociation



Reaction rates measured for this by Chan [75] for $v=0$ have allowed Hiskes to infer high-level rates using linear multipliers. This yields a rate of $\langle PE \rangle = 2 \times 10^{-7} \text{ cm}^3 \text{ s}^{-1}$ for the $6 \leq v \leq 9$ levels. The rate for excitation into electronic states



$\langle PD \rangle = 10^{-7} \text{ cm}^3 \text{ s}^{-1}$ is obtained by the same means. The ionization rate for molecular hydrogen under these

conditions, $\langle \text{ION} \rangle = 2 \times 10^{-8} \text{ cm}^3 \text{ s}^{-1}$, contributes little. The effects of these reactions will be represented by the combined primary over-excitation rate $\langle \text{PE} \rangle = 3.2 \times 10^{-7} \text{ cm}^3 \text{ s}^{-1}$.

Hiskes et al [56] consider theoretically the effect of molecular ("V-T") collisions on the $\text{H}_2(v)$ population. Their calculations indicate that the loss rate of $\text{H}_2(v)$ from $6 \leq v \leq 9$ due to these processes is small compared to the wall-loss component. They conclude that the principal effect of this process is to shift molecules in high ($v=14$) states to the useful band. They also note that the rates of production of H^- by this channel from low vibrational states are negligible.

De-excitation by collision with atomic hydrogen has been considered by Hiskes and Karo [68]. They estimate the total rate for this process to be $\sim 2 \times 10^{-10} \text{ cm}^3 \text{ s}^{-1}$ for the useful band. Although larger than the V-T effects, this depends upon the degree of dissociation of the neutral gas. Nightingale et al [69], as previously mentioned, estimate this at $\sim 2\%$ for moderate densities, giving a total loss rate an order of magnitude below that due to wall losses. At very high arc currents, this may become important.

Losses of $\text{H}_2(v)$ due to dissociative attachment are discussed in 2.2.1, and may be neglected in comparison with primary de-excitation.

The effects of wall collisions on $\text{H}_2(v)$ are hard to predict. Not all of the vibrational energy of an $\text{H}_2(v)$ molecule is lost in a single wall collision - they appear to

be able theoretically to survive a number of "bounces" before de-excitation to $v=0$. This number, b , is an important factor in assessing the wall-loss term, and the subject of much debate. Statistical studies [56,68] of this process have given values for b of between 1 and 50 (depending on the vibrational level of the molecule), but for molecules in the levels useful to $\langle DA \rangle$, b is probably near, and commonly taken to be, unity. The wall loss rate is given by

$$\langle WALL_v \rangle = \frac{N_v}{b\tau_v}$$

where τ_v^{-1} , the arrival rate of $H_2(v)$ molecules at the wall, has been estimated at $3 \times 10^4 \text{ s}^{-1}$ [56,57]. This is dominant at low plasma density.

2.2.2.3 Summary

$H_2(v)$ molecules are unaffected by the filter field and may diffuse freely throughout the source. In the absence of any data on H_3^+ channels, $H_2(v)$ production is therefore assumed to be dominated by E-V singlet excitation in the driver; loss by primary excitation at high N_p , and wall losses at lower density. The particle balance is therefore

$$N_o N_p \langle E - V \rangle = N_v N_p \langle PE \rangle + \frac{N_v}{\tau_v} \dots(2.2.3)$$

2.2.3 Summary and use of atomic model

The mechanism most likely to be responsible for the formation of H^- ions in the plasma volume is as follows; fast electrons accelerated across the sheath between the filaments and the plasma in the driver region of the source generate vibrationally-excited molecules in collisions. These collisions generate a population of very cold ($< 1eV$) electrons by ionization and primary cooling. H^- ions are produced by dissociative attachment of these cold electrons to the $H_2(v)$ molecules in the useful ($6 \leq v \leq 9$) band. This band has a relatively high population due to processes re-distributing excitation energy within the $H_2(v)$ group.

The $H_2(v)$ molecules are destroyed by over-excitation in collisions with electrons and de-excitation in wall collisions, the relative magnitudes of these two processes depending on plasma density. The H^- ions are destroyed by neutralization with positive hydrogen ions and collisions with hydrogen atoms. In addition, losses of H^- ions to the walls and in collisions with "warm" electrons may also be important, depending upon the local conditions.

These processes occur in a dynamic balance all through the source. The presence of the filter field inhibits the flow of warmer electrons from the driver to the extraction region, whilst presenting a lesser barrier to cold electrons, and none at all to neutral particles, the populations of which are assumed to be constant throughout the source. Thus the probability of negative ion survival is much enhanced

PROCESS	DRIVER		EXTRACTION		REF
	σ cm ²	$\langle \sigma v \rangle$ cm ³ s ⁻¹	σ cm ²	$\langle \sigma v \rangle$ cm ³ s ⁻¹	

H⁻ Production

1. Dissociative attachment $e^- + H_2(v) \rightarrow H_2^- \rightarrow H^- + H^*$	2×10^{-16}	1×10^{-8}	3×10^{-16}	1.6×10^{-8}	[52-53]
--	---------------------	--------------------	---------------------	----------------------	---------

H⁻ Destruction

2. Mutual neutralization $H^- + H_n^+ \rightarrow H_n + H$	$\langle MN \rangle = (1.0416 \times 10^7 \sqrt{M.T.})^{-1} \text{ s}^{-1}$				[64-65]
3. Electron detachment $e^- + H^- \rightarrow H + 2e^-$	3×10^{-15} 2×10^{-16}	1×10^{-6} 8×10^{-8}	$< 10^{-16}$	1×10^{-9}	[60]
4. Associative detachment $H^- + H \rightarrow H_2(v) + e^-$	-	-	-	1.3×10^{-9}	[67-68]
5. Wall losses $H^- + \text{wall} \rightarrow H + e^-$	$\langle WALL_- \rangle = 2.4 \times 10^4 \sqrt{T.} e^{-\frac{v_p}{T.}} \text{ s}^{-1}$				Pg. 42

H₂(6<v<9) Population

6. E-V singlet excitation $e^- + H_2 \rightarrow H_2^* \rightarrow H_2(v) + e^-$	1×10^{-17}	4×10^{-9}	-	-	[70]
---	---------------------	--------------------	---	---	------

H₂(6<v<9) Depopulation

7. Primary over-excitation $e^- + H_2(v) \rightarrow H_2 + e^-$	6×10^{-16}	3×10^{-7}	-	-	[75]
8. Ionization $e^- + H_2(v) \rightarrow H_2^+ + 2e^-$	3×10^{-17}	2×10^{-8}	-	-	[75]
9. Wall losses $H_2(v) + \text{wall} \rightarrow H_2$	$\langle WALL_v \rangle = \frac{A \bar{v}_v}{4V} \sim 3 \times 10^4 \text{ s}^{-1}$				[61-63]

Figure 2.2.1 Atomic processes used in the model

outside the driver region, giving a higher fractional H^- density. The key atomic processes are summarized in figure (2.2.1).

The particle-balance equations obtained in 2.2.1 and 2.2.2 may be combined to produce a "zero-dimensional model" describing H^- behavior outside the driver region. Assuming both N_p and the $\langle ED \rangle$ process are negligible here:

$$\begin{aligned}
 N_- &= \frac{N_v N_e \langle DA \rangle}{N_+ \langle MN \rangle + N_H \langle AD \rangle + G \sqrt{T_-} e^{-\left(\frac{v_p}{T_-}\right)}} \\
 &= \frac{N_e N_o N_p \langle E - V \rangle \langle DA \rangle}{\left(N_+ \langle MN \rangle + N_H \langle AD \rangle + G \sqrt{T_-} e^{-\left(\frac{v_p}{T_-}\right)} \right) (N_p \langle PE \rangle + \tau_v^{-1})} \\
 &\dots(2.2.4)
 \end{aligned}$$

Stealing a march by using some of the probe results in chapter 5 to obtain electron densities and temperatures, we may now use the above relationship to obtain a numerical estimate of the H^- ion density at the filter peak of the variable-filter source. The following values are used, for a 5A, 60v, 3mT discharge:

<u>Driver region</u>	<u>Filter region</u>	<u>Whole Source</u>	
$N_+ = 10^{11} \text{ cm}^{-3}$	$N_+ = 5 \times 10^{10} \text{ cm}^{-3}$	$N_O = 2 \times 10^{13} \text{ cm}^{-3}$	
$T_e = 1.5 \text{ eV}$	$T_e = 0.73 \text{ eV}$	$N_H = 2 \times 10^{11} \text{ cm}^{-3}$	[69]
$N_p = 10^{10} \text{ cm}^{-3}$	$N_p = 0$	$T_- = 0.3 \text{ eV}$	(est.)
$T_p = 16 \text{ eV}$	$V_p = +1.75 \text{ v}$	$T_O = 1500 \text{ K}$	[69]

N_+ is approximately equal to N_e throughout. Using the following rate coefficient values (in $\text{cm}^3 \text{ s}^{-1}$):

$$\begin{aligned} \langle E-V \rangle &= 4 \times 10^{-9} & \langle MN \rangle &= 6.5 \times 10^{-8} & \langle PE \rangle &= 3.2 \times 10^{-7} \\ \langle DA \rangle &= 1.6 \times 10^{-18} & \langle AD \rangle &= 1.3 \times 10^{-9} \end{aligned}$$

b is assumed to be 1, yielding a τ_v value of approximately 33 μs , thus N_- is given by

$$\begin{aligned} N_- &= \frac{5 \times 10^{10} \quad 2 \times 10^{13} \quad 10^{10} \quad \langle 4 \times 10^{-9} \rangle \quad \langle 1.6 \times 10^{-8} \rangle}{(5 \times 10^{10} \langle 6.5 \times 10^{-8} \rangle + 2 \times 10^{11} \langle 1.3 \times 10^{-9} \rangle + 39)} \\ &\quad \times (10^{10} \langle 3.2 \times 10^{-7} \rangle + 3 \times 10^{-4})^{-1} \\ &= 5.4 \times 10^9 \text{ cm}^{-3} \quad \dots(2.2.5) \end{aligned}$$

As will be seen in chapter 5.2.1, this value is within ~20% of the H^- density measured with Langmuir probes at the filter peak of the variable filter source, implying that the processes considered above are very probably those responsible for the volume generation of H^- ions.

2.3 Parametric dependence of an H^- generating plasma

The parametric variation of N_- may be examined by substituting results from section 2.1 into the equilibrium relations obtained above. In order to do this, it is necessary to make assumptions about the spatial distributions of the particles. All neutral densities are assumed spatially invariant, as neutrals are not directly affected by the filter. This is almost certainly an over-simplification [68], and is considered in more detail later on, but will do for a first approximation. H^- production and loss is thus assumed to be controlled entirely within the driver region. The wall loss rate of H^- is assumed constant with arc conditions. From the calculation in section 2.2, it may be seen that for a low T_- , wall losses are $< 1\%$ of the total H^- loss term. For a first stage, with T_- estimated as 0.3eV, wall losses may therefore be ignored. Finally, it is necessary to relate the atomic hydrogen density to the plasma density. Assuming H_0 is generated primarily by electronic dissociation of H_2 and loss is dominated by the walls, the relevant rates may be obtained from [75] and the gas temperature (estimated at 1500 K, $\sim 0.15\text{eV}$). Trow [42] points out that the wall loss must be modified by a survival probability of 86%, so with a neutral dissociation rate $\langle ND \rangle = 3 \times 10^{-9}$ [69] and a neutral mean free path of 15cm:

$$\begin{aligned}
N_H &= 2 \frac{\tau_H}{0.14} N_p N_o \langle ND \rangle \\
&= 2 \frac{2.5 \times 10^{-5}}{0.14} 2 \times 10^{13} 10^{10} \times \langle 3 \times 10^{-9} \rangle \\
&= 2 \times 10^{11} \text{ cm}^{-3} \quad \dots(2.3.1)
\end{aligned}$$

close to that expected from values obtained experimentally [69]. Thus N_H may be replaced by the expression $3.6 \times 10^{-4} \langle ND \rangle N_p N_o$. From eqn. (2.1.3), N_p may be expressed in terms of the positive ion density:

$$N_p = N_+ (N_o \langle ION \rangle \tau_+)^{-1}$$

so

$$N_H = \frac{3 \times 10^{-4} \langle ND \rangle N_+}{\tau_+ \langle ION \rangle}$$

Thus eqn. (2.2.4) may be re-written as

$$\begin{aligned}
N_- &= \frac{N_e N_o N_p \langle EV \rangle \langle DA \rangle}{N_+ (\langle MN \rangle + 3 \times 10^{-4} \langle ND \rangle \langle AD \rangle (\tau_+ \langle ION \rangle^{-1}))} \\
&\times \frac{1}{(N_p \langle PE \rangle + \tau_v^{-1})} \quad \dots(2.3.2)
\end{aligned}$$

The parameter dependencies of N_+ and N_e will be the same, and thus cancel each other. N_- is then governed by N_p , and therefore by events in the driver region. Two regimes are indicated; at low primary density, the loss of $H_2(v)$ molecules by primary over-excitation is low, and the negative ion fraction is limited by losses of $H_2(v)$ to the wall. Under these conditions, N_- varies directly with both N_o and the driver primary density. At higher primary densities, loss of $H_2(v)$ by primary over-excitation dominates, and the explicit dependence of N_- on N_p is removed due to the N_p dependence of the $\langle PE \rangle$ term. N_- is then only dependent on N_o , and on the variations of the rate coefficients. The wall bounce factor b will be important in determining the transfer point between the two regimes, but its value is not well known.

The parametric dependency of N_- may be obtained from eqn's (2.1.1) and (2.1.6);

$$N_p = \frac{I_{arc}}{eV} \left(N_o \langle ILP \rangle + \frac{V_{arc}}{\alpha_1 E \phi_1} \right)^{-1} \dots(2.3.3)$$

substituting this into (2.3.2) yields

$$N_- = \frac{N_e N_o I_{arc} \langle E - V \rangle \langle DA \rangle}{N_+ e V \left(N_o \langle ILP \rangle + \frac{V_{arc}}{\alpha_1 E \phi_1} \right)}$$

$$\times \frac{1}{\left[\langle MN \rangle + \frac{3 \times 10^{-4} \langle ND \rangle \langle AD \rangle}{\tau_- \langle ION \rangle} \right] \left[\frac{I_{arc} \langle PE \rangle}{e V} \left(N_o \langle ILP \rangle + \frac{V_{arc}}{\alpha_1 E \phi_1} \right)^{-1} + \tau_v^{-1} \right]}$$

...(2.3.4)

Since N_p is a direct function of I_{arc} , the saturation behavior of N_- with N_p is repeated for arc current. However, the pressure and voltage scaling of N_- below saturation will differ according to the dominant primary electron loss term: if this is inelastic gas collision, the pressure dependence below saturation will be removed; if wall losses, an inverse dependence of N_- on V_{arc} is introduced.

This relationship is a modified version of that obtained by Green et al [102], in which all wall losses were neglected. The wall-loss free version has been tested against extracted H^- current density data obtained from both the large and small Culham sources [43]. However, although good agreement is obtained in the saturation regime, this tacitly assumes that the negative ion velocity in the extraction system remains constant with I_{arc} . This may not be the case as the origin of v_- is unclear, and testing of

this theory against N_2 data is necessary. Note that in a source where primary losses are dominated by gas collisions, the pressure dependence below saturation is removed. The explicit inverse dependence of V_{arc} in a source where primaries are lost mainly to the walls must be considered in relation to the implicit arc voltage dependencies introduced by the rate coefficients. One of the other uncertainties in this discussion concerns the role of the H_3^+ ion in formation and destruction of $H_2(v)$ molecules, particularly in conjunction with the anode wall. These and other points are discussed in more detail in chapter 6.2.

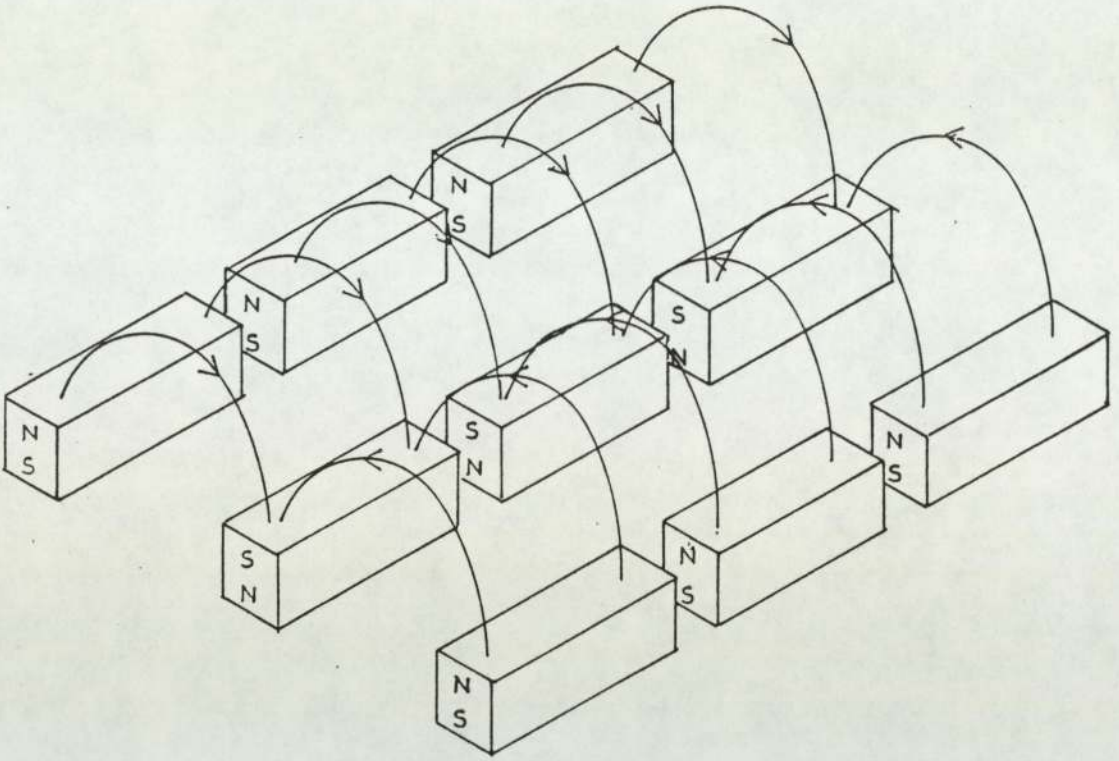
CHAPTER 3

Construction and operation of the multipole sources

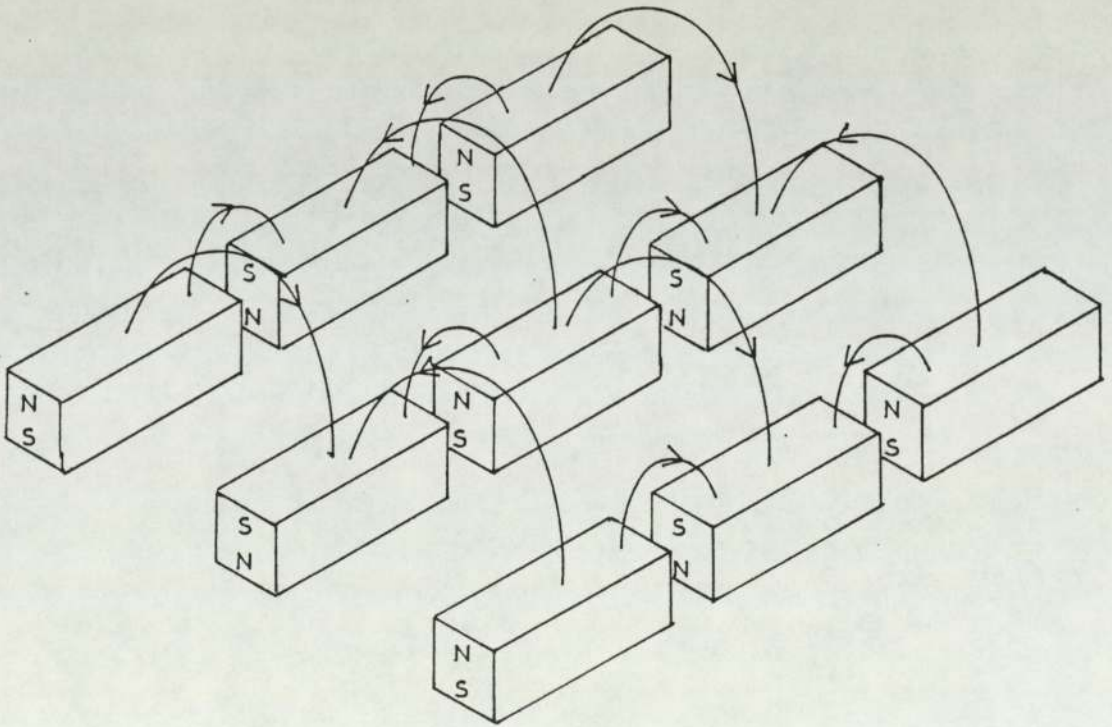
The design of both of the magnetic multipole sources used in this investigation is broadly similar. This being the case, section 3.1 describes the "generic" design of the multipole sources used to study the production of H^- ions. The experimental programme required the design and construction of one such source, and the development, construction and testing of diagnostic systems for both this and another already - existing source. The two sources are described in detail in sections 3.2 & 3.3. Section 3.4 describes the practical operation of a multipole source.

3.1 Generic design of the multipole H^- sources

The sources were constructed in a very similar way to a positive ion multipole source. This consists of a rectangular box-shaped vacuum vessel with walls of 1cm thick stainless steel or copper. Into the outside of five of these walls are machined slots into which high-intensity cobalt-samarium bar magnets are fitted. These are arranged to provide as short a range field as possible, usually by means of one of the two configurations, line-cusp or checkerboard, shown in figure (3.1.1). Of these, the line-cusp screens the anode more completely, but when only a few lines are present it can generate unwanted long-range



(a) Line - cusp array



(b) Checkerboard array

Figure 3.1.1 Multipole magnet configurations

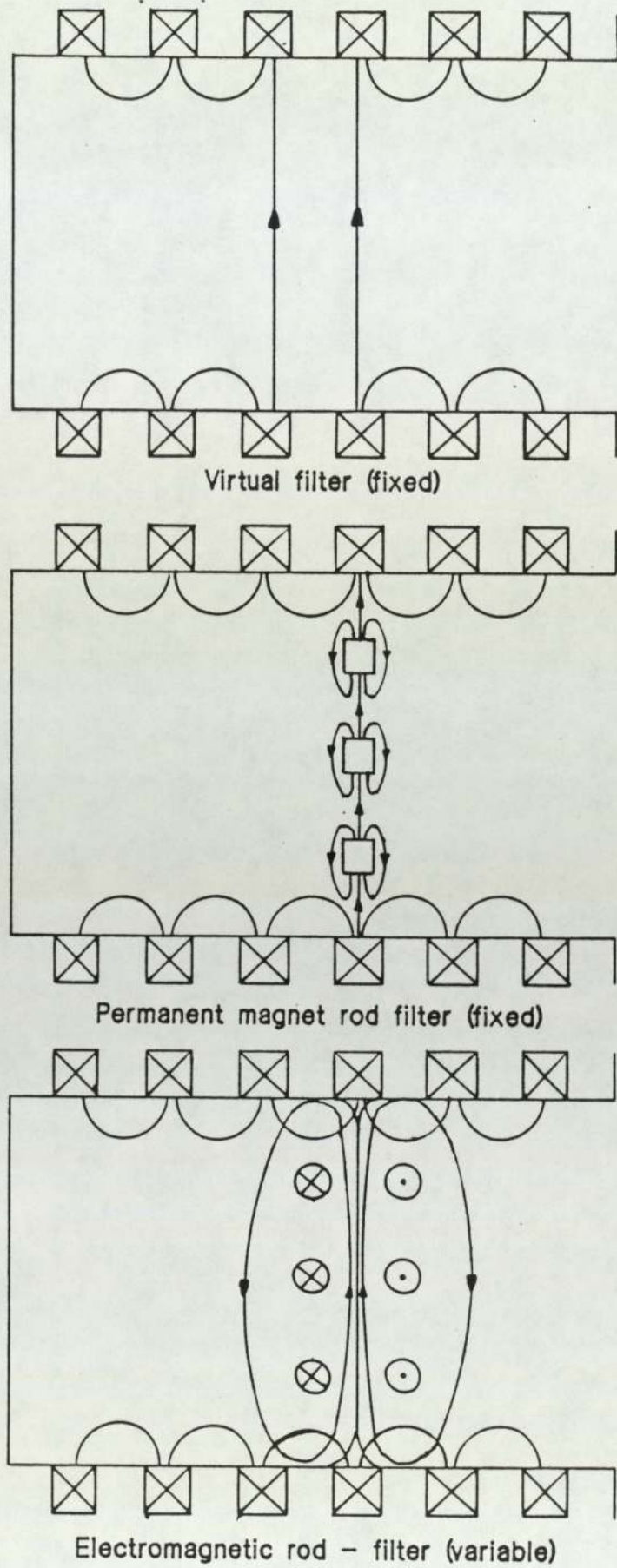


Figure 3.1.2 Types of magnetic filter

fields. Other channels carry water for cooling the anode. The sixth side of the source is formed by a cooled conducting plate, isolated from the rest of the source and capable of being biased relative to it. This is where the aperture through which H^- ions are extracted is situated, and consequently has become known as the beam-forming electrode (BFE), a term used even when no beam is extracted. The BFE itself is unshielded by magnetic fields, but the aperture is commonly screened by some form of short-range field to help reduce the extracted electron current.

The filter field may be generated either by means of a series of physical magnetic poles in the plasma (rod filter) or by means of long-range fields obtained by rearranging the multipole magnets on the exterior of the source (virtual filter). A virtual filter is easily built and non-intrusive, but the field of a rod-filter may be made much stronger. There is some debate about their relative effectiveness in terms of H^- production [76,77].

3.2 The fixed-filter source and beamline

This section describes the first of the two experimental assemblies used in the investigation. This consisted of a multipole source with a virtual filter of fixed intensity, mounted on a triode accelerator stack which was fixed to a horizontal 2.2m beamline. H^- ions could be extracted at a potential of up to 40kV, and analysed using beam diagnostics in the beamline vacuum vessel. Extraction was performed by

raising the source to a high negative potential, enabling the diagnostic systems in the beamline to remain at ground potential. However, this required that the services (power supplies, gas feed, vacuum etc.) for the source be raised to the same potential, and operated remotely.

3.2.1 The ion source and accelerator

This is shown in schematic form in figure (3.2.1), and consisted of a 24 x 20 x 20 cm stainless-steel box, following closely the generic design outlined in section 3.1. Service and diagnostic access ports fitted with VG 34mm metallic seals were mounted on all faces except the beam-forming electrode. Two pairs of high-current vacuum feedthroughs were mounted on opposite sides of the source, 8cm from the backplate. Between each pair a 1mm dia. tungsten wire filament was connected. A motorized metal-seal leak valve capable of remote operation (VG, type MD6-M) was connected to a service port on the backplate. Gas was fed to this via a flowmeter (MKS, type ST50), and a sealed-reference baratron (MKS, type H120) was mounted on a service port to calibrate it. The magnets were arranged in a line-cusp configuration, yielding a multipole field of peak value ~ 2 kilogauss, extending some 3cm into the source volume. The entire BFE, together with the other extraction electrodes, could be moved toward the backplate using spacing formers.

The virtual filter field was generated by one line of reversed external magnets, the second line from the BFE. The

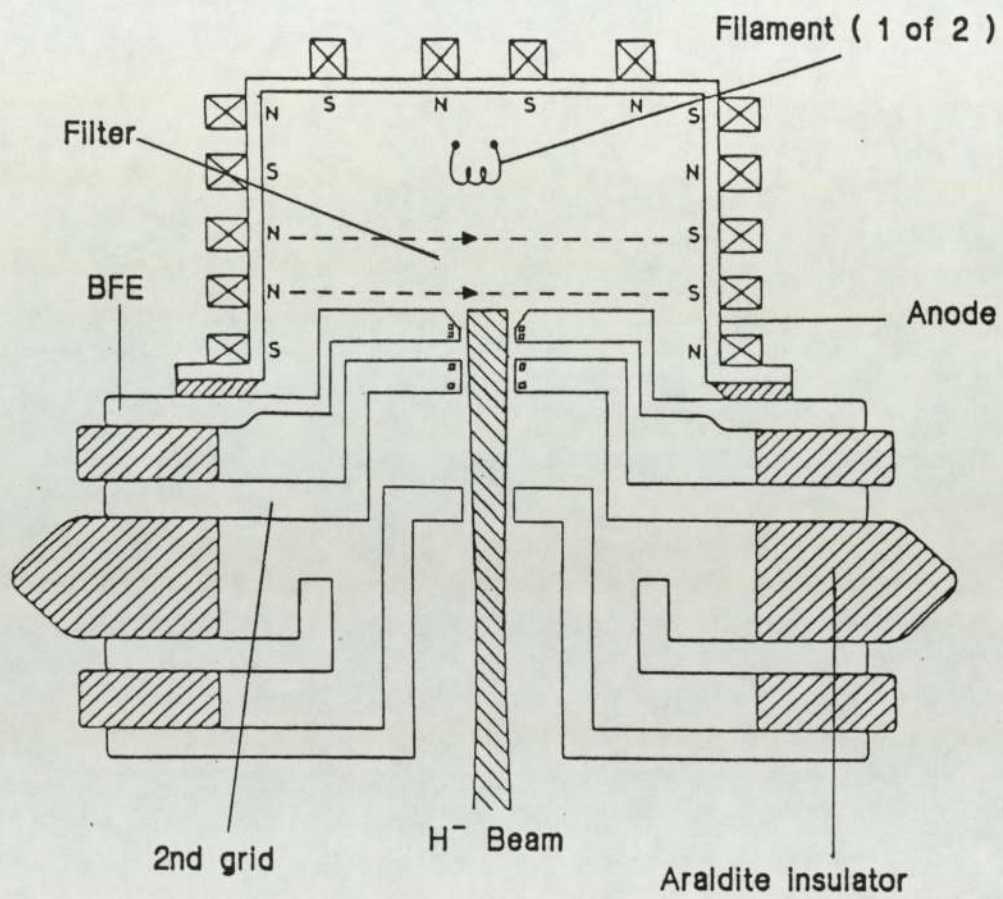


Figure 3.2.1 Schematic of fixed filter source and accelerator

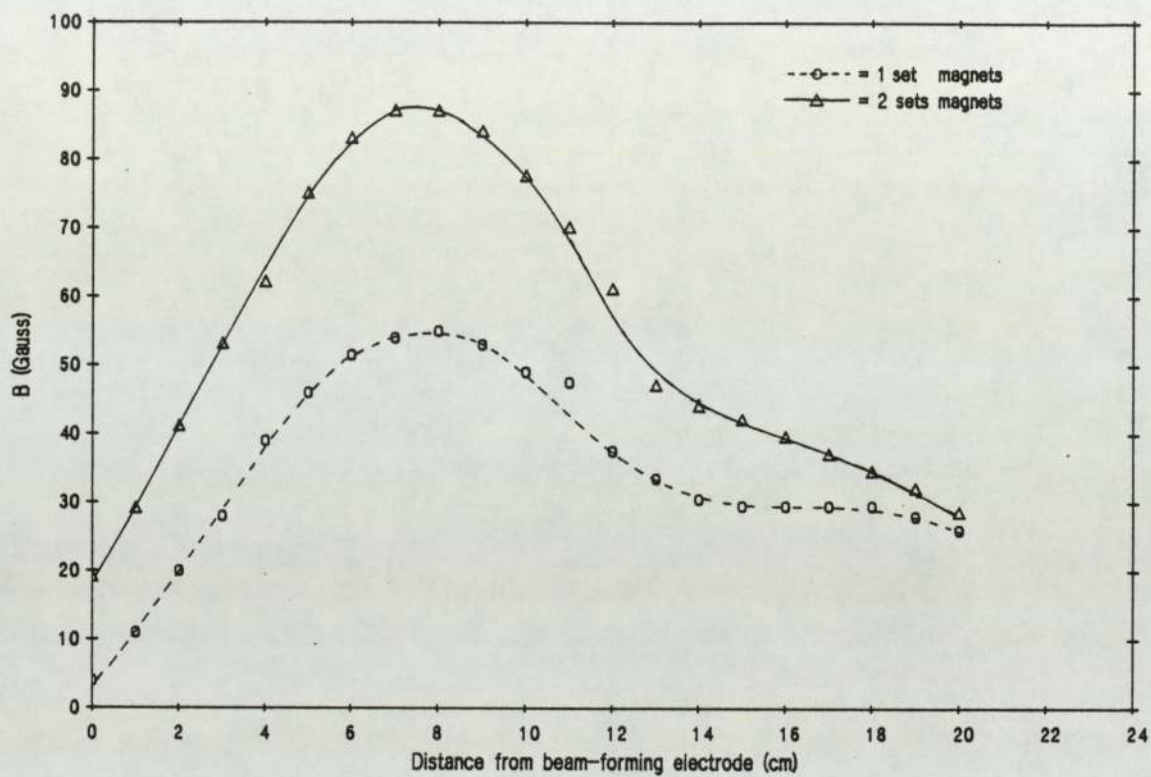


Figure 3.2.2 Axial variation of filter-field intensity
Fixed-filter source

field intensity as a function of distance is shown in figure (3.2.2). Both the filter field and that generated by the BFE suppressor magnets had the same sense. The addition of a second row of magnets attached top and bottom to the filter magnets produced an increase in field intensity, also shown in figure (3.2.2).

The accelerator was a tetrode device, but the third and fourth electrodes were both connected to ground, forming a triode. The insulators were 8cm thick araldite castings. The electrodes (grids) were watercooled copper rings, with replaceable aperture plates whose separation could be varied. The BFE housed two pairs of small cobalt samarium magnets covered by a watercooled plate as shown in figure (3.2.3). These formed an octupole electron suppression field of intensity ~ 100 gauss, which caused no net deflection or displacement of the H^- beam. More magnets were mounted in the electrodes above and below the aperture in the second grid, forming the quadrupole electron trap also shown in figure (3.2.3). The purpose of these was to deflect any extracted electrons onto the second grid, allowing H^- ions to pass through with only a small (~ 1 cm) displacement from the axis. The second grid was held at about 10% of the full acceleration potential, to reduce the power drain due to these extracted electrons. The suppressor and trap filtered out 90% of the electrons before the main acceleration took place, and deflected the remaining 10% so they impacted the third grid without leaving the accelerator.

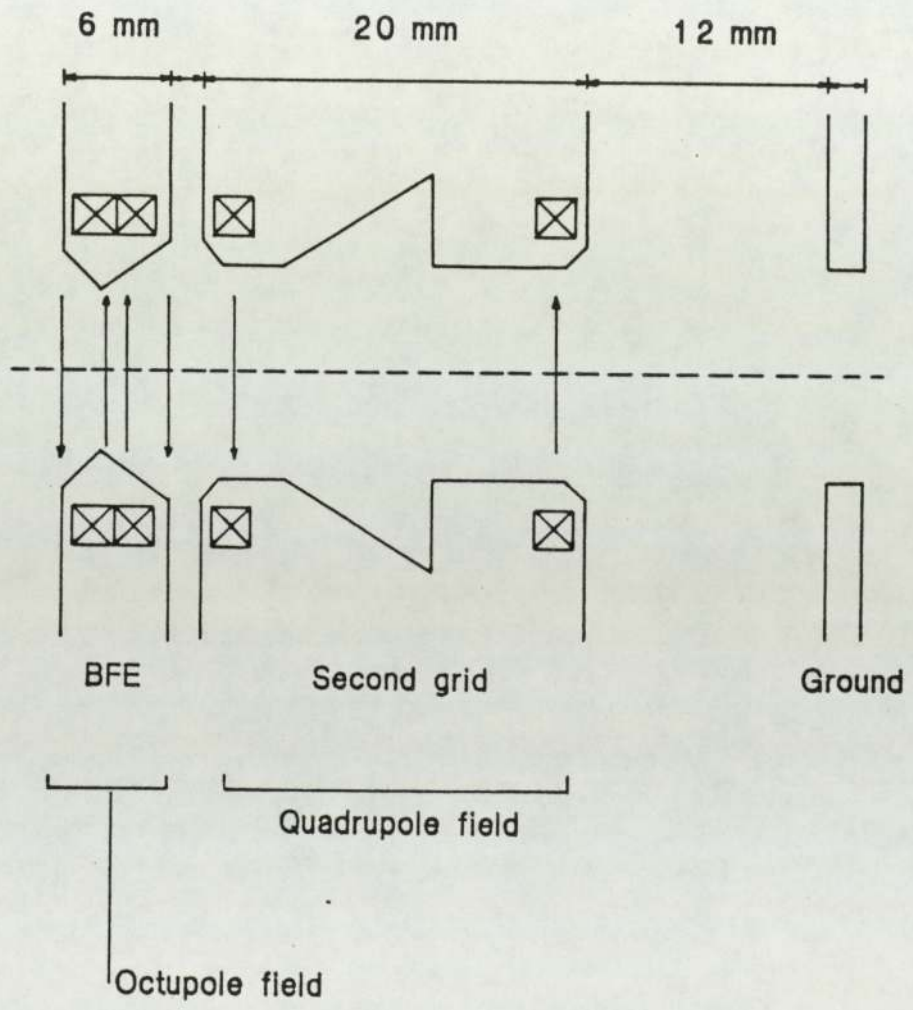


Figure 3.2.3 Electron control magnets in the accelerator

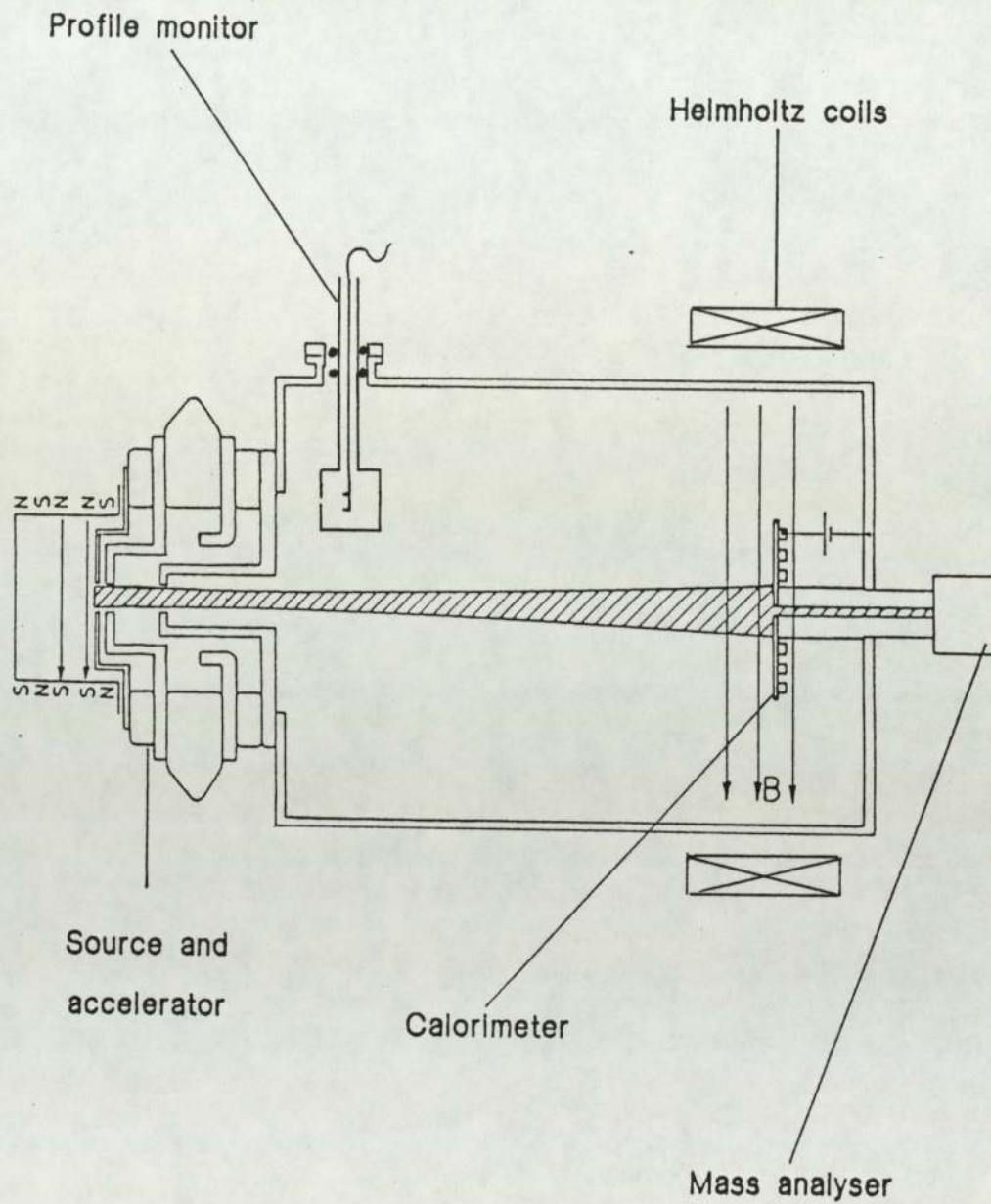


Figure 3.2.4 Schematic diagram of the beamline

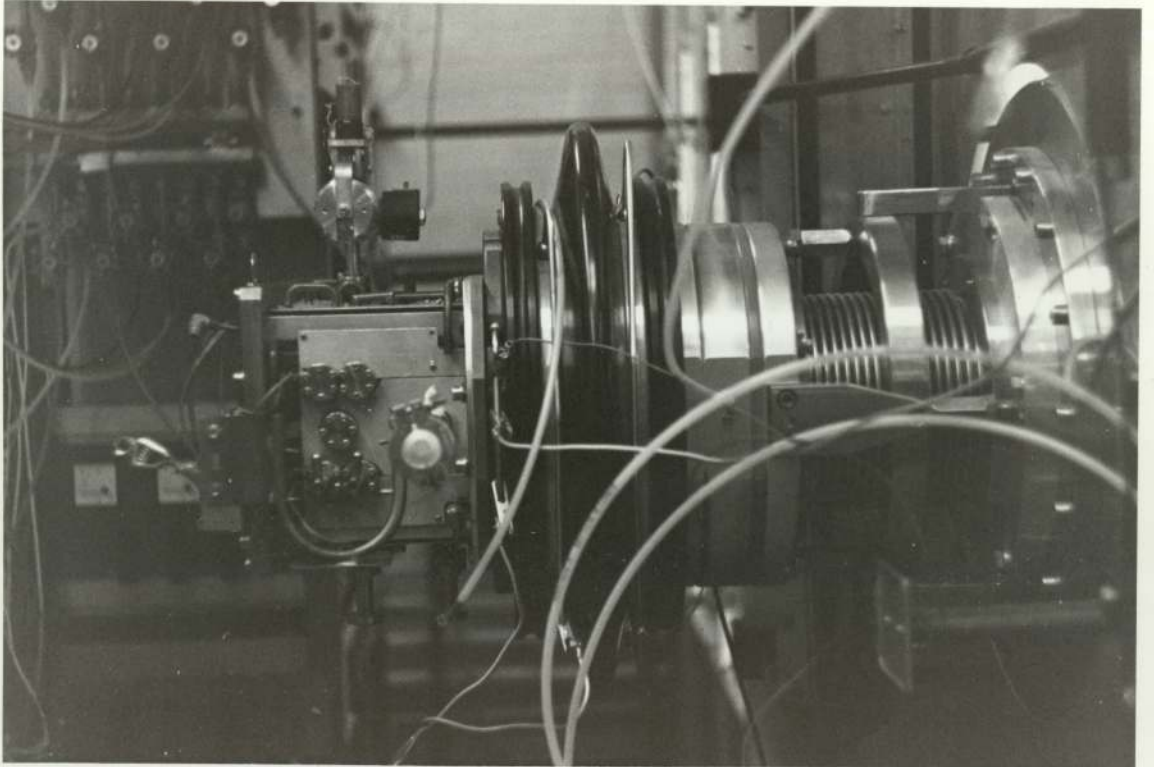


Figure 3.2.5 Fixed filter source, accelerator and bellows

3.2.2 The beamline

This is shown in schematic form in figure (3.2.4). The beamline consisted of a 2.2 metre long vacuum vessel approximately 1m in diameter, assembled from two stainless steel vessels. Apart from the ports for the pumping and vacuum measurement apparatus, the beamline was fitted with four 16cm diagnostic ports, a large 50cm diameter end port, and a 25cm viewport on top. Diagnostic apparatus was mounted internally, as described later on. Connections to these diagnostics were made via vacuum feedthroughs mounted on the diagnostic ports. The source / accelerator assembly was mounted onto the beamline via a stainless-steel bellows mounted in an adjustable frame, which allowed the beam generated by the accelerator to be steered. The source and accelerator may be seen mounted on the beamline via the bellows in figure (3.2.5).

3.2.3 The vacuum system

This is shown in schematic form in figure (3.2.6). The pumping apparatus consisted of a turbomolecular pump (Leybold-Hereaus, type TMP 1500 LF), backed by a tri-vane ballasted rotary pump (Leybold-Hereaus, type D60A), with a total throughput of 1500 ls^{-1} . The system was controlled by three electropneumatically-operated valves, two of 10cm bore in the roughing and backing lines, and one 50cm dia. gate valve mounted above the turbopump. These were controlled by interlocks, which also cut the H.V supply if a leak occurred.

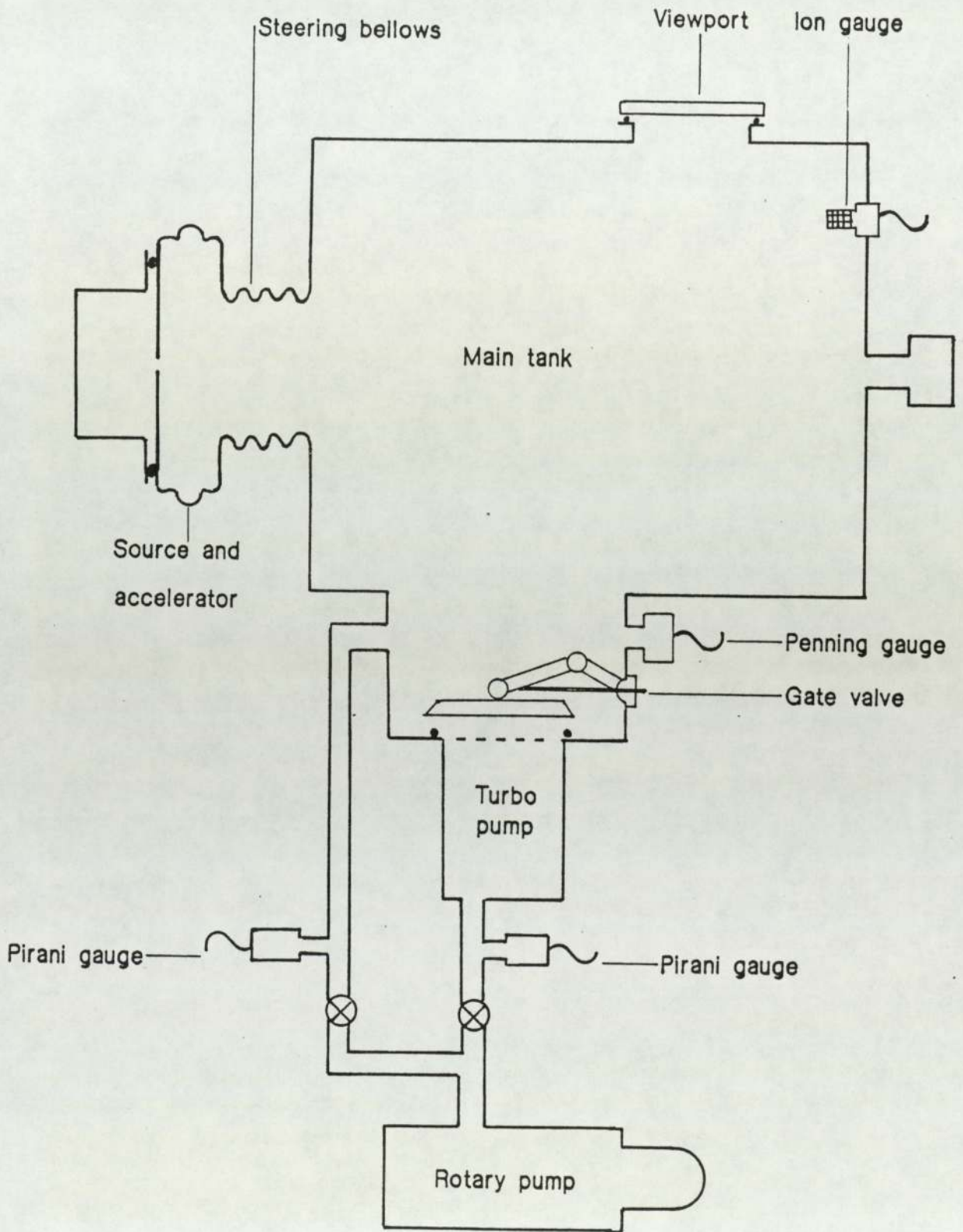


Figure 3.2.6 Schematic of vacuum system for fixed-filter source

Pressure in the system when near atmospheric was measured by Pirani gauges (Edwards, type 1101/PRL10) fitted to the roughing and backing lines. At lower pressures, Penning gauges (Edwards 1102, Leybold-Hereaus CM330) were employed, mounted on the beamline above the turbopump. An ionization gauge (VG, type IG-125A) was fitted to the beamline proper for high-vacuum measurements. The ultimate pressure, achievable after a 24-hour pumpdown was about 6×10^{-6} mTorr. However, due to the small size of the extraction aperture through which the source was pumped, the pressure in the source was typically an order of magnitude higher than that in the beamline. This gave a percentage residue of impurity gases under normal operating conditions of less than 1%.

3.2.4 Power supplies

A schematic diagram of the supply circuits is shown in figure (3.2.7). The arc and filament supplies were constructed in-house using transistors with a current capacity of >100A, and required watercooling. Power input to these was provided by means of a 40kV isolation transformer, which also supplied the other services. The BFE bias supply was a 100A 30v DC unit (Farnell, type H30/100). The main HT supply was manufactured by Hunting Ltd. (type 2400), and was capable of supplying 56mA at 60kV. The second grid "gradient" supply was a DC unit (HML, type 400) with a capacity of 50 mA at 7.5kV. With the exception of the main

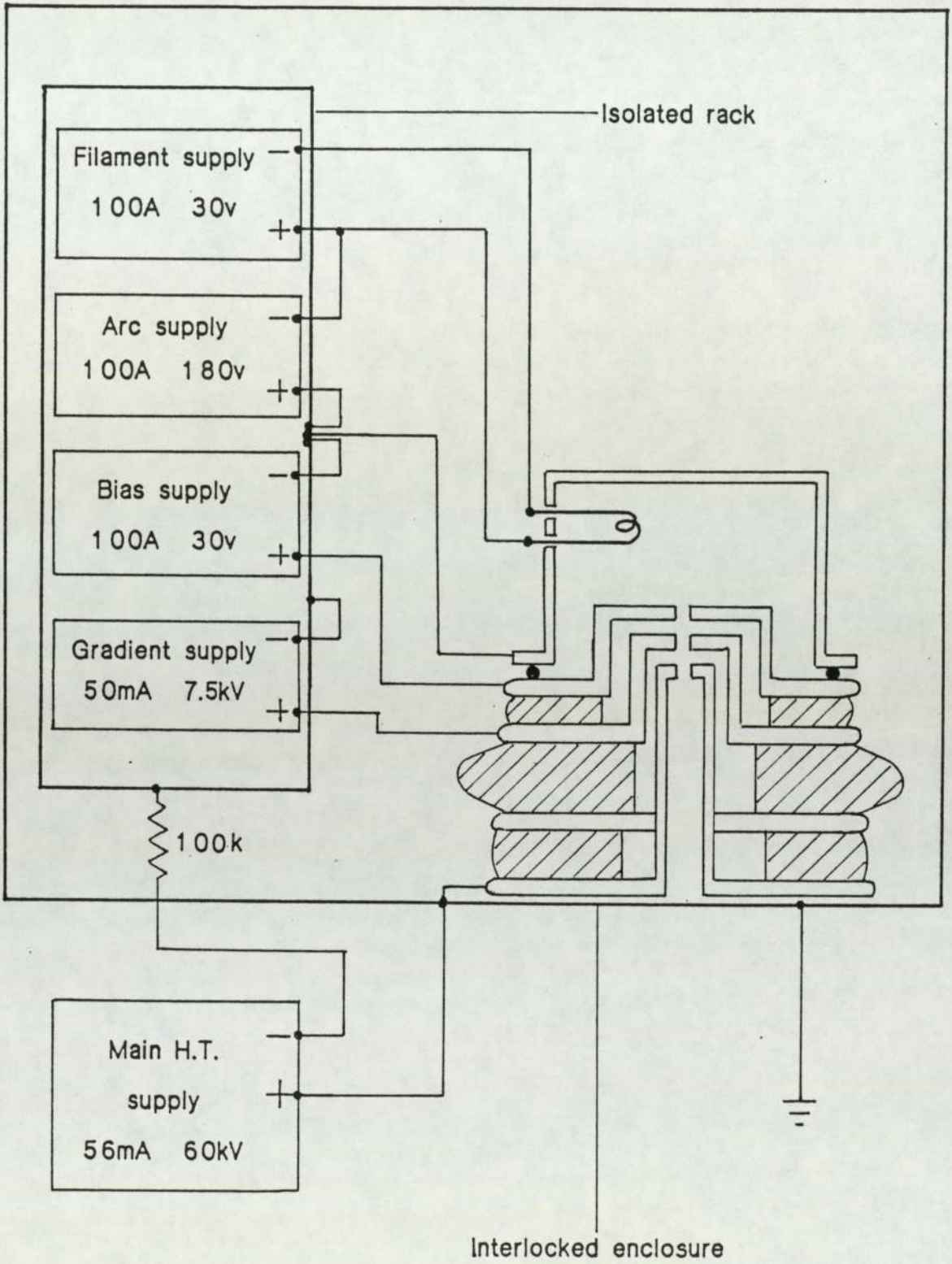


Figure 3.2.7 Schematic of fixed filter source power supplies

HT supply, all of the above units, together with the gas bottle, were mounted on an insulated plinth inside an interlocked enclosure. The beamline ran from inside this enclosure, thus isolating the source and all support systems from human contact. All controls were adjusted by means of 1 metre long insulated rods, and meters were read through earthed perspex windows. Interlocks detecting the presence of cooling water and the temperature of the source body were fitted to prevent the source overheating, and to the enclosure itself to prevent access whilst the source was running. Tripping any of these interlocks caused all the power (including the HV) to be cut off.

3.2.5 Diagnostic systems

The beamline carried four main beam diagnostics; a multi-element Faraday-cup and power calorimeter, a magnetic deflection mass analyser, a motorized beam profile monitor and a computer-driven Allison-type emittance probe. The latter two used the same port on the beamline, and were thus not used simultaneously. The positions of these diagnostics are indicated in figure (3.2.4).

The calorimeter consisted of a 2.75cm dia. central disk and a 9.7cm dia. inner ring, surrounded by a 20cm outer ring split into four segments. The disk and inner ring were water-cooled, with thermocouples allowing temperature differentials between inlet and outlet to be measured. They could also both be used as Faraday cups. The outer ring

functioned solely as a segmented Faraday cup, and was primarily used to detect an off-centre beam, and check the beam focus. In order to deflect any electrons emerging from the accelerator traps, a pair of Helmholtz coils capable of generating a field of ~ 20 gauss were mounted external to the tank either side of the calorimeter assembly, as shown in figure (3.2.4)

The mass analyser consisted of a pair of 0.05cm wide collimation slits in front of a line of five 0.05cm dia. apertures, each masking a small Faraday cup. Between the collimator and the apertures, the collimated beam passed between the poles of a large electromagnet. The signal obtained from any of the Faraday cups would yield a peak whenever the trajectory followed by an ion in the magnetic field matched the geometry of the system, allowing separation of ionic species using the field strength.

The profile monitor consisted of a 0.05cm dia. pinhole, masking a grid and Faraday cup mounted on a motorized sliding probe 0.7m long. This probe passed into the beamline through a piston seal. In use, the collector was biased positive relative to the beamline, the grid negative to the cup to suppress secondaries, and the probe moved slowly through the beam. The current collected by the cup as a function of position then gave the beam profile.

3.3 The variable-filter source

This section describes the second of the two experimental assemblies used. This was a hybrid of two multipole chambers, and consisted of a small rectangular source mounted on a cylindrical flange housing a variable electromagnetic rod-filter. The rectangular module formed the driver region, and the variable filter flange the extraction region. These were mounted vertically on a specially-modified pumping stand. The principle objective of this assembly was to allow spatially-resolved measurements of the multipole plasma to be made as a function of filter intensity and other discharge conditions. The probes used to do this are described in detail in the next chapter.

3.3.1 The ion source

Figure (3.3.1) shows a diagram of the variable filter source assembly. As mentioned above, it consisted of two separate units. The driver module comprised a stainless steel box-type source 11 cm deep, with a cross section of dimensions identical to those of the fixed filter source described in section 3.2. Service and diagnostic ports fitted with VG 34mm metal-seals were mounted on five faces. One of the diagnostic ports on the backplate carried a VG 70mm metal seal to accommodate the mass analyser probe. A pair of high-current vacuum feedthroughs were mounted on one of the long side walls, 4cm below the backplate. A single 1.5mm dia. tantalum wire filament was connected between them.

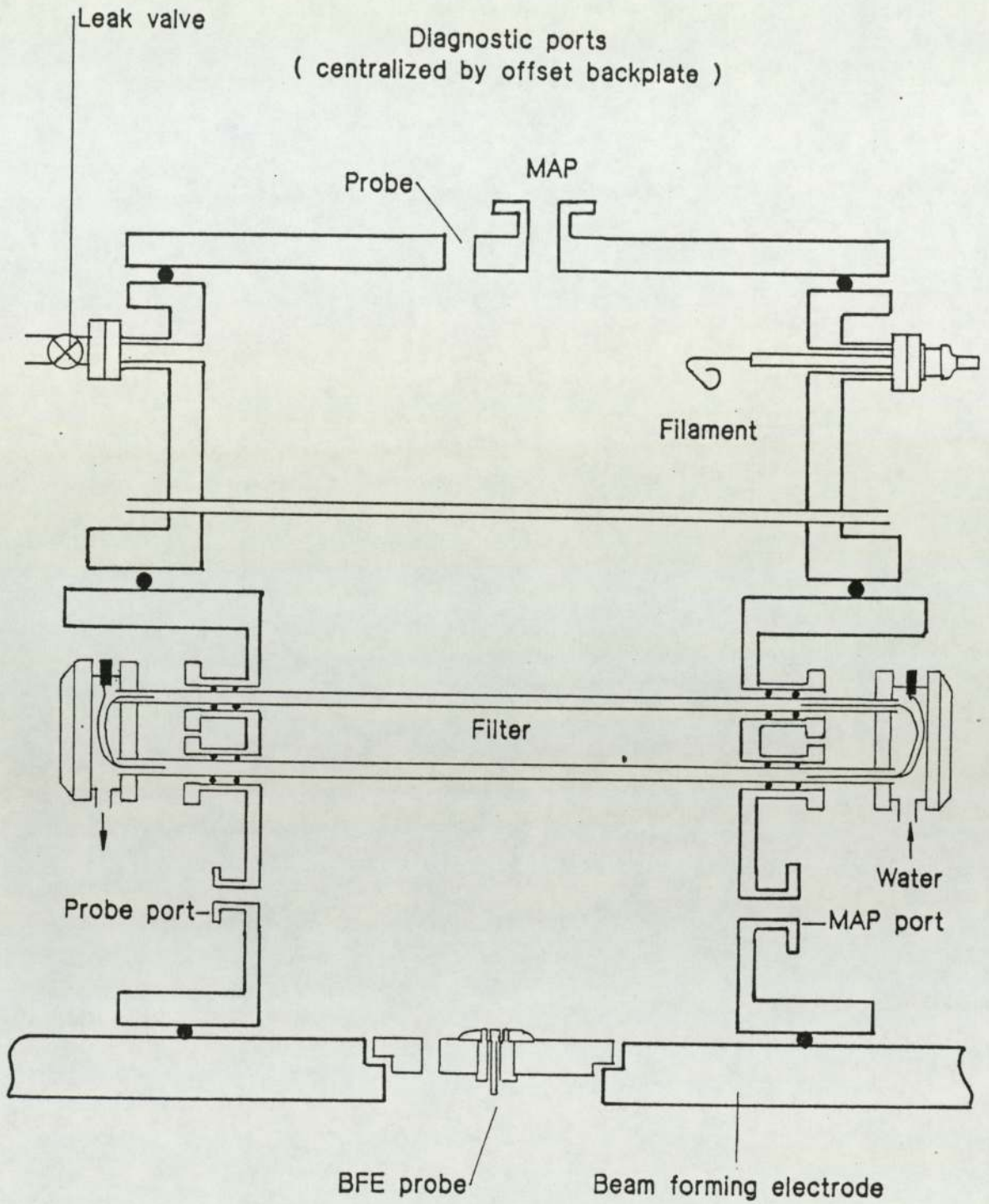


Figure 3.3.1 Schematic diagram of the variable-filter source

A metal-seal leak valve (VG, type MD6) was fitted to one of the service ports on the opposite wall. Gas was fed to this via a flowmeter (Hastings, type EALL-50/10), and a sealed-reference baratron (MKS, type H120) was fitted to a service port to calibrate this. The external magnets were arranged in a checkerboard pattern to avoid the generation of long-range fields at the edge of a line-cusp pattern. This yielded a multipole field projecting about 3cm into the plasma. A pair of 6mm dia. stainless-steel tubes were welded across the long axis of the module at the lower flange position, the remnants of an old rod-filter. The driver module was placed directly on top of the extraction module, atmospheric pressure being sufficient to seal the O-ring.

The extraction module consisted of a stainless-steel cylinder, 20cm in diameter and 16cm high. 2cm thick stainless steel flanges at each end fitted with O-rings permitted vacuum seals to the backplate and driver modules to be made. The top flange, on which the driver region was placed, was watercooled. Two rings of 12 vertically-mounted cobalt-samarium magnets were fixed to the outside of the cylinder in a vertical line-cusp pattern, and held in place with large Jubilee clips. Four pairs of VG metal-seal ports were welded to opposite sides of the cylinder. Into these were inserted PTFE inserts containing piston-seals. These provided the means of mounting four pairs of 8mm dia. stainless-steel tubes across the extraction module; one set 9cm and one 12cm from the BFE. Each pair of tubes was linked

together at either end by a manifold, which provided water and electrical connections. Twelve turns of 1mm dia. enamelled copper wire were wound through each pair, and connected to the manifolds. These were then connected externally in series, making a 48-turn watercooled solenoid. When an excitation current of 50 amps was passed through the coil, a peak field of ~85 gauss was obtained, the variation of this field with distance being shown in figure (3.3.2). The watercooling made DC operation of this field possible. The magnitude of the field was measured in use by a transverse Hall probe (Bell, type STB4-0204), mounted between the projecting ends of two pairs of filter rods. Two 34mm and one 70mm VG metal-seal ports were mounted below the filter rods, for diagnostic access. In order to aid the interpretation of spatially-resolved results, a schematic diagram is provided in figure (3.3.3) showing the positions of the main features of the assembly relative to the filter field and source walls.

The source assembly was placed directly onto the pumping flange of the vacuum system, which served as the BFE. The use of a thick O-ring to form this bottom seal permitted the source assembly to be isolated from the BFE, allowing it to be biased relative to the source. To permit this, the gasline was fitted with an araldite insulator. The assembly can be seen mounted on the pumping stand in figure (3.3.4).

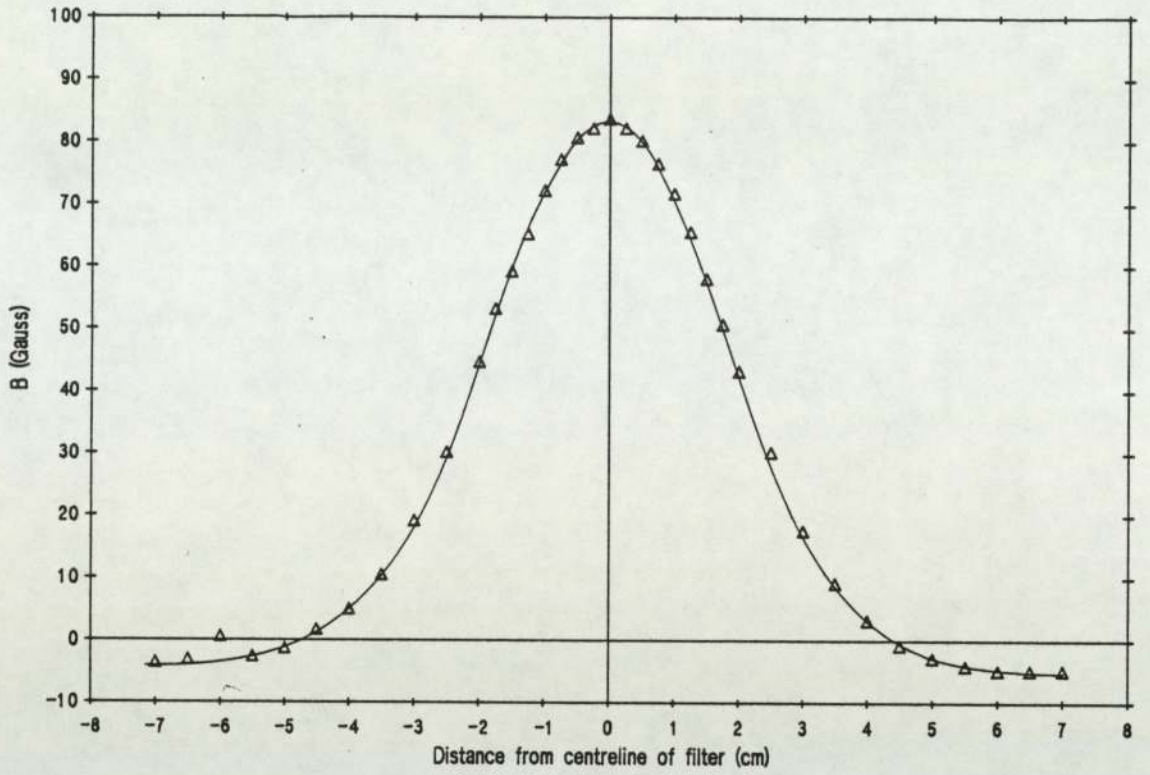


Figure 3.3.2 Axial variation of filter field intensity
Variable-filter source. Excitation current = 50A

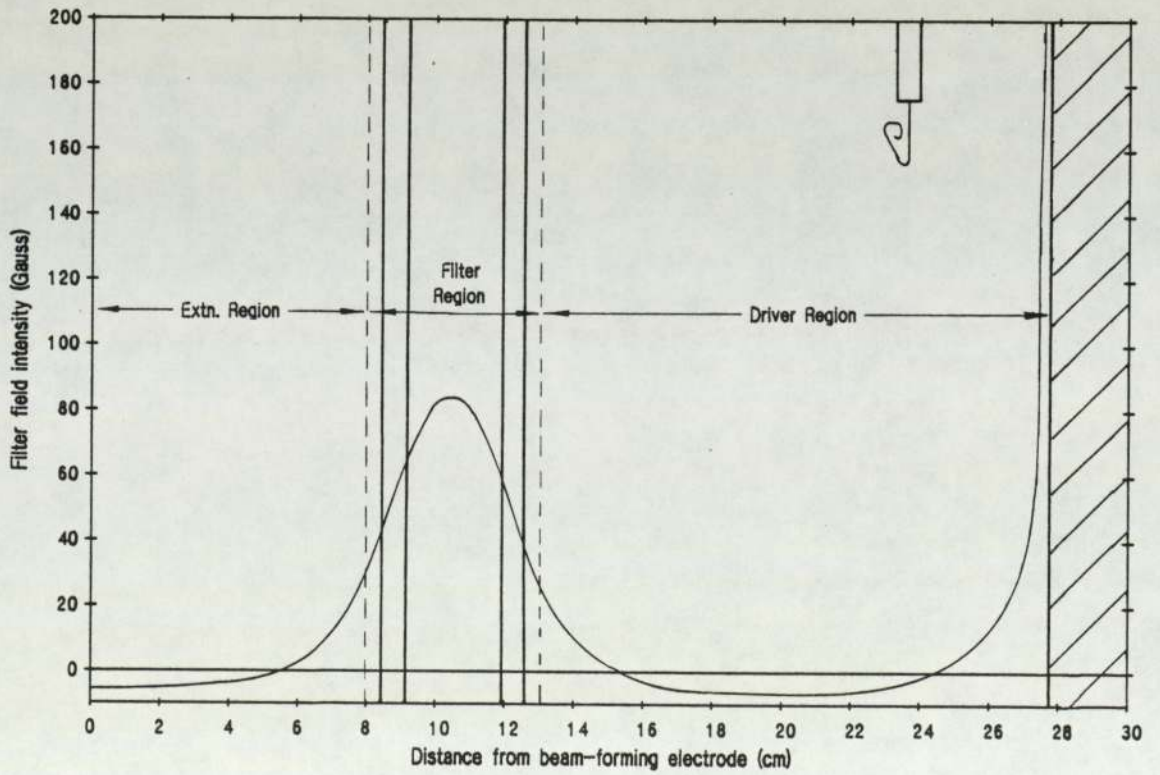


Figure 3.3.3 Location map of features in the variable-filter source
Filter excitation current = 50A

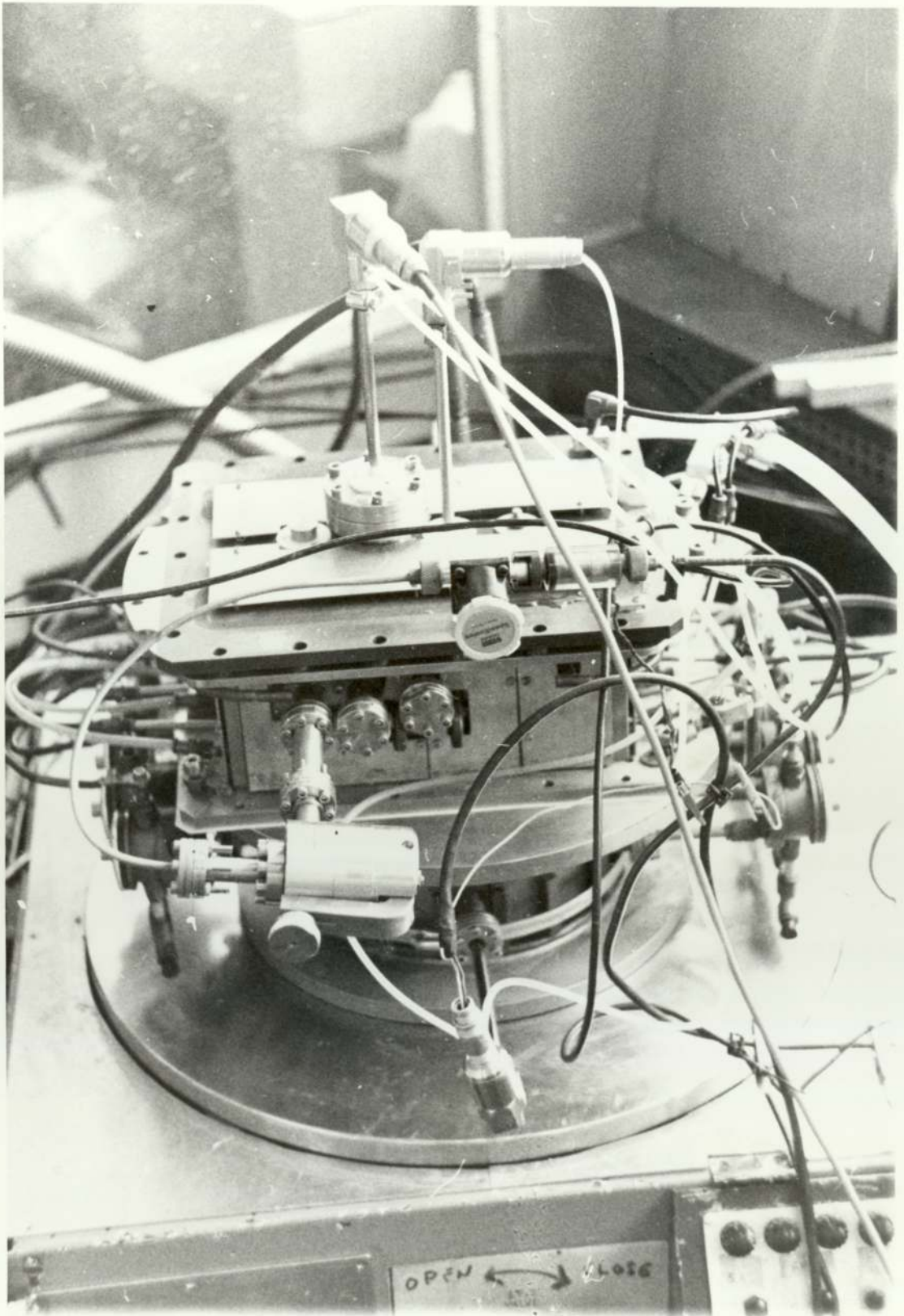


Figure 3.3.4 The variable - filter source assembly

3.3.2 The vacuum system

This is shown in schematic form in figure (3.3.5). As mentioned above, the source was pumped directly. The BFE/pumping flange was constructed from 2.5cm thick stainless steel to resist erosion by the plasma. A removable 15cm dia. plate in the centre carried a diagnostic probe, and a 1.2 cm dia. pumping aperture. This small aperture was necessary to reduce the total gas consumption. The flange was mounted on a 20cm manually-operated gate valve, to which the roughing line was connected. The connections for the BFE probe passed through the roughing line to a vacuum feedthrough. Below the gate valve was a 20cm freon-cooled baffle.

The pumping apparatus consisted of an 8-inch oil diffusion pump (Edwards, type E08) backed by an ancient oil-sealed rotary pump of indeterminate origin. Throughput of the system was $\sim 600 \text{ ls}^{-1}$. The system was controlled manually, using two viton-seal valves in the backing and roughing lines. Pressure measurement was achieved using Pirani gauges (Edwards, type 101) at high pressure, and a Penning gauge (Edwards, type 102) at lower pressures. The ultimate pressure, achievable after a 12-hour pumpdown, was $\sim 3 \times 10^{-7}$ mTorr. The source pressure was again about an order of magnitude above this due to the small pumping aperture. No liquid nitrogen trap was fitted. However, the freon baffle appeared adequate, as no sign of oil contamination was ever found in the source, and probe experiments with noble gases produced only the theoretically-predicted results.

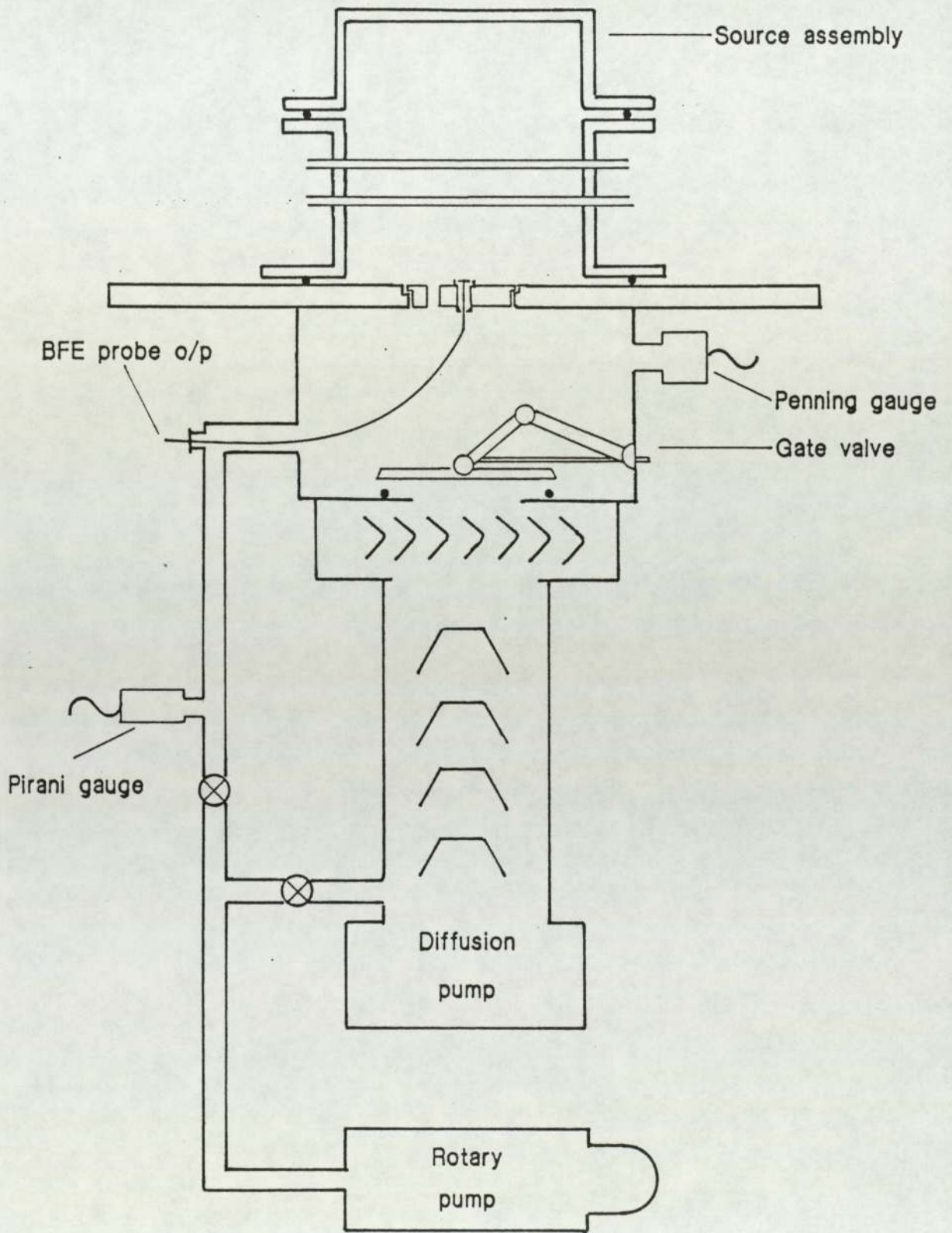


Figure 3.3.5 Schematic of variable filter source vacuum system

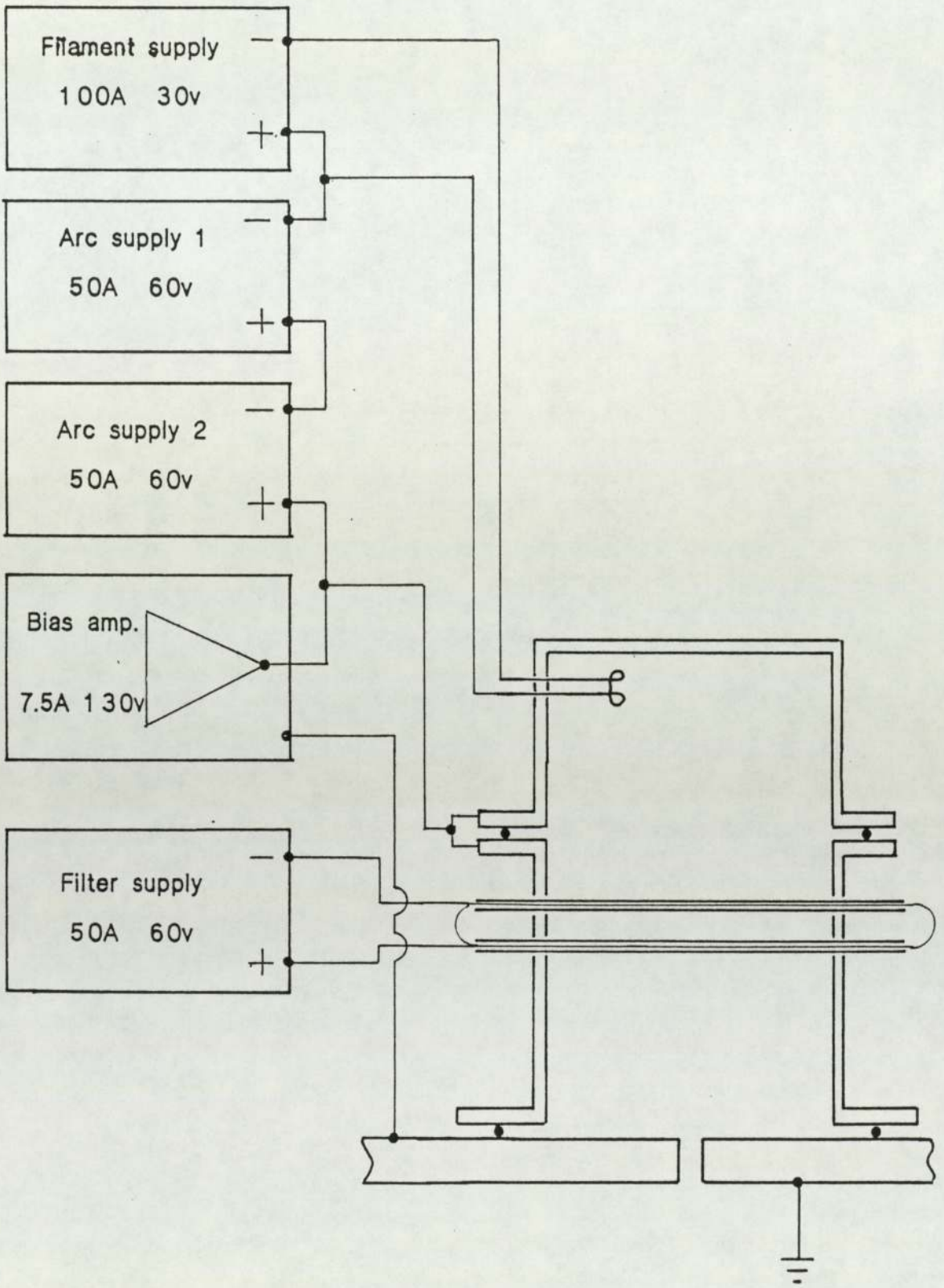


Figure 3.3.6 Schematic of power supplies for variable filter source

3.3.3 The power supplies

These are shown in schematic form in figure (3.3.6). The arc discharge supply consisted of two 60v 50A DC units (Farnell, type H60/50) connected in series, providing a maximum of 50A at 120v. These were used in constant-current mode, in an attempt to reduce fluctuation of the arc current. The filament heating current was supplied by a 30v 100A unit (Farnell, type H30 /100), used in constant-voltage mode. A third Farnell H60/50 unit supplied current to the filter field coils, which at maximum excitation drew the full 3kW output of the supply. The bias supply consisted of a bipolar power amplifier (HH S500D, used in mono mode) controlled with a battery and potentiometer. This was capable of providing bias voltages of $\pm 130\text{v}$ at 7.5A. Arc voltage was monitored using an opto-isolator / amplifier (Burr-Brown, type ISO 100AP) and arc current by a Hall-effect DC induction device (RS, type 257-436). Bias current was monitored using the voltage dropped across a 1 Ohm resistor in the bias supply line, and bias voltage was monitored using a resistor chain between the source and BFE.

3.4 Operation of a filament-driven multipole source

In use, the required cold filling pressure was first established by adjusting the leak valve. The filament heating current was then turned on, and the filament current raised to a level known to heat the filaments just enough

for emission to begin (85A in the case of the tungsten filaments, 70A for the tantalum ones). The arc supply was then switched on, and the arc voltage increased to the required level. During the latter operation, the arc current was monitored, and the filament heating current adjusted to correct any deviations from the required value.

The variable-filter source could be run continuously, since the total power input was seldom greater than 2kW, and a greater flow of cooling water was available. The fixed filter source, since it had two filaments, was subject to a higher thermal loading and often run at discharge powers exceeding 4kW. Consequently, a quasi-DC mode of operation was used, with a "pulse" lasting between 30 sec. and 5 mins.

The state of the anode surface has been shown to have an effect on the production of H^- ions [78]. The anode surface of both sources was subject to contamination by oxides, usually due to vacuum leaks letting air into the discharge. Such contamination may be seen in figure (3.4.1), which shows the backplate of the variable-filter source. The cusps tend to accumulate deposits faster, being directly exposed to the plasma. This picture clearly shows the checkerboard pattern of the magnets used in this source, and the discontinuities in the field caused by mismatching fields at the edges.

Contamination was removed from both sources when necessary by stripping down the source and scouring the components with a high-pressure sand-and-water jet. After such an operation, ultrasonic cleaning in volatile organic

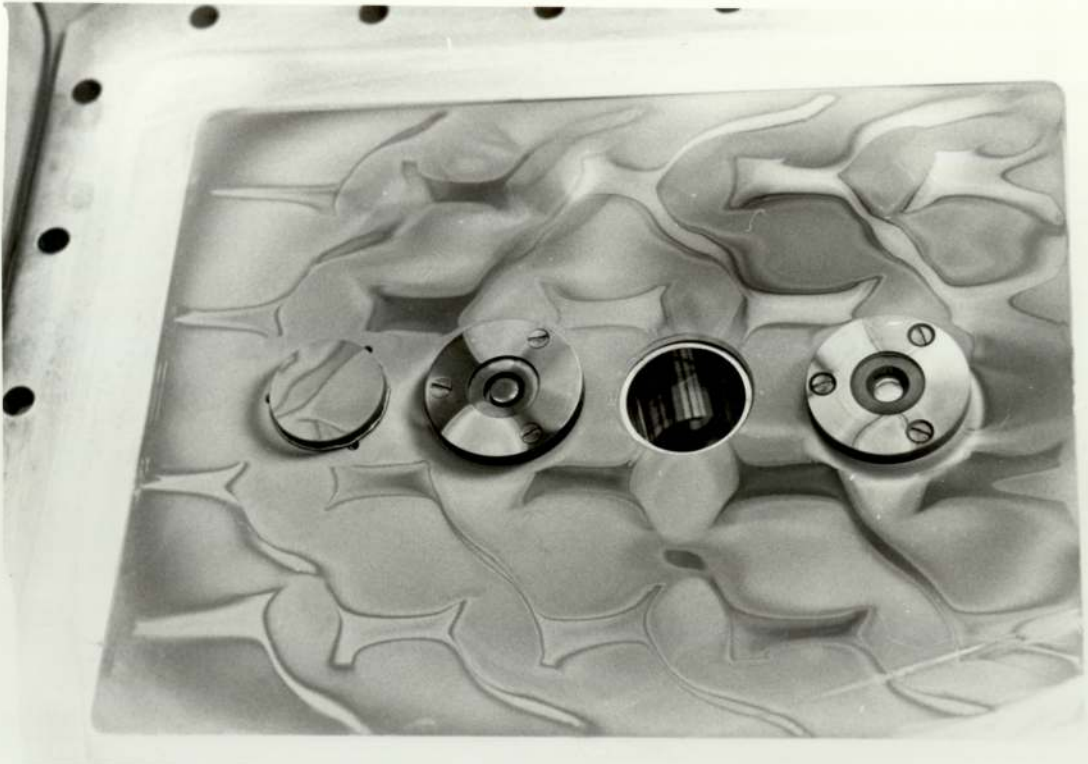


Figure 3.4.1 Contaminated backplate showing checkerboard pattern

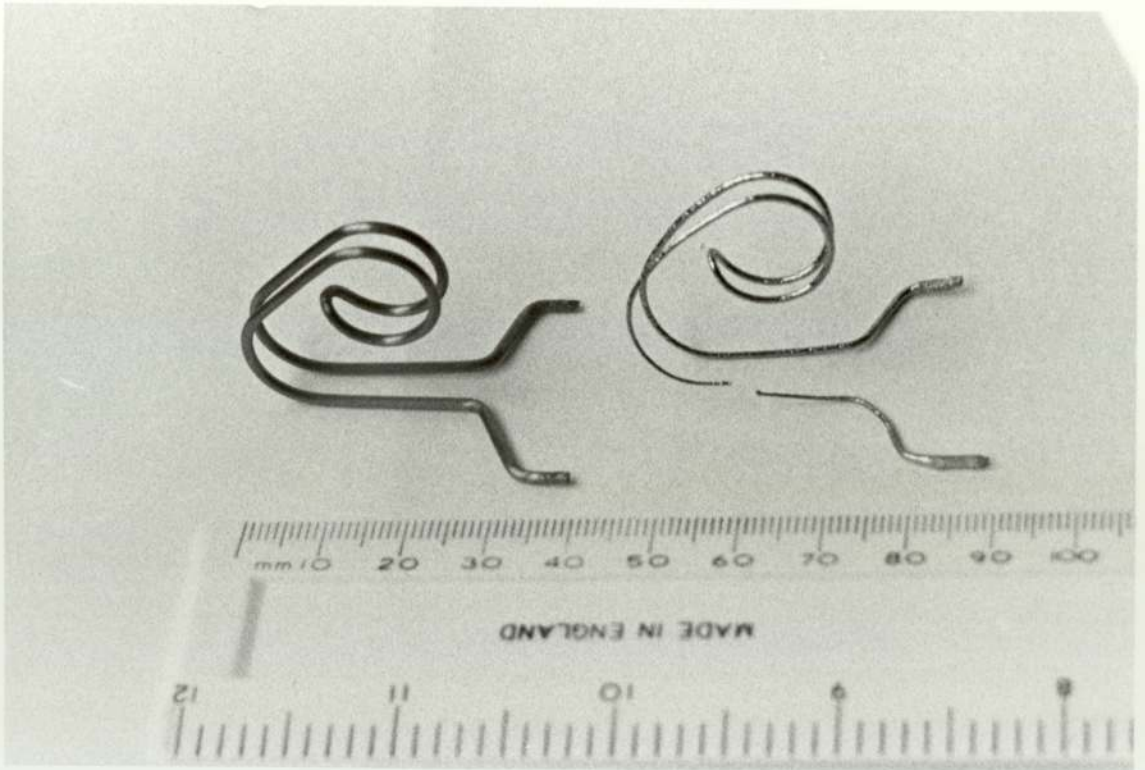


Figure 3.4.2 Erosion of tantalum filaments

solvents followed by prolonged pumping was necessary to clean and dry out the source. As a final stage, after pumpdown the filaments were used to perform a low-temperature bake-out of impurities (principally water) from the anode surface, over about 4 hours. In the variable-filter source, a further hour of ion-bombardment cleaning in an argon discharge was performed.

During operation, material from the filaments would be evaporated and deposited on the walls of the source. This gave a very clean surface, thought to be beneficial to the production of H^+ ions. The effect was much greater with tantalum filaments; figure (3.4.2) shows a well-used tantalum filament compared to a new one. Over 50% of the mass of the old filament has been evaporated away, over an operational life of ~100 hours.

Figure (3.4.3) shows the interior of the variable-filter source during a discharge. The picture was obtained by temporarily replacing the backplate of the source with a 3cm thick plate of armoured glass, atmospheric pressure serving to seal the O-ring. The plasma is most visible around the filament, but may be seen extending almost to the driver region walls. At this point, the cusp structure caused by the multipole field may be clearly seen, showing the discontinuities caused by ill-matched fields. The filter rods and BFE are visible beyond the driver plasma. A mobile planar probe can just be seen mounted horizontally in the extraction region.

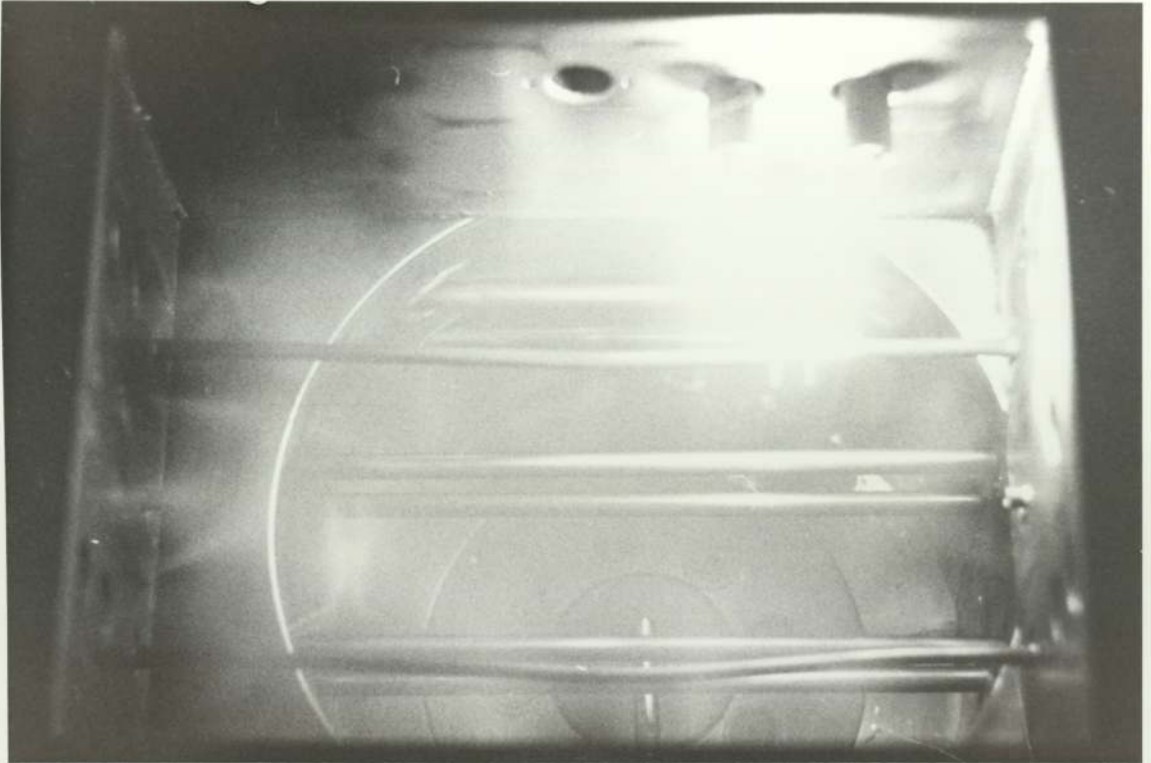


Figure 3.4.3 The variable – filter source in operation

CHAPTER 4

Diagnostic probes

This chapter describes in detail the diagnostic apparatus which it was possible to insert in the plasma volume, and discusses the theories used to analyse the results obtained from them. These diagnostic probes consisted of only two types; Langmuir probes, and a miniature electromagnetic mass analyser.

Langmuir probes are discussed in section 4.1; theory in 4.1.1, practical aspects in 4.1.2. In 4.1.1, the basic theory used to analyse characteristics obtained from a planar Langmuir probe is briefly reviewed. Experimental evidence showing that expansion of the Debye sheath prevents the ion-saturation region from truly saturating is presented, and a theoretical justification for the empirical correction of this effect developed. Screening of electrons from the probe by the filter field under certain conditions is discussed, and the results of experiments undertaken to quantify this effect presented. An empirical correction valid for a planar probe screened by a parallel magnetic field is obtained, and justified with reference to existing theoretical work. The calculation of negative ion densities using the probe saturation current ratio is discussed, with reference to recent theoretical developments in this area. The theories used in this investigation relating to Langmuir probes are

then summarized. In 4.1.2, the construction of the Langmuir probes used in this study is discussed, and the computerized probe analysis system built to facilitate their use is briefly described.

In section 4.2, the mass analyser probe is discussed. The principles of it's operation are first explained, and the design and construction of the probe described with reference to these. The practical use of the probe is then discussed.

4.1 Langmuir probes

In this investigation, only planar Langmuir probes were used. The principal advantage of this type of probe is the relative simplicity of the corresponding theory. The disadvantages are the existence of significant edge-effects (and the consequent restriction on the minimum diameter of the probe), and a slightly more complicated and intrusive design. Recent work [94] on cylindrical probes in multipole sources suggests that these may have advantages over the planar type for some applications, but since reproducible and self-consistent results were obtained from planar probes, there seemed no advantage in changing to cylindrical types.

4.1.1 Theoretical considerations

4.1.1.1 Basic planar probe theory

Langmuir probe data obtained in this study was analysed using a version of the simple theory of plane probes in a collisionless plasma due to Langmuir and Mott-Smith [81]. Ion collection was treated as in Boyd and Thompson [82]. With the exception of the correction factors described below, the effects of magnetic fields, negative ions, in-sheath ionization and the probe edges were ignored. If evidence of a dual-temperature electron population emerged, a bi-Maxwellian distribution was assumed, values for the hotter species were determined and those of the colder species corrected accordingly. Although this assumption was made arbitrarily on the basis of the shape of the characteristic,

there is recent evidence to support it [83,84]. A more detailed resume of probe theory is given in appendix A, but in brief, the particle fluxes to the probe are given by:

$$I_e = \frac{e A_p N_e \bar{v}_e}{4} = e A_p N_e \sqrt{\frac{kT_e}{2\pi M_e}} \quad \dots(4.1.1a)$$

$$I_p = \frac{e A_p N_p \bar{v}_p}{4} = e A_p N_p \sqrt{\frac{kT_p}{2\pi M_e}} \quad \dots(4.1.1b)$$

$$I_+ = e A_p N_+ C_s = 0.6 e A_p N_+ \sqrt{\frac{kT_e}{M_+}} \quad \dots(4.1.1c)$$

where all the symbols are as defined in the symbology.

4.1.1.2 Sheath expansion in the ion saturation region

Early probe experiments in the small magnetic multipole source showed large errors in the measured value of the ion-saturation current. Examination of this region showed a definite increase in ion current with respect to probe potential. However, although fitting a line to this region and extrapolating back to the plasma potential gave an improved result, the values derived for N_+ from this were still unreliable, as the value of I_+ obtained by this method varied significantly with the voltage range of the line segment fitted to. To identify the cause of this, a detailed investigation of the ion saturation region was undertaken.

4.1.1.2.1 Experimental evidence

A number of experiments were performed using a small (3mm dia.) planar probe in both regions of the small magnetic multipole source. The experimental arrangement is shown in figure (4.1.1). The voltage applied to the probe was scanned between 0 and -400 volts, and the current and voltage monitored using a chart recorder. This was repeated over a range of discharge conditions. A typical family of I-V curves obtained using this method is shown in figure (4.1.2).

The curves all showed that the ion current increased in a nonlinear fashion with probe voltage, and that the index in all cases was slightly < 1 . To reliably fit a line to this region, it was necessary to identify this index, here denoted γ . Assuming that the measured ion current I_m may be expressed in terms of a constant saturation current I_+ and a voltage dependent term;

$$I_m = I_+ + \beta I_+ V^\gamma \quad \dots(4.1.2)$$

differentiating this yields

$$\frac{dI_m}{dV} = \beta \gamma I_+ V^{\gamma-1}$$

Since I_+ is constant, taking the logarithm of both sides

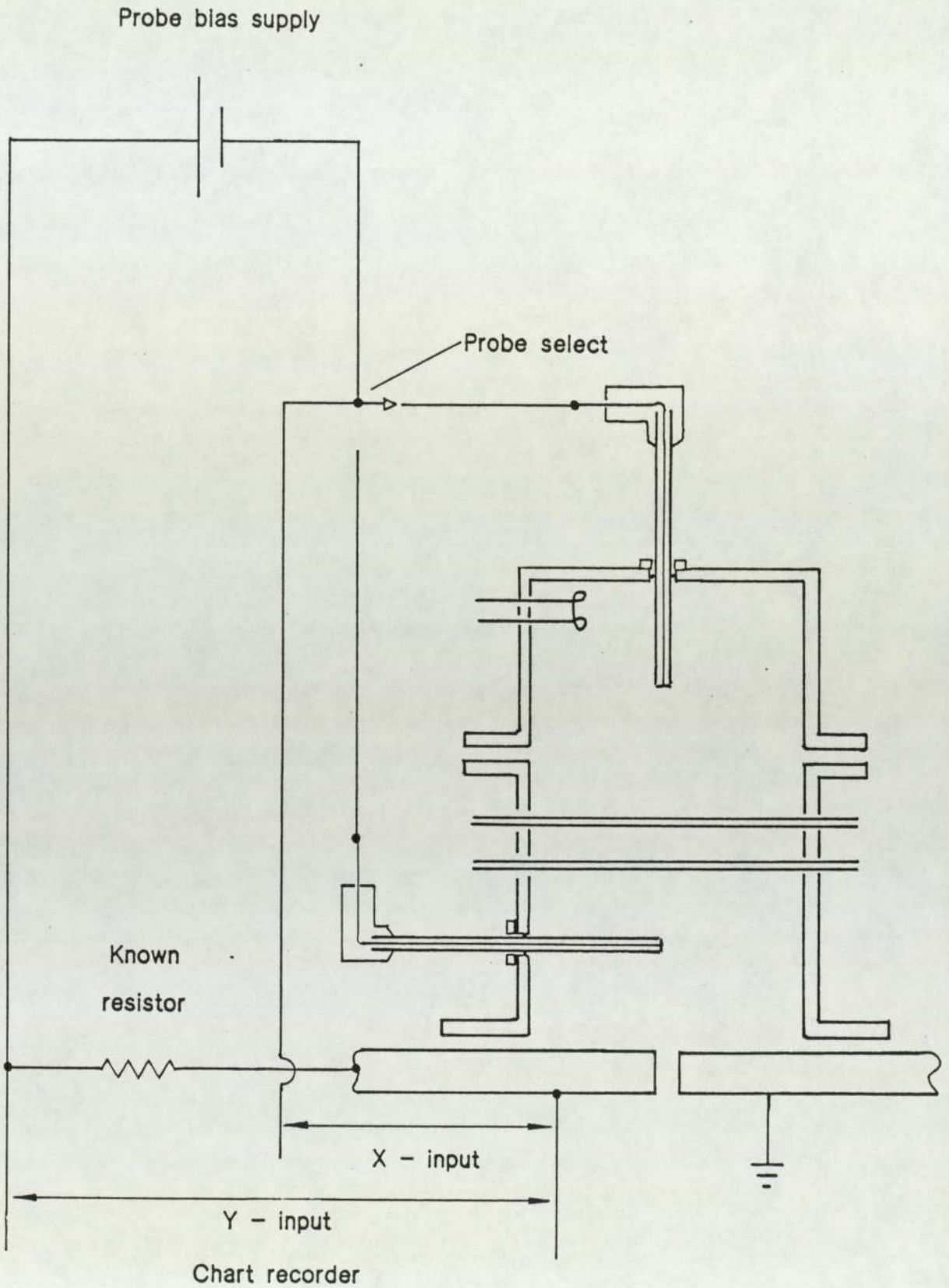


Figure 4.1.1 Experimental arrangement for sheath expansion study

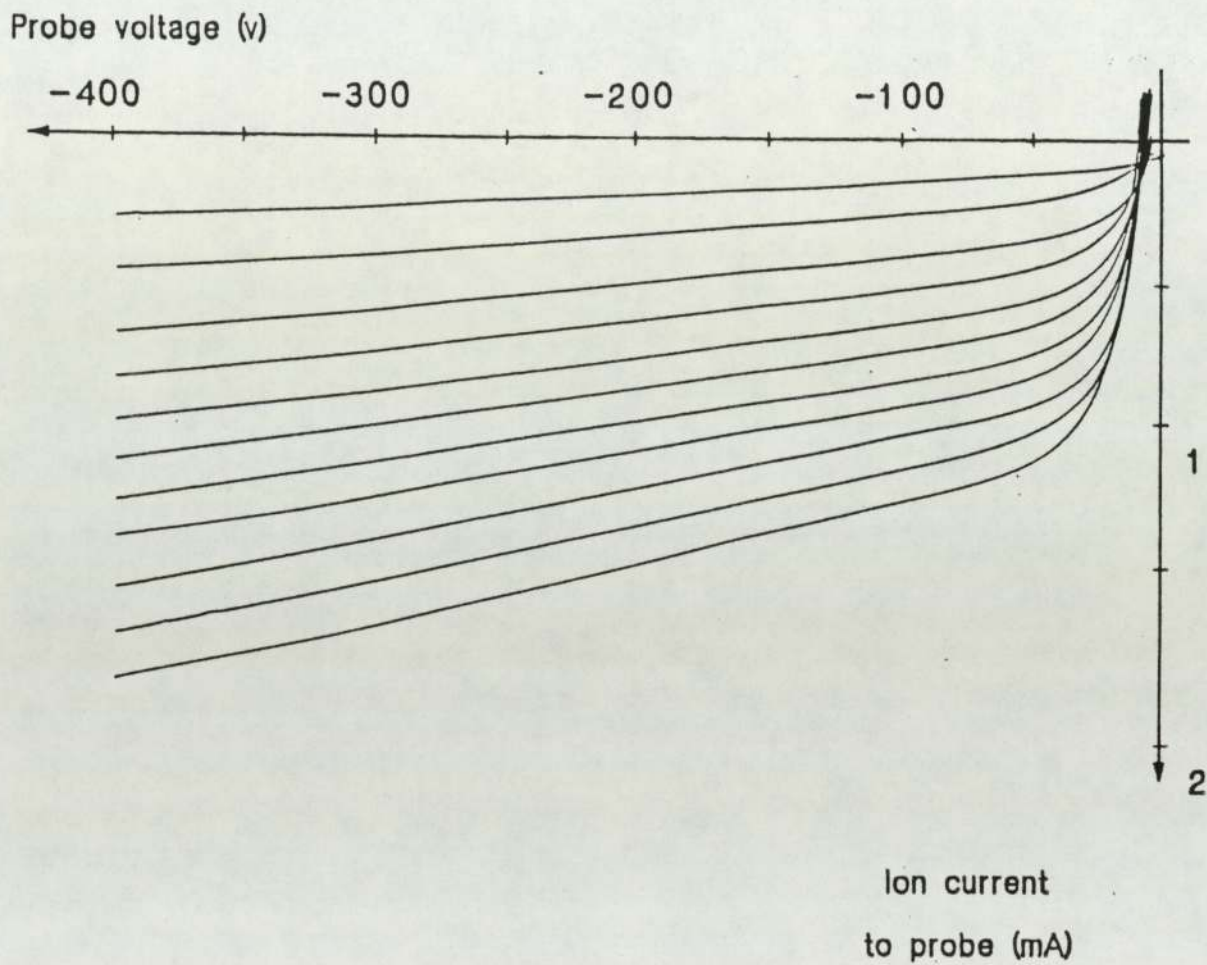


Figure 4.1.2 Typical probe traces from the expansion experiment

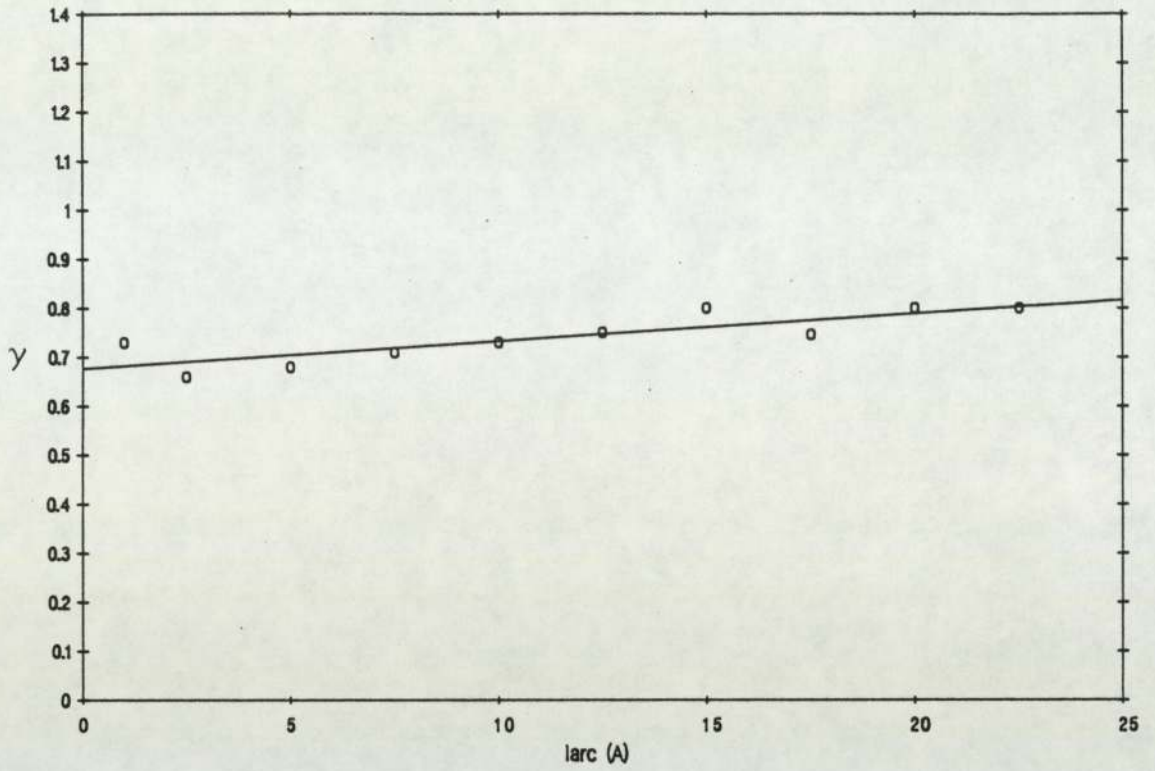


Figure 4.13 Variation of index of expansion with arc current
 Varc = 60v Pres = 3mT

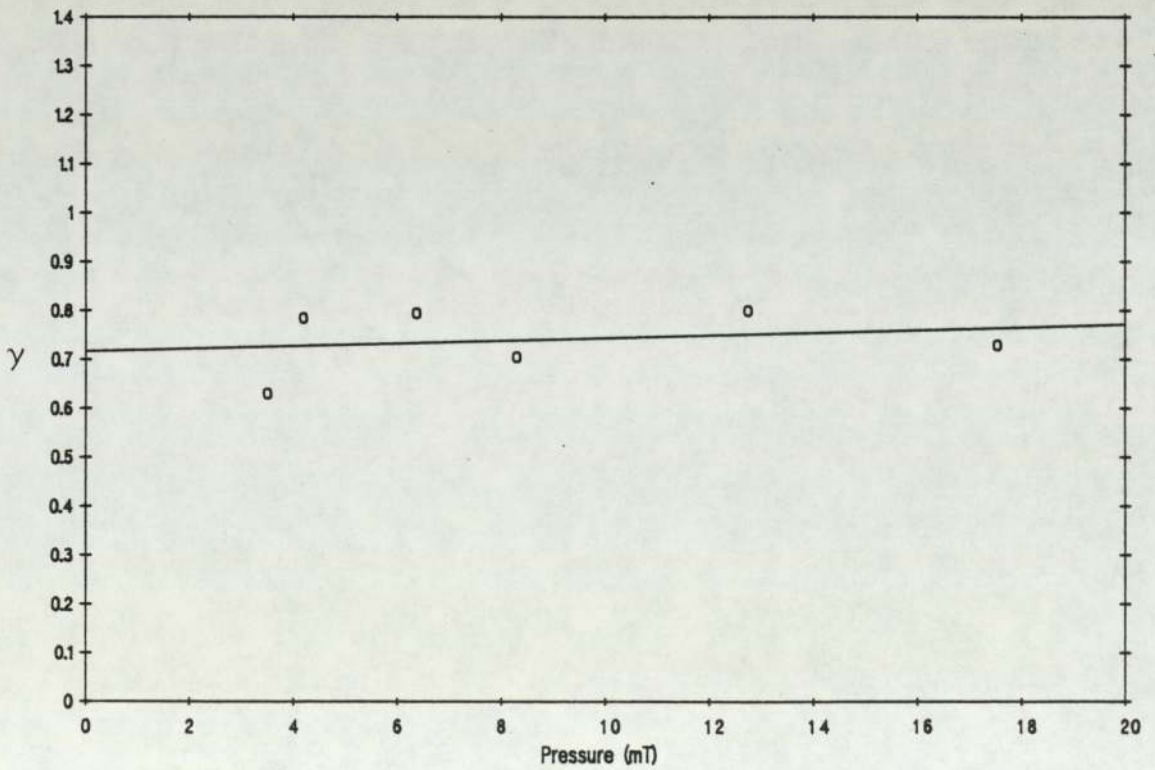


Figure 4.14 Variation of index of expansion with pressure
 larc = 5A Varc = 60v

gives

$$\ln\left(\frac{dI_m}{dV}\right) = \ln(\beta\gamma I_+) + (\gamma - 1)\ln(V) \quad \dots(4.1.3)$$

A plot of $\ln\left(\frac{dI_m}{dV}\right)$ vs. $\ln(V)$ will therefore have a gradient of $(\gamma - 1)$. Using this method, the results shown in figures (4.1.3) & (4.1.4) were obtained, showing that over a wide range of conditions

$$0.7 \leq \gamma \leq 0.8 \quad \dots(4.1.4)$$

4.1.1.2.2 Theoretical expression

The gap between the edge of the ion-sheath and the probe face may be considered as a plane diode, in which the sheath edge emits ions and the probe face absorbs them. In this situation, the Child-Langmuir law for current transport across the gap is

$$J_+ = \frac{4\epsilon_0}{9} \sqrt{\frac{2e}{M_+}} \frac{V^{\frac{3}{2}}}{d^2}$$

where d is the gap distance and V the (negative) probe voltage. If the sheath expands with voltage, this gap may be conveniently expressed in terms of a number κ of Debye lengths, so

$$d^2 = (\kappa \lambda_D)^2$$

The Debye length may be expressed as

$$\lambda_D = \sqrt{\frac{\epsilon_0 T}{e N_+}}$$

where T is the electron temperature in "Boltzmann units", (kT_e/e) . Substituting in the Debye expression for the sheath thickness thus obtained, the current density is given as

$$J_+ = \frac{4\epsilon_0}{9} \sqrt{\frac{2}{M_+}} \frac{(eV)^{\frac{3}{2}}}{T} \frac{N_+}{\kappa^2}$$

From the previous section, the ion current density collected by the probe is also given by

$$J_+ = 0.6 e N_+ \sqrt{\frac{eT}{M_+}}$$

equating these two expressions gives

$$\kappa^2 = \frac{4\sqrt{2}}{0.6 \times 9} \frac{V^{\frac{3}{2}}}{T^{\frac{3}{2}}}$$

and therefore

$$\kappa = 1.018 \left(\frac{V}{T} \right)^{0.75} \quad \dots(4.1.5)$$

Applying this to the probes now, the total collected positive ion current will be given by the current flowing into the sheath area. The latter may be expressed as the sum of the probe area itself, plus that of the hemispherical ring comprising the sheath edge, as shown in figure (4.1.5) Assuming terms in $(\kappa \lambda_D)^2$ are comparatively small;

$$\begin{aligned} I_m &= J_+ \pi a^2 + J_+ 2\pi^2 a (\lambda_D \kappa) \\ &= I_+ + I_+ \left(\frac{2\pi \lambda_D \kappa}{a} \right) \end{aligned}$$

substituting in the expressions obtained for κ and λ_D , this becomes

$$I_m = I_+ \left(1 + \frac{2\pi}{a} \sqrt{\frac{\epsilon_0 T}{e N_+}} 1.018 \frac{V^{\frac{3}{4}}}{T^{\frac{3}{4}}} \right)$$

Using the probe-theory expression for J_+ , this may be written as

$$I_m = I_+ \left(1 + \frac{1.44 \times 10^{-3}}{a \sqrt{J_+}} V^{0.75} \right) \quad \dots(4.1.6)$$

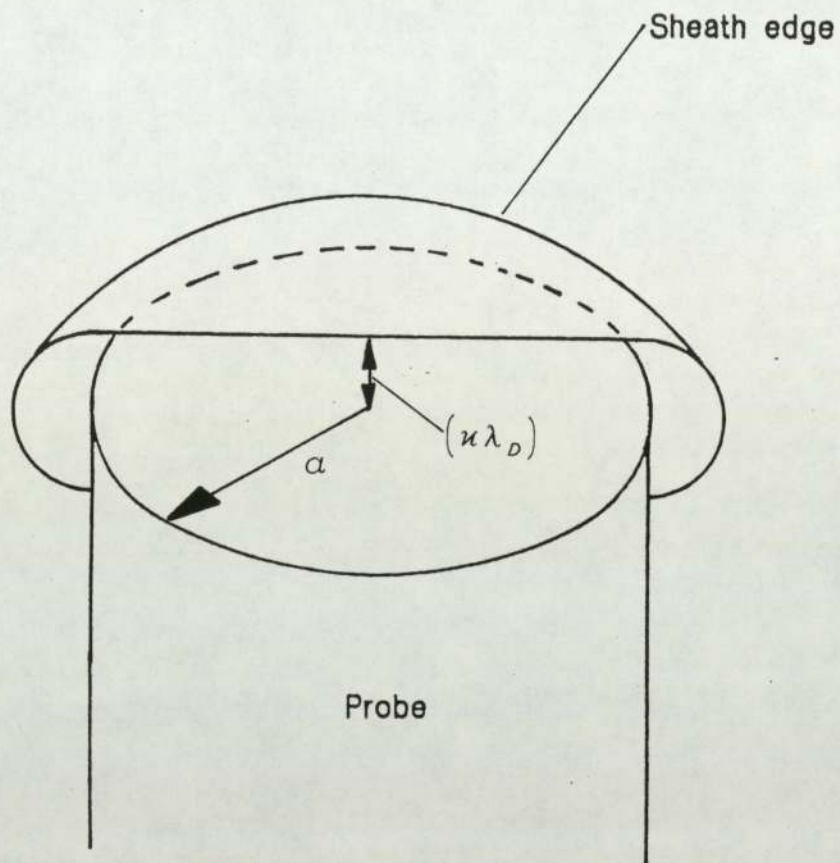


Figure 4.1.5 Geometry of sheath expansion for a planar probe

This predicts that the additional current due to sheath expansion will grow proportionally less as the plasma density and probe radius increase. This is reasonable, the first being a consequence of the Debye screening and the second reflecting the simple geometrical relationship of the area of a circle to its circumference. Comparing eqn. (4.1.6) with the empirical relationship of eqn. (4.1.2), it is possible to compare the value of β obtained from the intercept of eqn. (4.1.3) with that derived from eqn. (4.1.6). For a typical 5A discharge, I_+ has a value of 0.6 mA, so with $a = 0.15$ cm $J_+ = 85 \text{ A m}^{-2}$. Data from the appropriate log plot of eqn. (4.1.3) yields an intercept of $6.2 \times 10^{-5} \text{ A v}^{-1}$, a value that changes only slightly with arc conditions. Since $\gamma = 0.75$, this yields a value from eqn. (4.1.3) of $\beta = 0.14$. Substituting the relevant values in eqn. (4.1.6) yields $\beta = 0.11$, quite a good agreement. The variation with plasma density requires that proper use of the above expression be an iterative process. However, the range of J_+ in this study is not large, and the correction factor is small anyway, so assuming independence of J_+ for a first solution will introduce only a small error.

Thus the expansion effect may be compensated for by fitting the ion-saturation line to a voltage ordinate of $V^{0.75}$. A more elegant solution would be to measure the expansion of each ion-saturation trace using the method described above, and fit a line to that index for extrapolation to the plasma potential. However, since this would require extensive use

of the Logarithm function in PASCAL, the execution speed, and therefore the utility of the code, would suffer greatly. This method might be an option if a faster processor was used.

4.1.1.3 Electron screening by the filter field

The electron saturation region of the characteristic obtained from a planar Langmuir probe with its face parallel to a magnetic field is distorted from the zero-field state, the magnitude of the saturation electron current being reduced in the presence of the field. The effect on the ion saturation region for field intensities less than a few hundred gauss, however, is negligible due to the very much larger ionic mass. It is necessary to consider the implications of this effect when the mobile planar probe is mounted on the source backplate and positioned within the influence of the filter field, as in an axial scan through the source. The screening effect causes the ratio of positive to negative saturation probe currents I_-/I_+ , denoted here as R, to be reduced [85]. This leads to a problem, since the reduction in this ratio from the ideal state is used to estimate the fractional negative ion density in the source, as discussed in section (4.1.1.4). To allow this technique to be used in the presence of magnetic fields, therefore, it is necessary to perform a correction for the electron screening effect.

To determine the form of this correction, a series of experiments were performed using the mobile planar probe mounted at the peak of the filter field, as described above, over a wide range of filter field values and discharge conditions. To isolate the effect of the electron screening, the experiments were all run in noble gas discharges, the reasoning being that the noble gases do not form stable negative ions. Any reduction in ratio, therefore, could be entirely attributed to the screening effect.

4.1.1.3.1 Experimental evidence for electron screening

The existence of the screening effect under the conditions obtaining in the small variable multipole source is confirmed by the results shown in figure (4.1.6). This shows the variation in saturation current ratio with filter field intensity obtained in an helium discharge. For one dataset, the probe is positioned at the fringes of the field's influence, 3cm beyond the peak field position in the direction of the beam-forming electrode. The maximum field in this position is < 20 gauss, as shown in figure (3.3.2). No significant variation is displayed as the filter field is increased to it's maximum value. In the other dataset, the same conditions apply, save that in this case the probe is positioned at the peak of the filter field. The ratio now shows a significant decrease when the filter field intensity is increased beyond ~30 gauss. Below this level, no attenuation is apparent. The cause of this decrease in ratio

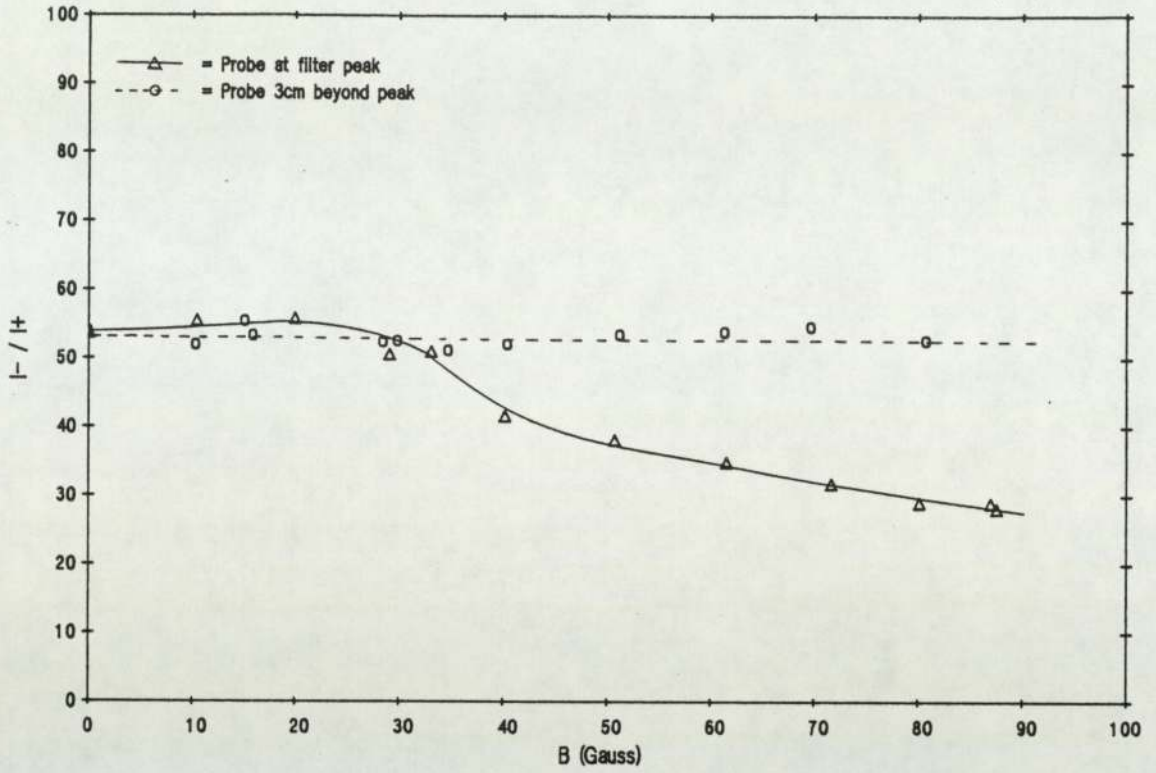


Figure 4.16 Variation of I_-/I_+ with Filter field intensity
Helium discharge Iarc = 5A Varc = 60v Pres = 5mT

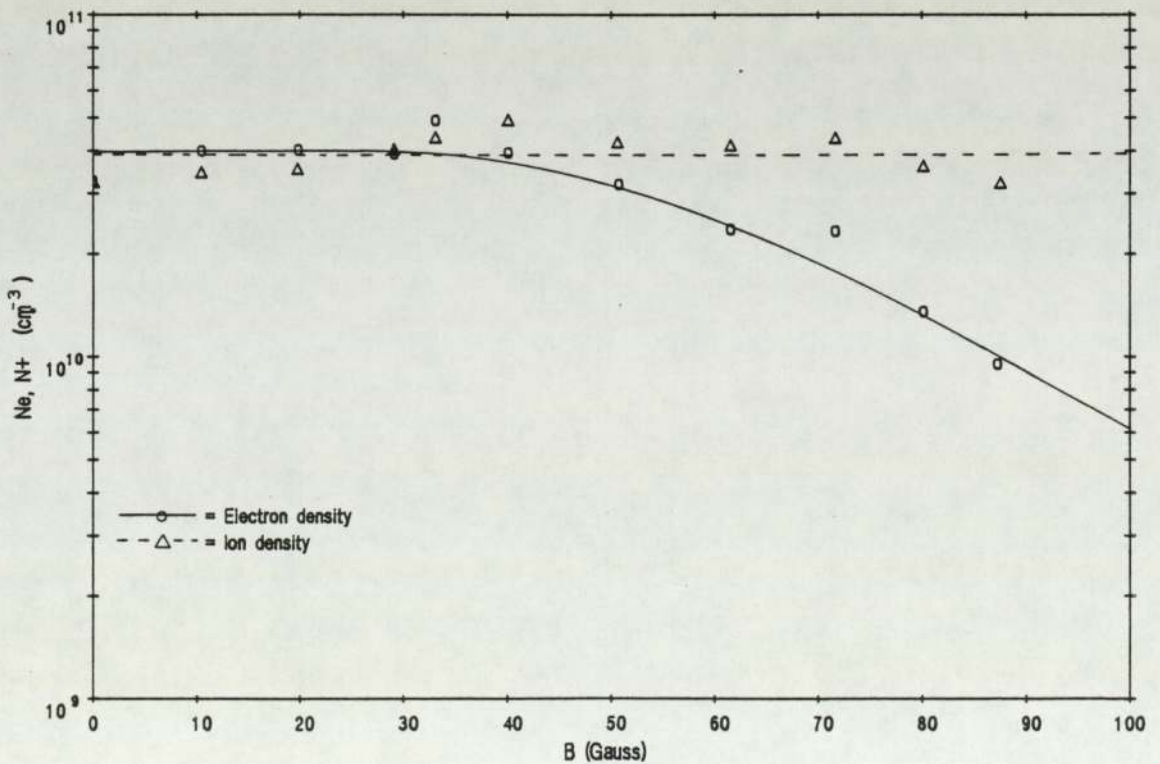


Figure 4.17 Variation of electron and ion densities with B
Helium discharge Iarc = 5A Varc = 60v Pres = 5mT

may be seen in figure (4.1.7), which shows the variation of ion and electron densities in the second experiment. The ion density seen by the probe remains constant with field intensity, whereas the electron density shows an apparent fall. Screening of the electrons by the field is thus confirmed.

Figure (4.1.8) shows the ratio-field attenuation curves obtained from a helium discharge over a range of cold filling pressures, other discharge parameters being held constant. The same behavior as figure (4.1.6) is evident in each case, the curve showing a plateau up to ~ 30 gauss, followed by a strong attenuation with increasing field. No significant variation between the different pressures, within the limits of error ($\sim 10\%$), is evident. The screening effect thus appears (rather surprisingly) to be largely independent of pressure, and by implication, electron temperature.

Figure (4.1.9) shows the family of curves obtained from a helium discharge over a range of arc current values, the other discharge parameters being held to the same values as in figure (4.1.8), and the pressure at 10mT. The behavior pattern noted for figure (4.1.6) again occurs, and no significant variation between the curves is obvious. The screening effect appears to be independent of arc current, and therefore of plasma density.

Figure (4.1.10) shows the curves obtained from a helium discharge for two different arc voltage values, the other discharge parameters being held to the reference values

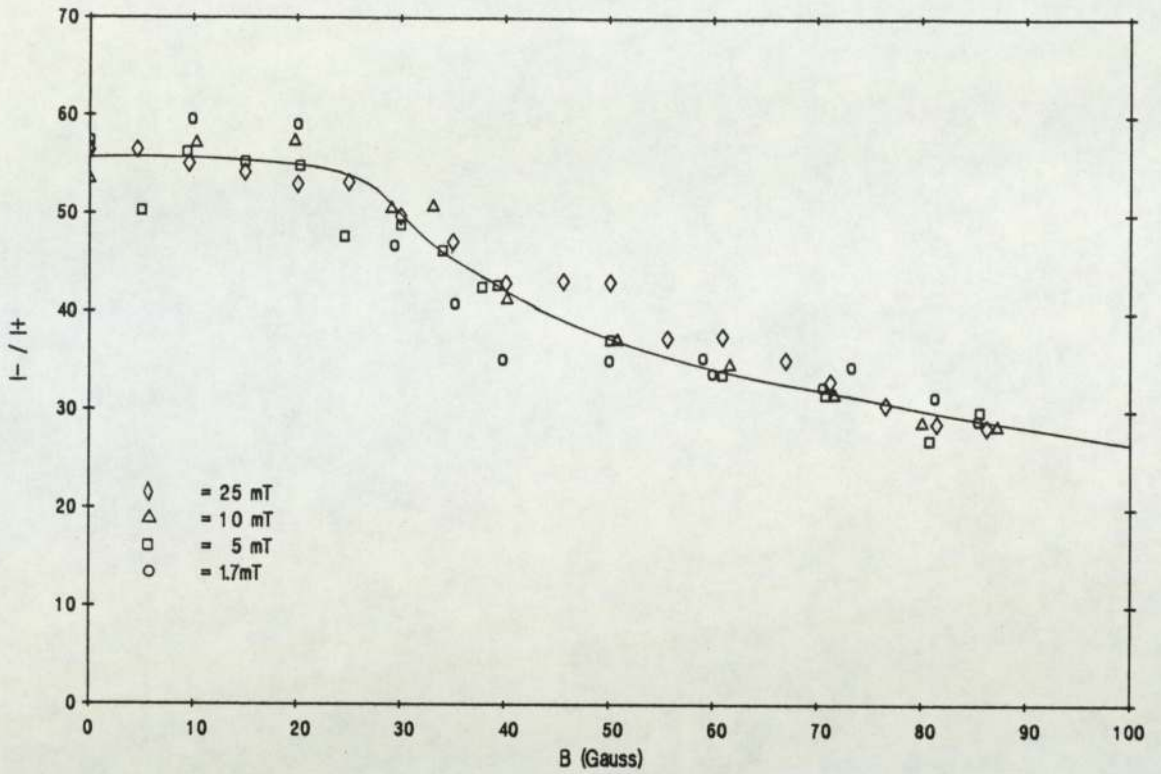


Figure 4.18 Variation of ratio I/B curve with pressure
Helium discharge $I_{arc} = 5A$ $V_{arc} = 60v$

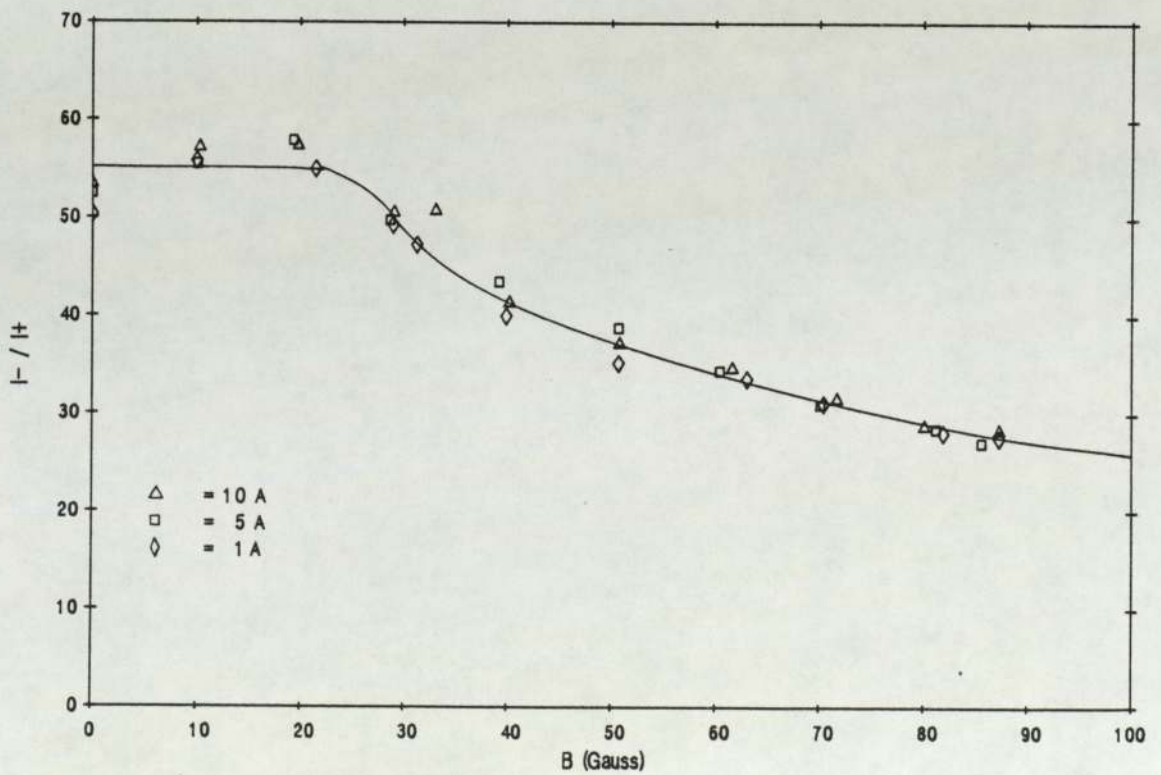


Figure 4.19 Variation of ratio I/B curve with arc current
Helium discharge $V_{arc} = 60v$ $Pres = 10mT$

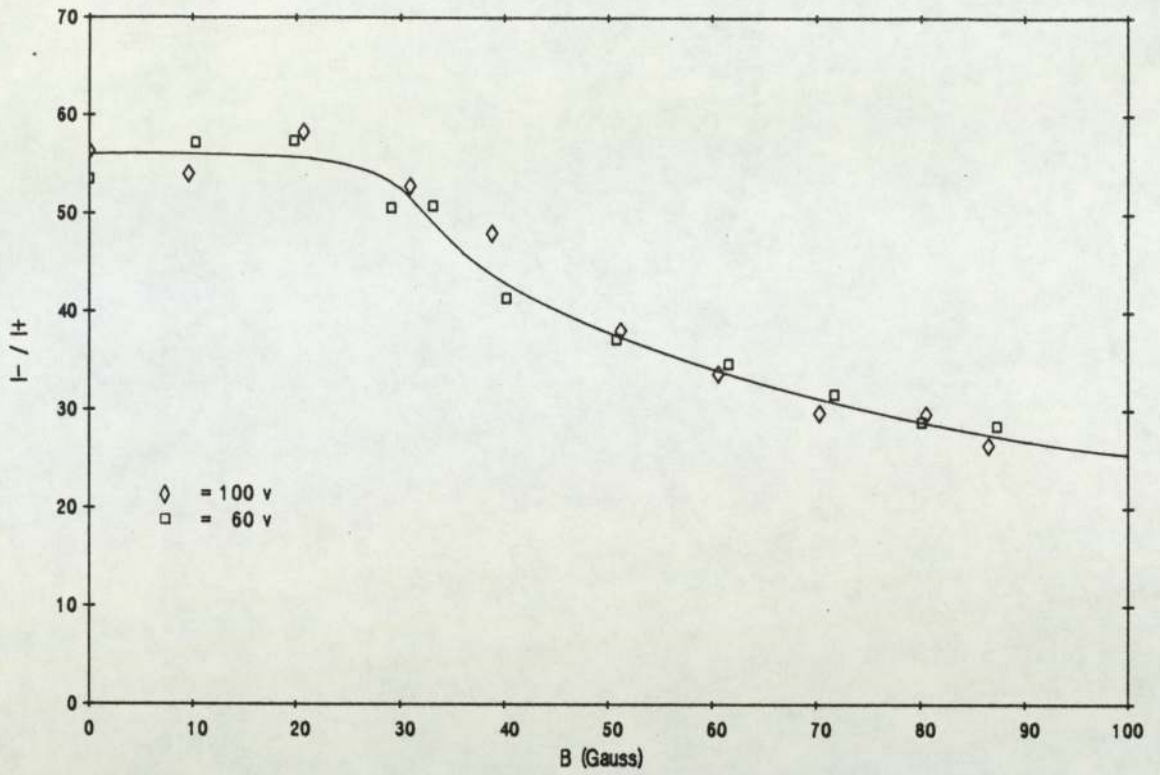


Figure 4.1.10 Variation of ratio I/I_0 vs B curve with arc voltage
Helium discharge $I_{arc} = 5A$ Pres = 10mT

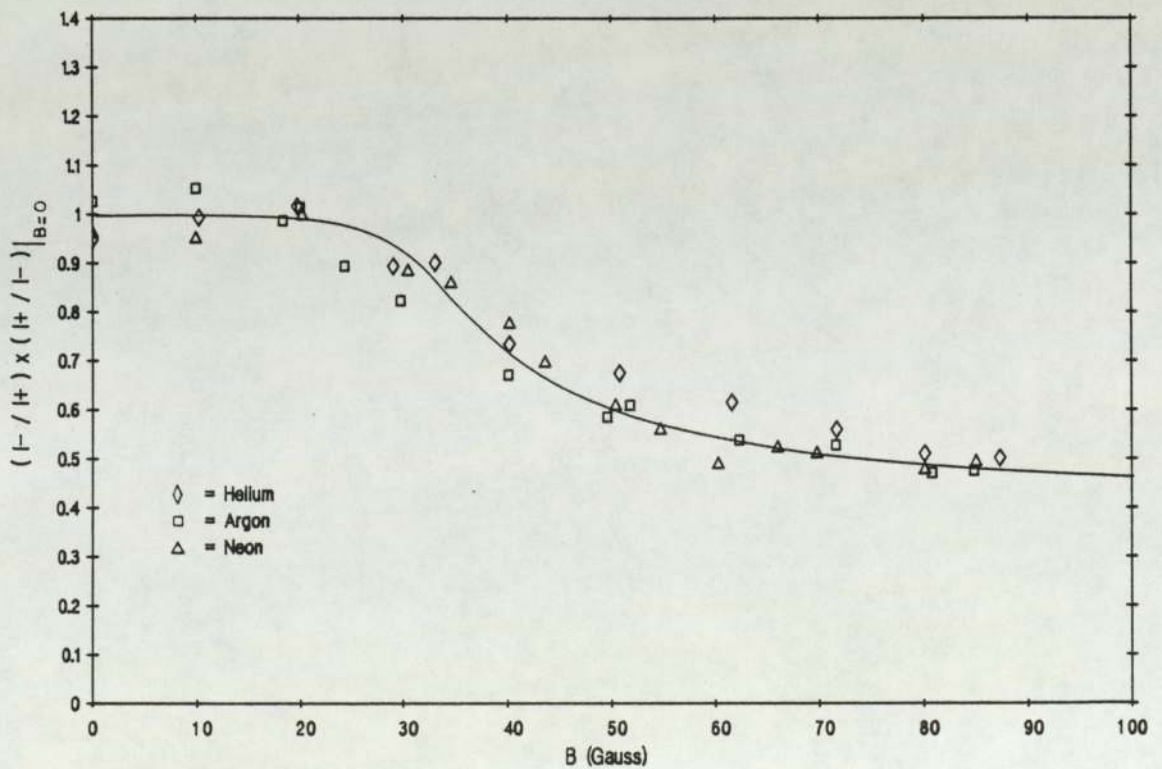


Figure 4.1.11 Variation of normalized ratio $(I/I_0) \times (I_0/I_0)|_{B=0}$ vs B curve with ionic mass
 $I_{arc} = 5A$ $V_{arc} = 60v$ Pres. = 10mT

defined above. The behavior pattern noted above is repeated once again, and no significant difference between the curves is evident. The screening effect appears to be independent of arc voltage, and therefore of primary electron temperature and density.

Figure (4.1.11) shows the variation of the saturation current ratio expressed as a fraction of the ideal ratio (that expected in a field- and negative ion- free discharge) with filter field intensity. This allows the absolute value of the ratio to be ignored. The curves were obtained from discharges at the reference conditions in helium, neon and argon. Once again, the behavior noted for figure (4.1.6) occurs, and once again, there is no significant difference between the curves. The screening effect thus appears to be independent of the ionic mass.

The experiments described above led to the following conclusions:

1. That a reduction in probe saturation current ratio due to the effect of the filter field on the probe is occurring under the conditions to be found in the filter region of the variable-filter source.
2. That this reduction is due to the electrons being screened from the probe by the filter field.
3. That the screening effect appears to obey a

critical-field rule, with attenuation of the ratio occurring only when the filter field intensity is > 30 Gauss.

4. That the magnitude and form of the screening effect for the geometry of probe and field described above appear to be independent of everything save the intensity of the filter field.

Examining the data obtained, it is apparent that if the absolute value of the saturation current ratio is represented as a fraction of the ideal ratio, all of the points lie on a universal curve. Ignoring the region below 30 gauss, the attenuation of this ratio varies as the inverse of the filter field intensity. This is shown in figure (4.1.12). The relation

$$R |_{B \neq 0} = R |_{B=0} \left(\frac{18.44}{B} + 0.28 \right) \quad \dots(4.1.7)$$

for $B > 30$ gauss has a statistical correlation of 89.5%. Previously published work [86] on noble gas discharges in a fixed rod-filter multipole indicated no screening effect existed. However, the filter field in these noble-gas experiments was found to have been reduced to less than 35 gauss by thermal degradation of the magnets, probably due to an interrupted water supply. The conclusion that electron screening does not occur for fields of the intensity used for

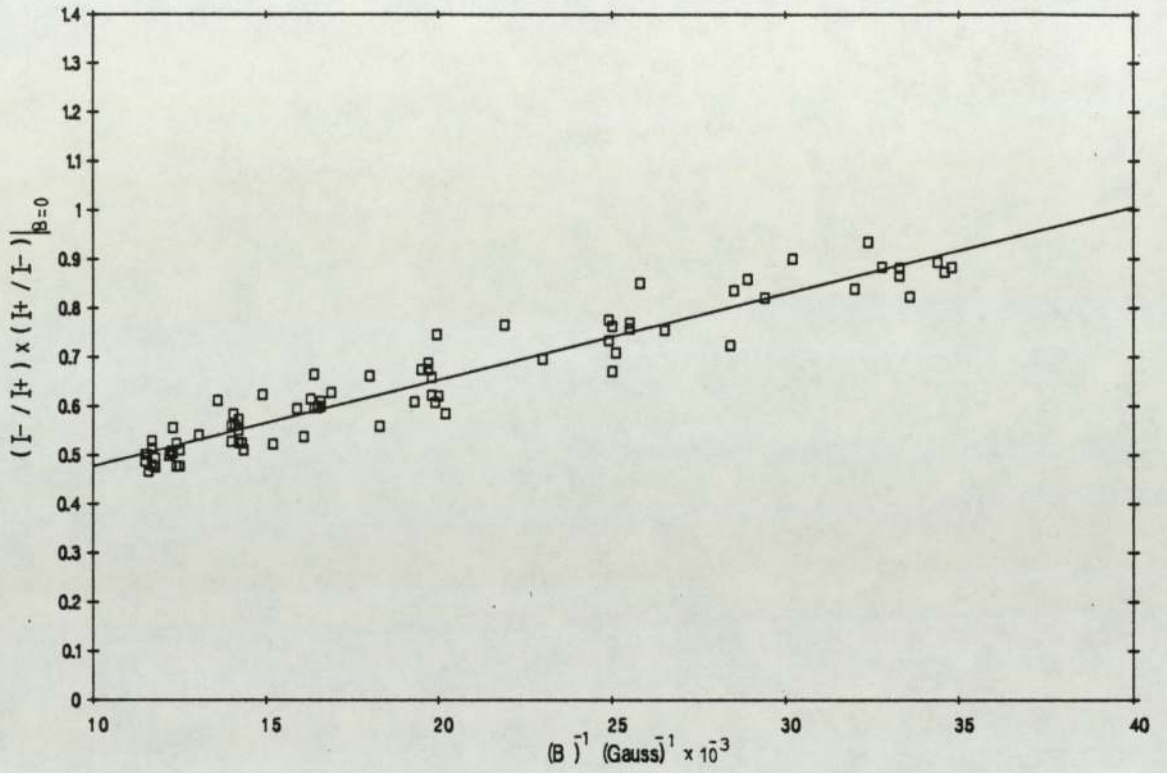


Figure 4.1.12 Universal curve for ratio attenuation by the filter field
 All $B > 30$ gauss data from figures 4.1.8 to 4.1.11

H^- ion-source filters must therefore be discarded.

4.1.1.3.2 Theoretical treatment of electron screening

An electron in a magnetic field will attempt to follow a circular trajectory defined by the Larmor radius in the plane perpendicular to the fieldlines. Thus any electron attempting to travel perpendicular to a magnetic fieldline is forced into a helical trajectory with the fieldline as the centre, leading to a reduction in the mobility of electrons in the transverse direction. The characteristics of the plasma are therefore no longer isotropic, as motion parallel to the fieldlines is unaffected. In addition, ions, with a much lower charge to mass ratio, will be far less affected than electrons. In fact, under the conditions obtaining in a multipole ion source, the effect on the ions may be considered negligible.

An electron may travel perpendicular to a magnetic fieldline only when some external force acts on it to disrupt it's helical trajectory and send it off in another direction. Thus electrons cross a field by a "random walk" diffusion process. The mechanism governing diffusion is that providing the external force for the random walk, and is characterized by the mean free path λ , the distance the electron travels, on average, before experiencing another random change in direction. The simple probe theory discussed so far assumes the effects of collisions between plasma particles may be ignored, - that is, the mean free path of an electron is long

compared with the probe dimension. In the presence of a magnetic field, λ in the perpendicular direction is reduced to the Larmor radius, and collisions within the sheath become important. A double complication arises from the anisotropy so introduced, electron transport along the fieldlines remaining relatively unaffected.

A magnetic field therefore has two effects on electron collection by a probe of arbitrary shape. Firstly, since λ is small for a strong field, the probe itself can block electrons from a given volume being collected. The distribution of particles arriving at a probe is therefore no longer isotropic. For a convex-shaped probe, this geometrical "self-shadowing" leads to a reduction in collected current. This effect has been studied by Bohm et al [87] and Chen [89] who obtain the result that the collected current in the limiting case of very small λ (i.e. a strong field) is attenuated by a factor $\sim \lambda/a$ from the zero-field state, where a is the characteristic probe dimension (usually the radius). In the case of a plane probe, this shadowing is present without the field, and it may thus be seen that a strong enough magnetic field has the effect of making all probes behave in a planar fashion. Obviously, a magnetic field has no effect on the self-shadowing of a planar probe.

Secondly, the field alters electron transport to the probe. In this case, it is necessary to consider a planar Langmuir probe with it's face parallel to a magnetic field of

intensity B gauss ($B < 100G$). When the probe is made positive of V_f , electrons are drawn from the plasma and absorbed by the probe. This depletes the line of magnetic field, or "flux tube", directly in front of the probe, of electrons. If the field did not exist, the electrons would be replenished from the plasma body at a rate governed by the electron thermal velocity. In the presence of the field, however, the depleted flux-tube must be replenished by diffusion of electrons across the magnetic field, at a greatly reduced rate. Since the large-scale neutrality of the plasma may not be violated, this has the effect of reducing the maximum allowable electron current drawn by the probe to a value at which the reduced diffusion rate of the electrons can maintain neutrality, normally a small fraction of the zero-field value. However, the attenuation of the current is not a simple factor given by a reduced transverse diffusion coefficient; the anisotropic nature of the plasma leads to the reduction in transverse electron flux to the probe being offset to some extent by collection from some distance along the fieldlines. This can be thought of as an increase in the area of the probe along the field, with all electron transport into this increased area being governed by the reduced diffusion coefficient. Shotet [88] mentions the possibility of electrons injected through conductive walls "shorting out" the ends of the fieldlines, but the presence of the CoSa containment magnets makes this process unlikely in this case.

Bohm et al [87] suggest that this increased surface area A_λ be defined as being one Larmor radius away from the probe in the direction perpendicular to the field, and one mean-free path away in the parallel direction, as shown in figure (4.1.13). Electron motion within this surface is considered free, and all electrons reach it by means of the process described by the reduced diffusion coefficient. The current to the probe is then given in terms of the density just outside this surface, N_λ , by

$$I_e = \frac{A_p N_\lambda e \bar{v}_e}{4K} \quad \dots(4.1.8)$$

It is necessary to express N_λ in terms of the density in the undisturbed plasma N_e . Chen [89] (after Bohm [87]) has studied this for a probe of arbitrary shape in a magnetic field B , directed along the z direction. It is possible to obtain an expression for the total current entering the surface by integrating J_e over A_λ . This is achieved by transforming the relationships to a space contracted in the z direction by a factor $\sqrt{\Omega}$, where

$$\sqrt{\Omega} = \sqrt{\frac{D_\perp}{D_\parallel}} = \sqrt{\frac{1}{1 + \omega^2 \tau^2}} \quad \dots(4.1.9)$$

For B values of more than a very few gauss, this reduces to

$$\sqrt{\Omega} = (\omega \tau)^{-1}$$

Since $\omega = \frac{\bar{v}_e}{r_e}$ and $\tau = \frac{\lambda}{v_e}$, the coefficient may be expressed as

$$\sqrt{\Omega} = \frac{r_e}{\lambda} \quad \dots(4.1.10)$$

The integral of the flux into this contracted area is obtained by means of a formal analogy with the capacitance relative to infinity of the area A_λ . This yields for the reduced current

$$I_e = I_{e0} \left(K + \frac{A \bar{v}_e}{16 \pi \sqrt{\Omega} C D} \right)^{-1} \quad \dots(4.1.11)$$

where I_{e0} is the current in the absence of a magnetic field, and K a constant between 0.5 and 1 derived from the probe self shadowing previously discussed. Bohm's derivation of this result is considered in more detail in appendix A.

The current to the probe is thus dependent on the capacitance C of the transformed area of the probe relative to infinity. This varies little with the probe shape, but the orientation of the probe causes it to change. In the case of figure (4.1.13), the transformed area is that given by one face of a complex ellipsoid surface with a semi-minor axis of $(a+r_e)$, a semi-major axis $\sqrt{\Omega}(a+\lambda)$ and a height of r_e . This forms a distorted oblate hemispheroid, the normalized capacitance of which has been shown by Smythe

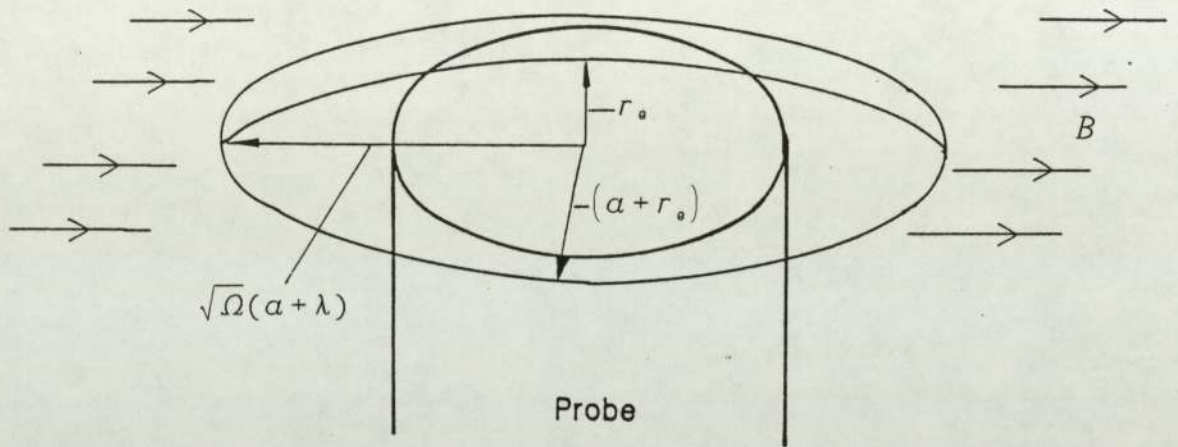


Figure 4.1.13 Probe area distorted by a parallel magnetic field

[105] to be given by

$$C = \frac{(a+r_e)(t^2-1)}{\tan^{-1}(t^2-1)}$$

where $t = \frac{a+r_e}{r_e}$. Provided that the conditions

$$r_e < a < r_i \quad \dots(4.1.12a)$$

and

$$\frac{a}{r_e} > 1 \quad \dots(4.1.12b)$$

are met, Bohm et al [87] show that under these conditions

$$C = \frac{a}{2}$$

Chen [89] notes that the area of collection defined by C is extremely insensitive to the physical shape of the probe.

The most obvious mechanism for electron diffusion in the weakly-ionized plasma of the multipole source is collision with neutral gas molecules. If the value of D from kinetic theory is substituted into equation (4.1.11) for a plane probe of area πa^2 :

$$I_e = I_{e0} \left(K + \frac{6a}{16r_e} \right)^{-1} \quad \dots(4.1.13)$$

Thus for moderate fields, until the Larmor radius term dominates over K, I_e is independent of B. This begins to happen when $B \sim 30$ gauss. After this point, I_e varies inversely with B, as observed. If $B > 30$ gauss, for B in gauss, the attenuated electron current is given by

$$I_e = I_{e0} \frac{10\sqrt{T_e}}{aB} \dots(4.1.14)$$

which is in qualitative agreement with the empirical equation (4.1.7). This shows that the attenuated ratio depends most strongly on the inverse of the magnetic field, as observed experimentally. Through the electron velocity term in the Larmor radius, a dependence on $\sqrt{T_e}$ is also predicted. This is not obvious from the data, but the range of T_e observed in the experimental series was small, and a dependence on $\sqrt{T_e}$ would therefore be difficult to spot. The inverse dependence on the probe radius was not tested. The other obvious feature of the filter-field attenuation is the critical field of 30 gauss required before significant attenuation occurred. For a 0.15cm radius probe, this is the field strength at which both conditions are just satisfied, and at which the Larmor radius term in eqn. (4.1.13) begins to dominate over K. For this probe, the theory would cease to become valid if $B > 400$ gauss. However, at this point non-classical diffusion mechanisms may become important.

Holmes [90,91] considers the case where diffusion across a magnetic field under these circumstances is dominated by electron-electron rather than electron-neutral interactions. However, the relationship of eqn. (4.1.15) holds for both Coulomb and gas collisions. It is not therefore possible to ascertain from these results which mechanism governs the transport of electrons across the field to the probe, only that it is classical in form.

4.1.1.4 The measurement of negative ion densities using Langmuir probes

The characteristic obtained from a Langmuir probe in a negative-ion rich plasma differs from that of the negative-ion free case. The negative ions are, of course, collected along with the electrons when the probe is biased positive of V_f . Due to their greater mass, they cannot move as quickly as the electrons. The saturation negative current to a probe biased at plasma potential, I_- , can then be considered as a flux of a single species of "hybrid" particle with an increased mass, governed by a hybrid ion-electron velocity significantly less than the electron thermal velocity in the pure electron case. Collection of positive ions may be considered to be unaffected to a first approximation. Thus the presence of negative ions leads to a reduction in the ratio of I_- to the saturation positive current obtained from a negatively biased probe I_+ . This ratio is denoted here as R . The magnitude of this reduction may therefore be used to estimate the fractional density of negative ions in the plasma.

It is important to note that R may also be affected by other plasma conditions:

1. Screening of electrons due to a parallel magnetic field will reduce I_- and therefore R , as already discussed.

2. The presence of positive molecular hydrogen ions of increased mass will lead to a reduction in I_+ , increasing R .
3. In the case of the noble-gas discharges, the presence of multiply-charged positive ions will lead to an increase in I_+ , reducing R.

Extreme caution must therefore be exercised in the calculation of negative ion densities from R values. Corrections for the above effects, if considered significant, must be applied to obtain the "ideal" ratio expected in the absence of negative ions if a reliable estimate for N_- is to be obtained.

4.1.1.4.1 Correcting R to obtain the "ideal" Ratio

Experimental values for R must be corrected for the above effects before N_- may be calculated. These corrections take the following forms:

1. The correction for the reduction of I_- by a magnetic field is discussed at some length in chapter (4.1.2.3). The empirical equation (4.1.7) is used, where the probe face is parallel to a field > 30 gauss. A comparison with the value expected from a negative ion-free discharge is made to determine the fall in ratio caused by negative ions.

2. The presence of positive molecular ions of hydrogen are accounted for by the use of a hybrid mass in place of the proton mass. Mass-analysis data from the small fixed filter source (figure 5.2.23) gives a value of ~ 2.8 hydrogen masses for this over a wide range of conditions.
3. The presence of multiply-charged noble-gas ions is of importance in the "calibration" noble-gas discharges known not to produce negative ions in measurable quantities. The increase in the charge/mass ratio so achieved leads to an increase in I_+ . Provided the fractional density of the multiply-charged ion(s) are known, the expected decrease in R may be calculated. If the fractional density of doubly-charged ions is represented by

$$\frac{N_{++}}{N_+} = \frac{F}{1-F}$$

the total ion current is given from probe theory by Equation (4.1.1c), as

$$\begin{aligned} J_{TOT} &= J_+ + J_{++} \\ &= eN_+C_s + 2eN_{++}C_s \\ &= eN_+C_s \left(1 + 2 \frac{N_{++}}{N_+} \right) \end{aligned}$$

$$J_{TOT} = J_+ \left(1 + \frac{2F}{1-F} \right)$$

...(4.1.15)

In the absence of mass analysis data, the fractional density of multiply-charged ions may be estimated from the appropriate ionization cross-sections. For example, in the case of neon, examination of the threshold ionization levels leads to the conclusion that only singly or doubly charged ions are likely in a 60 v arc discharge. The positive ion density for any species is given from the model of ionization in multipole sources due to Green [26] by eqn. (2.1.3). So ignoring stepwise multiple ionization, the fractional density of doubly-charged neon is given crudely by the ratio of cross sections

$$\frac{N_{++}}{N_+} = \frac{\sigma_{++}}{\sigma_+}$$

which on substitution of the relevant data gives a value for R of 120. Similar calculations for Argon and Helium give results of 170 and 56 respectively.

4.1.2.4.2 Using R to obtain negative ion densities

The fractional negative ion density may be found from R by the use of an appropriate theory linking the two quantities. The first theory allowing this was developed by Doucet [92]. A more sophisticated theory, including the effects of negative ions on positive ion collection has been developed by Lea [93].

Doucet theory

This assumes that the only effect of H^- ions on the probe characteristic is to increase the average mass of negative current carriers and so reduce the absolute magnitude of I_- , given by the sum of electron and negative ion currents;

$$I_- = I_e + I_{H^-}$$

The fractional density of H^- ions, F_r , is given by

$$F_r = \frac{N_-}{N_+}$$

from the overall neutrality of the plasma. This gives for the ratio R

$$\frac{I_-}{I_+} = \frac{F_r}{0.6} \sqrt{\frac{M_+}{2\pi M_-}} + \frac{(1-F_r)}{0.6} \sqrt{\frac{M_+}{2\pi M_e}}$$

F is generally < 0.8 , so this simplifies to

$$\frac{I_-}{I_+} = \frac{(1 - F_r)}{0.6} \sqrt{\frac{M_+}{2\pi M_e}} \quad \dots(4.1.16)$$

thus enabling N_- to be determined from the probe ratio. However, this expression has several shortcomings; Doucet himself points out that it is imprecise wherever $N_- \ll N_+$, unfortunately an all too common condition in these sources!. In addition, local production of negative ions (in the presheath) is ignored, as are the effects of negative ions on the formation of the sheath and on the collection of positive ions. These act to further lower the ratio, and therefore the Doucet theory tends to overestimate F_r . The relationship of R to F_r for the Doucet theory is shown in figure (4.1.14).

Lea theory

This also considers the increase in effective electron mass due to the presence of negative ions. However, their presence during positive ion collection (negative probe bias) also alters the potential V_s between the sheath edge and plasma body, usually given by the Bohm sheath criterion as $kT_e/2e$ (see appendix A). This alters the flux of positive ions crossing the presheath, and hence R. The main object of the theory is to relate V_s to the ratio of negative to positive ion densities at the sheath edge, using an

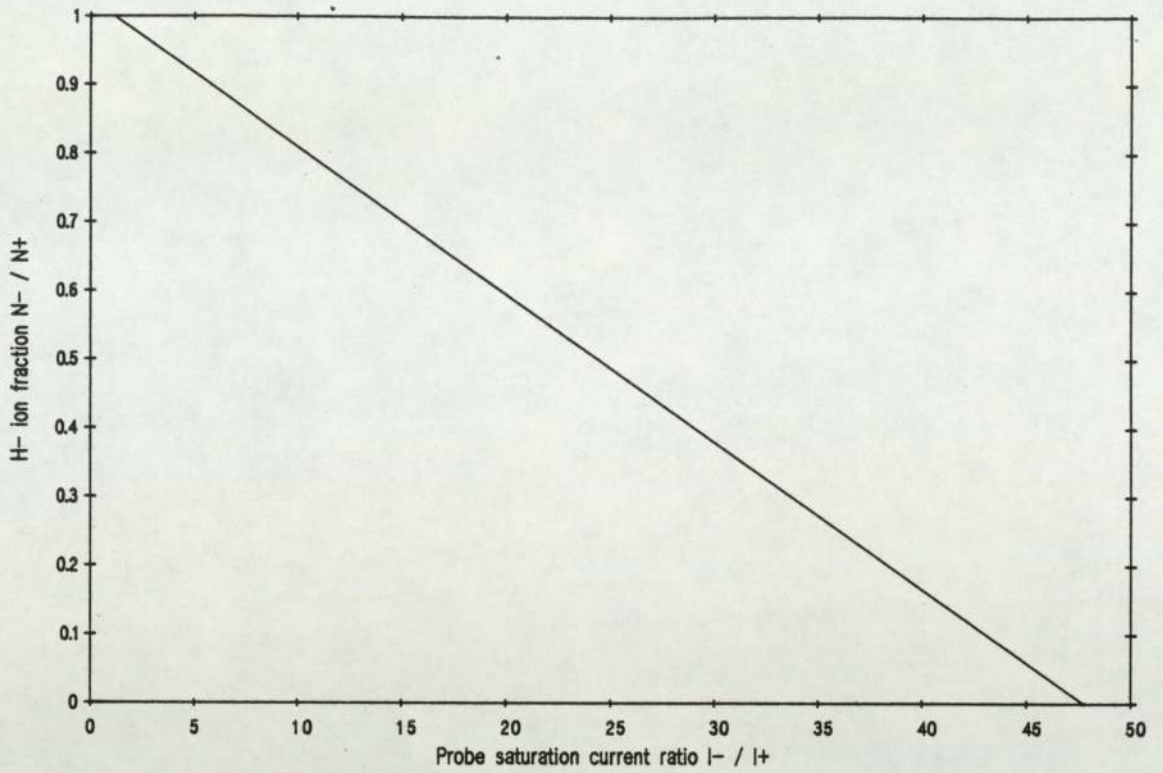


Figure 4.1.14 $R_c - F_r$ curve for Doucet theory
 $M^+ = 2.8 \text{ amu}$

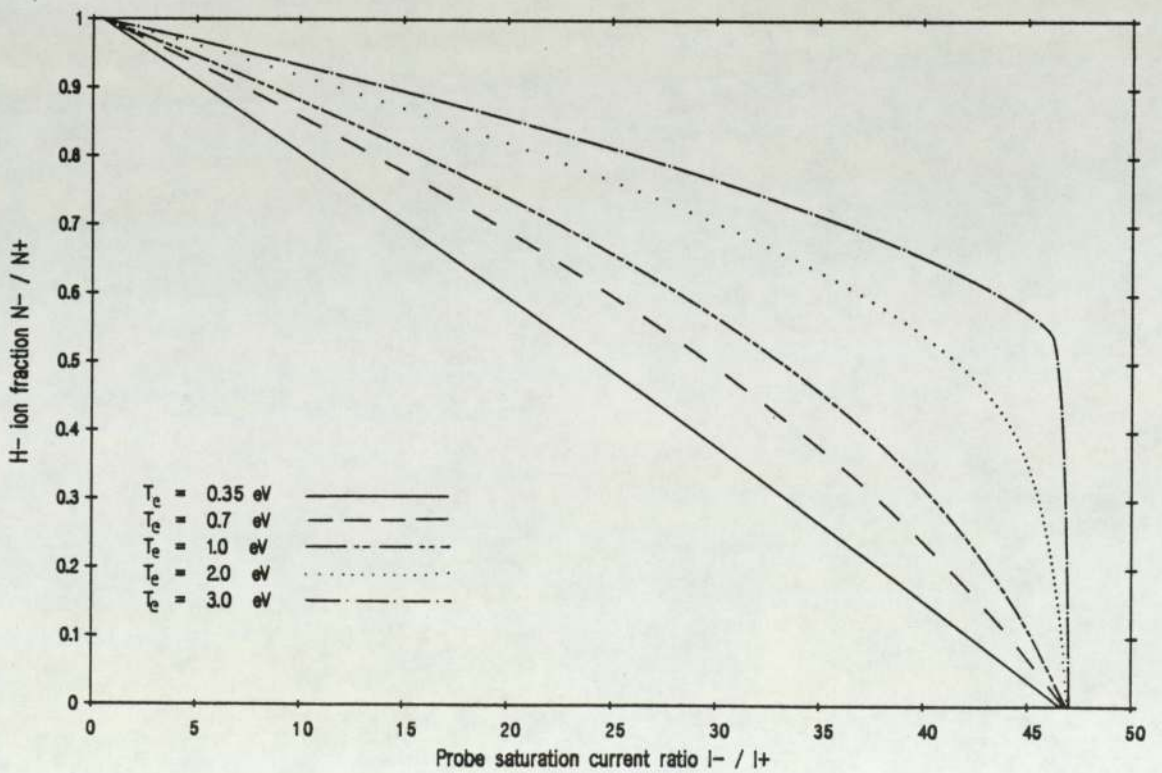


Figure 4.1.15 $R_c - F_r$ curves for Lea theory - Boltzmann attenuation model
 $M^+ = 2.8 \text{ amu}$ $T_- = 0.3 \text{ eV}$ $T_+ = 0.3 \text{ eV}$

expression for V_s obtained from the relationship

$$\frac{dN_+}{dV} = \frac{d}{dV}(N_e + N_-) \quad \dots(4.1.17)$$

This ratio is then related to the ratio of densities in the plasma volume, F_r , using the value obtained for V_s . The process must therefore be iterative. Having thus found V_s for given values of N_- and N_+ , I_- and I_+ may then be calculated from simple probe theory to obtain R, using

$$I_- = -N_e e A_p \sqrt{\frac{kT_e}{2\pi M_e}} - N_- e A_p \sqrt{\frac{kT_-}{2\pi M_-}} + N_+ e A_p \sqrt{\frac{kT_+}{2\pi M_+}} \quad \dots(4.1.18a)$$

$$I_+ = N_+ e A_p e^{\left(\frac{eV_s}{kT_e}\right)} \sqrt{\frac{-2eV_s}{M_+}} \quad \dots(4.1.18b)$$

A curve of F_r as a function of R may therefore be obtained. The expression for V_s obtained from eqn. (4.1.17) varies according to the principal source of H^- ions close to the probe:

1. Diffusion of H^- from the plasma body

Assuming that just within the sheath, negative ions and electrons obey a Maxwellian distribution about the temperatures kT_- and kT_+ , both the negative ion and

electron densities at the probe may be obtained from the plasma body values by assuming a Boltzmann attenuation by the presheath potential V_s :

$$N_{-s} = N_- e^{\left(\frac{eV_s}{kT_-}\right)} \quad \dots(4.1.19a)$$

$$N_{es} = N_e e^{\left(\frac{eV_s}{kT_e}\right)} \quad \dots(4.1.19b)$$

where the subscript s refers to quantities measured at the sheath edge. V_s is given in this case by

$$V_s = - \frac{kT_e T_- \left(N_e e^{\left(\frac{eV_s}{kT_e}\right)} + N_- e^{\left(\frac{eV_s}{kT_-}\right)} \right)}{2e \left(T_- N_e e^{\left(\frac{eV_s}{kT_e}\right)} + T_e N_- e^{\left(\frac{eV_s}{kT_-}\right)} \right)} \quad \dots(4.1.20)$$

Substitution of this into eqn. (4.1.18) allows R to be determined in terms of F_r for known values of M_+ , T_e , T_- and T_+ . The family of curves obtained for a range of T_e values using this model is shown in figure (4.1.15).

2. Local production of H^- in the presheath

In this case, the presheath potential V_s will be determined by the atomic reaction rates governing H^- production in the source, rather than the Maxwellian distribution given in eqn. (4.1.19a). Lea considers this situation when H^- formation is dominated by dissociative attachment, and H^- loss by mutual neutralization and electron

detachment. The H^- density in the presheath is then given by

$$N_{-s} = \frac{N_{es} N_v \langle DA \rangle}{N_{+s} \langle MN \rangle + N_{es} \langle ED \rangle} \quad \dots(4.1.21)$$

If the density of vibrationally excited gas molecules N_v is assumed to be spatially independent, V_s is given by:

$$V_s = - \frac{kT_e \frac{N_{+s}}{N_{es}} \left(\left(\frac{N_{+s}}{N_{es}} \right)^2 + \frac{N_{-s} N_{+s}}{N_{es} N_{es}} + \frac{\langle ED \rangle}{\langle MN \rangle} \left(2 \frac{N_{+s}}{N_{es}} + \frac{N_{-s}}{N_{es}} \right) + \frac{\langle ED \rangle^2}{\langle MN \rangle^2} \right)}{2e \left(\left(\frac{N_{+s}}{N_{es}} \right)^2 + \frac{N_{-s} N_{+s}^2}{N_{es} N_{es}^2} + \frac{\langle ED \rangle}{\langle MN \rangle} \left(2 \frac{N_{+s}}{N_{es}} + \frac{N_{-s} N_{+s}}{N_{es} N_{es}} \right) + \frac{\langle ED \rangle^2}{\langle MN \rangle^2} \right)} \quad \dots(4.1.22)$$

Here, relating the in-sheath densities to F_r must also be done iteratively. Once this is done, substitution of V_s into eqn. (4.1.18) allows R to be determined for a given F_r provided T_- , T_+ and M_+ are known. The family of curves obtained over a range of T_e values for this model is shown in figure (4.1.16).

Lea's derivation of these results [93] is examined in more detail in appendix A. The uncertainties inherent in the measurement of H^- ion densities using this method are discussed in appendix D.

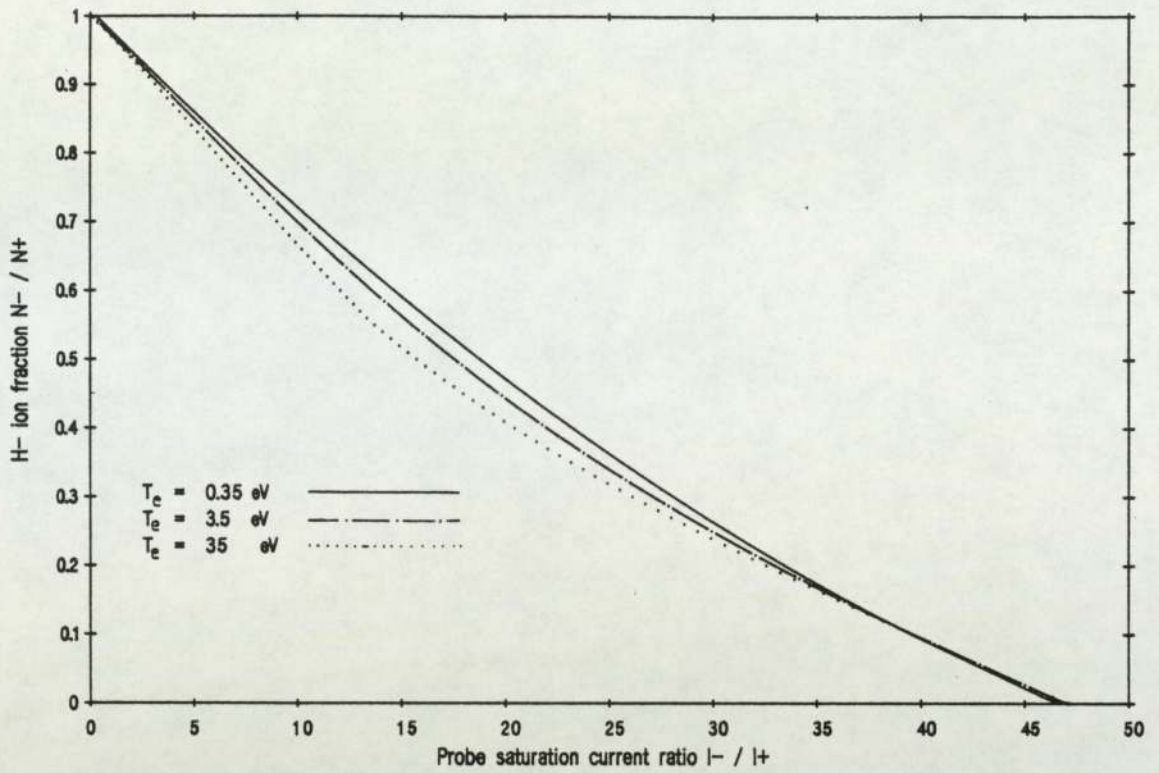


Figure 4.116 $R_c - F_r$ curves for Lea theory - local production model
 $M^+ = 2.8 \text{ amu}$ $T_- = 0.3 \text{ eV}$ $T_+ = 0.3 \text{ eV}$

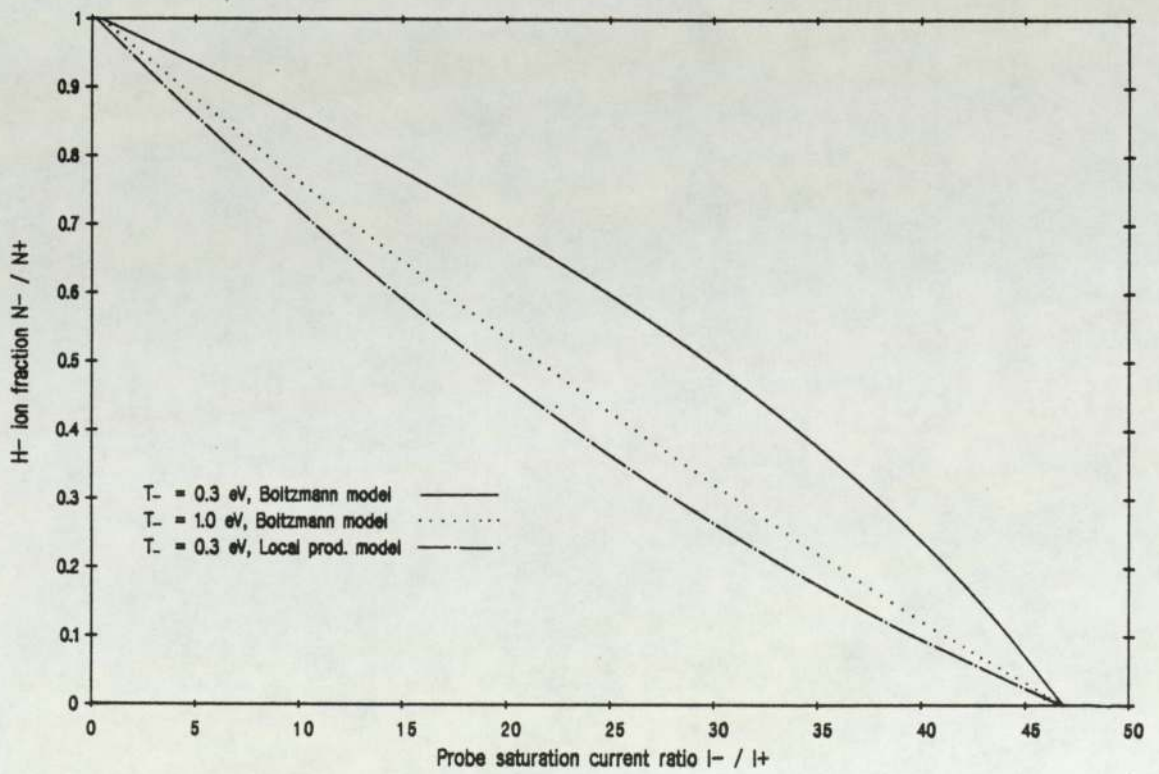


Figure 4.117 Effect of varying T_- on Lea theory curves
 $M^+ = 2.8 \text{ amu}$ $T_e = 0.7 \text{ eV}$ $T_+ = 0.3 \text{ eV}$

Discussion and comparison

Given the reasons mentioned above, the Doucet theory was not considered for use. Selection of the appropriate Lea-theory model was therefore necessary. The relative significance of each model depends primarily on the ratio of kT_- to kT_e . For a presheath potential V_s of $-0.5v$ [82] and an estimated negative ion temperature of $0.2eV$, the fraction of volume-generated H^- present at the sheath edge is given by eqn. (4.1.19a),

$$e^{\left(\frac{0.5}{0.2}\right)} = e^{-2.5} = 0.082$$

Thus under these conditions, only 8% of the negative ions collected by the probe originate in the plasma volume. However, as mentioned in chapter 2, recent experiments have led to estimates of the negative ion temperature as high as $1eV$. Under these conditions, nearly 60 % of the H^- ions could reach the wall, and the Boltzmann distribution model becomes important. Figure (4.1.15) would suggest a problem, as the Boltzmann model is unstable if T_e is greater than quite a small value. However, figure (4.1.17) shows that for a high T_- , the Boltzmann model follows the local production model quite closely. Thus for $T_- \sim V_p$, the N_- result is practically independent of the model used. Given these arguments, the local production model was used to calculate H^- ion densities from R.

4.1.2.5 Summary of Langmuir probe theories

To summarize, plasma parameters were obtained from the probe characteristics by analyses using the following theoretical expressions:

T_e : Calculated from the gradient of the line fitted to the thermal transition region data, corrected for I_p . (eqn. (4.1.1a))

T_p : Calculated from the gradient of the line fitted to the primary region data. (eqn. (4.1.1b))

V_p : Calculated from the intersection of electron saturation and transition regions.

V_f : Measured as voltage intercept of probe characteristic.

I_e : Calculated from I_- after subtraction of I_p , I_- corrected for magnetic screening when in the presence of a parallel field > 30 gauss, using eqn. (4.1.7). I_{H-} contribution ignored.

I_p : Calculated from the line fitted to the primary transition region at V_p .

I_+ : Calculated from a line fitted to the ion saturation region data projected back to V_p . Corrected for Debye sheath expansion (eqn. 4.1.5).

N_e : Calculated from I_e using eqn.(4.1.1a).

N_p : Calculated from I_p using eqn.(4.1.1b).

N_+ : Calculated from I_+ using eqn.(4.1.1c).

N_- : Calculated from corrected ratio R_c using the local production model of Lea theory, by iteration using eqn.'s (4.1.18) and (4.1.22).

4.1.2 Practical use of Langmuir probes

4.1.2.1 Design and construction of the planar probes

Three designs of planar probe were used in the investigation, two fixed in position and one capable of being moved. All consisted essentially of sheathed rods, the ends of which were exposed to the plasma to form the probe face.

Mobile probe

The mobile probe is shown in figure (4.1.18). It consisted of a watercooled shaft made from a pair of concentric stainless steel tubes, with the probe head mounted on one end and a vacuum sealed manifold head on the other. The shaft passed into the source through a double O-ring piston seal, providing mobility in the direction of the normal to the probe face. Cooling water was fed in through ports on the manifold head and circulated between the tubes to protect the probe head and the O-rings in the piston seal. Two fins attached to the inner tube ran the entire length of the shaft to ensure the flow was not short-circuited. Connections to the probe head passed down the centre of the inner tube in a ceramic insulator, and were connected to a vacuum feedthrough on the manifold head.

The probe head itself is shown in more detail in the inset. The probe face was formed by the end of the small central cylinder. This was surrounded by and insulated from a metal tube, the edge of which formed a guard ring around

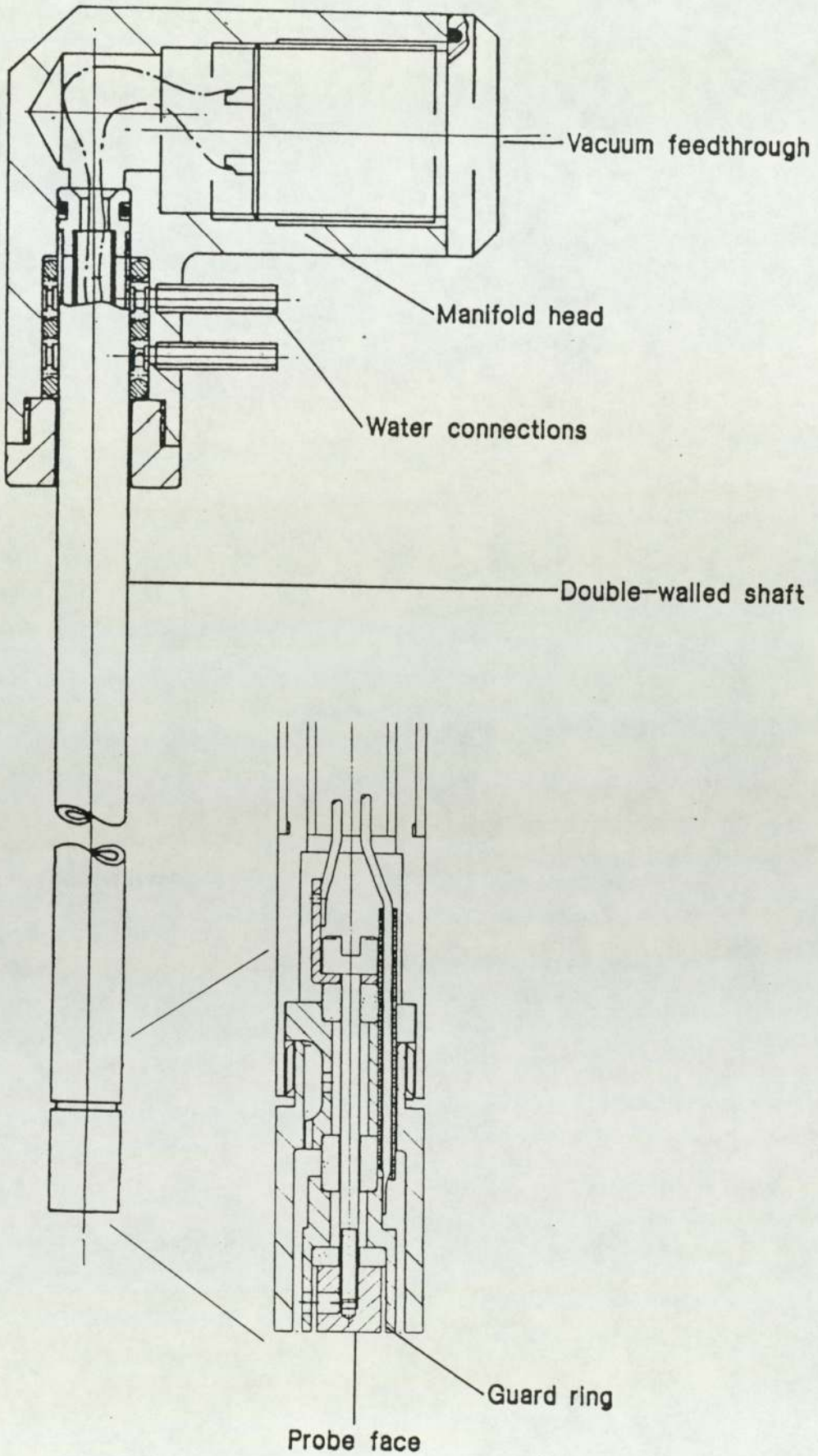


Figure 4.1.18 Construction of the mobile Langmuir probe

the probe face. This was itself surrounded by and insulated from an extension of the outer shaft tube. This extension screwed into the shaft, and served as a retaining nut for the probe head assembly. Contacts to the head and guard ring were made by spot-welded inconel wires. All insulation was provided by high-temperature Alumina ceramics.

In use, the tube assembly was left "floating" (disconnected from earth) to avoid drawing a large current from the plasma. The guard ring was originally intended to be maintained at the potential of the probe face with a PSU separate from that used to drive the probe, in order to reduce the edge-effects. However, this was found to have little effect on the characteristic, and it was therefore left floating. Since the insulators were hidden from the plasma, the deposition of filament-metal on the probe had little effect. Two of these probes may be seen in figure (3.3.4), one mounted vertically on the backplate for an axial scan, the other horizontally in the extraction region for a radial scan. The third shaft entering the large flange is attached to the mass analyser probe described later on.

Fixed probes

The type 1 fixed probe is shown in figure (4.1.19). It consisted of a stainless-steel or tungsten rod 3mm in diameter, threaded at one end and screwed into a modified VG 6mm dia. copper vacuum feedthrough. A length of alumina ceramic tube was pushed over the rod, exposing only the end

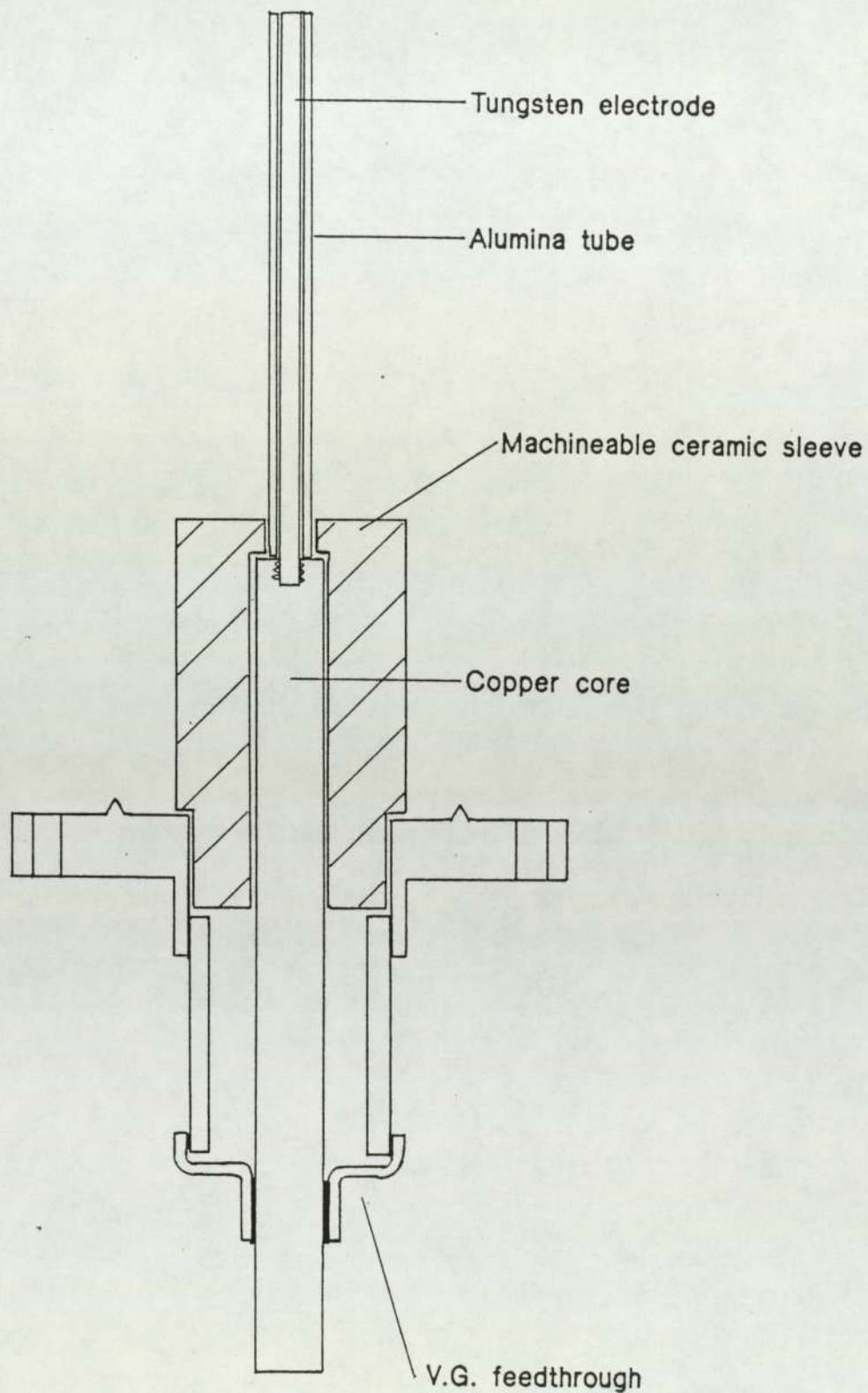


Figure 4.1.19 Type 1. fixed Langmuir probe

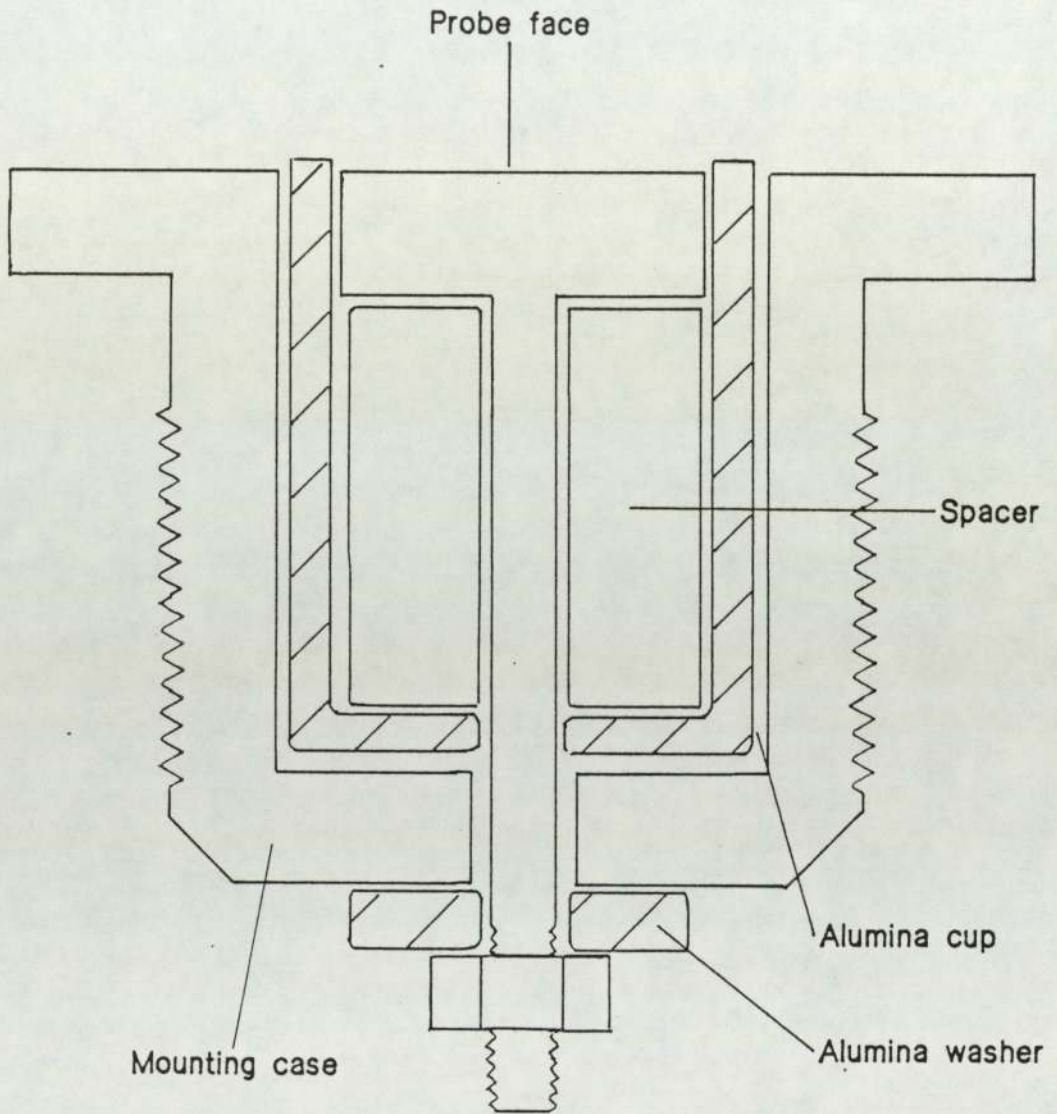


Figure 4.1.20 Type 2. fixed Langmuir probe

to the plasma, thus forming the probe face. The feedthrough bolted directly to the diagnostic ports on the source(s). In use, the probe relied on radiation and conduction for cooling. The exposed insulator proved susceptible to metallic deposition, leading to a spuriously-large probe area after prolonged use. This could be cured by regular cleaning with an abrasive agent.

The type 2 fixed probe is shown in figure (4.1.20). It consisted of a small (~3mm dia.) stainless steel disk mounted on a threaded rod. This was mounted in a small cylindrical alumina cup, defining the probe face. The whole assembly was screwed into a stainless steel case fitted with an exterior thread. The probe was mounted directly onto the BFE of the small variable-filter source, on the vertical axis. Again, the probe was uncooled, and suffered from metallic deposition due to the exposed insulator, cured by the methods described above.

4.1.2.2 LPA - the computer-based probe analysis system

To improve the accuracy and speed of analysis of probe characteristics, a system operated by a microcomputer was developed to directly control a planar Langmuir probe, acquire and analyse the characteristic, and store the analysed results and raw data in disk files. In addition, several subsystems were written to allow the processing and display of analysed results. The system operated on a "shot"

basis to reduce thermal loading, rather than the "interactive" system which has been successfully employed with smaller probes [95].

The LPA system is quite extensive, in terms of both hardware and software. Accordingly, only a brief synopsis of both aspects is given here. A full description may be found in appendix B.

4.1.2.2.1 Hardware

The system centred around an IBM PC XT microcomputer. This was connected to the probe circuit via an interface unit (3D, type IBM-R), which sampled data using a fast 12-bit analogue to digital converter (ADC). This interface also controlled a 12-bit 4-channel digital to analogue converter (DAC), allowing voltage signals to be generated by the computer. The probe circuitry is shown in figure (4.1.21).

The probe voltage was varied by amplifying a tailored voltage sweep generated from the DAC using a low-impedance power amplifier (Analogue Associates, type A400) used as a voltage-controlled power supply. The current flowing through the circuit was monitored using one of a series of accurately-known sensing resistors. Due to common-mode problems, these were situated in the earth-return line of the circuit, and the amplifier chassis was thus left floating relative to earth to avoid bypassing them. The voltage applied to the probe was monitored using a high-value resistor chain between the probe and reference electrode, and

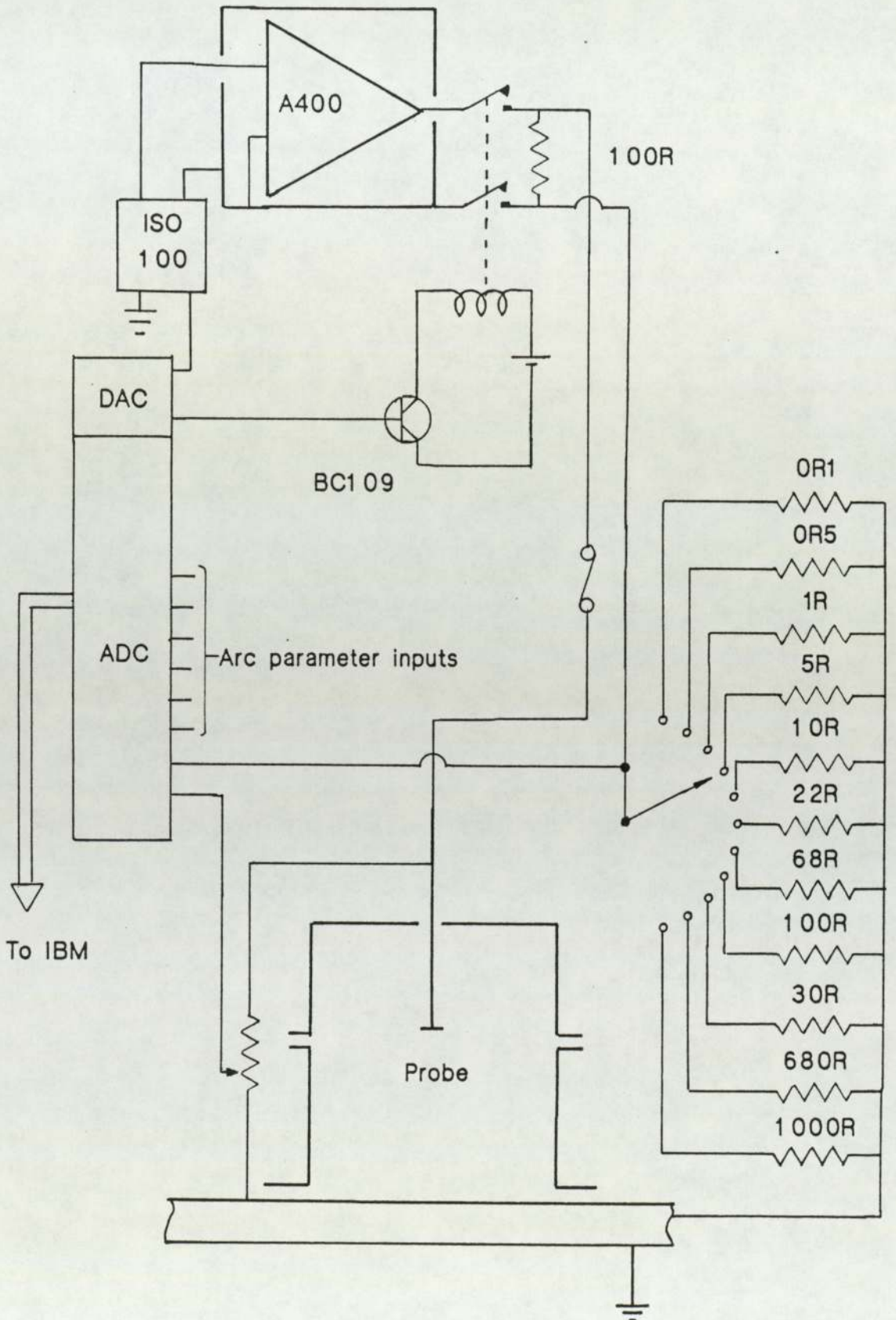


Figure 4.1.21 Probe circuit for the LPA system

the two signals fed into the ADC. These gave the system a voltage resolution of 0.06 V / bit and a current resolution of between 0.5 μ A and 5 mA /bit, depending upon the resistor in use.

The probe and electronics were protected by a normally-open relay in the probe line, isolating the amplifier from the probe when not being swept. The relay was enabled by using one channel of the DAC to trigger a transistor switch which closed the relay for the shot period. Additional protection was provided by an inline fuse. This prevented large currents flowing in the probe circuit in the event of the probe area suddenly increasing or the probe line contacting earth, for example, in the sudden melting of a probe.

Arc parameters were monitored by the ADC during a shot. Arc current was monitored via a Hall-effect DC current sensor, and arc voltage by an opto-isolator chip (Burr Brown, type ISO 100AP - see appendix B) All other sensors were input directly to the ADC via trimmer resistors.

4.1.2.2.2 Software

The software for the LPA system was written in TURBOPASCAL version 3.01A, and comprised some 10 000 lines. The compiled machine code totalled about 130 kBytes. The acquisition and analysis section comprised roughly 54 kBytes of this, and remained resident in memory throughout system operation since execution speed in this section was

important. The subsystems were loaded from disk into an "overlay area" in the code by LPA when required. To maximize execution speed the acquisition and analysis was run on a "shot" basis, using a pre-defined "template" containing parameters governing the sweep. Variable voltage resolutions were employed to reduce the total amount of data. Like data and results, templates could be stored for future use. Probe traces and fitted lines were displayed on the VDU to allow visual correlation checks to be made. The section controlling the acquisition and analysis of probe data is the most important, and is shown in flowchart form in figure (4.1.22). A description of the rest of LPA may be found in appendix B.

Data acquisition consisted of first reading the arc parameter ADC channels and storing the results. The probe was then swept according to the template, and the I-V trace held in memory. Acquisition was completed by again scanning the parameter channels and averaging with those already stored. Acquisition took between 0.1 and 20 seconds, depending on the sweep design.

Probe data was then sorted, normalized and smoothed. A line was fitted to the ion saturation region as described in section 4.1.2.1. The ion saturation current was checked by extrapolation of this line back to $(V_p + V_{bias})$, with V_p guessed at 0v in the first instance. Logarithms of the current values were then obtained. The existence of a primary electron region, and the positions of all the regions

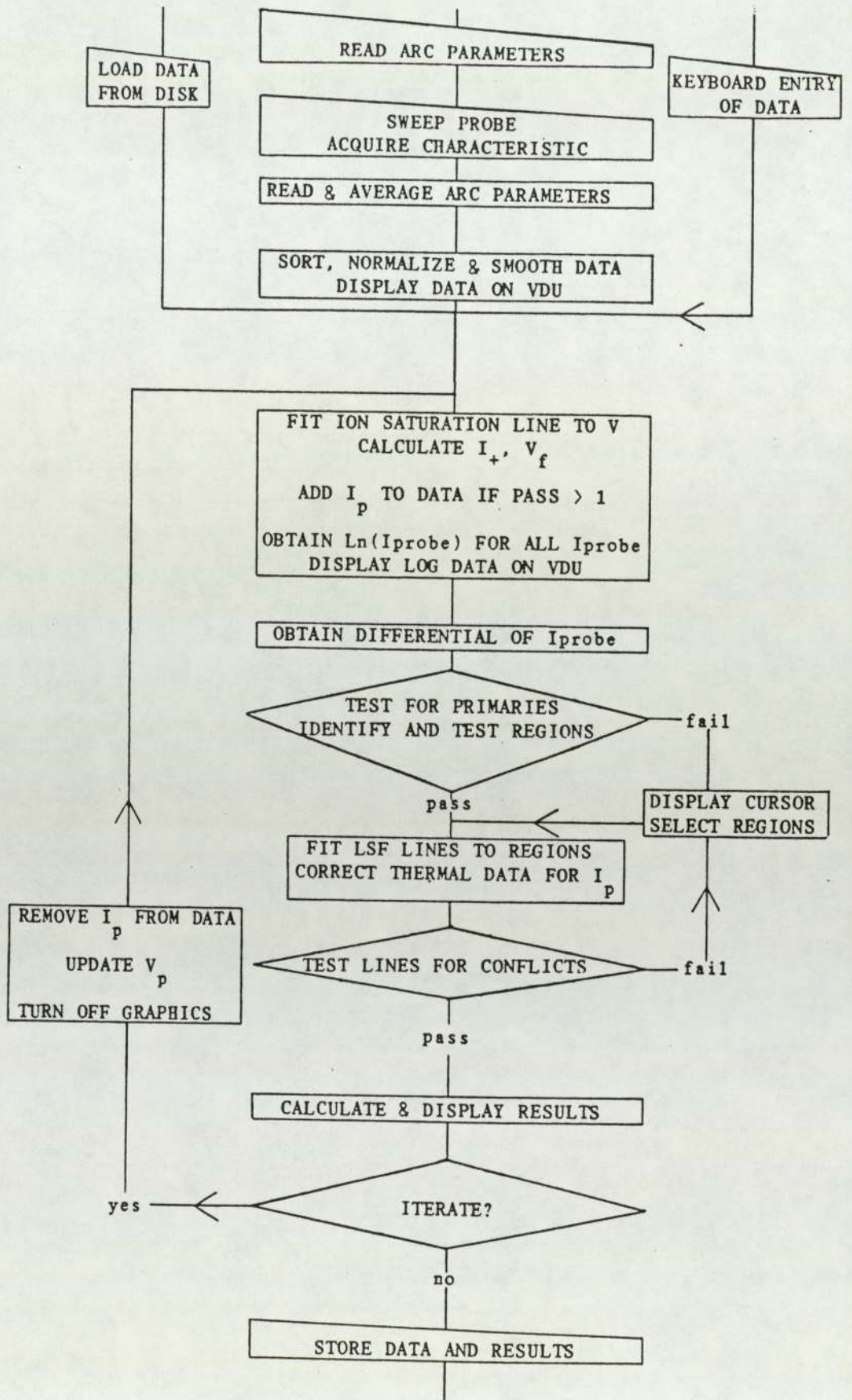


Figure 4.1.22 Flowchart of LPA data analysis and acquisition

were identified by testing the differential of the probe current. Where this failed, a cursor could be used to manually select the regions. Least-squares-fit lines were then fitted to the data in each region. The points in the thermal region were corrected for primaries. Data from the fitted lines was then used to calculate the plasma parameters, in accordance with the theory in section (4.1.1). The option of an iterative calculation was then offered, with the primary region line being used to subtract the primary electron contribution from the data. Data analysis recommenced with fitting the ion saturation line, using the recently calculated value for V_p . This cycle could be repeated indefinitely, but generally converged to a stable solution after ~ 3 cycles. A single cycle lasted between 10 and 50 seconds.

The results obtained using LPA were compared with results obtained from manual analysis of chart-recorder traces in an extensive series of validation experiments. These demonstrated that the results obtained with LPA were reliable (that is, reproducible) and agreed with manually-obtained results to within $\sim 10\%$ on average. The accuracy of this validation process was limited, due to the problems of attempting to measure the I_+ values from a recorder trace and fit them to the $V^{0.75}$ ordinate, and in fact the LPA results are probably the more accurate. The rapid capture and storage of probe traces using LPA made experimental work much quicker. A properly-detailed manual

analysis of a probe trace, including fitting an ion-saturation line and correction for primaries took about one hour. The corresponding LPA cycle was between 70 and 500 times faster, more accurate and offered the possibility of iteration to remove high-energy primaries from the ion region. Manual analysis of all the traces captured and used in this study would by itself have taken over 5 years continuous work.

4.2 The mass analyser probe

The second type of probe inserted into the multipole plasma in this investigation was an extremely small electromagnetic mass analyser, consisting of a solenoidal electromagnetic lens fed by a small two-grid extraction system. The solenoidal lens was chosen as a separation device due to its cylindrical geometry, which simplified the construction of small high-accuracy components considerably, thus reducing the overall size of the assembly to about that of a cotton-reel. Similar devices [96] based on a more traditional magnetic-deflection technique are considerably larger. The principles of operation of this device are discussed in section 4.2.1, and its detailed design and construction in section 4.2.2. The drive circuitry and use of the probe are covered in section 4.2.3.

4.2.1 Principles of operation

The mass analyser depends for its operation upon the ability of a solenoidal electron lens (similar to those in electron microscopes) to focus a parallel beam of charged particles to a narrow waist. This is utilized as shown in figure (4.2.1). A beamlet is extracted from the plasma by the two accelerator grids. It passes into the field-gap of the magnetic lens, where the trajectory of the charged particles is altered, bringing the beamlet to a focus at a distance f . This distance is determined by the intensity of the lens field and the mass and axial velocity of the charged

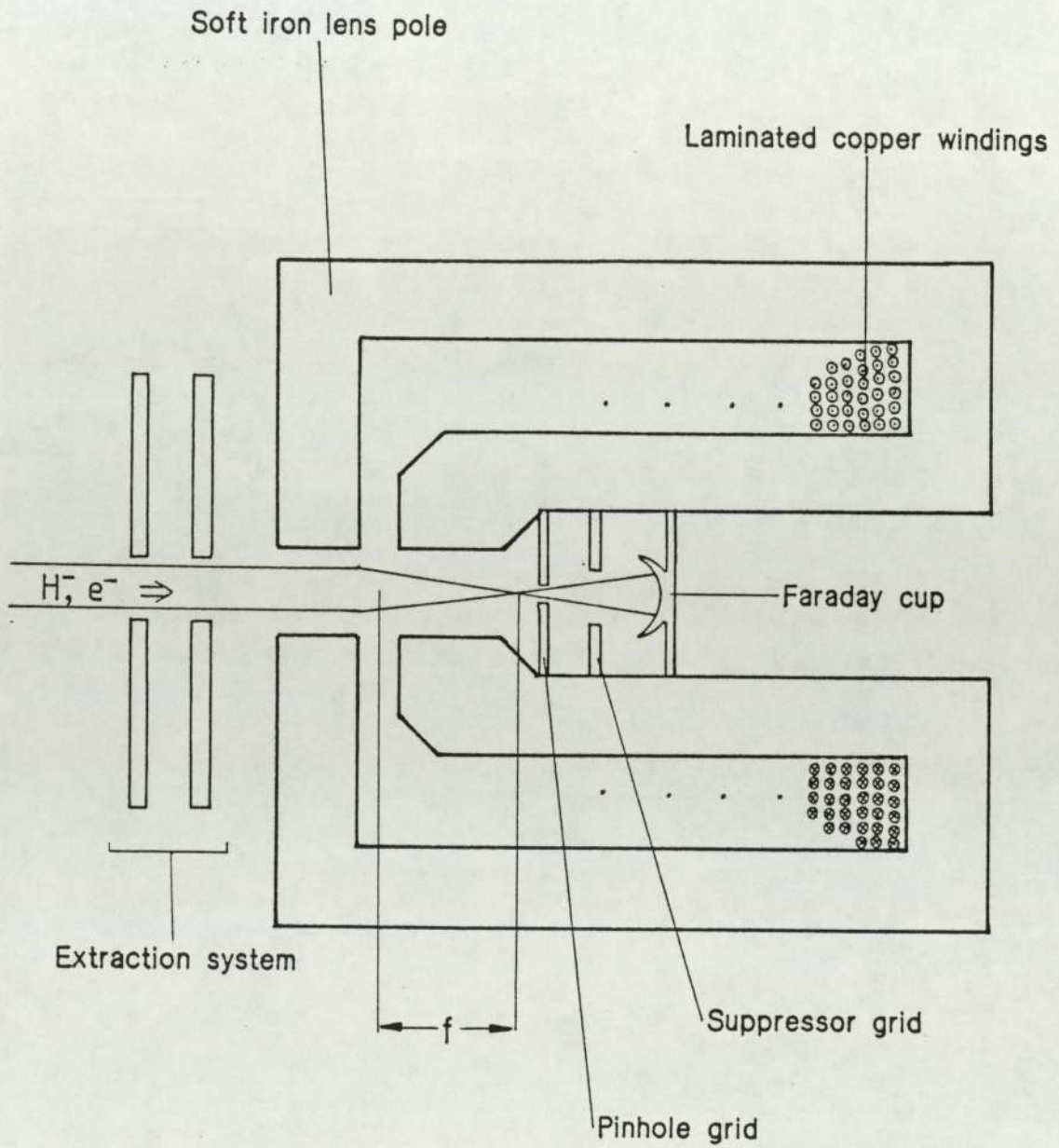


Figure 4.2.1 Schematic diagram of the mass analyser probe

particles, according to known electron-optical laws. In this case, the paraxial ray equation [97] for a charged particle at a distance r from the lens axis is expressed as;

$$\frac{d^2r}{dz^2} = \left(\frac{eB_z}{8MV} \right) r = -k^2 r \quad \dots(4.2.1)$$

where B_z is the intensity of the lens field, V the accelerating voltage and M the particle mass. B_z is a direct function of the lens excitation (NI , where N is the number of turns on the lens coil and I the current passing through them) and the field length S of the lens. For a solenoidal field

$$B_z = \frac{\mu_0 NI}{S}$$

equation (4.2.1) has a solution

$$f = \frac{1}{k \sin ks}$$

where

$$k = \sqrt{\frac{e}{8MV} \frac{\mu_0 NI}{S}}$$

Thus if I is varied, the focal length f of the beamlet for a given mass and acceleration voltage also varies.

A small axial pinhole is placed the other side of the

lens, with a Faraday cup behind this. The current reaching this cup is governed by the number of charged particles passing through the pinhole. Thus if the Faraday cup current is plotted as a function of I for a constant V , peaks should occur as the focal lengths of different species of charged particle match the distance between the lens focal plane and the pinhole.

4.2.2 Design and construction

The practical design of the mass analyser probe head is shown in figure (4.2.2). The head was mounted via a screw thread in the base onto the watercooled mobile Langmuir probe shaft described in section (4.1.2). Connections to the mass analyser head were provided via a multi-pin vacuum feedthrough, the connectors passing through the shaft being insulated with a four-bore ceramic tube. The entire head measured 3.5cm long and 2.7cm in dia., and weighed ~100g.

The accelerator consisted of two 0.4mm thick stainless-steel plates, each with a 0.5mm dia. axial hole. These were mounted in rebates machined into an annular insulator, and held in place by the end-cap of the stainless-steel case, which also served to hold the outer grid at floating potential. The 1mm gap between the plates was maintained by a ceramic washer. This held the inner plate in contact with the lens outer pole piece, which was raised to the acceleration potential along with the entire detection assembly.

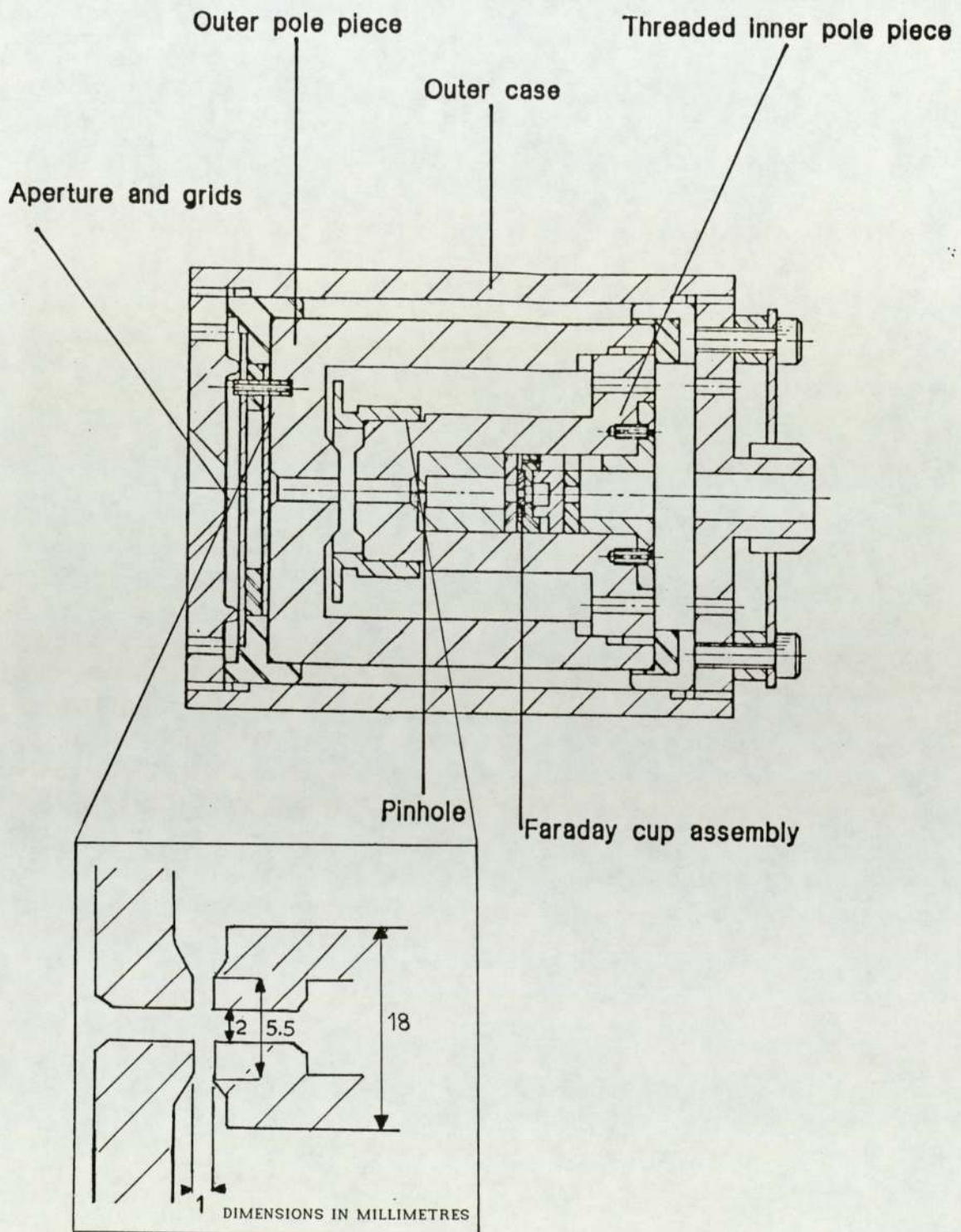


Figure 4.2.2 Practical design of mass analyser probe

The lens pole pieces were machined from Armaco iron, to optimum dimensions specified by the equations described in (4.2.1) and by Mulvey [98], and Dugas et al [99]. The coil consisted of 720 turns of 0.25mm dia. enamelled copper wire, with a maximum pulsed capacity of ~ 4.9 Amps. One end of this was in electrical contact with the pole piece, the other being fed through the rear. The coil was wound onto the inner piece, which was then screwed into the outer. The lens itself was supported away from the casing by a pair of annular ceramic insulators, held in place by the shaft mounting flange. The exact dimensions of the lens gap are shown in the inset to figure (4.2.2).

The detection components were mounted in a bore in the inner pole piece. They consisted of a 0.3mm dia. pinhole grid, followed by a larger second grid to suppress secondary electrons, and finally a Faraday cup, all machined from stainless steel and separated by ceramic washers. The pinhole grid was in electrical contact with the inner pole piece. Connections to the second grid and Faraday cup were fed through holes in the ceramic washers. The detector head assembly is shown partially disassembled in figure (4.2.3). The assembly was held in place by an insulated retaining tube bolted to the inner pole piece. The mass analyser probe is shown mounted on the watercooled shaft in figure (4.2.4).

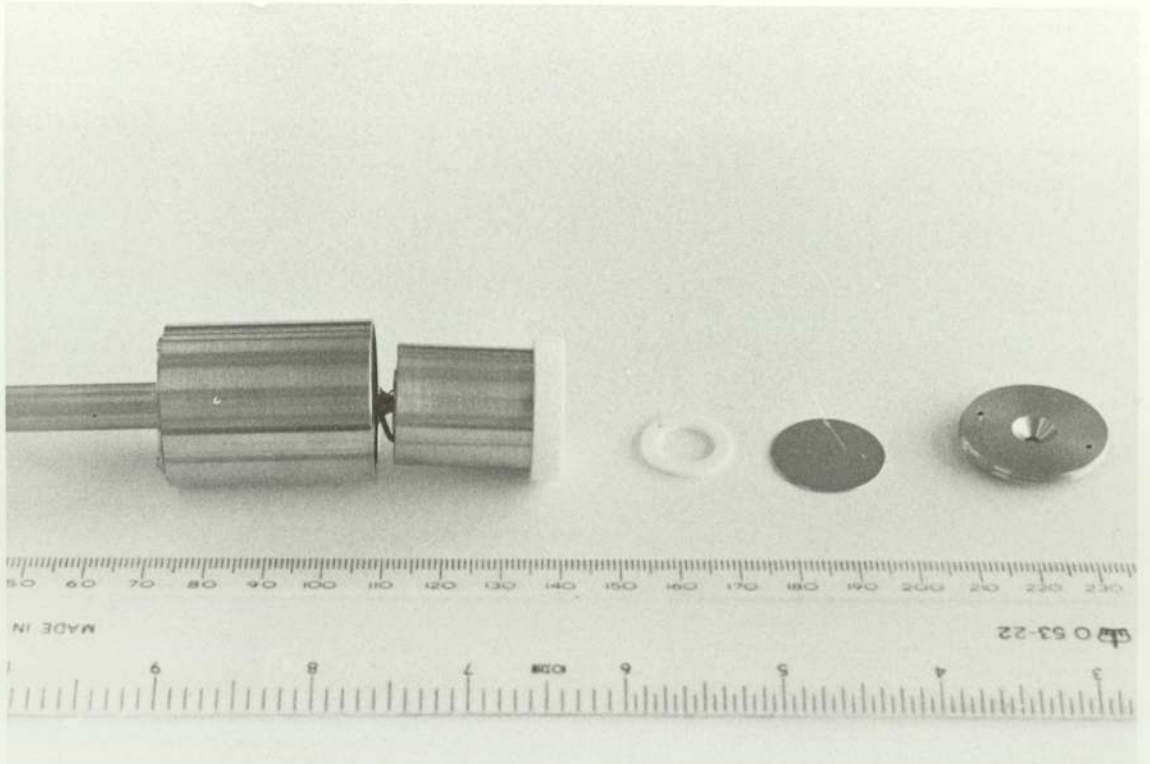


Figure 4.2.3 Mass analyser probe detector head components

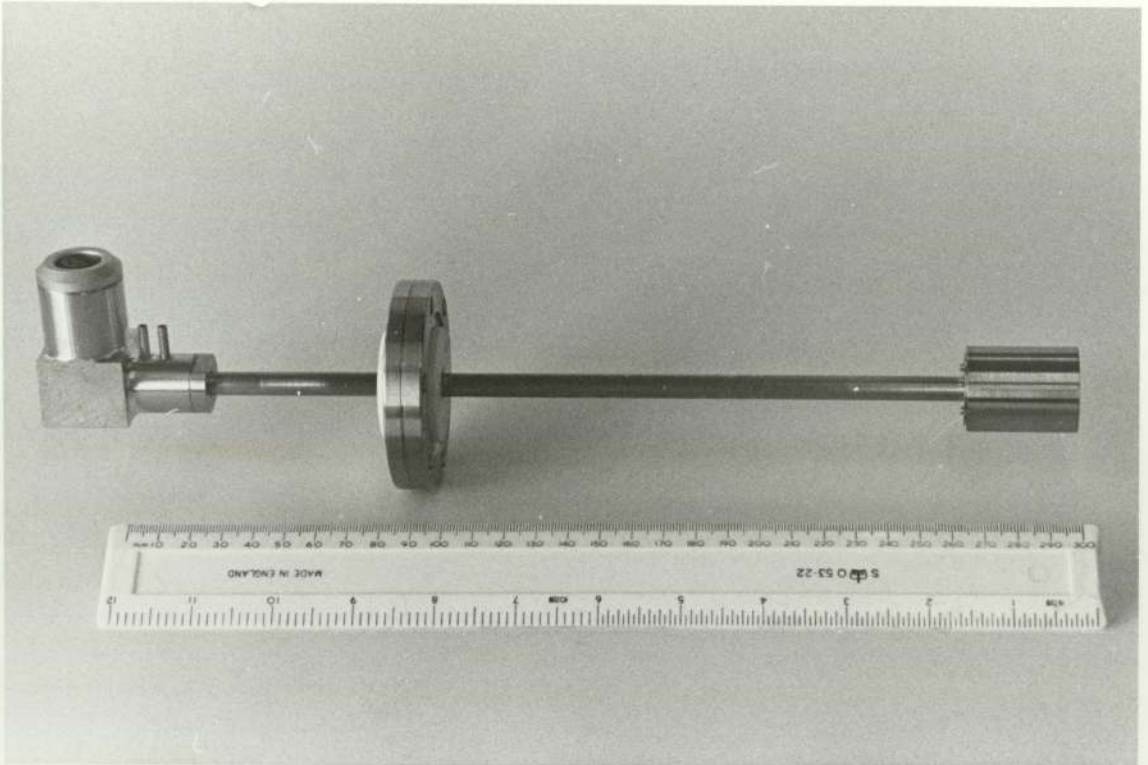


Figure 4.2.4 Mass analyser probe assembled onto watercooled shaft

4.2.3 Use of the Probe

A schematic diagram of the circuit used to drive the mass analyser probe is shown in figure (4.2.5). The accelerator voltage supply maintains the entire lens and detector assembly at a potential V above floating potential, to avoid deceleration of the beam. Typically, $V = +250$ volts. The Faraday cup was maintained at $\sim 10v$ positive of this, to ensure collection of all electrons and ions passing through the pinhole. The second grid was held negative of the Faraday cup to reflect any electrons ejected from the cup.

The coil supply was originally intended to be a capacitor, giving a $10mS$ pulse of current through the coil to reduce the heat loading. However, it was necessary to isolate all detection contacts from earth using ISO 100AP optoisolators. The practical bandwidth of these devices at the signal levels available from the M.A.P is DC to $<1kHz$. Hence although transmission of the current pulse was successful, the much narrower signal pulse was smoothed away. Thus the coil pulse was supplied from a battery and potentiometer arrangement operated with a long insulated stick, giving a pulse duration of ~ 1 sec. The voltage developed across a $1\text{-}\Omega$ resistor by the current pulse was transferred using an ISO 100 to the X-input of a Nicolet 3091 digital storage oscilloscope. The current collected by the Faraday cup was monitored in a similar fashion using a $100k$ resistor, and fed to the Y-input of the scope. The height

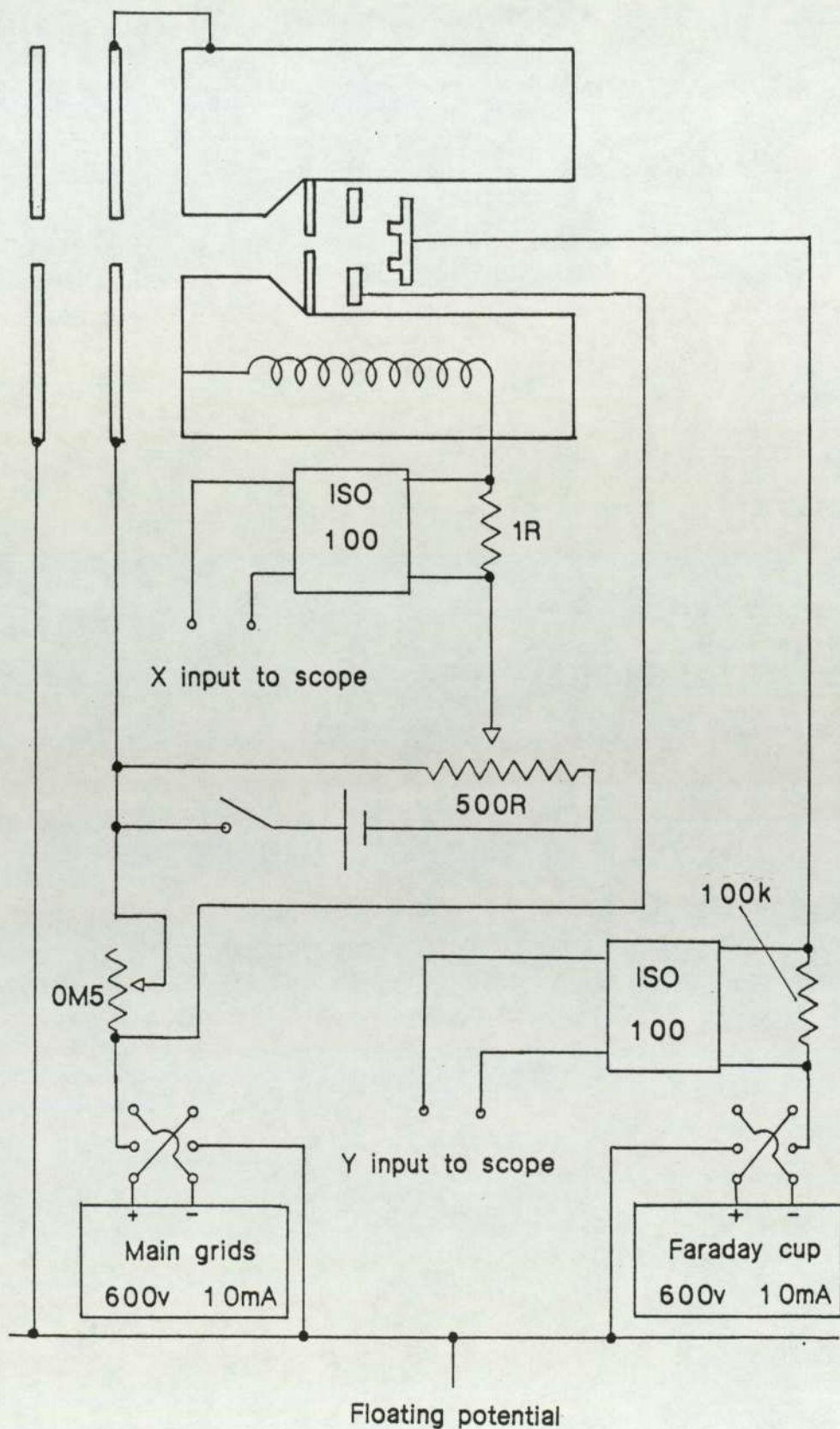


Figure 4.2.5 Schematic diagram of MAP control circuit

and position of the peaks were measured using the scope cursor function, and the traces recorded on photographic film.

CHAPTER 5

Experimental procedure and results

This chapter describes the main programme of experiments performed on the ion sources and presents the results obtained, which form a spatial and parametric survey of a filtered magnetic multipole source. These results are discussed and compared with theory in chapter 6. The chapter is divided into three sections. Section 5.1 presents the results describing the behavior of the parameters characterizing the basic plasma, divided into sub-sections according to the type of arc condition being varied. Section 5.2 similarly presents measurements of negative ion density, obtained from probe calculation (5.2.1) and beam extraction (5.2.2). Section 5.3 describes the results obtained from the mass analyser probe. A considerable number of results are presented, so a summary of the most important observations is included at the end of each sub-section. The majority of the probe results were obtained from the variable-filter source; where this is not so the fact is stated explicitly. All extracted beam data was obtained from the fixed-filter source. Many references are made to the various regions of the sources; these are as defined in chapter 3. Abbreviations for experimental and plasma parameters are as defined in the symbology.

5.1 Measurements of basic plasma parameters

This section describes the series of experiments performed to determine how the basic plasma parameters (electron and ion densities, electron temperatures, plasma potential) at a given position within the source varied with the arc conditions. In particular, the effect of the filter field was studied.

5.1.1 Spatial variation

As stated in chapter 2, all the sources used in this investigation were constructed so as to generate a spatially nonhomogeneous plasma, this apparently being necessary for efficient volume H^- production. Information about the spatial variation of the plasma was therefore necessary to test the assumptions about the mechanisms of H^- production. Accordingly, experiments were performed to study both the axial and transverse variation of the plasma. These took the form of probe measurements in the small variable filter source, using the mobile planar probe.

5.1.1.1 Axial variation

The mobile planar probe was mounted on the central backplate port of the source, as shown in figure (3.3.4). This allowed it to be traversed from the near-backplate position (26 cm from the BFE), through the filter, to within 4 cm of the BFE. This was done both with the filter inactive and at full excitation, for source pressures of 3mT and 10mT.

Probe traces were captured at discrete positions along the axis, with the discharge being switched off whilst the probe was moved to prevent contamination through the piston seal.

The variation in plasma density (N_+) with distance from the BFE at 3mT is shown in figure (5.1.1). In the absence of the filter field, N_+ falls slowly from the backplate position up to 20 cm from the BFE, roughly midway between the plane of the filament and the poorly shielded area at the top of the filter module. At this point, the rate of attenuation increases and the density falls steeply with distance, to a final value an order of magnitude below that in the driver module. The values (driver: $N_+ \sim 10^{11} \text{ cm}^{-3}$, extraction: $N_+ \sim 10^{10} \text{ cm}^{-3}$) are typical of the densities encountered in this source. The variations are approximately linear.

In the presence of the full (80 gauss) filter field, several new features emerge. The driver region plateau rises in absolute magnitude by some 30%. A more rapid attenuation of the plasma with distance in the region of the filter occurs, and the absolute magnitude of the extraction region density falls by some 50%. In addition, a significant difference between the electron and ion density in the filter and extraction regions emerges. This is shown and examined in detail in section 5.2.1. Note that the region of attenuation appears to shift from the top of the filter module to the filter itself, indicating that the filter field is now the main attenuating force. The axial variation in thermal (bulk) electron temperature is shown in figure

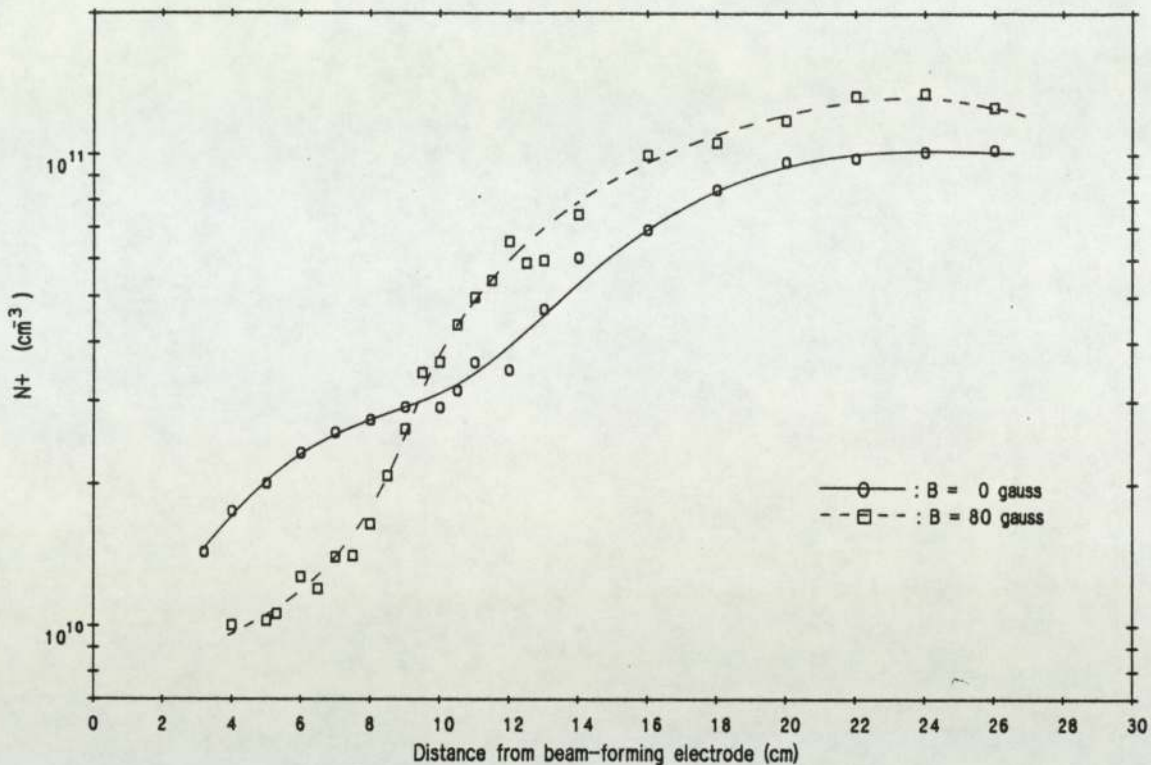


Figure 5.1 Axial variation of plasma density
 $I_{arc} = 5A$ $V_{arc} = 60v$ $Pres. = 3mT$

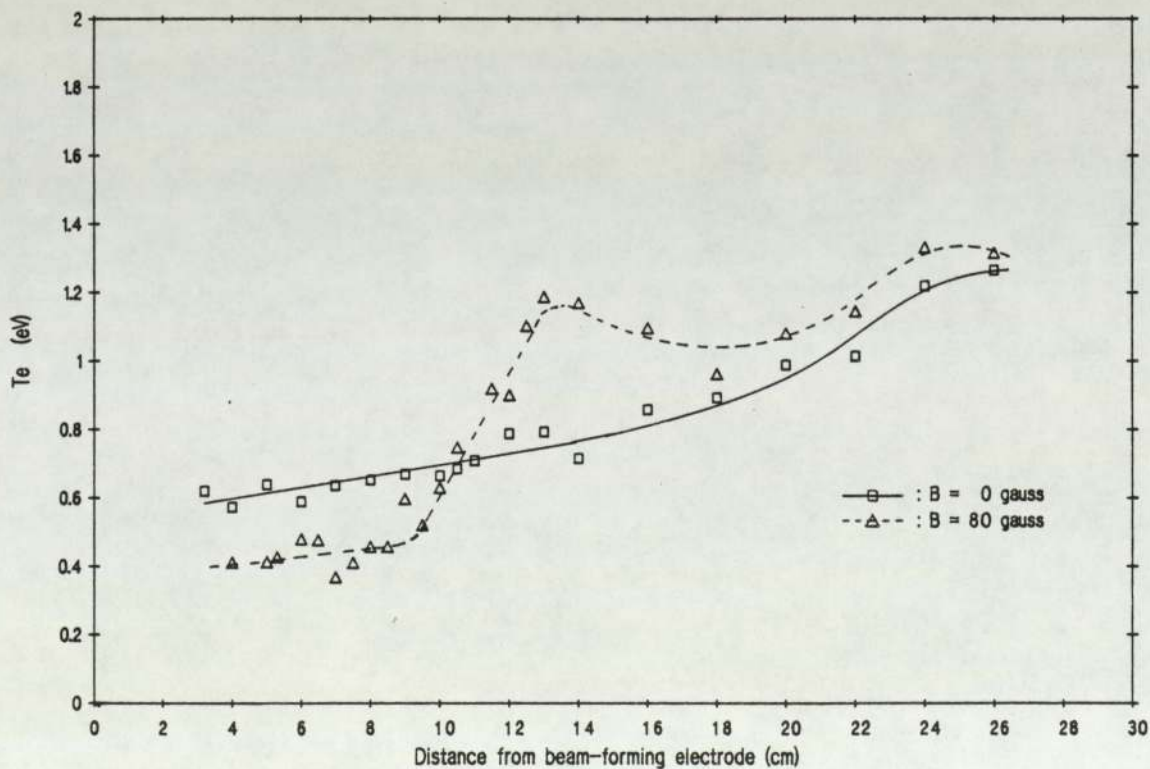


Figure 5.2 Axial variation of thermal electron temperature
 $I_{arc} = 5A$ $V_{arc} = 60v$ $Pres. = 3mT$

(5.1.2). In the absence of the filter field T_e shows an approximately linear fall from the centre of the driver region to the beam-forming electrode, with a small peak at the filament position. The absolute magnitudes of temperature are again typical; 1-2 eV in the driver region and $\sim 0.3-0.6$ eV in the extraction region. With the filter field on, the attenuation gradient is altered. The absolute magnitudes of temperature in the extremes of the two regions remain similar, but the transition region between the two is confined to a narrow region centred on the filter.

A useful quantity to examine is the product of plasma density and electron temperature $N_+ T_e$. If small numerical constants arising from the implied average over the electron distribution function are ignored, this parameter can be said to represent the energy density, in eV cm^{-3} , of the bulk plasma. The bulk energy density $N_+ T_e$ is plotted as a function of axial distance in figure (5.1.3). The scatter evident in the N_+ and T_e curves is much reduced. In the absence of the filter field, $N_+ T_e$ falls in a smooth exponential from backplate to BFE. With the filter field on, three sharply-defined exponentials emerge: a shallow fall from backplate to 13cm from the BFE, a steep fall to 8cm and another shallow fall to the BFE. Practically the entire order-of-magnitude reduction in $N_+ T_e$ is confined to the central portion. This is centred on the filter, and occurs over a distance corresponding exactly to the thickness of the filter at the 30 gauss contour. In the driver region, there

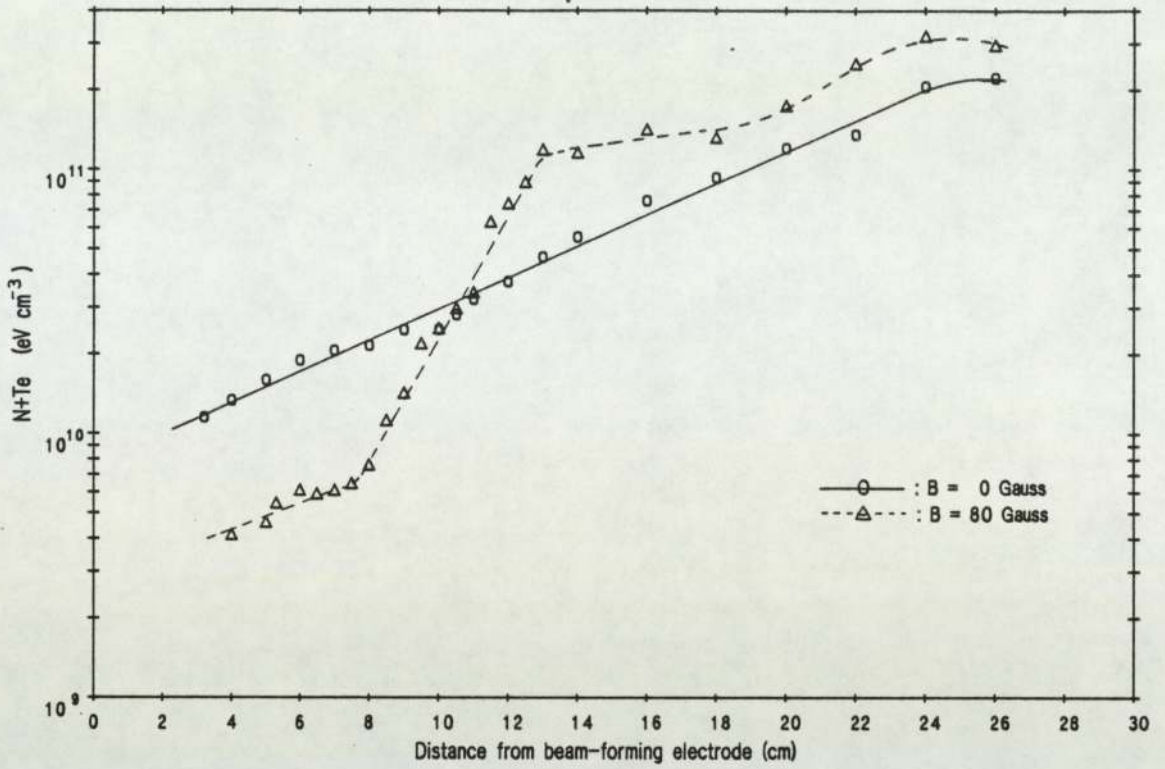


Figure 5.13 Axial variation of bulk energy density
Iarc = 5A Varc = 60v Pres. = 3mT

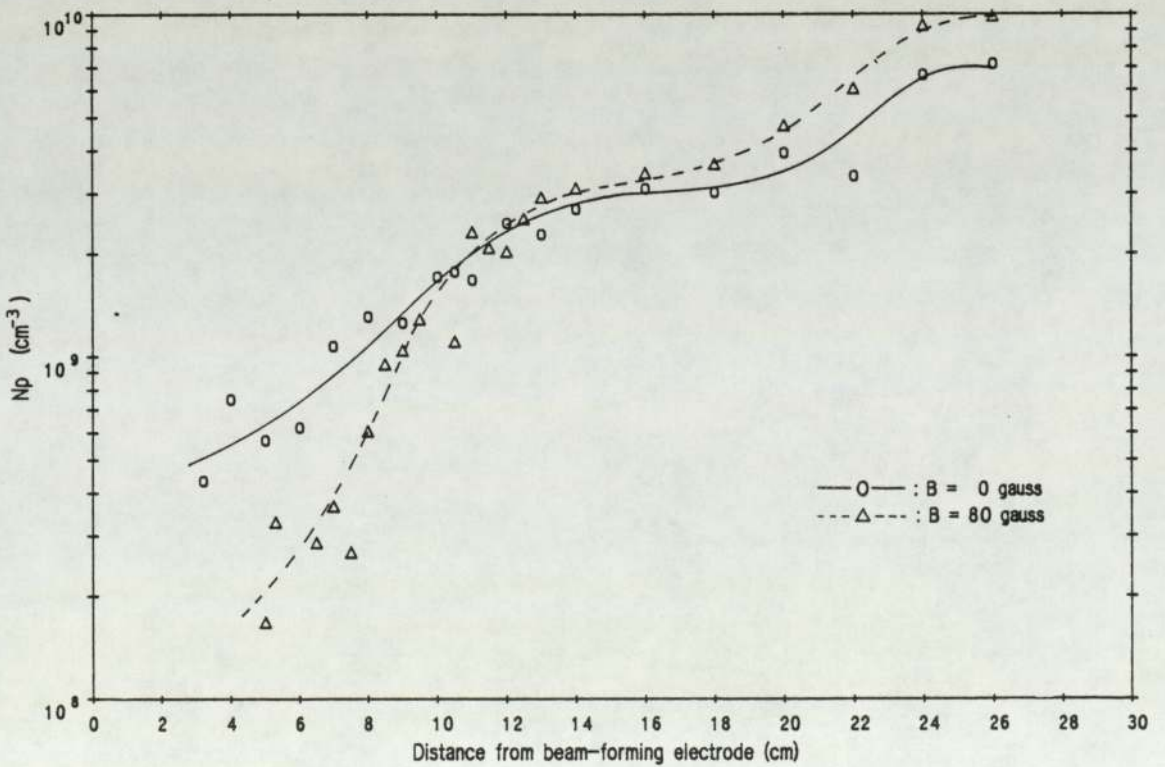


Figure 5.14 Axial variation of primary electron density
Iarc = 5A Varc = 60v Pres. = 3mT

is again a small peak at the filament position.

Langmuir probe traces captured in the variable filter source showed strong evidence of a "primary" electron population in the plasma. As will be seen, this is something of a misnomer in this source, as in many cases the "primary" electron energy is below the threshold level for the formation of a hydrogen ion in a single collision, and might more properly be termed a "superthermal" group. The variation of the primary electron density N_p with distance can be seen in figure (5.1.4). In the absence of the filter field, a peak in the region of the filament is seen. This suffers a rapid 50% fall in ~ 3 cm, giving way to a shallower exponential fall, which continues through the source. The T_p variation is shown in figure (5.1.5). As may be seen, the most prominent feature is the relatively high peak (~ 20 eV) in the filament region, followed by a sharp fall within 3cm to a plateau value of 5eV, which then remains constant through to the BFE. In the presence of the filter field, both N_p and T_p are altered. The N_p variation displays the filament-region peak, but the driver region plateau is higher. This plateau is maintained to ~ 13 cm from the BFE (the start of the 30 gauss filter position) where N_p drops exponentially, falling over an order of magnitude in 6cm to a small value in the extraction region. The effect on the T_p variation is similar, and more clearly seen. T_p reaches its minimum value at the filter peak, and is constant thereafter. In the extraction region, low signal levels led to noise in

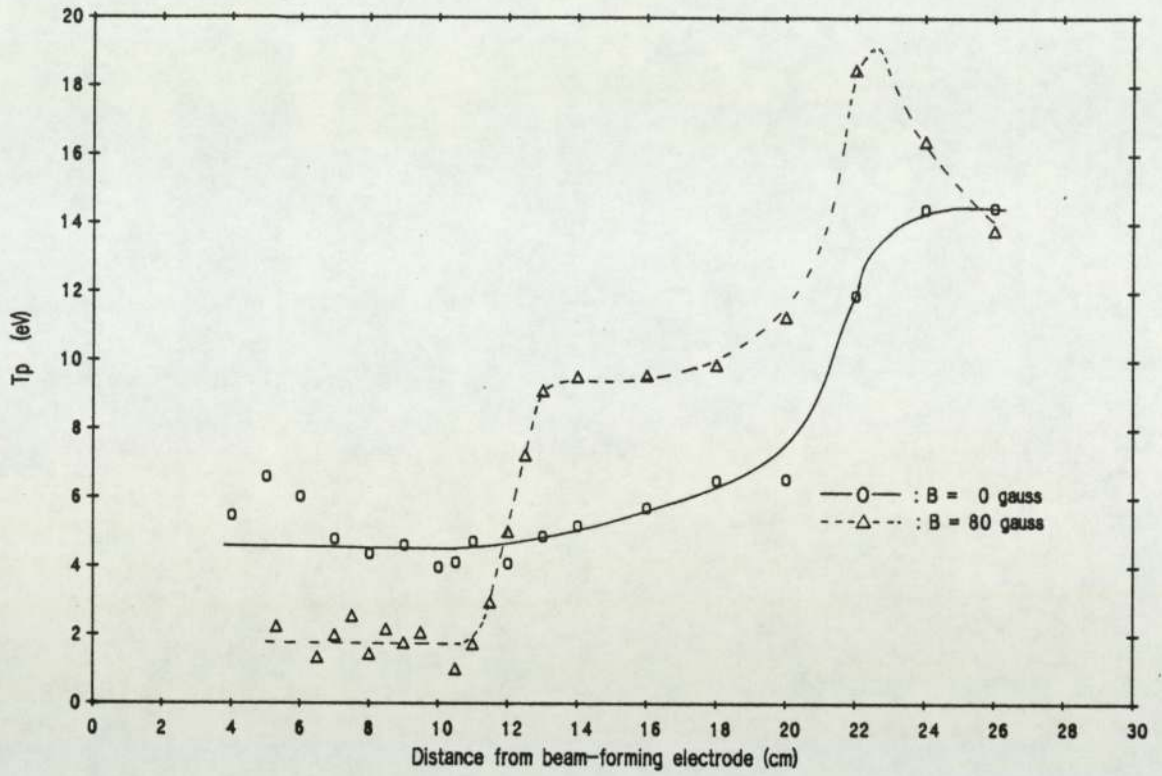


Figure 5.15 Axial variation of primary electron temperature
 $I_{arc} = 5A$ $V_{arc} = 60v$ $Pres. = 3mT$

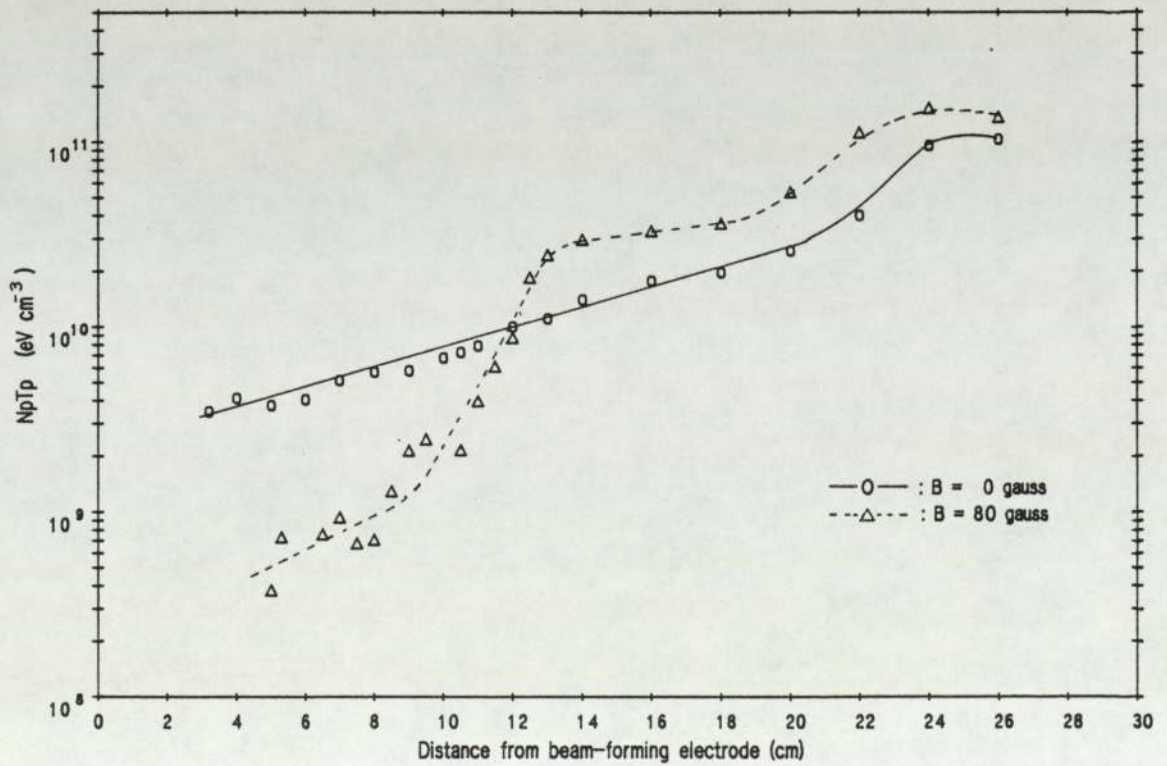


Figure 5.16 Axial variation of primary energy density
 $I_{arc} = 5A$ $V_{arc} = 60v$ $Pres. = 3mT$

the primary region of the probe characteristics, resulting in a larger amount of scatter.

Figure (5.1.6) shows the axial variation of the primary electron energy density $N_p T_p$ with and without the filter field. The scatter evident in figures (5.1.4) and (5.1.5) is much reduced. The variation is almost identical to that of $N_+ T_e$, save for a more prominent peak in the filament region, and a greater effect of the filter field on the driver and extraction region plateaus. Note the very low values of $N_p T_p$ in the extraction region. The very low primary temperature is a characteristic feature of the source with the filter fully active. In fact, it is questionable whether electrons with an energy so far below the ionization threshold may be referred to as "primaries" at all, and this must be remembered when examining "primary" electron temperature and density values measured in the extraction region.

The variation of V_p with and without the filter field is shown in figure (5.1.7). The result in both cases is remarkably similar, V_p showing a variation similar to that of T_e . The presence of the field causes the regions immediately adjacent to the filter to vary slightly so attenuation is more closely associated with the filter region, but the difference in V_p between driver and extraction regions is altered little. The V_p values of +1.2v and +2.7v in the driver and extraction regions are again typical.

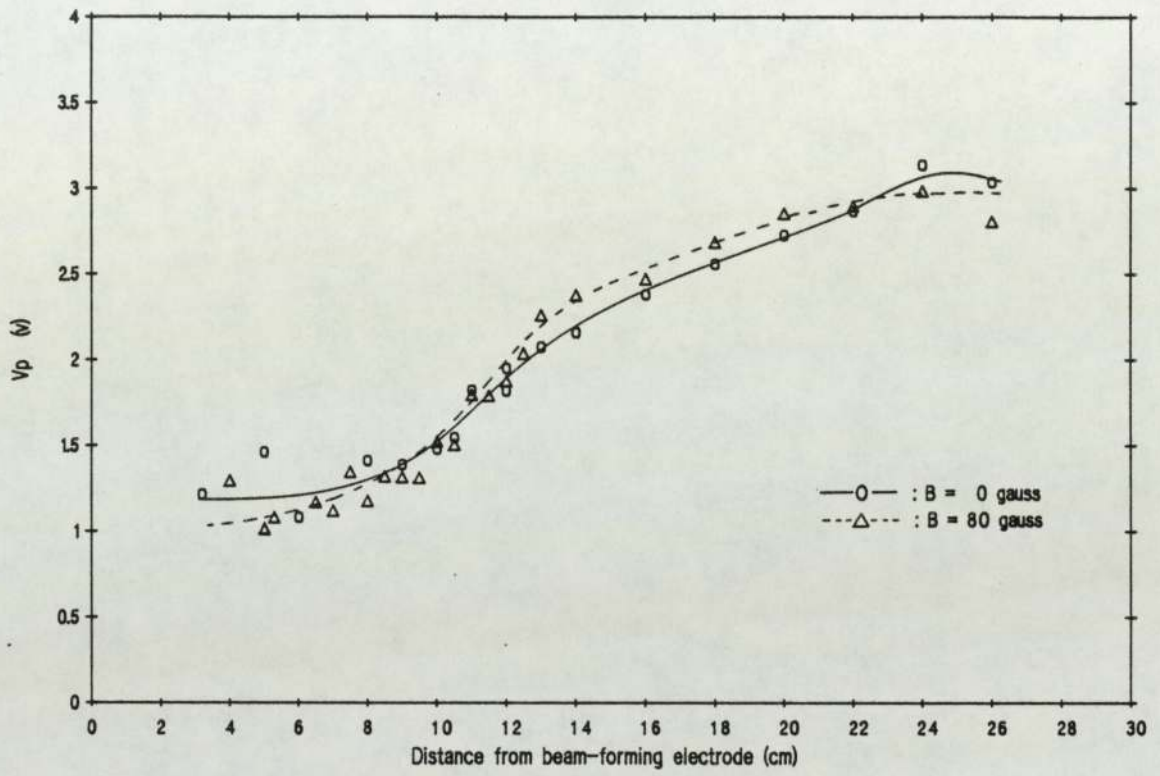


Figure 5.1.7 Axial variation of plasma potential
 $I_{arc} = 5A$ $V_{arc} = 60v$ $Pres. = 3mT$

5.1.1.2 Transverse variation

The mobile planar probe was mounted on the small horizontal extraction region port (see figure (3.2.1)). This allowed it to be traversed from the wall of the extraction region to approximately 3cm beyond the axis of the chamber, parallel to the filter field but perpendicular to the filter rods. A radial profile of the discharge at approximately 5cm from the beam-forming electrode could thus be obtained. This was done at a source pressure of 3mT and a discharge current of 5A for several values of filter field and arc voltage. The technique used in the axial scan experiment was again employed to prevent contamination.

The variation in N_+ across the extraction region between the source axis and the vessel wall is shown in figure (5.1.8). The very low signal levels obtained closer than 2cm proved impossible to analyse successfully. In the absence of the filter field, N_+ remains constant with transverse distance, up until ~ 5cm from the vessel wall. Moving further toward the wall produces an exponential fall of a factor of 2 in 3cm. The presence of the filter field causes the region of attenuation to shrink by 1cm, and consequently the gradient to the wall increases. The radial variation in T_e is shown in figure (5.1.9). With no filter field, T_e falls in a slow linear fashion with distance, up until 3.5cm from the wall, then halves in the 1.5 cm after this point. With the filter field present, T_e is roughly constant over the radius at 50% of the zero-field value. Note the peak

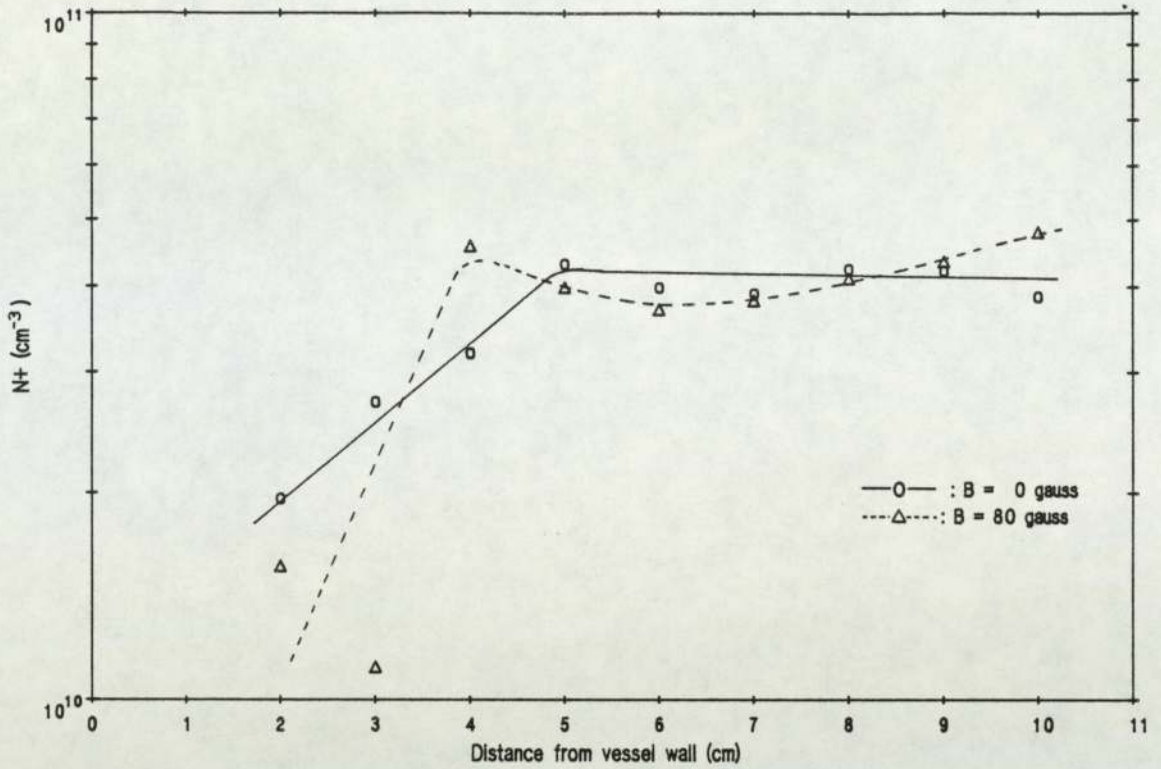


Figure 5.1.8 Radial variation of plasma density

Iarc = 5A Varc = 80v Pres. = 3mT

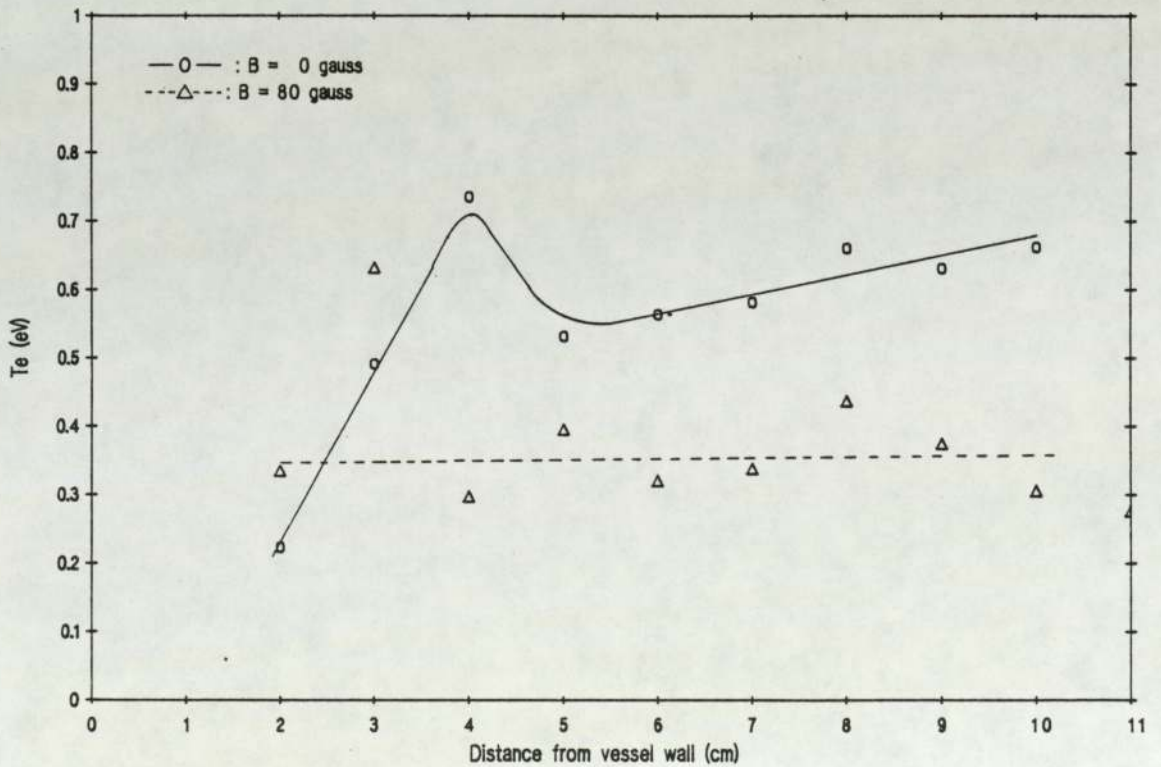


Figure 5.1.9 Radial variation of thermal electron temperature

Iarc = 5A Varc = 80v Pres. = 3mT

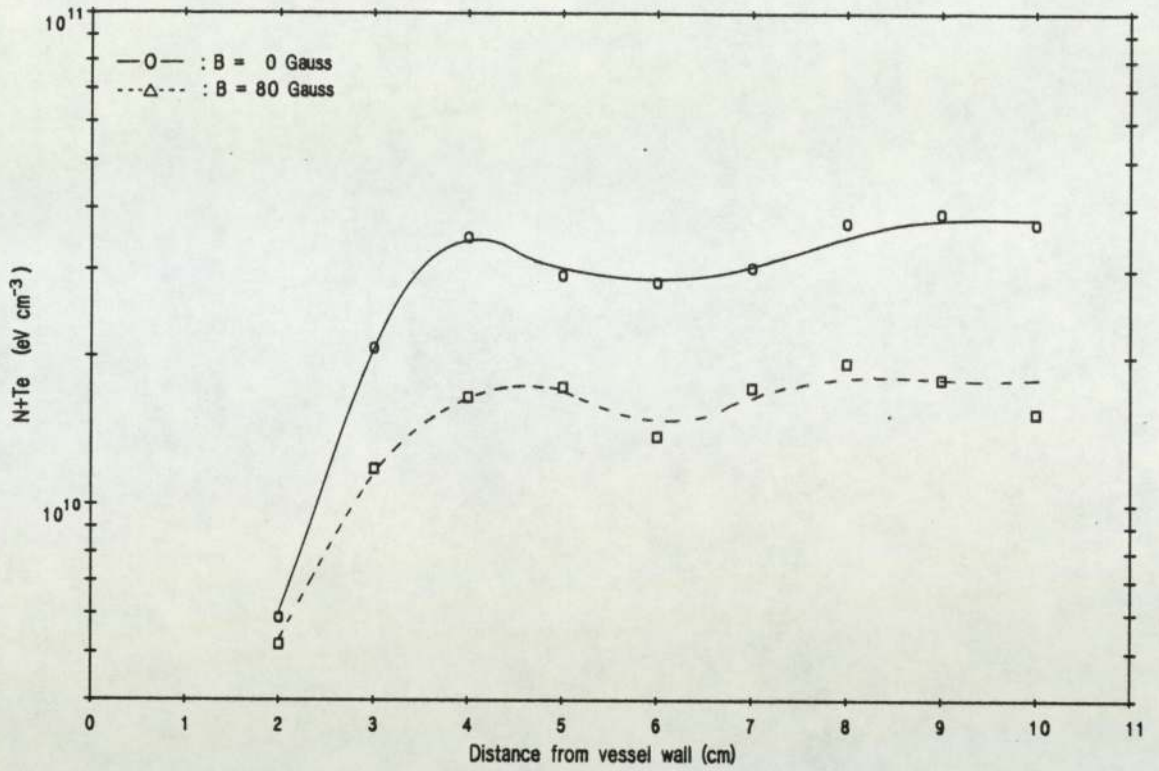


Figure 5.1.10 Radial variation of bulk energy density
 I_{arc} = 5A V_{arc} = 80v Pres. = 3mT

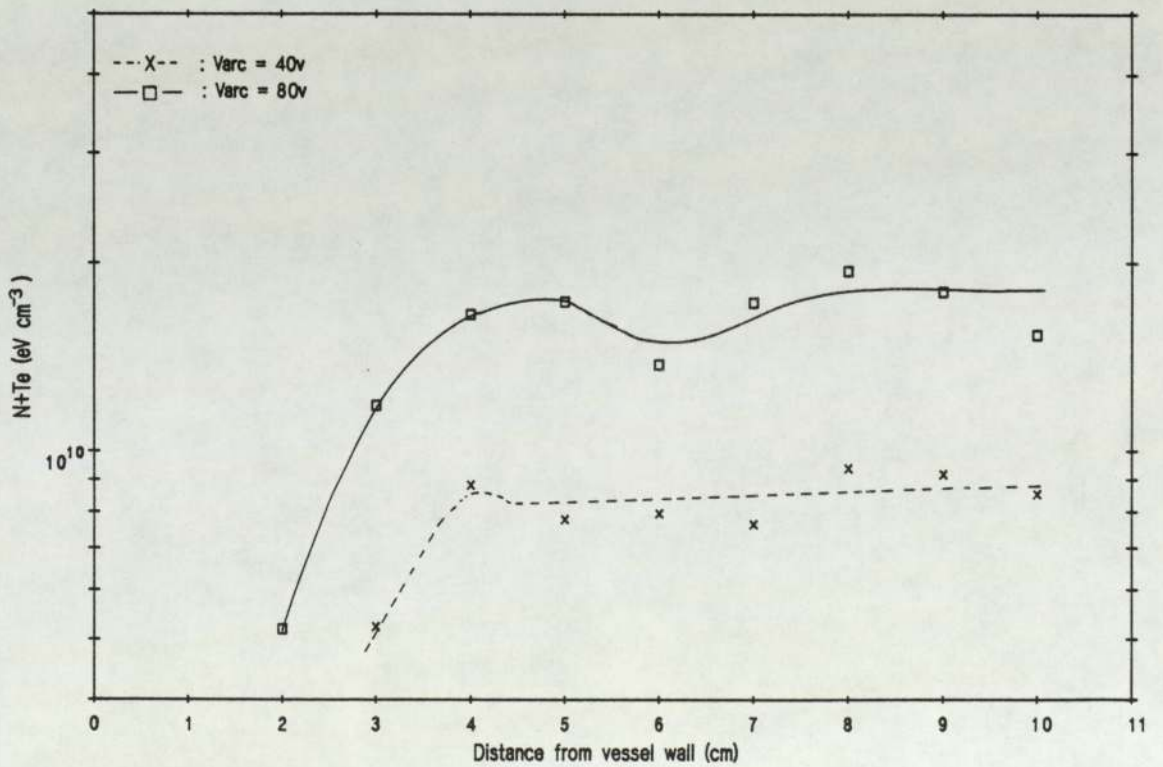


Figure 5.1.11 Radial variation of N+Te for two arc voltages
 I_{arc} = 5A Pres. = 3mT B = 80 Gauss

just before the attenuation commences; this may be due to electrons being reflected into the probe face by the wall fields, introducing an extra non-random velocity and thus increasing T_e . Figure (5.1.10) shows the bulk energy density $N_e T_e$ as a function of radial distance. The variation in this case is much clearer: $N_e T_e$ is constant up to a point 3.5cm from the wall, where a sharp fall occurs. The only effect of the filter field is to reduce the level of the constant region. Figure (5.1.11) shows the same variation for two different voltages. Very little difference, except in the absolute magnitude of the plateau, is evident. In particular, the point at which the wall-field attenuation begins is invariant with voltage.

The radial variation of N_p across the extraction region is shown in figure (5.1.12). N_p appears constant up to a point ~ 3.5 cm from the wall, where an order of magnitude fall occurs. The filter field reduces the constant level to 30% of the zero-field value, the signal level being too low to detect primaries beyond 3cm from the wall. The radial variation of T_p is shown in figure (5.1.13). The zero gauss curve shows T_p to be constant at ~ 5 eV up to 5cm from the wall. The peak attributed to electron reflection occurs, T_p then falling rapidly to 1eV in the remaining 1.5cm. The 80 gauss curve shows T_p to be constant over the entire measurable radius at 2eV. Figure (5.1.14) shows $N_p T_p$ as a function of radial distance. The N_p behavior is repeated, with an order of magnitude difference between the zero and 80

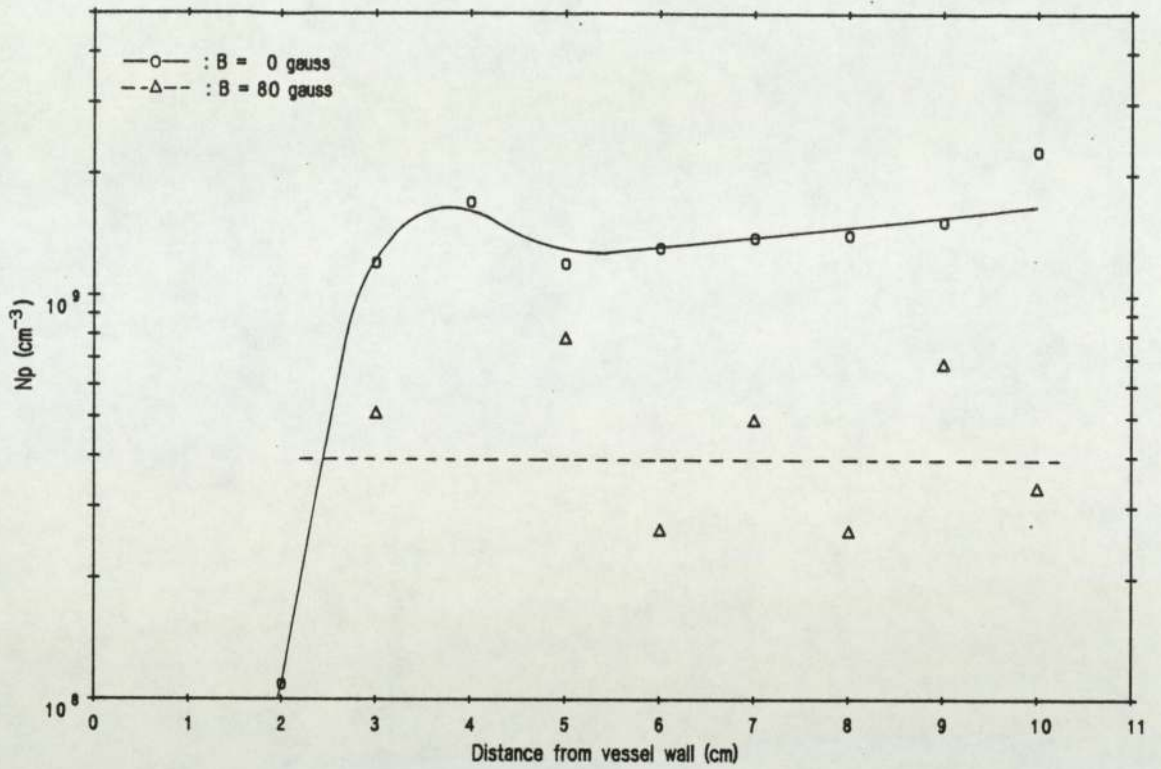


Figure 5.112 Radial variation of primary electron density
 Iarc = 5A Pres. = 3mT Varc = 80v

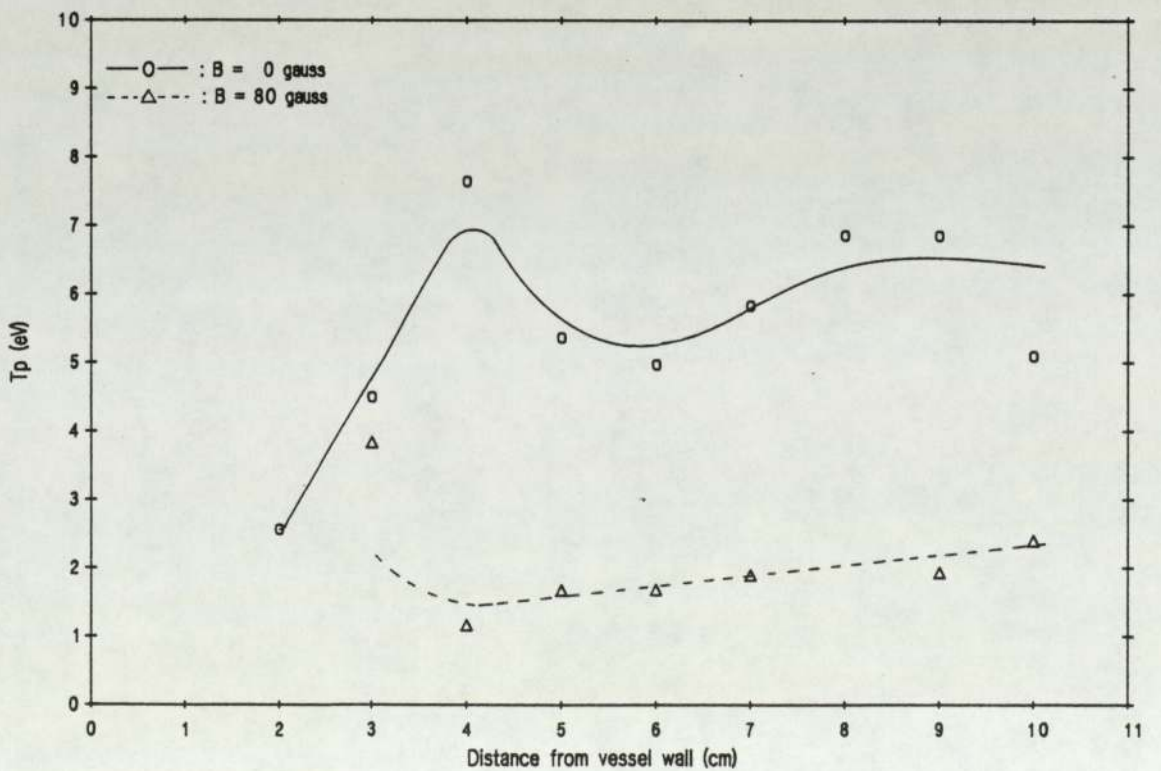


Figure 5.113 Radial variation of primary electron temperature
 Iarc = 5A Varc = 80v Pres. = 3mT

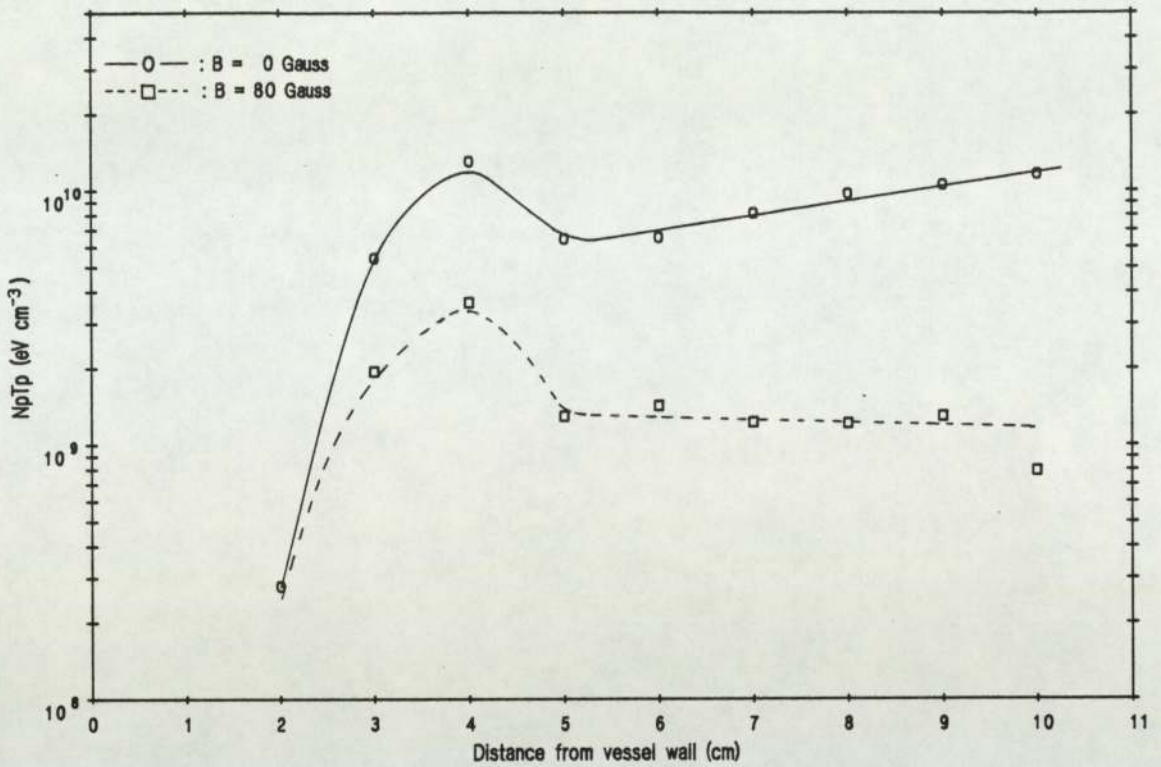


Figure 5.1.14 Radial variation of primary energy density
 $I_{arc} = 5A$ $V_{arc} = 80v$ Pres. = 3mT

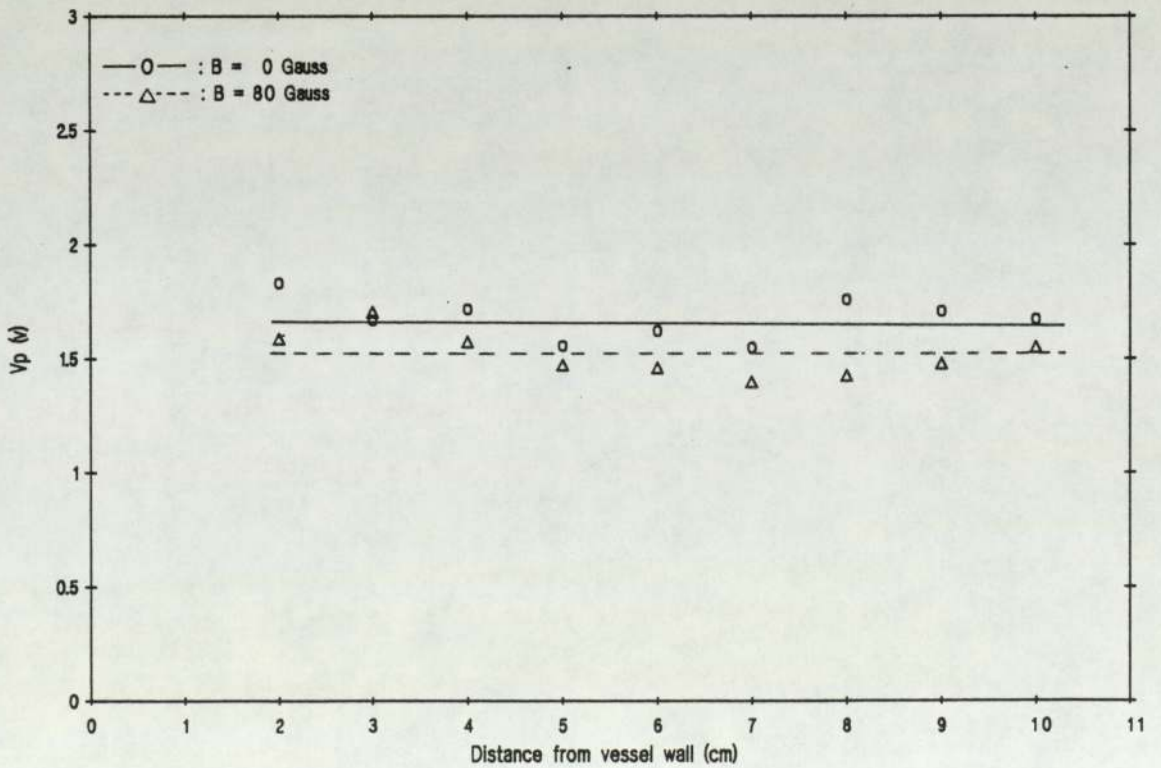


Figure 5.1.15 Radial variation of plasma potential
 $I_{arc} = 5A$ $V_{arc} = 80v$ Pres. = 3mT

gauss cases. The Radial variation of V_p in the extraction region is shown in figure (5.1.15). In both the zero and the 80 gauss cases, V_p remains constant at $\sim 1.6v$ across the entire measurable range.

5.1.1.3 Summary - spatial variation of plasma parameters

The principal observations from this series of experiments are as follows:

Axial variation

1. The basic plasma in the source is most dense, both in terms of energy and of number of particles, in the region directly adjacent to the filament. In the absence of the filter field, the energy density falls off exponentially as the BFE is approached. A peak in the filament region indicates the main region of plasma production.
2. The principal effect of the filter field appears to be that of restricting the attenuation to a 5cm wide band centered on the filter, corresponding to the 30 - gauss contour. This generates three exponential axial decays, shallow in the driver and extraction region and rapid in the filter region. The absolute values either side of the filter are altered by its presence, although not greatly. One exception to this the primary electron behavior, the energy density in the extraction region being cut to < 1% of it's peak value. At the other extreme, the plasma potential difference is hardly altered at all.

3. Significant differences exist between positive and negative number densities outside the driver region. These are examined in detail in chapter 5.2.1.

Transverse variation

1. The plasma is uniform across the majority of the diameter of the extraction region, up to within ~ 3 cm of the walls of the vessel. Beyond this, the plasma is attenuated strongly. Measurements closer than 2cm from the wall provided signal levels too low to analyse.
2. The volume of plasma as determined by the number density appears to increase radially by a small amount if the filter is active. It does not vary with arc voltage.
3. The primary electron population of the extraction region in the presence of the filter is very low in comparison with the plasma density, across the entire radius.
4. The plasma potential is invariant across the radius.

5.1.2 Arc - parametric variation

The plasma within this type of multipole source is affected most strongly by the conditions under which the arc discharge is operated; principally the arc current and voltage, the source filling pressure, and to a lesser extent the filter field intensity. In order to attempt to relate the H^- ion density to these parameters via some type of scaling laws, it was important to understand their effect on the basic plasma parameters. Accordingly, several series of experiments were performed to study the effects of varying the arc conditions on the plasma at four locations within a source:

1. The driver region

Measurements in the variable filter source were obtained using the mobile planar probe mounted vertically on the central backplate port used for the axial spatial scan. The probe face was positioned on and perpendicular to the vertical axis of the source, 24cm from the beam-forming electrode, in the plane of the filament. The transverse field in this position due to the backplate magnets was measured at < 10 gauss. Some measurements were obtained from the fixed-filter source, using a type 1 fixed probe mounted in the same position.

2. The extraction region

Measurements in the variable filter source were obtained

using the mobile planar mounted horizontally on the extraction region port used in the transverse spatial scan. The probe face was positioned on and parallel to the vertical axis of the source, 5.5cm from the beam-forming electrode.

3. The beam-forming electrode

Measurements in the variable filter source were obtained using a type 2. fixed probe mounted on the beam forming electrode, with it's face parallel to the BFE.

4. The filter region

Measurements in the variable filter source were obtained using the mobile planar probe mounted vertically on the central backplate port used for the axial spatial scan. The probe face was positioned on and perpendicular to the vertical axis of the source, 10.5cm from the beam-forming electrode. This placed it at the peak of the filter field, with it's face parallel to the fieldlines.

5.1.2.1 Arc current (I_{arc}) variation

The current flowing in the filament to source-body arc was varied by altering the DC filament-heating current, thereby affecting the rate of thermionic electron emission from the filament, all other parameters being held constant. The exact dependence of I_{arc} on the heater current varied with both source conditions (pressure, arc voltage) and plasma parameters (ionic mass, density and temperature, which determine the plasma resistivity). Since an increase in density (e.g. due to an increase in I_{arc}) causes a decrease in plasma resistivity, this variable dependence allowed the possibility of positive feedback, which could cause I_{arc} to drift considerably for a given heater current. If allowed to continue, this drift could very rapidly become a "thermal runaway", which on two occasions provided an arc powerful enough to burn through the 1cm-thick stainless steel walls of the fixed-filter source in a short time, despite the water-cooling channels. Careful monitoring of the arc current during source operation was therefore necessary.

Figure (5.1.16) shows the variation of the plasma density with arc current in the driver and extraction regions of the variable filter source. The relation is less than linear in both regions, the index being between 0.6 and 0.7. Figure (5.1.17) shows a similar variation in the driver region thermal electron temperature with I_{arc} under the same conditions. In the extraction region, T_e increases very slowly indeed with I_{arc} . Figure (5.1.18) shows the the bulk

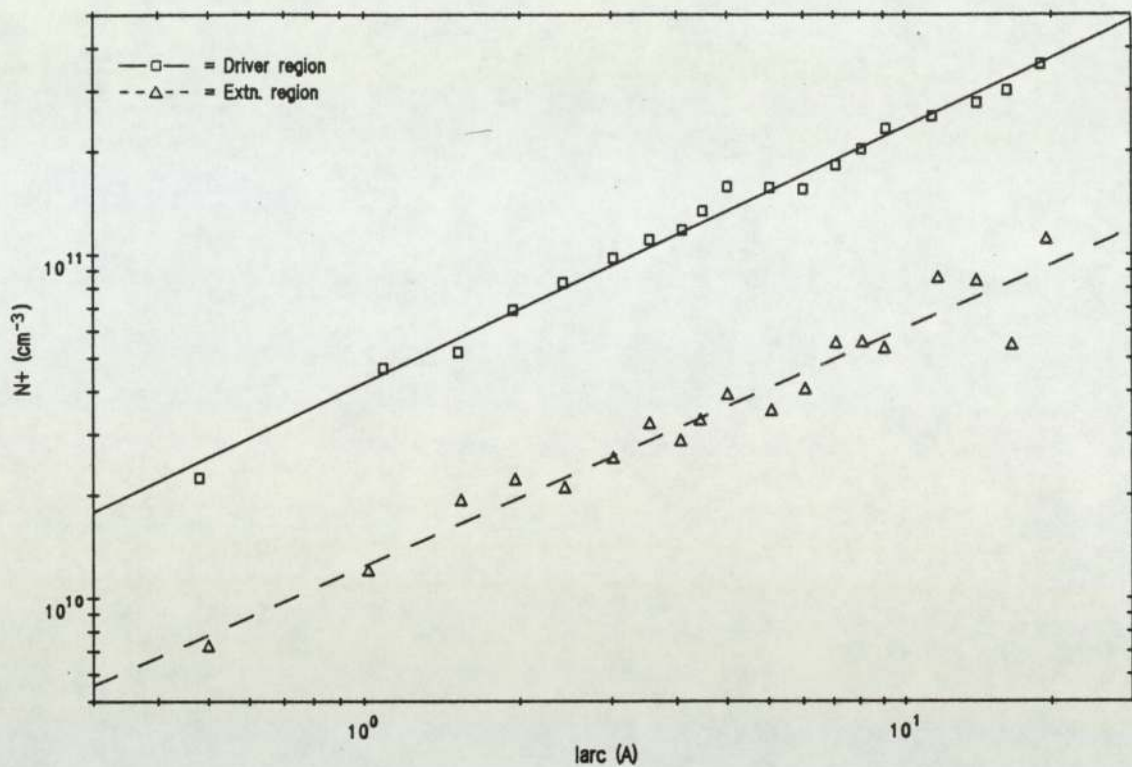


Figure 5.1.16 Variation of plasma density with arc current
 $V_{\text{arc}} = 60\text{v}$ Pres. = 3mT B = 80 Gauss

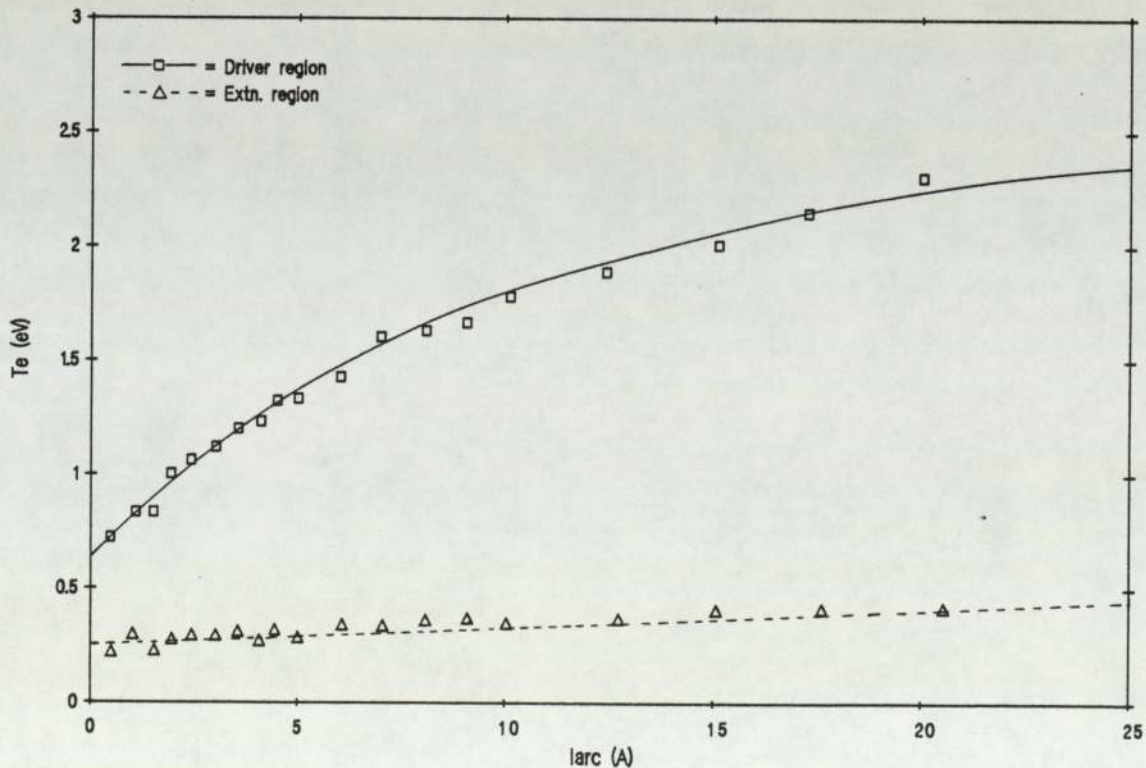


Figure 5.1.17 Variation of thermal electron temperature with arc current
 $V_{\text{arc}} = 60\text{v}$ Pres. = 3mT B = 80 gauss

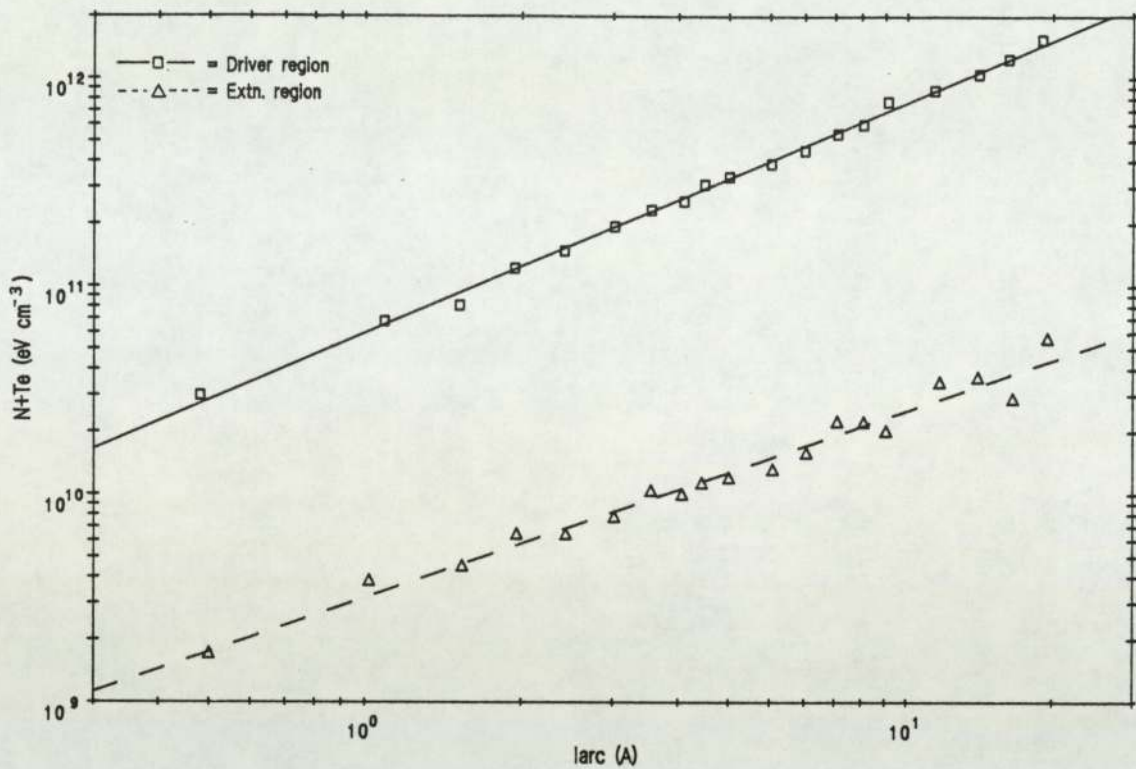


Figure 5.1.18 Variation of bulk energy density with arc current
 $V_{arc} = 60\text{v}$ Pres. = 3mT B = 80 gauss

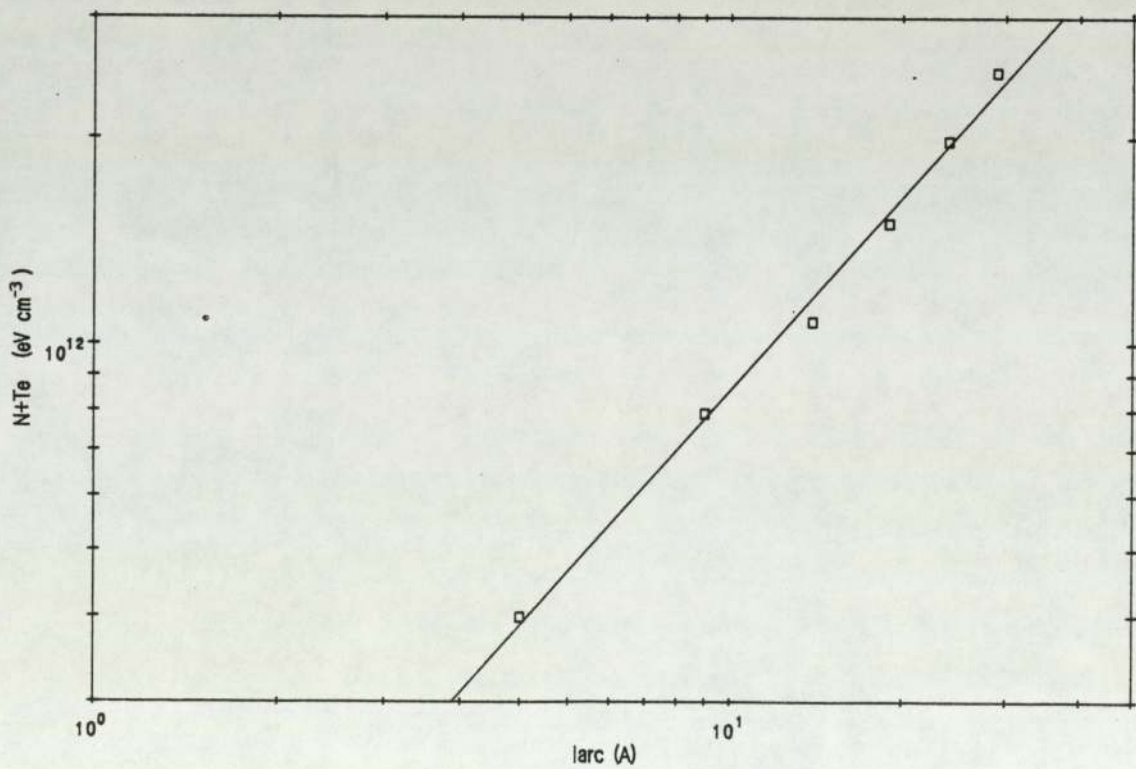


Figure 5.1.19 Var. of $N+Te$ with I_{arc} in the fixed-filter source
 $V_{arc} = 60\text{v}$ Pres. = 3mT Driver region

energy density $N_+ T_e$ as a function of Iarc for these conditions. The relationship is directly linear (index = 1.07) to a high degree of correlation in the driver region, and only slightly less so (index = 0.9) in the extraction region. This is in accordance with the theory outlined in chapter 2.1, and the results of other studies [44]. Ignoring numerical constants of order 1, it may therefore be stated that the bulk energy density (eV cm^{-3}) of the plasma is proportional to the rate of input of ionizing electrons. Figure (5.1.19) shows that the relationship also holds in the fixed-filter source.

In the variable filter source, evidence of a primary electron population was generally clear in the driver region, but much less obvious elsewhere in the source, leading to the increased scatter in the extraction region and BFE results. Primaries were not detected in the fixed-filter source by the earlier version of the probe analysis system used here. Figure (5.1.20) shows the variation in primary electron density with arc current in the variable-filter source. A highly-linear relationship is evident in the driver region, as predicted by Green et al [26]. In the extraction region the relationship holds, but noisier data due to lower signal levels reduces the correlation. Figure (5.1.21) shows the variation in primary electron temperature with Iarc under the same conditions. T_p appears to be virtually independent of the arc current, showing a very slow increase ($< 0.1\text{eV/Amp}$) in the driver region and a small fall followed by invariance

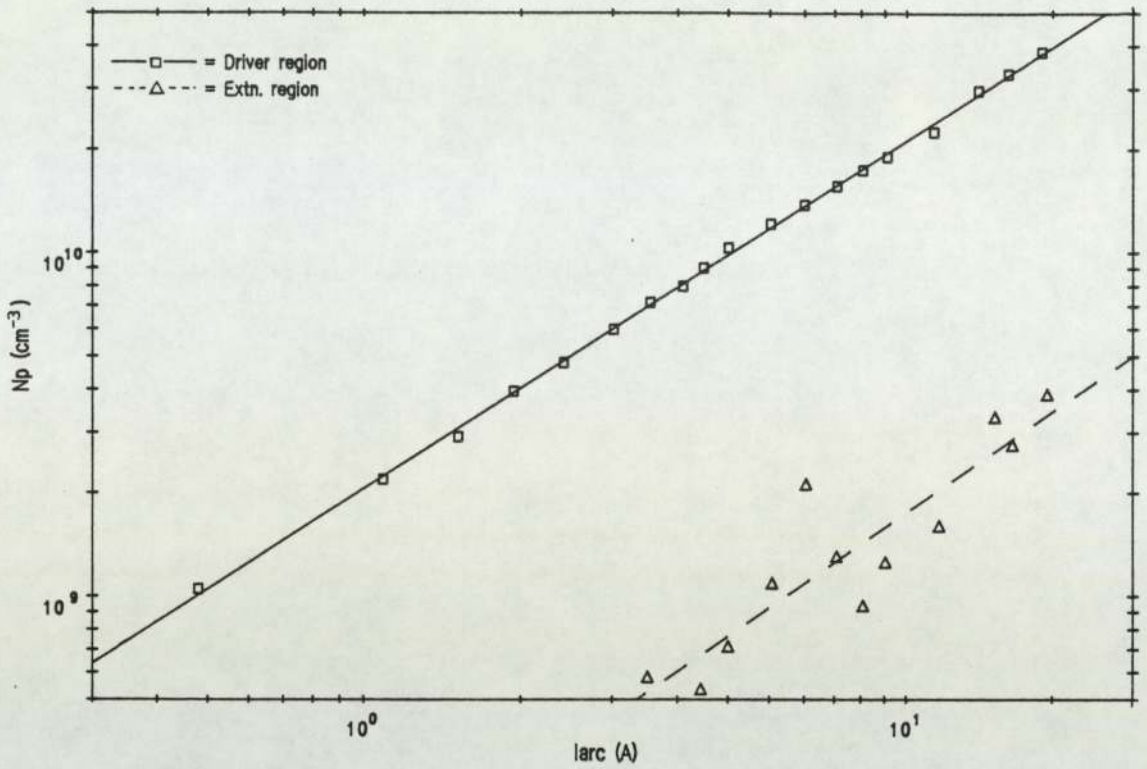


Figure 5.120 Variation of primary electron density with Iarc
 Varc = 60v Pres. = 3mT B = 80 gauss

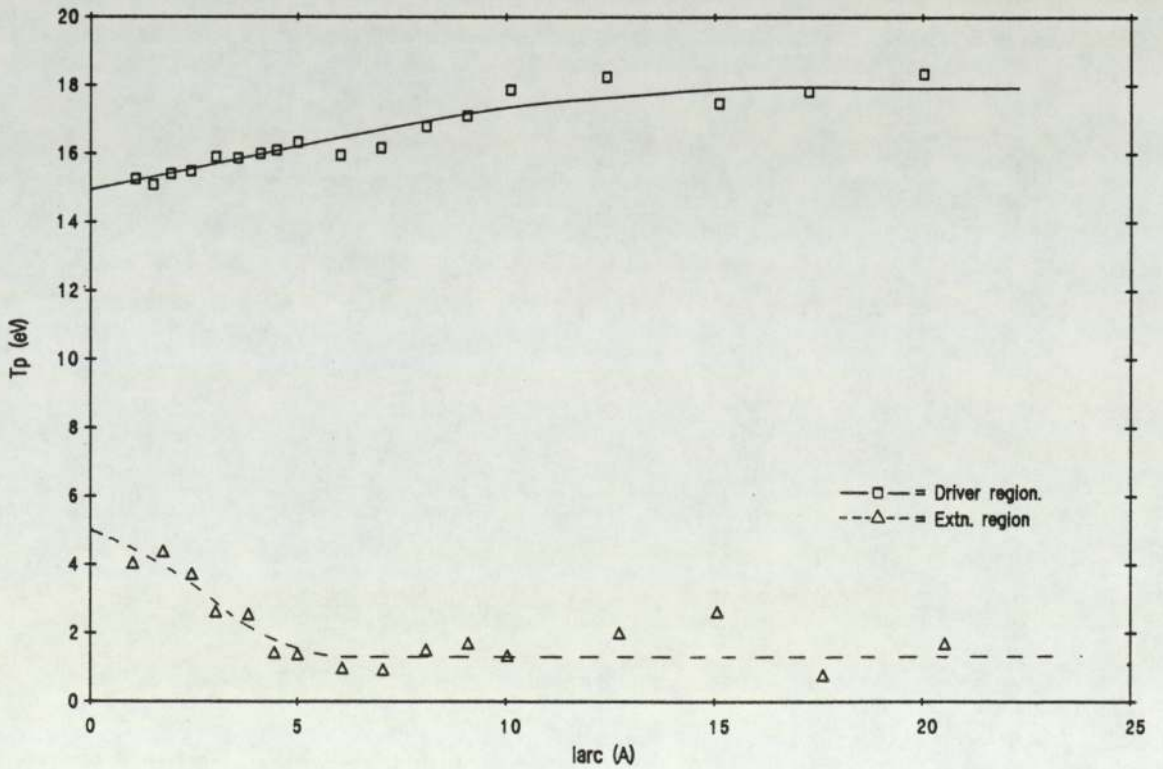


Figure 5.121 Variation of primary electron temperature with arc current
 Varc = 60v Pres. = 3mT B = 80 Gauss

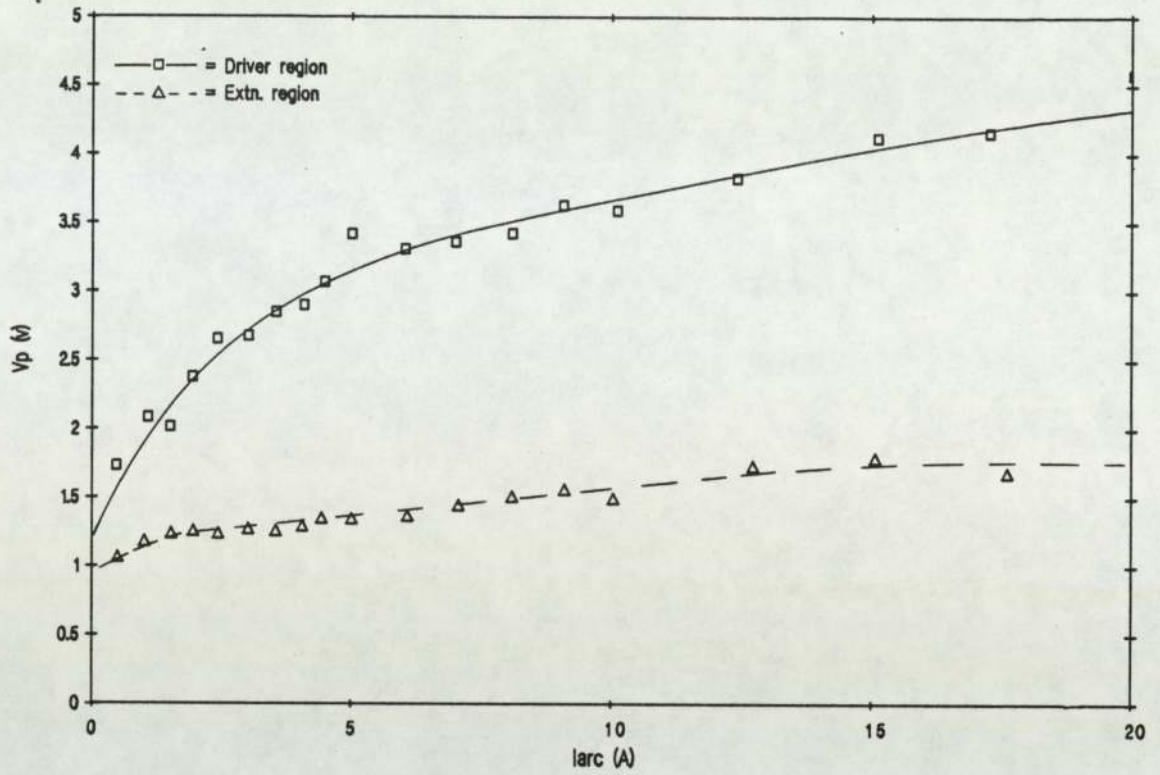


Figure 5.1.22 Variation of plasma potential with arc current

Varc = 60v Pres = 3mT B = 80 Gauss

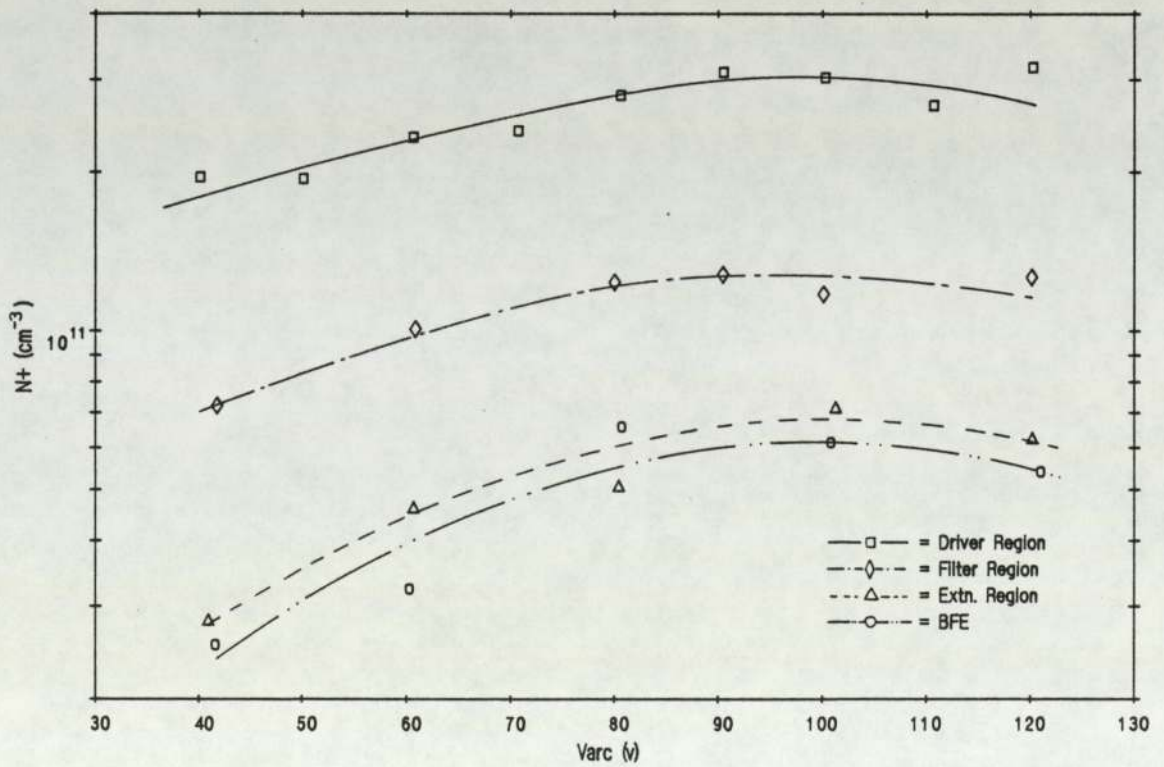


Figure 5.1.23 Variation of plasma density with arc voltage

Iarc = 5A Pres. = 3mT B = 80 gauss

in the extraction region. The variation in plasma potential (V_p) with I_{arc} in the variable filter source is shown in figure (5.1.22). A slow rise with arc current at less than linear dependence is evident, similar to that of T_e but weaker. The buildup of a small potential across the filter with increasing I_{arc} may be seen, the driver region becoming more positive as I_{arc} increases whilst the extraction region value remains constant.

5.1.2.2 Arc voltage (V_{arc}) variation

The potential between the heated filament cathode and the source body anode could be varied very simply, using the D.C. arc current supply in a voltage-controlled mode. This altered the initial injection energy of the ionizing electrons, and therefore the probability of ionization occurring. Ultimately this determined the arc current, and careful monitoring of this during alteration of the voltage was therefore necessary. Being directly controlled, V_{arc} did not drift like I_{arc} .

Figure (5.1.23) shows the variation in N_+ with V_{arc} at various positions within the variable-filter source. A shallow saturation curve is evident in all regions. N_+ varies slowest with V_{arc} in the driver region. The peak value of N_+ occurs at around 95v. This voltage remains invariant as the other arc parameters are varied. Figure (5.1.24) shows the variation in T_e with V_{arc} under the same conditions; T_e appears invariant with V_{arc} in all the

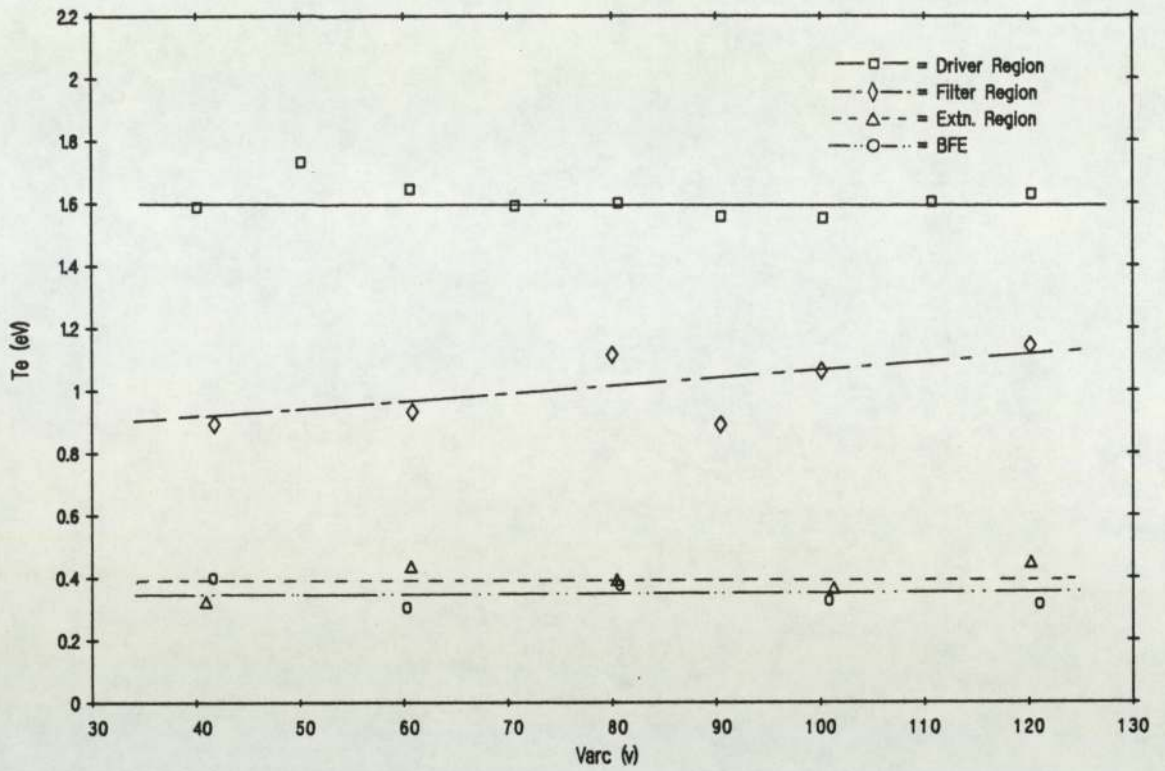


Figure 5.1.24 Variation of thermal electron temperature with arc voltage
 $I_{arc} = 5A$ Pres. = 3mT B = 80 Gauss

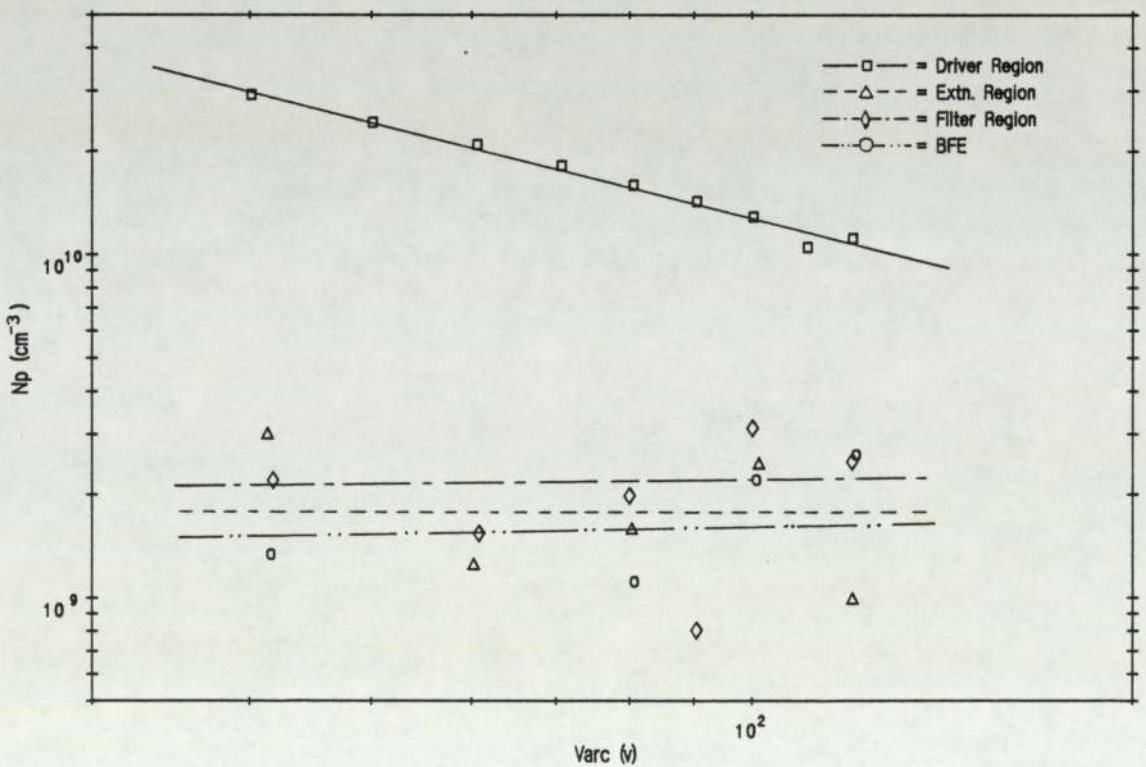


Figure 5.1.25 Variation of primary electron density with Varc
 $I_{arc} = 5A$ Pres. = 3mT B = 80 Gauss

regions, save for a very slow increase in the filter region which may be a probe/field artifact.

Figure (5.1.25) shows the variation in N_p with Varc in the variable-filter source. Outside of the driver region, N_p is more or less invariant with Varc, although the large amount of scatter makes this difficult to establish. In the driver region, N_p appears to have a negative or inverse dependence on Varc. Figure (5.1.26) shows N_p values obtained at different pressures in the driver region plotted against $(1/\text{Varc})$. A good fit to a line is obtained in most cases, the gradient increasing with pressure. Note that at the highest pressure, the relationship begins to break down. Figure (5.1.27) shows the variation in T_p with Varc at various positions in the source. A strong linear relationship is evident in the driver, T_p being about 25% of Varc. In the extraction region and at the BFE, the relationship is very much weaker, and T_p appears approximately independent of Varc. Note that outside the driver region, the absolute value of T_p never rises above 7eV. The primary energy density $N_p T_p$ is plotted in figure (5.1.28). This appears to be constant with Varc in all regions. Values outside the driver region are up to two orders of magnitude less than those in the driver.

The variation in V_p with Varc under the same conditions is shown in figure (5.1.29). A very weak increase is just discernible in all regions, the gradient of which falls with distance from the driver region. Note that increasing Varc

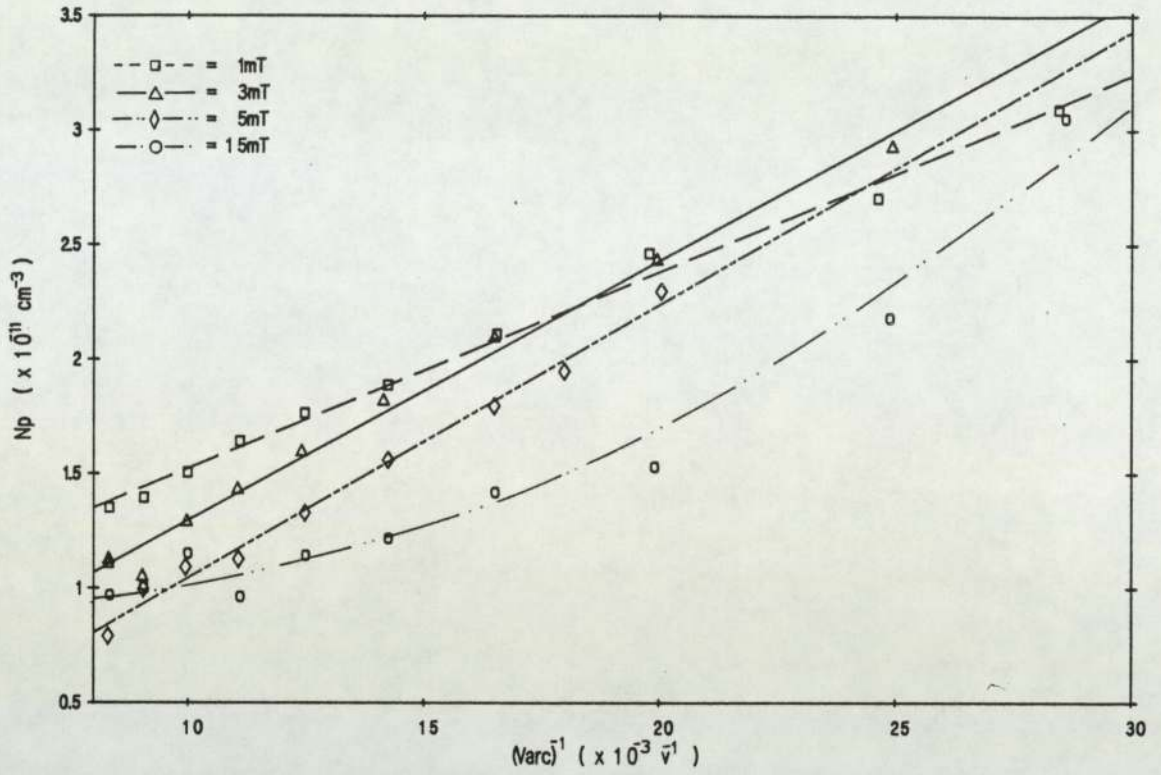


Figure 5.126 Inverse variation of N_p with Varc at four pressures
 $\text{larc} = 5\text{A}$ $B = 80 \text{ Gauss}$ Driver region

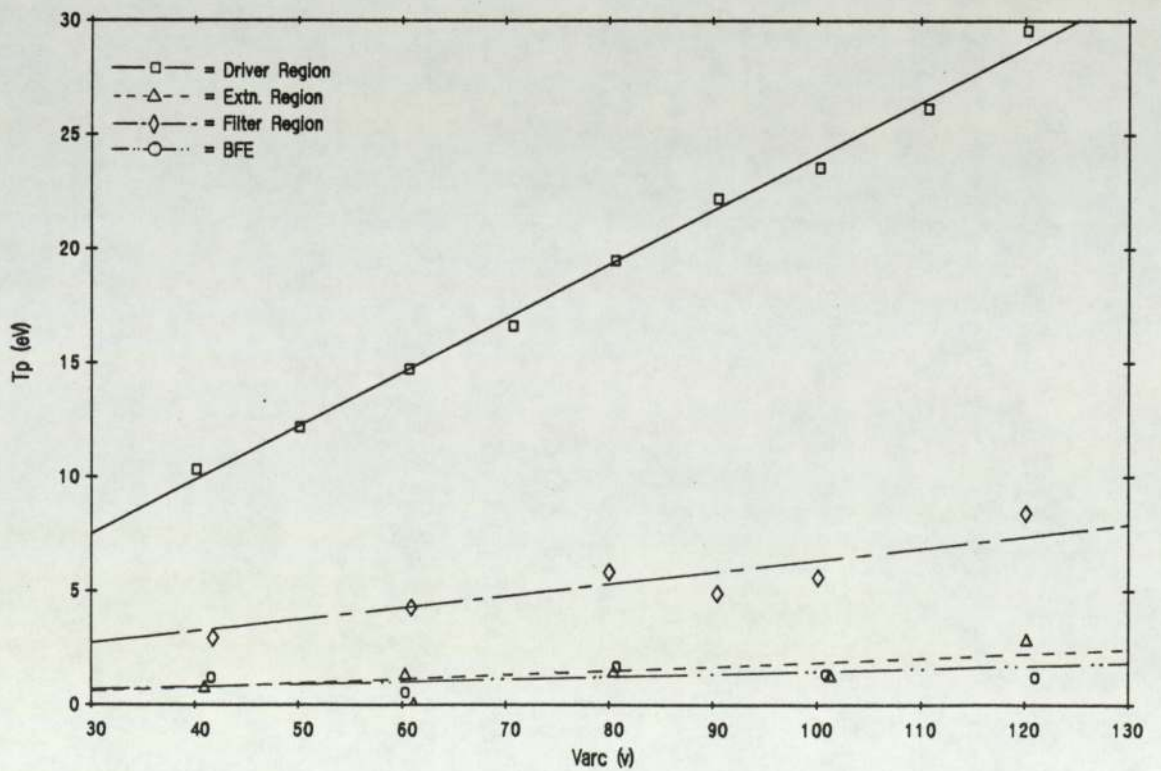


Figure 5.127 Variation of primary electron temperature with arc voltage
 $\text{larc} = 5\text{A}$ $\text{Pres.} = 3\text{mT}$ $B = 80 \text{ Gauss}$

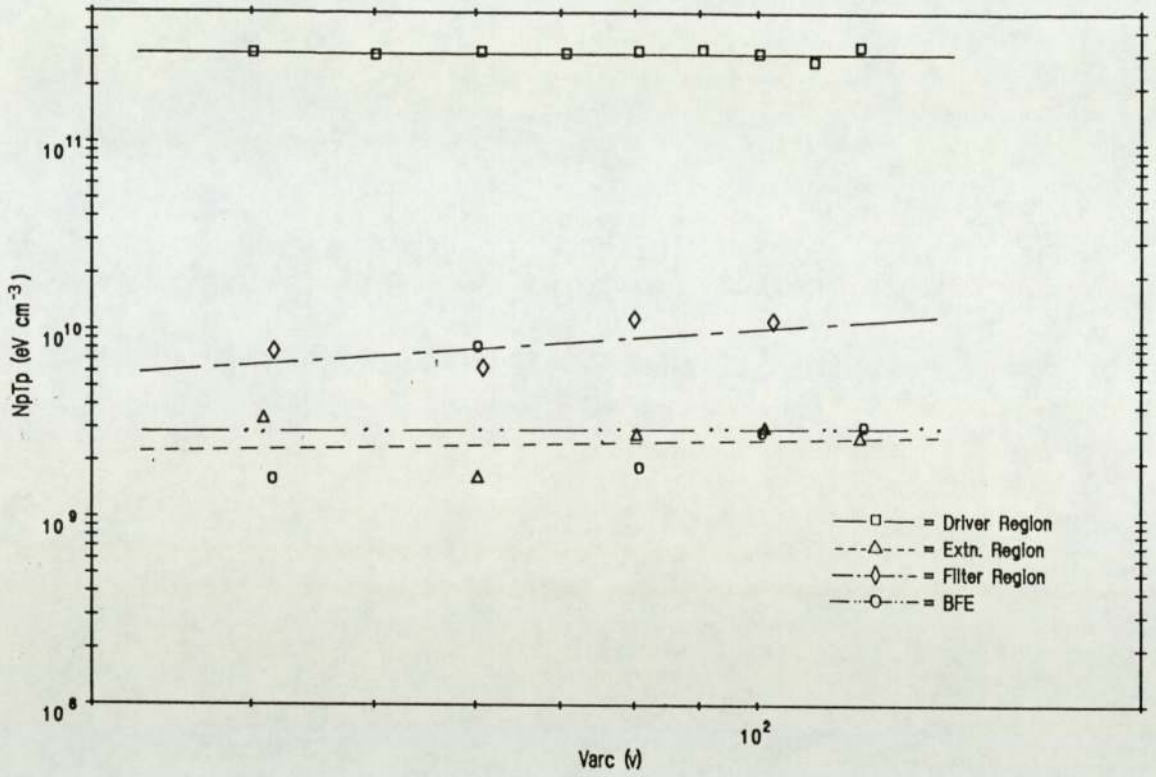


Figure 5.1.28 Variation of primary energy density with arc voltage
 $I_{arc} = 5A$ Pres. = 3mT B = 80 Gauss

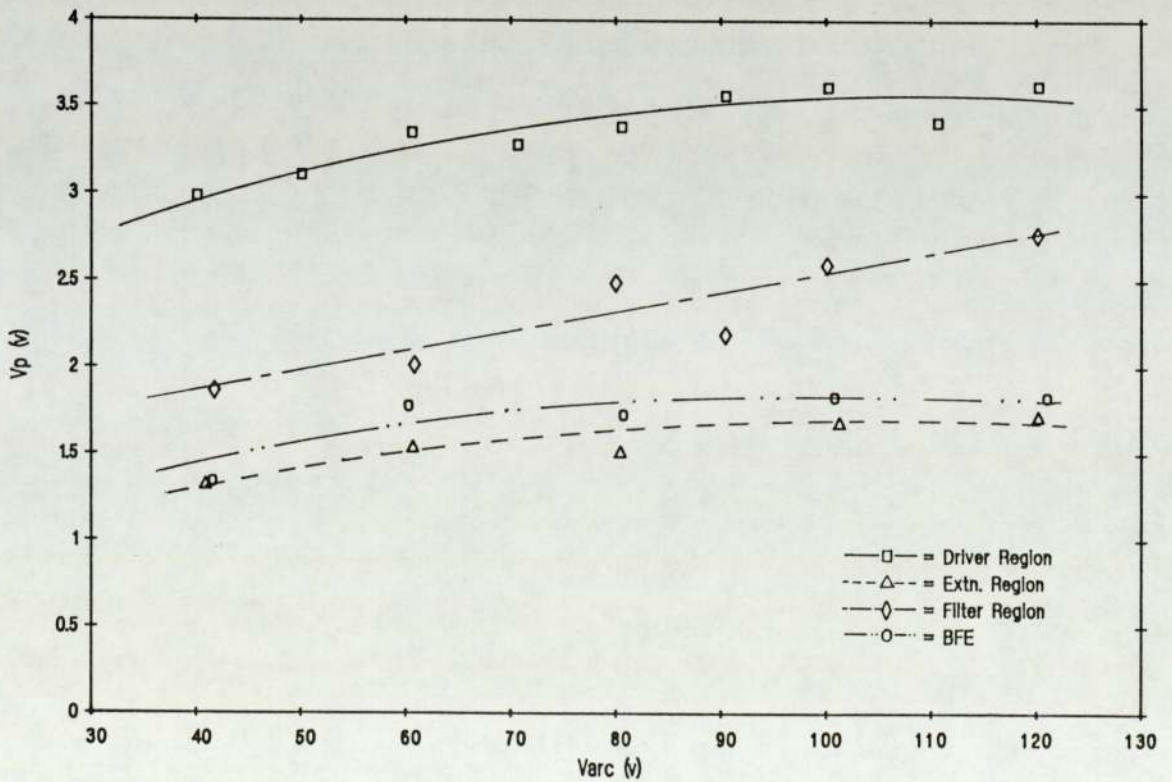


Figure 5.1.29 Variation of plasma potential with arc voltage
 $I_{arc} = 5A$ Pres. = 3mT B = 80 gauss

does not produce any perceptible increase in the potential across the filter.

5.1.2.3 Source pressure variation

The cold filling pressure of the gas in which the arc discharge was struck could be altered simply by adjusting the rate of gas flow into the source, using the metal-seal leak-valve. The pressure was very sensitive to the setting of this valve, and required some time to settle to a steady value after an adjustment. Thermal expansion of the valve components usually led to some drifting of the pressure over a period of about 20 min. Since the rate of ionization in the source depends in part on the density of gas molecules, this once again led to drifting of the arc current. To avoid having to adjust the pressure frequently, the pressure-scan data presented below was obtained by collating results from experiments in which an easy-to-adjust parameter (e.g. Varc) was varied. It should be noted that the pressure was not directly monitored. Pressure was calculated with a calibration curve from measurements of the gas flow rate into the source made using the MKS flowmeter. This curve was measured at irregular intervals, using a rarely-available high-accuracy baratron (capacitance manometer).

Figure (5.1.30) shows the variation in N_+ with pressure at three locations within the variable-filter source. A saturation curve is evident in all regions. However, saturation is not actually achieved in the driver region

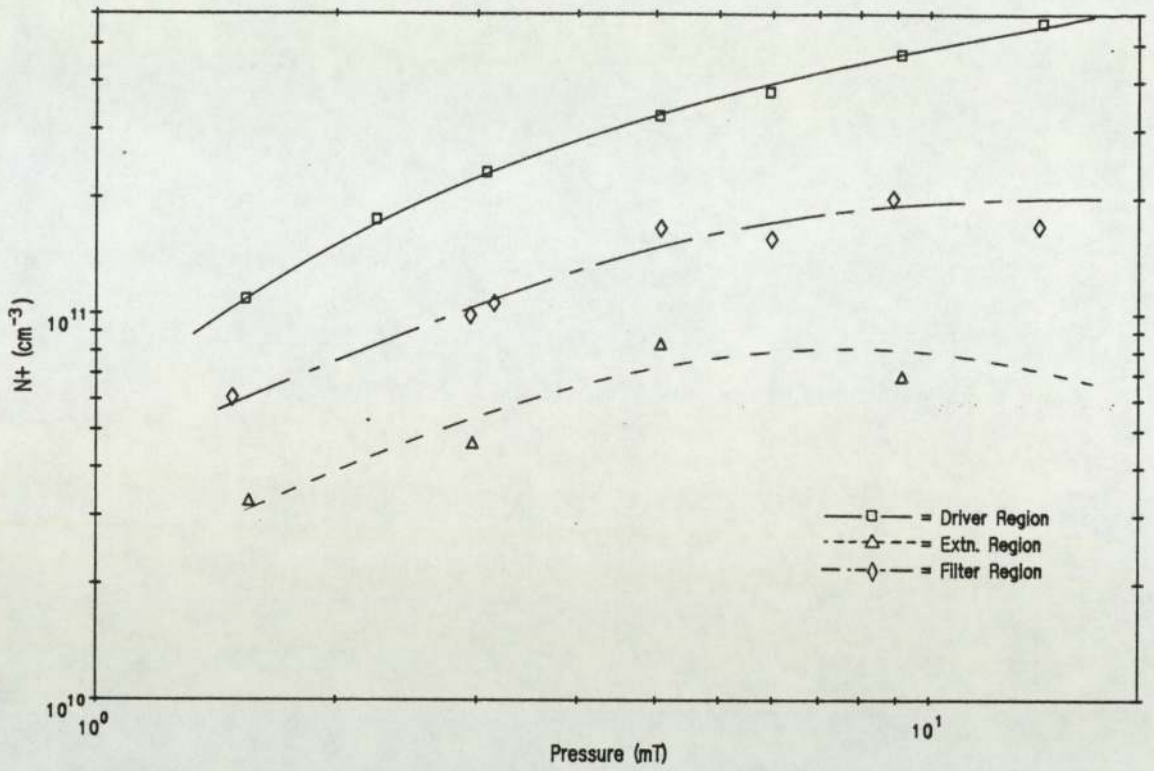


Figure 5.130 Variation of plasma density with pressure
Iarc = 5A Varc = 60v B = 80 Gauss

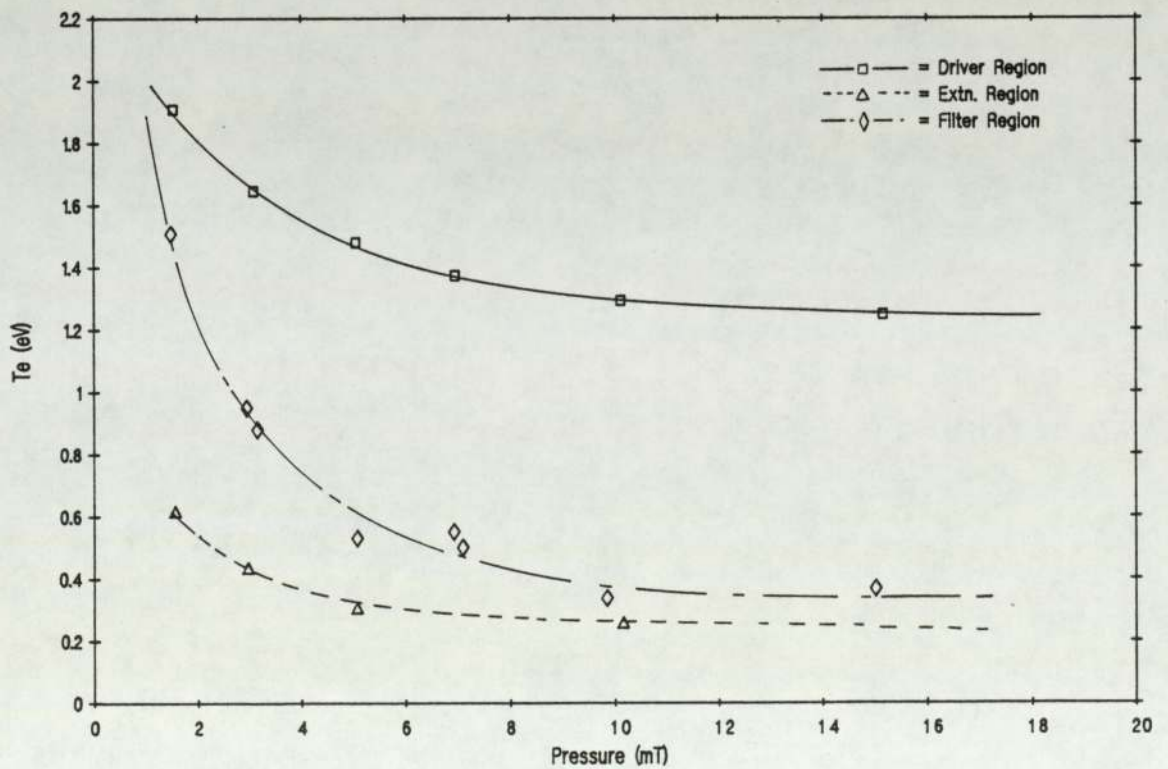


Figure 5.131 Variation of thermal electron temperature with pressure
Iarc = 5A Varc = 60v B = 80 Gauss

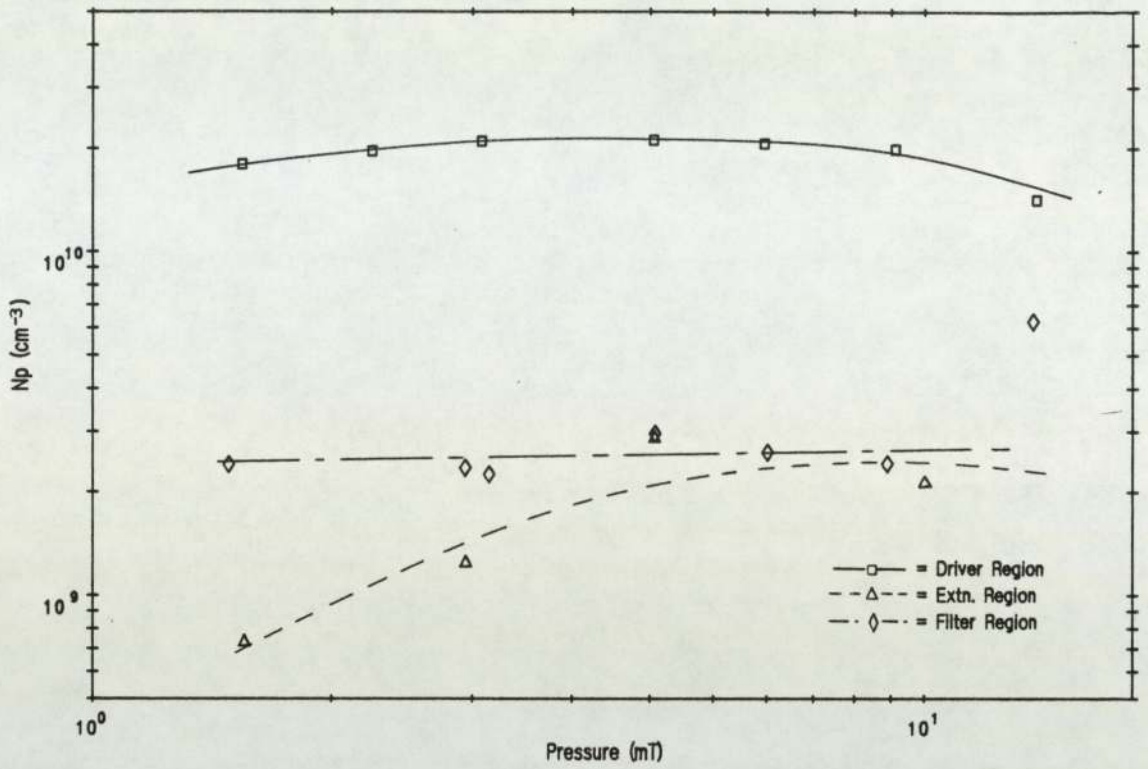


Figure 5.132 Variation of primary electron density with pressure
 Iarc = 5A Varc = 60v B = 80 Gauss

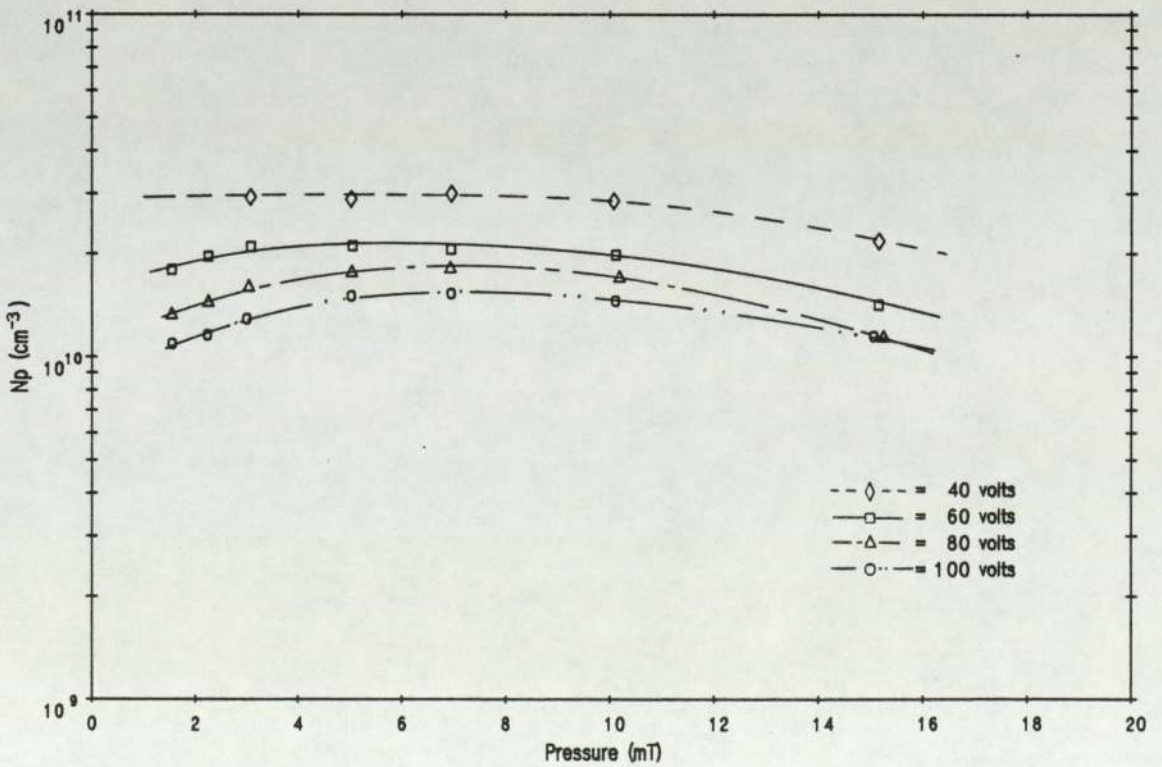


Figure 5.133 N_p / pressure dependance at four arc voltages
 Iarc = 5A B = 80 Gauss

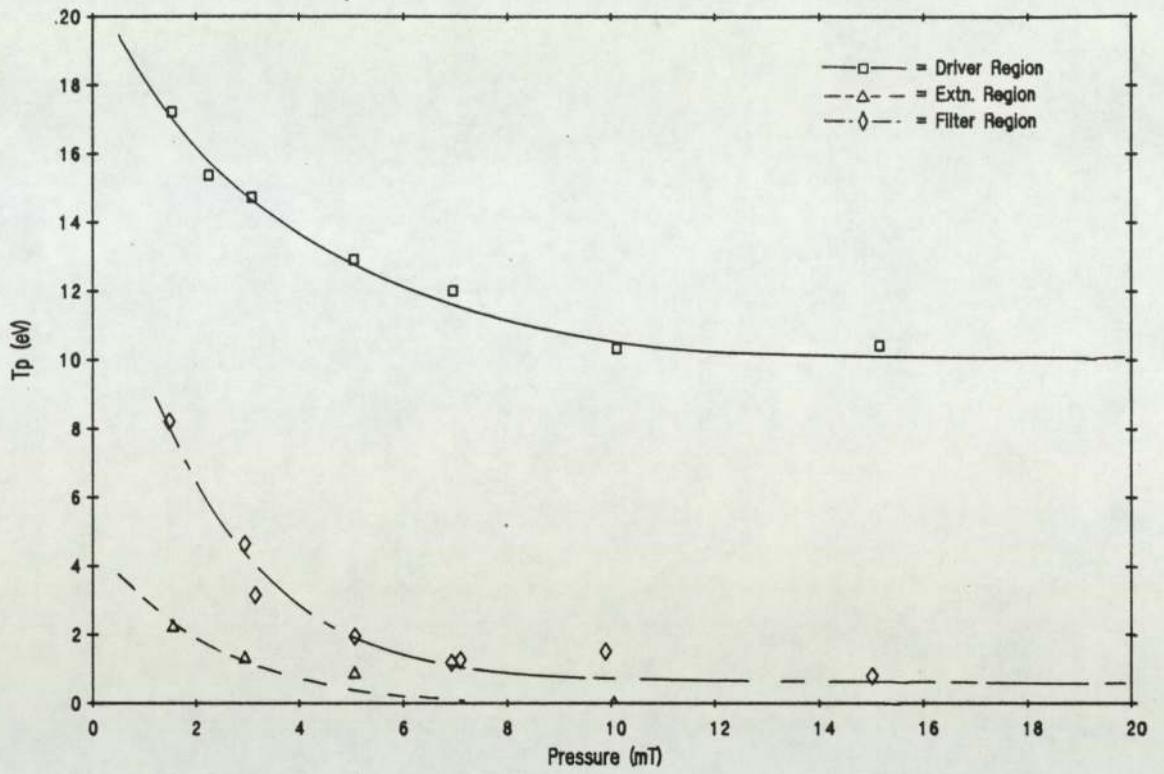


Figure 5.134 Variation of primary electron temperature with Pressure
 $I_{arc} = 5A$ $V_{arc} = 60v$ $B = 80$ Gauss

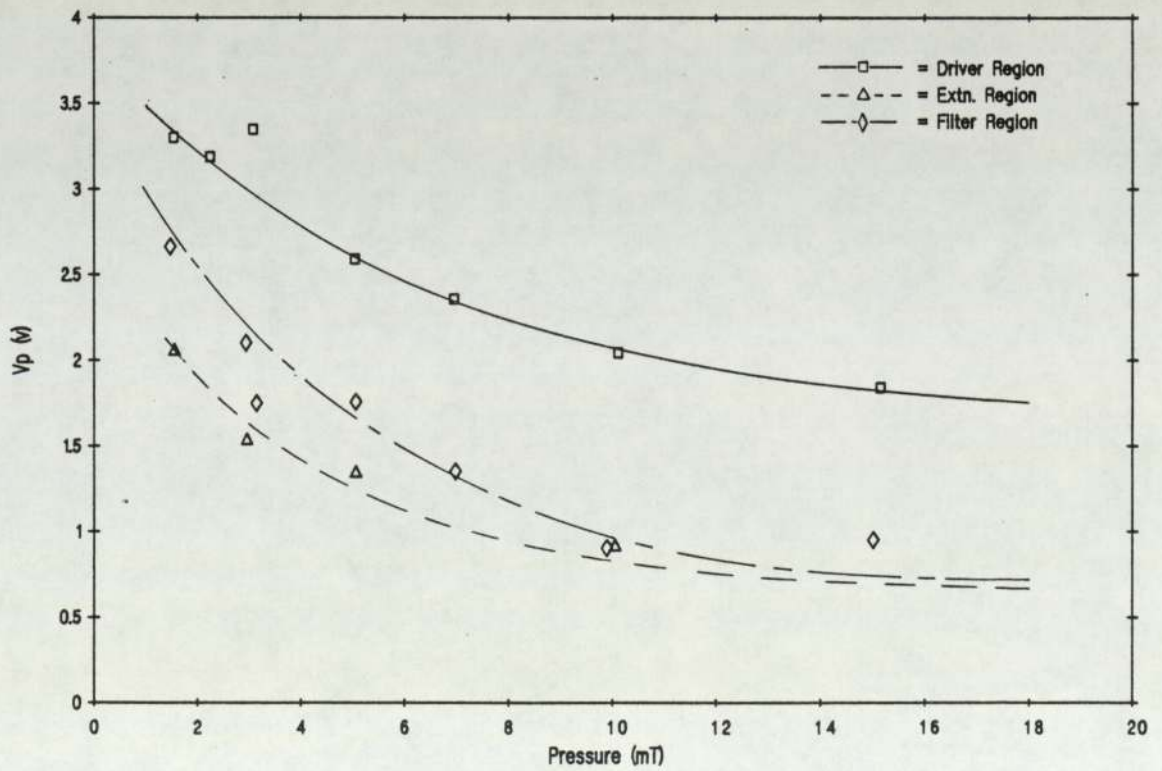


Figure 5.135 Variation of plasma potential with pressure
 $I_{arc} = 5A$ $V_{arc} = 60v$ $B = 80$ Gauss

under these conditions. The fall-off in N_+ is more rapid outside of the driver region. Figure (5.1.31) shows the variation in T_e with pressure under the same conditions. T_e shows a weak inverse dependence on pressure in all regions, a logarithmic plot yielding a value for the index of ~ 0.2 .

Figure (5.1.32) shows the variation in N_p with pressure in the variable-filter source. N_p appears largely independent of pressure in all regions, although noise makes the extraction region difficult to study. This invariance is also shown for four different arc voltages in the driver region in figure (5.1.33). Figure (5.1.34) shows the variation of T_p with pressure under the same conditions. Like T_e , T_p varies inversely with pressure with an index ~ 0.2 . The variation of V_p with pressure is shown in figure (5.1.35). In all regions, a quasi-inverse relationship is evident, similar to, and with the same index as, that of T_e . Once again, the potential difference between driver and extraction regions is not altered.

5.1.2.4 Filter field intensity variation

The intensity of the magnetic filter field in the variable-filter source could be varied by altering the current flowing through the coils of the electromagnetic filter rods. Once set, this required little adjustment. Since the field intensity had no direct effect on the ionization processes, the arc current did not drift as badly for a field adjustment as for adjustments of the other arc

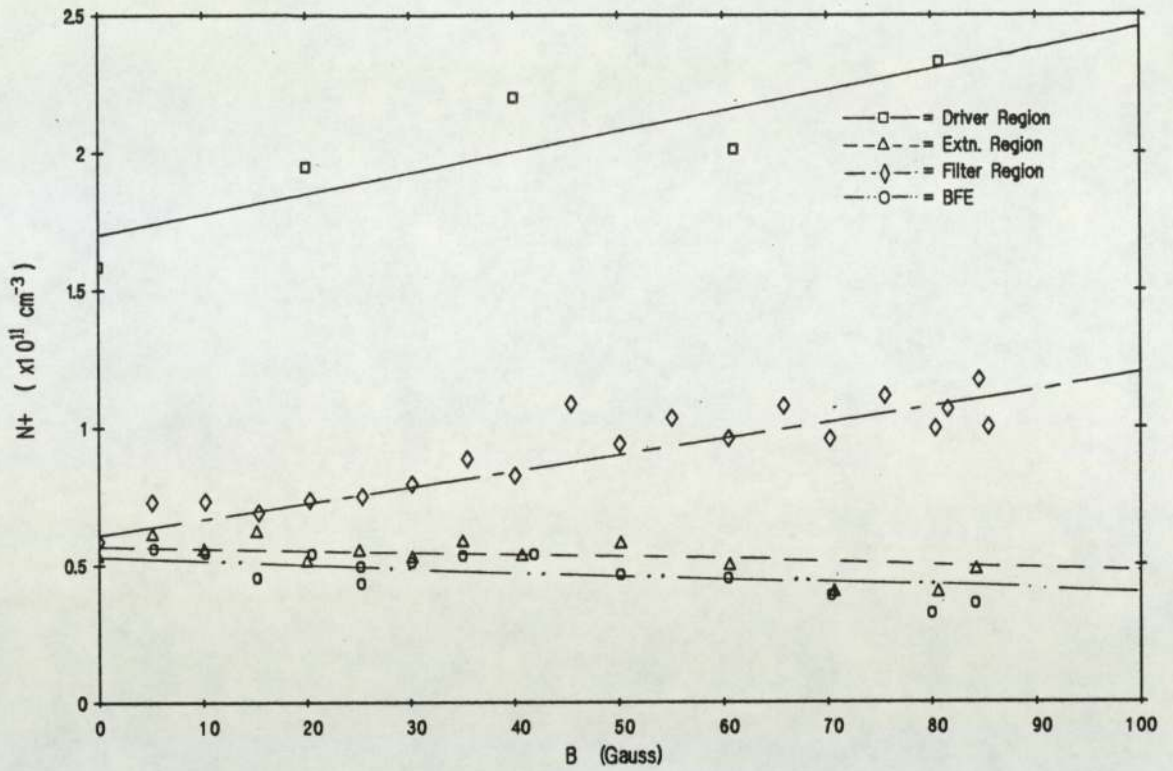


Figure 5.136 Variation of plasma density with filter field intensity
 Iarc = 10A Varc = 60v Pres = 3mT

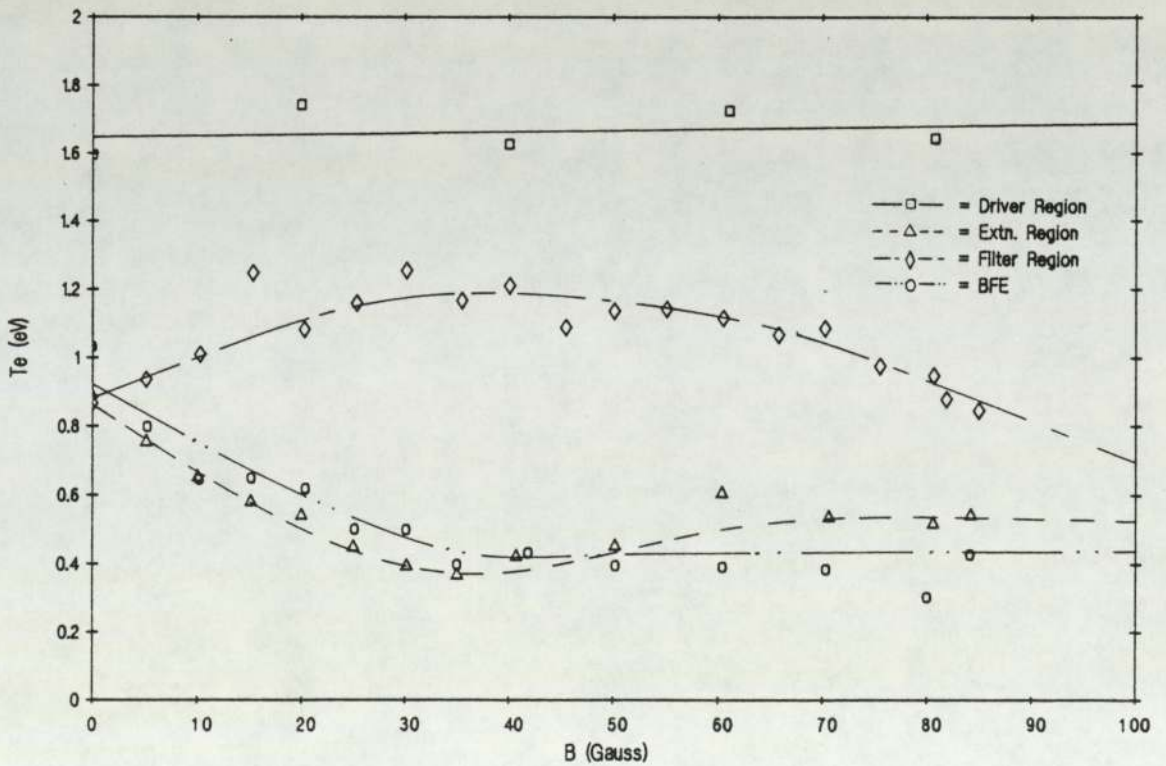


Figure 5.137 Variation of thermal electron temperature with B
 Iarc = 5A Varc = 60v Pres. = 3mT

parameters. Field intensity was measured directly, using a Hall-probe gaussmeter mounted between the filter rods projecting from the source.

Figure (5.1.36) shows the variation in N_+ with field intensity at various positions within the variable-filter source. The driver and filter regions both show a slow linear increase with B , whereas the extraction and BFE regions show a linear decrease. Figure (5.1.37) shows the variation in T_e under the same conditions. As may be seen, T_e is invariant in the driver region. On the opposite side of the filter, T_e falls linearly with B up to ~ 30 gauss, and is invariant thereafter. The nearly-constant filter region curve is subject here to a variable amount of magnetic screening, and therefore must be interpreted with caution.

Figure (5.1.38) shows the variation in N_p with field intensity at the same positions. In the driver region, N_p shows a very slow linear increase with B . The filter region shows a fall due to the screening effect of the probe, (I_p is here uncorrected) whereas the extraction region and BFE appear roughly independent of B , although the scatter here is very great. Figure (5.1.39) shows the variation of T_p with field intensity under the same conditions. In the driver region, T_p falls slowly with field intensity. In the filter region, this is also approximately true. In the extraction region and at the BFE, T_p shows the same critical 30-gauss field behavior as T_e . V_p is plotted as a function of field intensity in figure (5.1.40), and appears completely

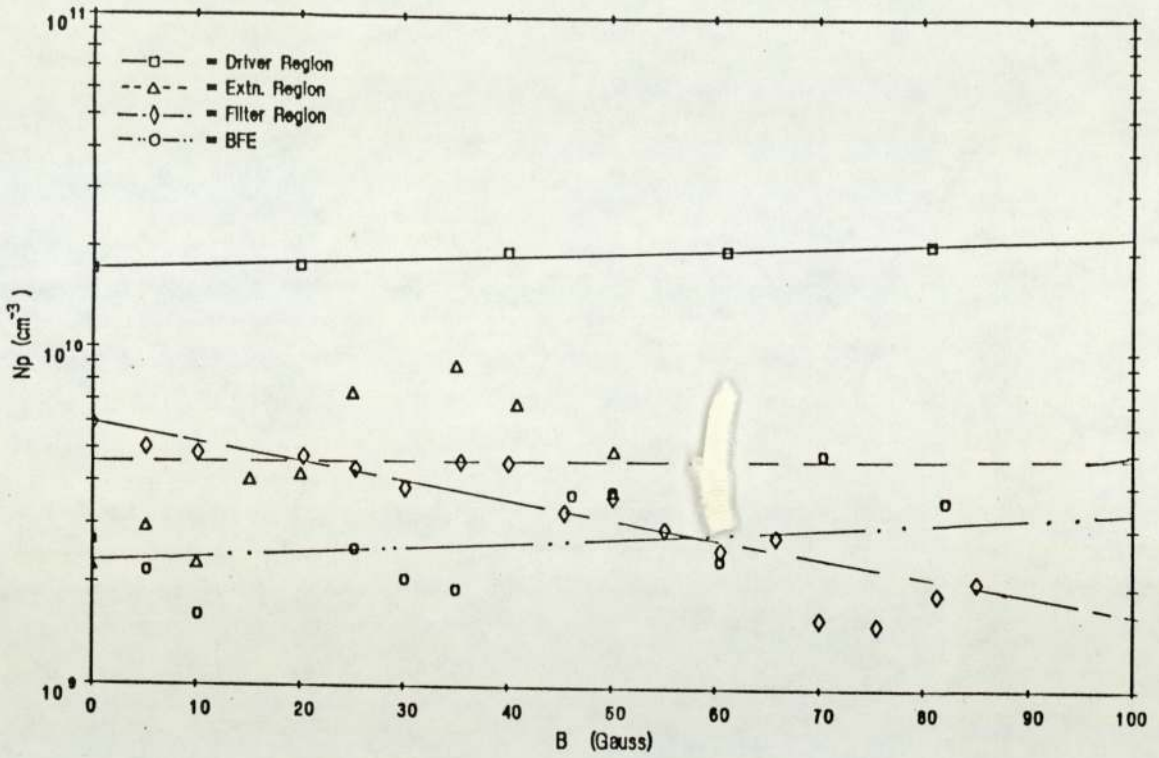


Figure 5.138 Variation of primary density with filter field intensity
Iarc = 5A Varc = 60V Pres. = 3mT

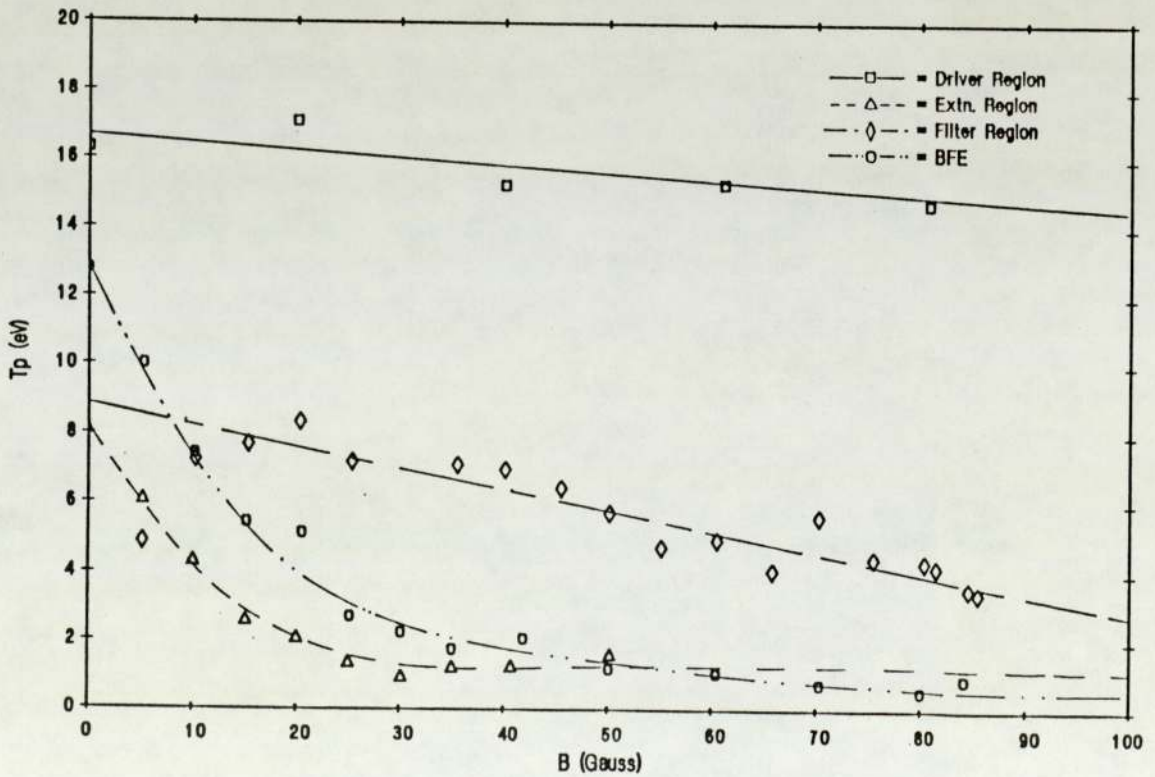


Figure 5.139 Variation of primary electron temperature with B
Iarc = 5A Varc = 60v Pres. = 3mT

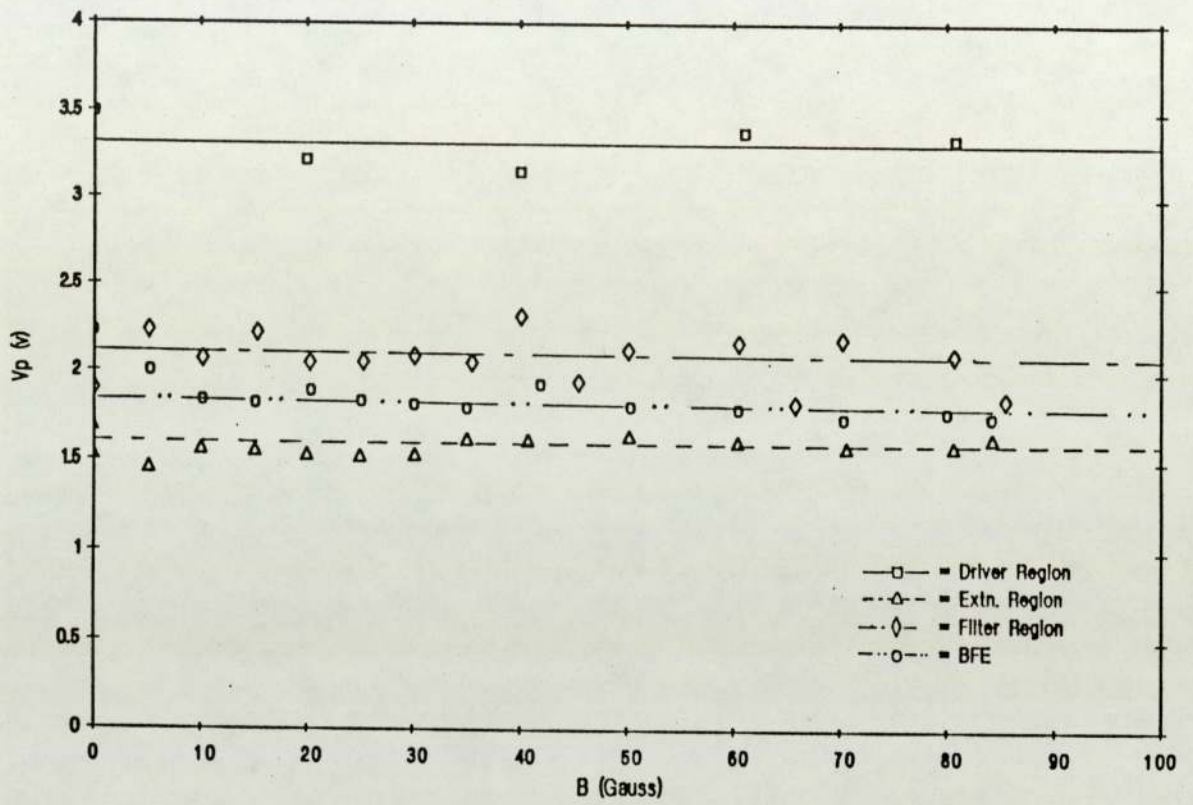


Figure 5.1.40 Variation of plasma potential with filter field intensity
 Iarc = 5A Varc = 60v Pres. = 3mT

independent of B in all regions.

Note that values of T_e , T_p and V_p appear higher at the BFE than in the extraction region, in direct contradiction to the results of section 5.1.1. This is probably due to the orientation of the BFE probe at right angles to the source axis, compared to the extraction region probe which is parallel to the axis. Any drift of plasma down the axis will thus result in an increased probe-directed velocity, altering the energy measurements. This is also true of the results obtained in the arc voltage experiments of section 5.2.1.2.

5.1.2.5 Summary of observations - arc parameter experiments

The principal observations from this series of experiments can be summarized as follows:

Arc current

The plasma density scaling with arc current is best described by the linear variation of the bulk energy density

$N_+ T_e$:

$$N_+ T_e \propto I_{arc} \quad \dots(5.1.1)$$

This relation holds over the entire experimental range of I_{arc} , in all regions of both sources and for all values of every other arc condition varied in these experiments. The gradient of this line varies directly with pressure, arc voltage, and in the driver region with the presence of the

filter field. In the extraction region and at the BFE, the gradient varies inversely with the presence of the filter field.

The primary electron density scales in a linear fashion with I_{arc} :

$$N_p \propto I_{arc} \quad \dots(5.1.2)$$

The gradient varies directly with pressure, and in the driver region, with the presence of the filter field. It varies inversely with arc voltage, and in the extraction region with the presence of the filter field. The primary electron temperature is approximately independent of I_{arc} .

The plasma potential, like T_e , increases slowly with I_{arc} (with an index ~ 0.5), more rapidly in the driver region than anywhere else. This causes an increase of the small p.d. between driver and extraction regions with I_{arc} , the driver region becoming more positive.

Arc voltage

The plasma density displays a saturation curve when plotted against V_{arc} . The knee of the curve occurs at $\sim 95v$, and remains invariant with other arc parameters. The electron temperature does not appear to vary with V_{arc} at all.

The primary electron density in the driver region is inversely proportional to V_{arc} :

$$N_p \propto \frac{1}{V_{arc}} \quad \dots(5.1.3)$$

The gradient varies with pressure, and in the driver region, inversely with the presence of the filter field. Outside of the driver region, N_p does not vary with V_{arc} at all. The primary electron temperature scales in a linear fashion with V_{arc} :

$$T_p \propto V_{arc} \quad \dots(5.1.4)$$

The gradient varies slowly as the inverse of pressure. The presence of the filter field has a negligible effect in the driver region, but elsewhere causes the relationship to become extremely weak.

The plasma potential shows a weak increase with V_{arc} , the gradient of which is invariant with both pressure and filter field. The p.d. across the filter is invariant.

Pressure

The plasma density in the driver region shows a saturation curve when plotted against pressure. The point of saturation is not reached in the driver, but is achieved in the other regions. The thermal electron temperature varies in a weak inverse fashion with pressure:

$$T_e \propto P^{0.2} \quad \dots(5.1.5)$$

The presence of the filter and Varc both have little effect on the variation. The primary electron temperature has the same dependence on pressure as T_e :

$$T_p \propto P^{0.2} \quad \dots(5.1.6)$$

as does V_p :

$$V_p \propto P^{0.2} \quad \dots(5.1.7)$$

The latter holds in all regions, and hence the p.d. across the filter is unaffected.

Filter field intensity

The plasma density in the driver region varies in a weak linear fashion with B. Outside of the driver, this dependence becomes negative.

$$N_+ \propto B \quad (\text{Driver}) \quad \dots(5.1.8a)$$

$$N_+ \propto -B \quad (\text{Extraction}) \quad \dots(5.1.8b)$$

Pressure and Varc have no effect on this variation. The electron temperature in the driver region is invariant with field intensity. Outside of the driver region, T_e shows a linear fall up to $B = 30$ gauss. Beyond this T_e is invariant

with B . The primary electron temperature in the driver region shows a slow linear fall with field intensity. The gradient is inversely proportional to pressure. Outside the driver, T_p shows the same dependence as T_e :

$$T_p \propto -B \quad (\text{Driver}) \quad \dots(5.1.9a)$$

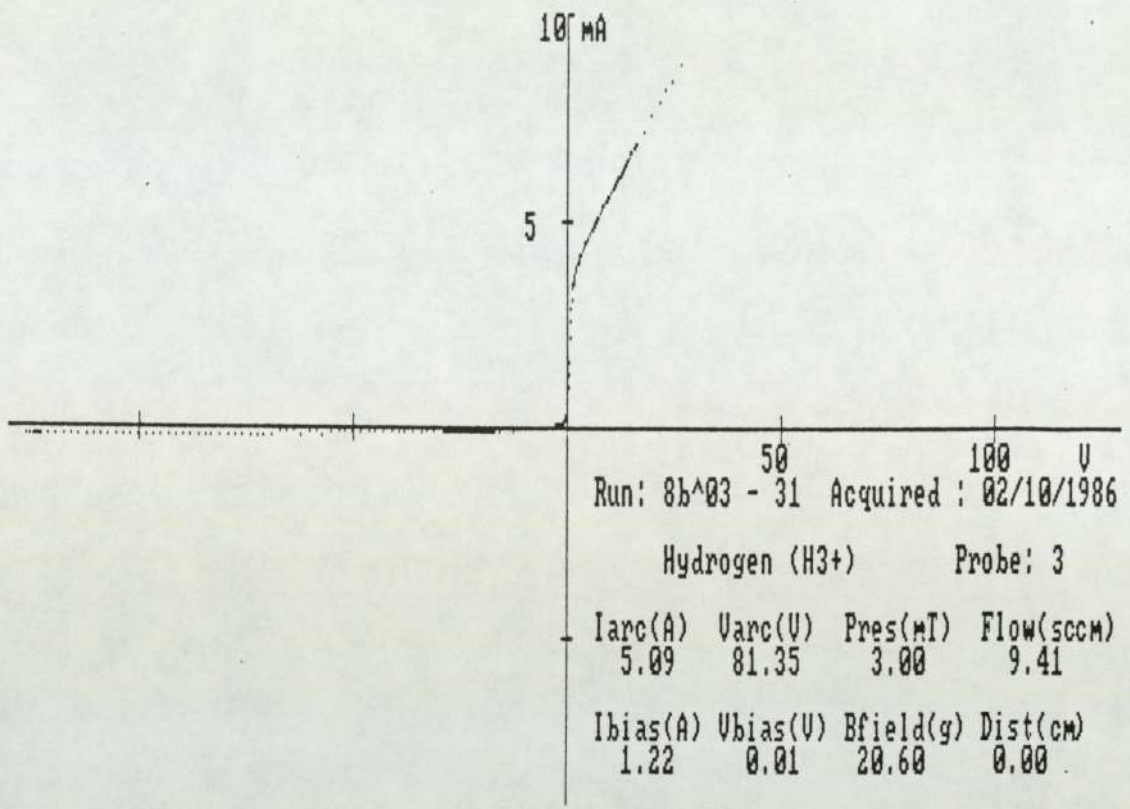
$$T_e, T_p \propto -B \quad (\text{Extraction, } B < 30) \quad \dots(5.1.9b)$$

The plasma potential in all regions is invariant with B , and so the p.d. across the filter is also invariant.

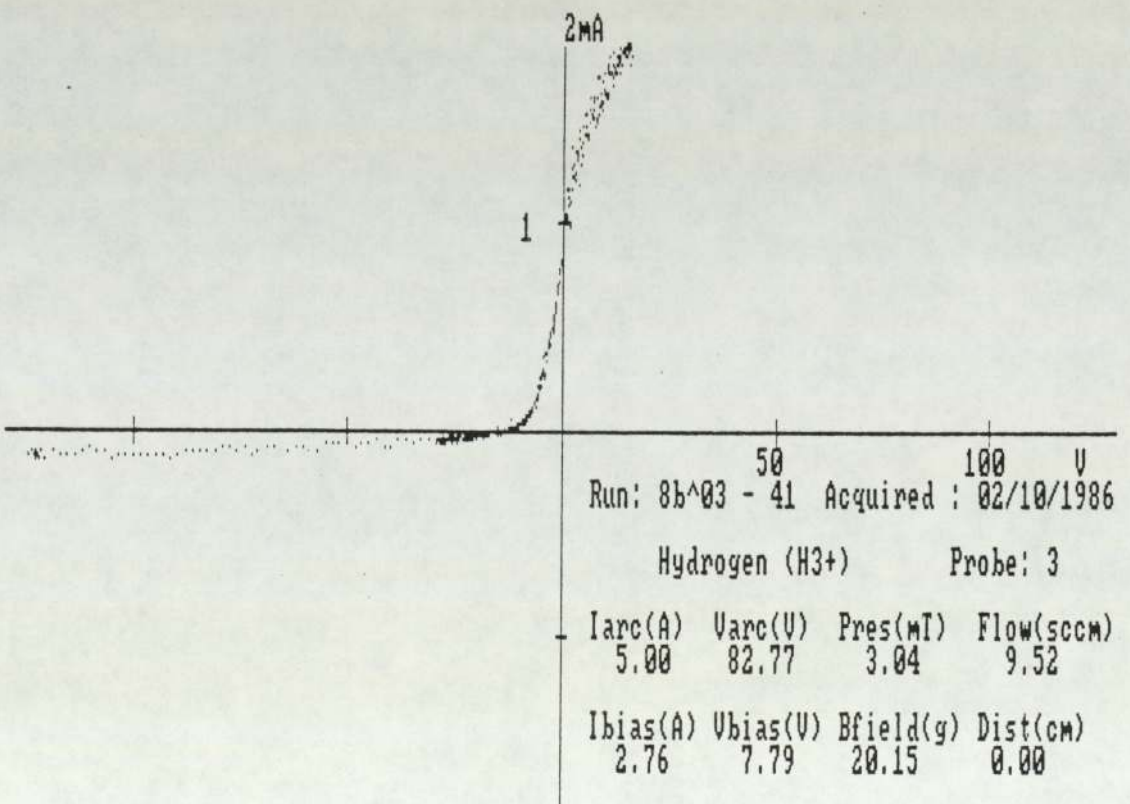
5.1.3 Bias voltage variation

In order to provide a greater fractional yield of extracted H^- ions to electrons, many experimenters [21,33,36,43] have utilized a potential between the beam-forming electrode and the source body. This is known to have an effect on both the extracted electron and H^- ion fluxes, but the nature and extent of the effect on the source plasma is unclear. Accordingly, a series of experiments were performed to study this.

The bias potential could easily be altered using a D.C power supply. In the case of the variable source a high power D.C. amplifier was used to provide a bipolar bias supply. By convention, a positive bias potential means the BFE is positive with reference to the source body. The bias potential had no direct effect upon the ionization processes in the source, and therefore alteration caused no drifting of the other arc parameters. However, at positive bias potentials of more than $\sim 3v$ the discharge became extremely noisy, as illustrated in figure (5.1.41). This shows two probe characteristics obtained at the BFE of the variable source, at bias voltages of 0v and +7.8v. This noise may be due to the discharge entering an unstable regime (as noted by Limpaecher and MacKenzie [24] in the original multipole source), and is probably connected with the effective removal of the Debye sheath at the BFE when $V_{bias} > V_p$. It should be noted that since the BFE formed the reference electrode for the probes, V_p and V_s required correction for V_{bias} and



(a) $V_{bias} = 0v$



(b) $V_{bias} = +7.8v$

Figure 5.1.41 Discharge noise induced by positive BFE bias

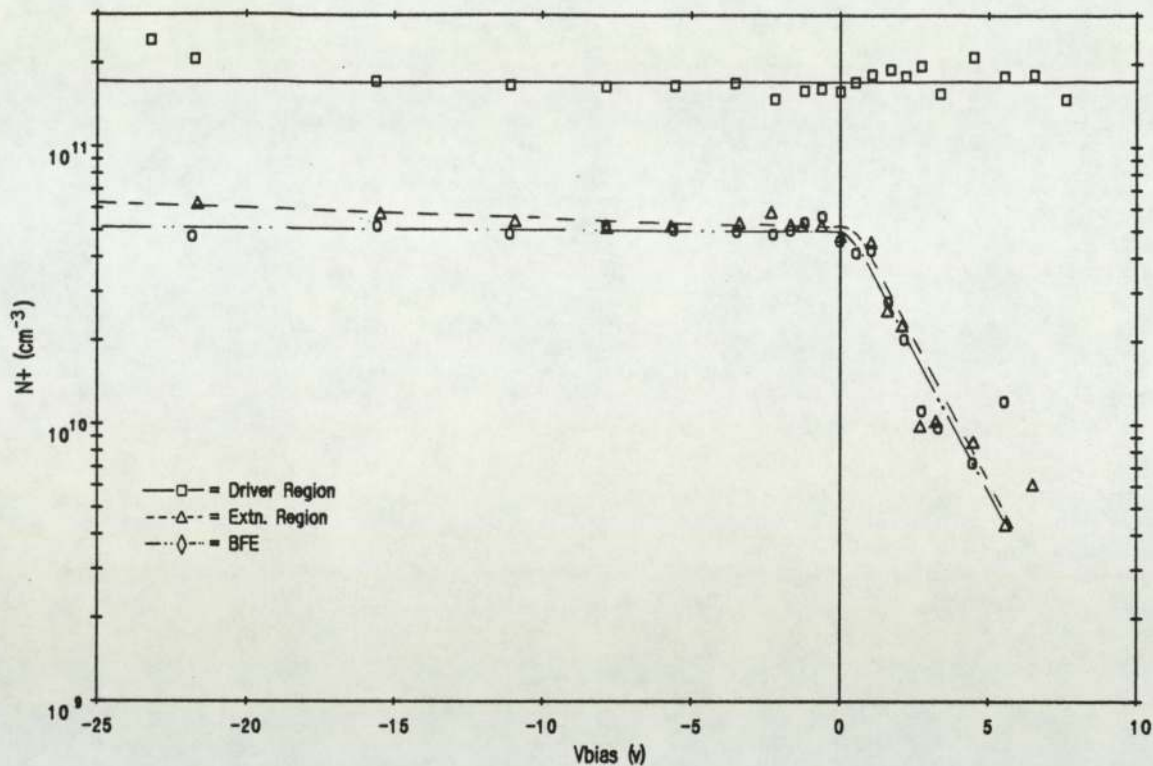


Figure 5.1.42 Variation of plasma density with bias voltage
 $I_{\text{arc}} = 5\text{A}$ $V_{\text{arc}} = 60\text{V}$ $P_{\text{res.}} = 3\text{mT}$ $B = 80$ gauss

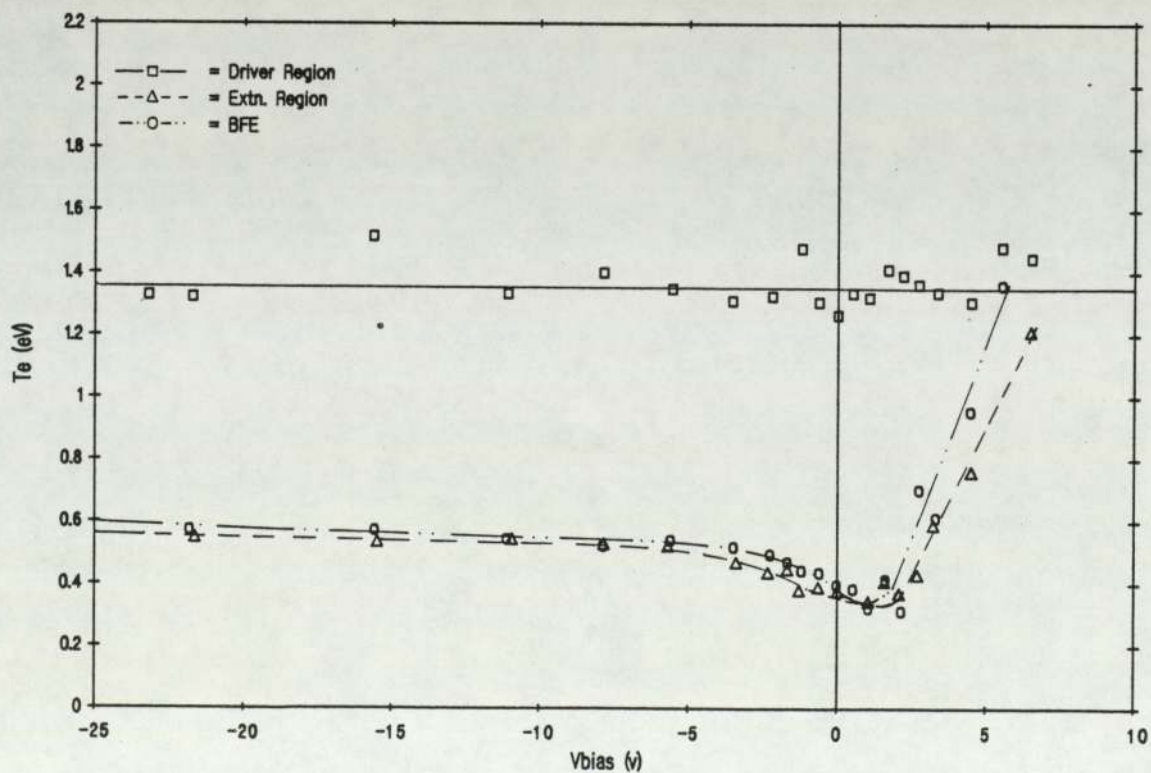


Figure 5.1.43 Variation of thermal electron temperature with bias voltage
 $I_{\text{arc}} = 5\text{A}$ $V_{\text{arc}} = 60\text{V}$ $P_{\text{res.}} = 3\text{mT}$ $B = 80$ gauss

are shown here so corrected.

Figure (5.1.42) shows the variation in N_+ with bias potential at three points in the variable filter source. In the driver region, N_+ is independent of V_{bias} over the full range. Outside of the driver, a positive bias potential produces an exponential fall in N_+ of an order of magnitude in +5v, whereas negative bias causes no change. Data obtained from positive bias experiments in the fixed filter source shows a similar behavior. Figure (5.1.43) shows the variation in T_e under the same conditions. Again, the driver region is unaffected. Elsewhere, a positive bias produces a rapid linear increase in T_e , after the bias is increased beyond a value $\sim V_p$. A negative bias produces a small increase in T_e initially, but this saturates within $\sim 3v$. The increase in T_e with positive bias is more rapid for the BFE probe than the extraction region probe. As already mentioned, the BFE probe is mounted facing the axis whereas the face of the extraction region probe is parallel to it. This implies that the increase in T_e may be due to the acceleration of electrons into the probe by an axial drift velocity induced by the bias potential, the effect being greater in the BFE case.

Figure (5.1.44) shows the primary electron density N_p as a function of bias potential. The driver region values show no dependence at all on V_{bias} , demonstrating that primaries are especially well "insulated" by the filter. In direct contradiction to the plasma density variation, the extraction

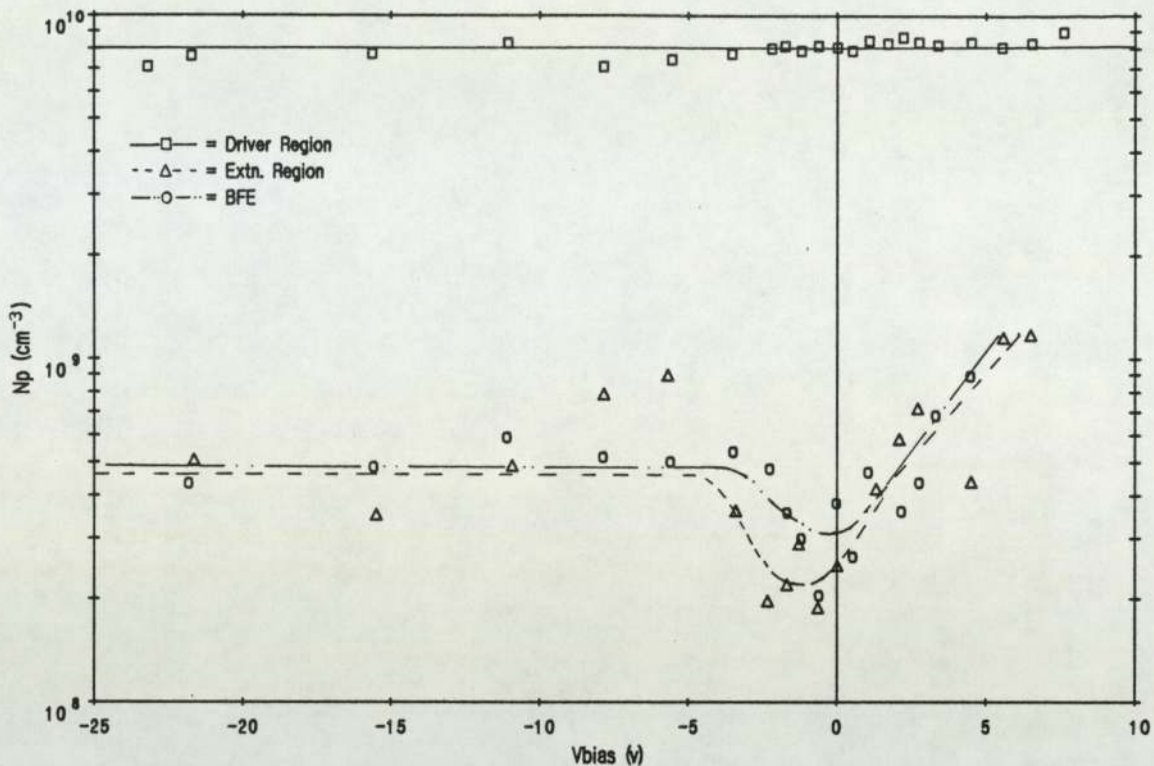


Figure 5.144 Variation of primary electron density with Vbias
 Iarc = 5A Varc = 60v Pres. = 3mT B = 80 Gauss

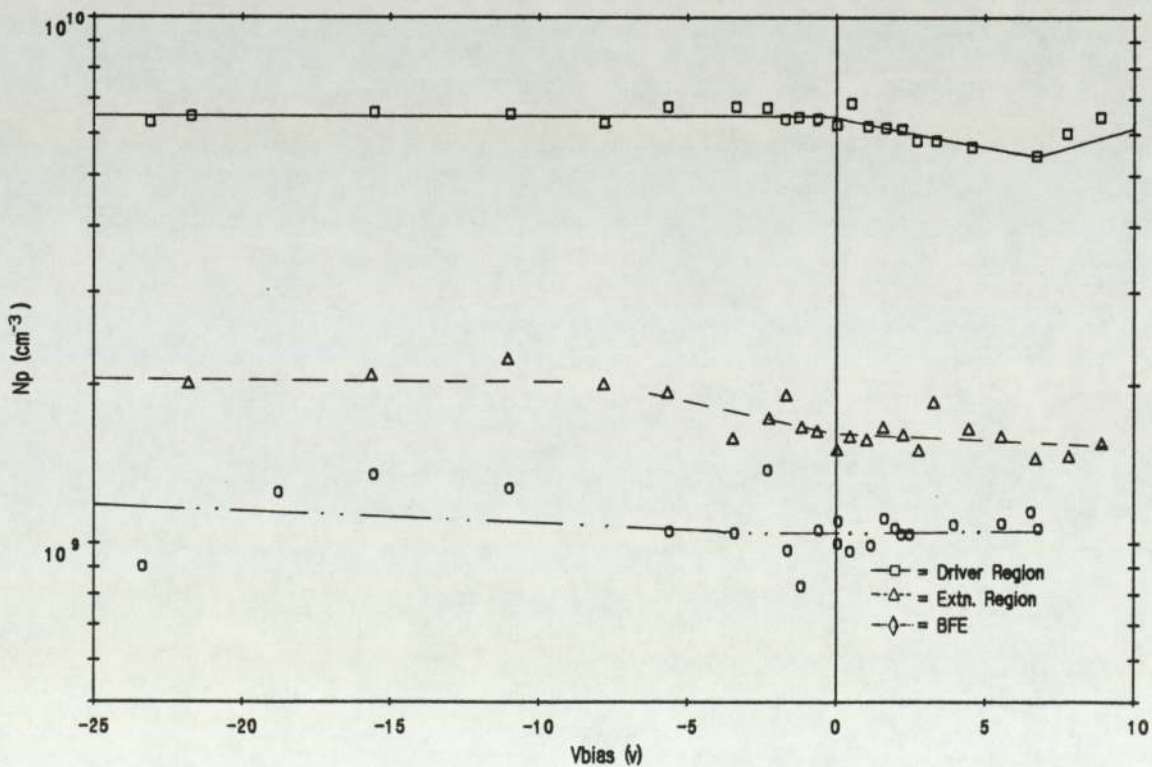


Figure 5.145 Variation of primary electron density with Vbias
 Iarc = 5A Varc = 60v Pres. = 3mT B = 0 Gauss

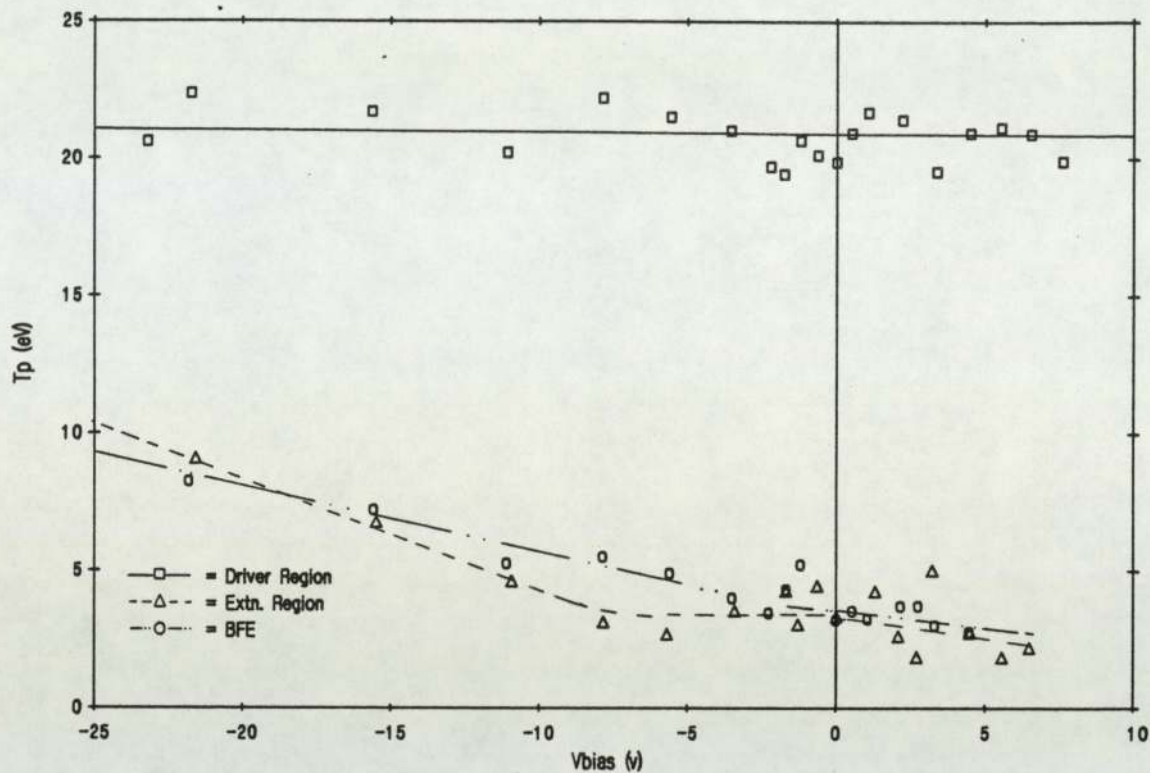


Figure 5.146 Variation of primary electron temperature with Vbias
 $I_{arc} = 5A$ $V_{arc} = 60v$ $P_{res.} = 3mT$ $B = 80$ Gauss

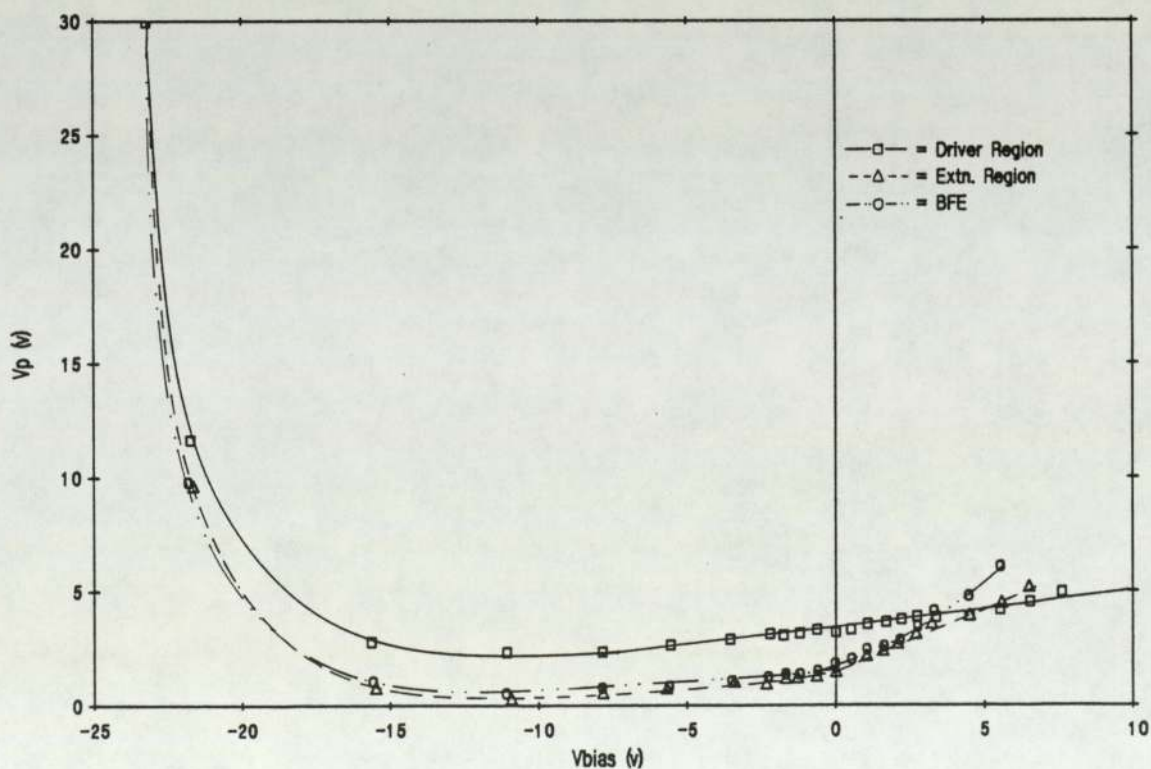


Figure 5.147 Variation of plasma potential with Vbias
 $I_{arc} = 5A$ $V_{arc} = 60v$ $P_{res.} = 3mT$ $B = 80$ Gauss

region and BFE results show an increase of nearly an order of magnitude over 5v for positive bias, and a slightly smaller increase followed by saturation for negative bias. It is interesting to note that the bias variation obtained from the BFE probe in the absence of a filter field is almost independent of bias voltage outside the driver, as shown in figure (5.1.45). In the driver, V_{bias} causes a similar but very much weaker effect to that of N_+ at the BFE. Figure (5.1.46) shows that T_p is largely invariant with bias potential in all regions, although highly negative voltages ($-V_{bias} > 15v$) cause T_p to double outside the driver.

The effect of bias voltage on the plasma potential V_p is shown in figure (5.1.47). The driver region shows a shallow rise for a positive bias, and a similar shallow fall for negative bias, the gradient of the resulting line being ~ 0.1 . Outside the driver, the effect is repeated tenfold. However, when $(-V_{bias}) > T_p$, V_p shows a dramatic rise in all the regions, of over an order of magnitude. The behavior in the extraction region is similar but exaggerated. It is possible this is an instrumental artifact, arising from some breakdown in the isolation circuitry.

Figure (5.1.48) shows the axial variation in plasma density N_+ for four values of bias voltage in the variable filter source. The filter is fully active. A positive bias voltage causes a fall in N_+ evenly throughout the extraction region, leaving the density gradient between the 30-gauss contour of the filter and the BFE unchanged. A negative bias

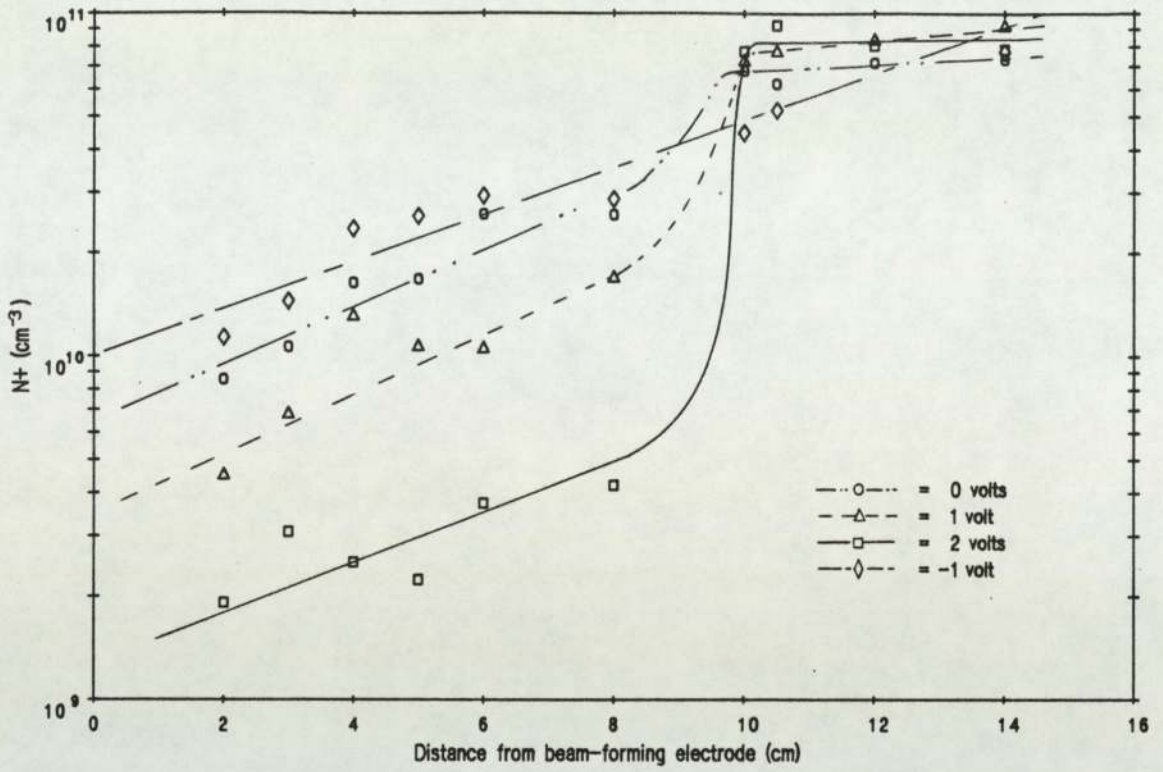


Figure 5.1.48 Axial Variation of N_+ as a function of V_{bias}
 $I_{\text{arc}} = 5\text{A}$ $V_{\text{arc}} = 60\text{v}$ $P_{\text{res.}} = 3\text{mT}$ $B = 80$ Gauss

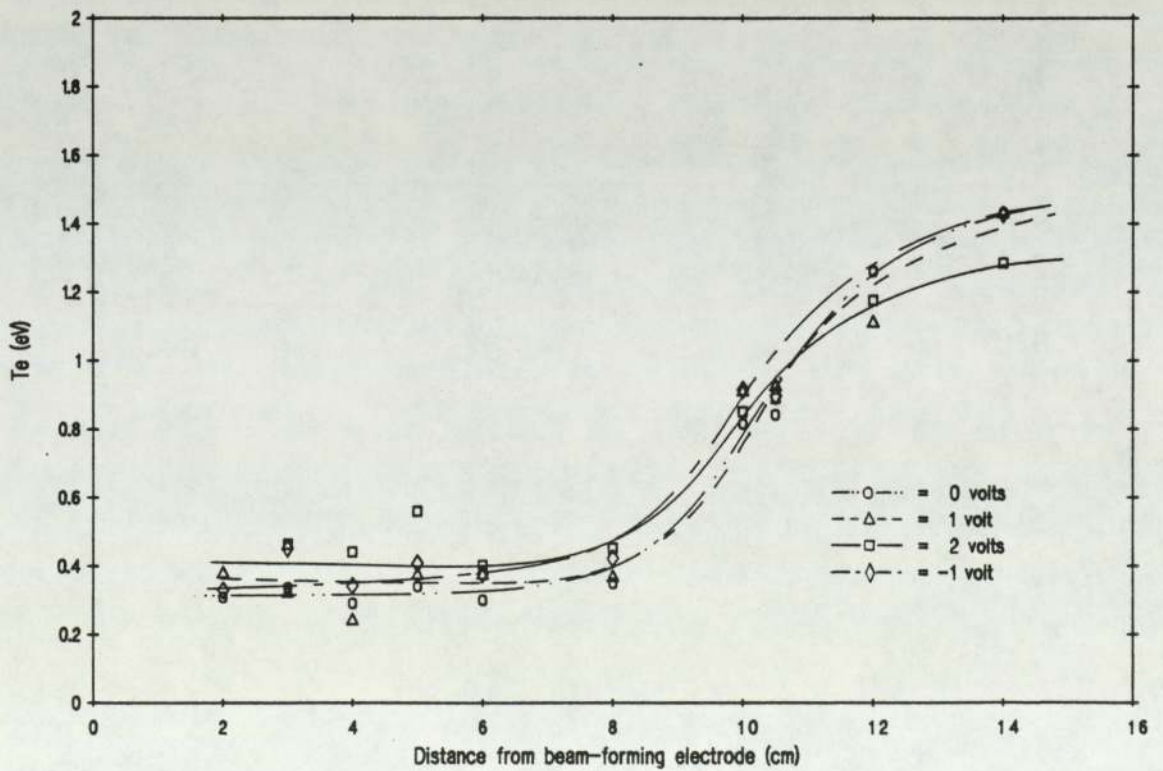


Figure 5.1.49 Axial Variation of T_e as a function of V_{bias}
 $I_{\text{arc}} = 5\text{A}$ $V_{\text{arc}} = 60\text{v}$ $P_{\text{res.}} = 3\text{mT}$ $B = 80$ Gauss

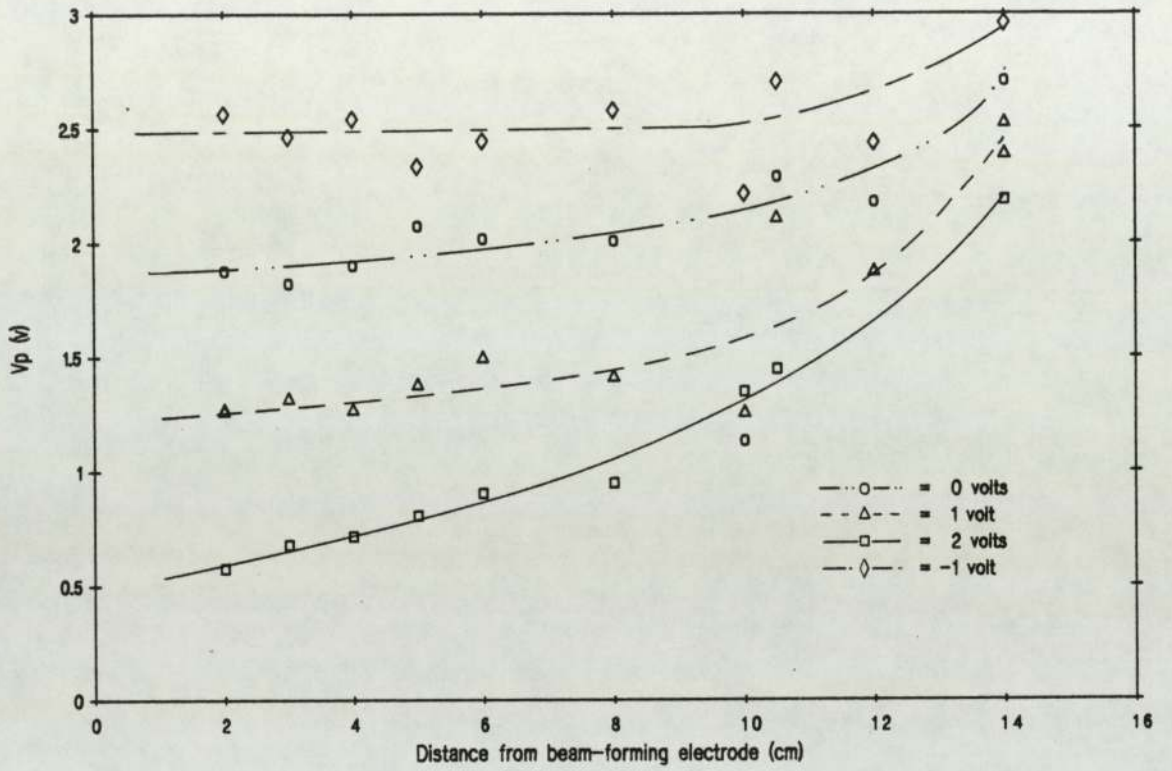


Figure 5.150 Axial Variation of V_p as a function of V_{bias}
 $I_{arc} = 5A$ $V_{arc} = 60v$ $P_{res.} = 3mT$ $B = 80$ Gauss

causes a very small increase in N_+ in the same manner. The driver region values are largely unaffected by bias potential. Figure (5.1.49) shows the small variation in T_e under the same conditions. The large variations in T_e seen by the BFE probe in figure (5.1.43) are not evident here, although these large increases were only observed when $V_{bias} \gtrsim +2v$. Figure (5.1.50) shows that some of the difference in plasma potential caused by the bias can leak into the driver region. In the case of a positive bias, the effect on the extraction region potential reduces the small potential between driver and extraction regions. In the negative case, it increases it. The changes in V_p at the BFE are roughly the same as the changes in V_{bias} generating them, whilst in the driver the changes are reduced to $\sim 30\%$ of the BFE value.

To summarize, the main observations made in this series of experiments are as follows;

1. The effect of the bias potential is confined to the extraction region, between the BFE and the filter. Within this region, the effect is universal, in that it does not appear to diminish in magnitude with distance from the BFE. The driver region is unaffected by bias. The one exception to this is the penetration of weak electric fields caused by the axial variation in plasma potential.

2. In the extraction region and at the BFE, a positive bias causes an exponential reduction in plasma density, and a linear increase in temperature. A negative bias produces a small increase in both N_+ and T_e .

$$N_+ \propto e^{-V_{bias}} \quad \dots(5.1.10)$$

3. In the same regions, a positive bias causes N_p to increase. A negative bias has a similar but lesser effect. Bias has little effect on T_p except for high negative potentials .

$$N_p \propto e^{V_{bias}} \quad \dots(5.1.11)$$

4. A positive bias voltage reduces the potential difference between driver and extraction regions, this practically disappearing when $V_{bias} = +2v$.

$$\Delta V_p \propto -V_{bias} \quad \dots(5.1.12)$$

5. Under no circumstances did the plasma potential become negative, although for negative V_{bias} V_p fell to $< 0.5v$ at the BFE.

5.2 Measurements of H^- density

Where possible, measurements of negative ion density (N_-) were made under the same conditions as the basic plasma experiments described in section 5.1. This was easy to arrange for the probe experiments (section 5.2.1), but difficult in the case of the extracted beam results of section 5.2.2.

5.2.1 Measurements of N_- obtained from probe-ratio data

Fractional negative ion densities measured from the probe saturation current ratio were calculated using the theory due to Lea [93] after correction for electron screening, as described in chapter 4. These are denoted F_r to distinguish them from direct measurement of H^- , as it is important to note that the observed probe ratios may possibly be affected by variations in the positive ion species ratio, and hence the effective ion mass. This was determined experimentally by mass-analysis of a beam extracted from the fixed-filter source, as described in section 5.2.2. The positive ion species ratio obtained was assumed to be similar for both of the sources. This was then used in eqn. (4.1.1) to determine the effective ionic mass in the source, assuming no negative ions were present. A value for M_+ of 2.8 was obtained by this means. The negative ion density, N_{-r} , was then obtained using the calculated value for F_r in conjunction with the corresponding N_+ value from section 5.1. The possible errors involved in this process are

discussed in appendix D.

5.2.1.1 Spatial variation

Figure (5.2.1) shows the saturation current ratio R as a function of axial distance through the source, with the filter both inactive and at full excitation (80 gauss). The results are shown uncorrected for electron screening, and for the active-filter case display a prominent dip centered exactly on the filter peak. However, a considerable difference exists between the two field-free regions either side of the filter, the extraction region results being some 20% lower. Figure (5.2.2) shows the same data after correction for electron screening. The strong structure directly attributable to the filter-field is removed. The corrected ratio shows a sharp decrease from the driver region plateau, beginning at the driver-region edge of the filter. This levels off at the peak of the filter into a plateau at 80% of the driver value. Results close to the backplate show a small reduction in ratio, some of which may be due to the influence of the confinement magnets. Close to the BFE the ratio shows a rise, due possibly to the extremely low signal levels here. Fig (5.2.3) shows the fractional negative ion density F_r ($=N_{-r}/N_+$) calculated from the corrected ratio, for pressures of 3mT & 10mT. Both show an extremely rapid rise from "noise" level at the filter peak. The 10mT result shows a plateau value of 0.16, whereas the 3mT result has a

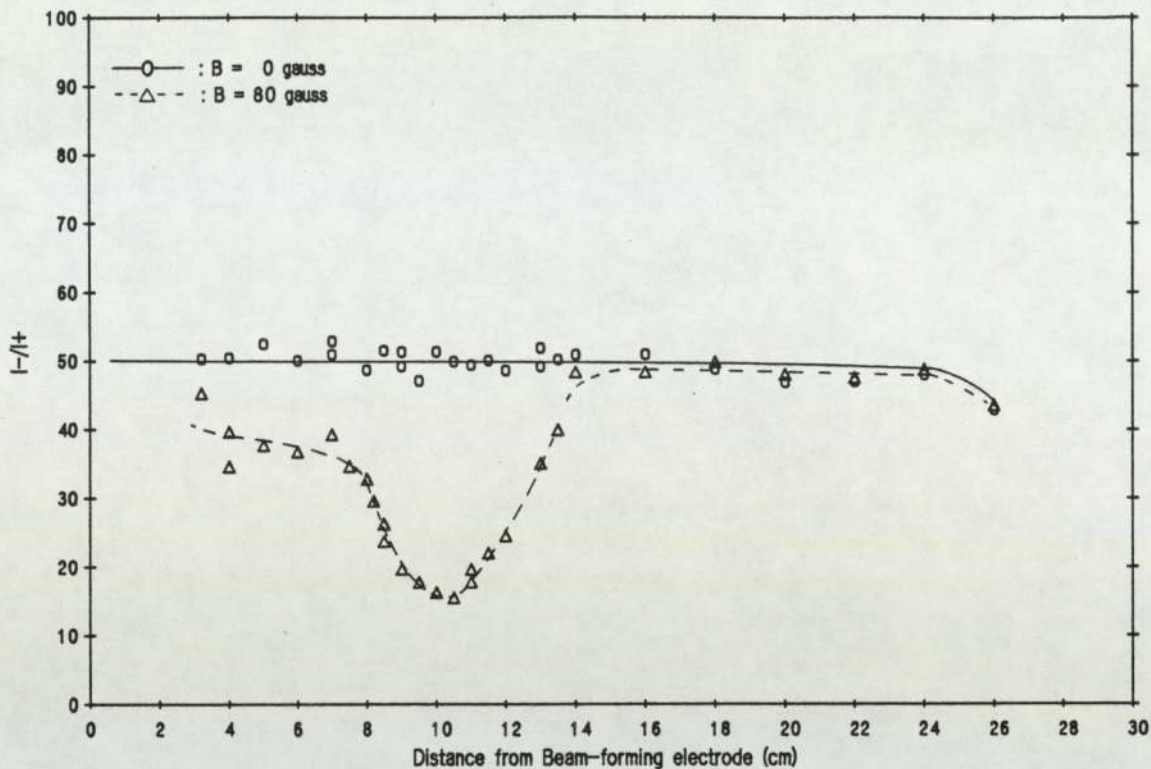


Figure 5.21 Axial variation of I_-/I_+ - Uncorrected for screening
 $I_{arc} = 5A$ $V_{arc} = 60v$ $Pres. = 10mT$

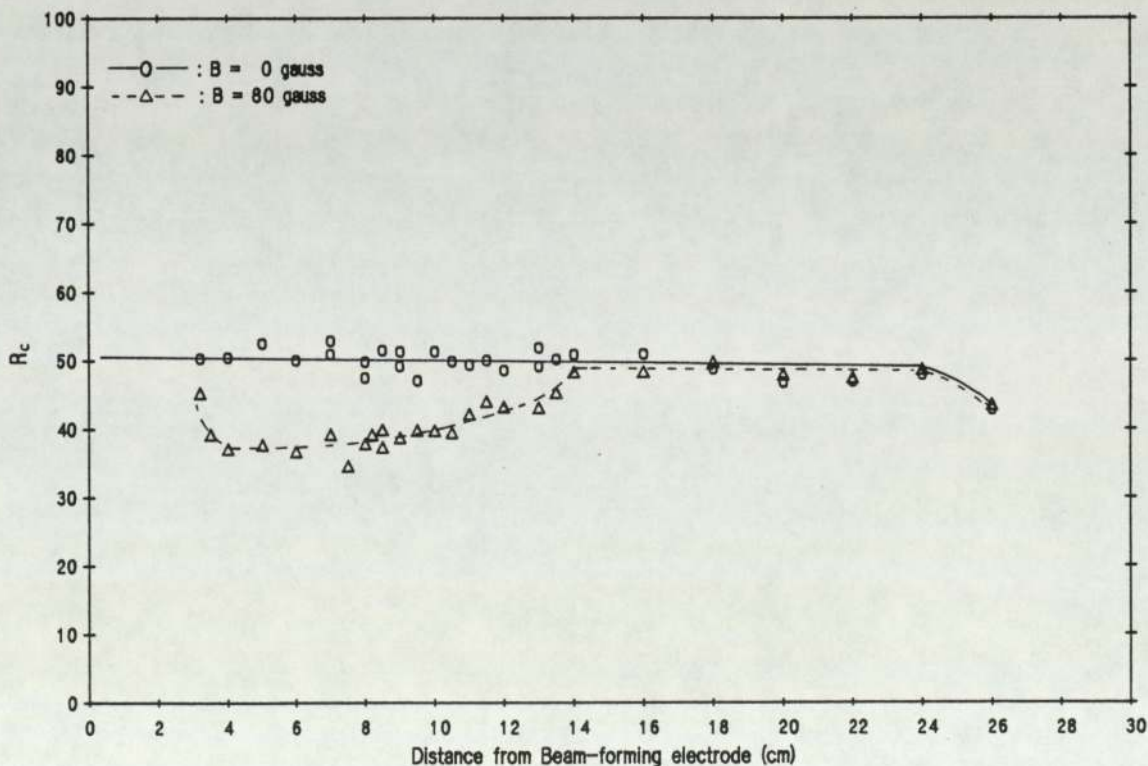


Figure 5.22 Axial variation of I_-/I_+ ($=R_c$) - Corrected for screening
 $I_{arc} = 5A$ $V_{arc} = 60v$ $Pres. = 10mT$

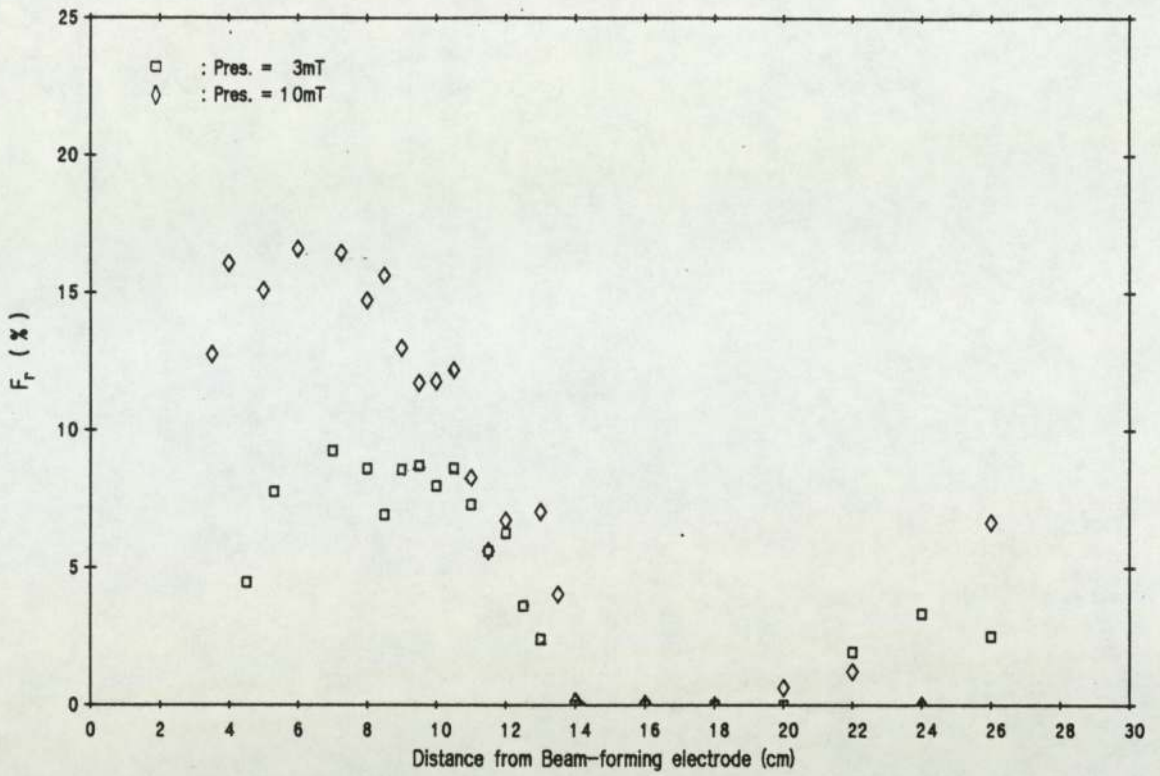


Figure 5.2.3 Axial variation of H^- ion fraction
 $I_{arc} = 5A$ $V_{arc} = 60v$ $B = 80$ gauss

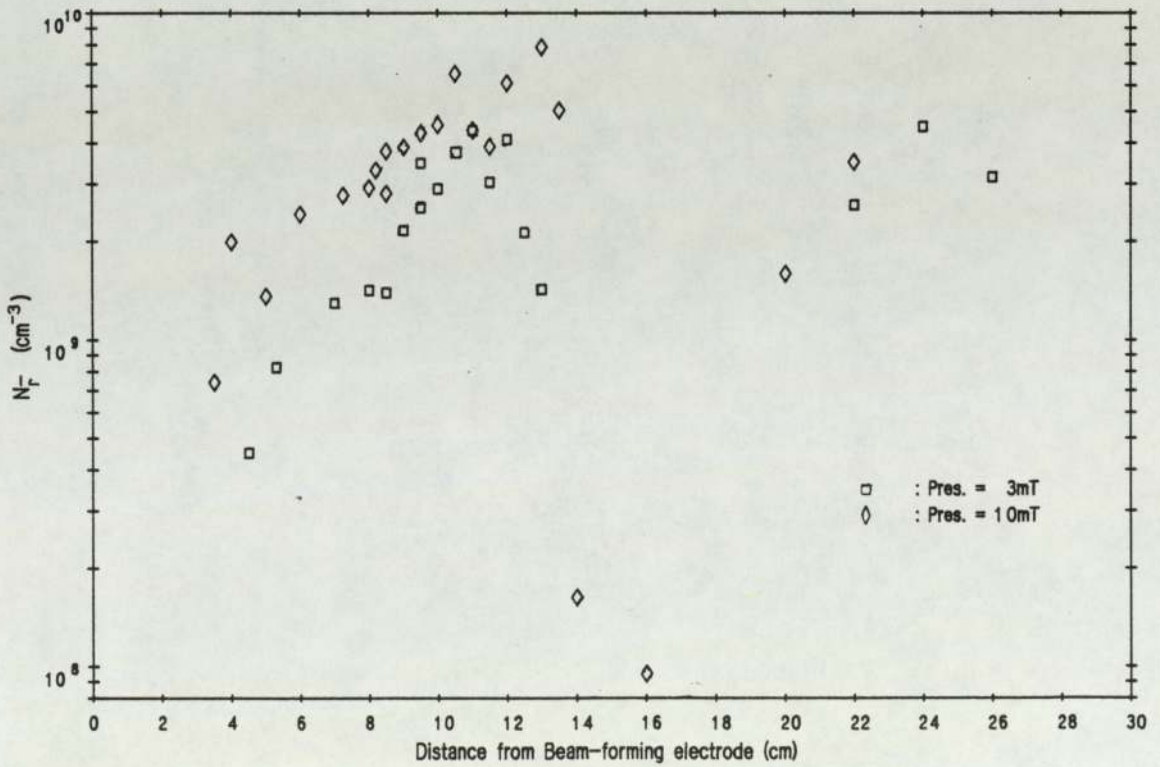


Figure 5.2.4 Axial variation of H^- ion density
 $I_{arc} = 5A$ $V_{arc} = 60v$ $B = 80$ Gauss

peak value of 0.09. The 10mT peak is some 3cm closer to the BFE than the 3mT one.

Combining this result with the positive ion density variation shown in figure (5.1.1) the axial variation of N_{-r} with distance is obtained, as shown in figure (5.2.4). In the 10mT case, N_{-r} rises sharply as the 30-gauss contour is crossed, reaching a value of $\sim 7 \times 10^9 \text{ cm}^{-3}$ at 11cm from the BFE. N_{-r} then falls in an exponential fashion as the BFE is approached, reaching $\sim 10^9 \text{ cm}^{-3}$ at 4cm from the BFE. Results close to the BFE show much scatter, and fall to low levels, possibly due to the low signals mentioned earlier. This behavior is repeated in the 3mT case, save that the absolute value of N_{-r} is some 65% of it's value at 10mT, and the exponential fall from the filter to the appears slightly more rapid. Unlike the F_r curves, the N_{-r} peaks appear at the same position for both pressures. Whilst negative ions doubtless do exist in the driver, the high values of N_{-r} seen here in the driver region are almost certainly erroneous. The probe ratio is subject to scatter. This yields false N_{-r} values, which are amplified by high densities in the driver. In addition, no correction was performed for probe screening by the confinement magnets close to the backplate.

Figure (5.2.5) shows R as a function of radial distance across the extraction region, with the filter both active and inactive. From the axis to within 4cm of the walls, the ratio is constant. A very sharp fall occurs close to the wall due to the influence of the confinement magnets. Close

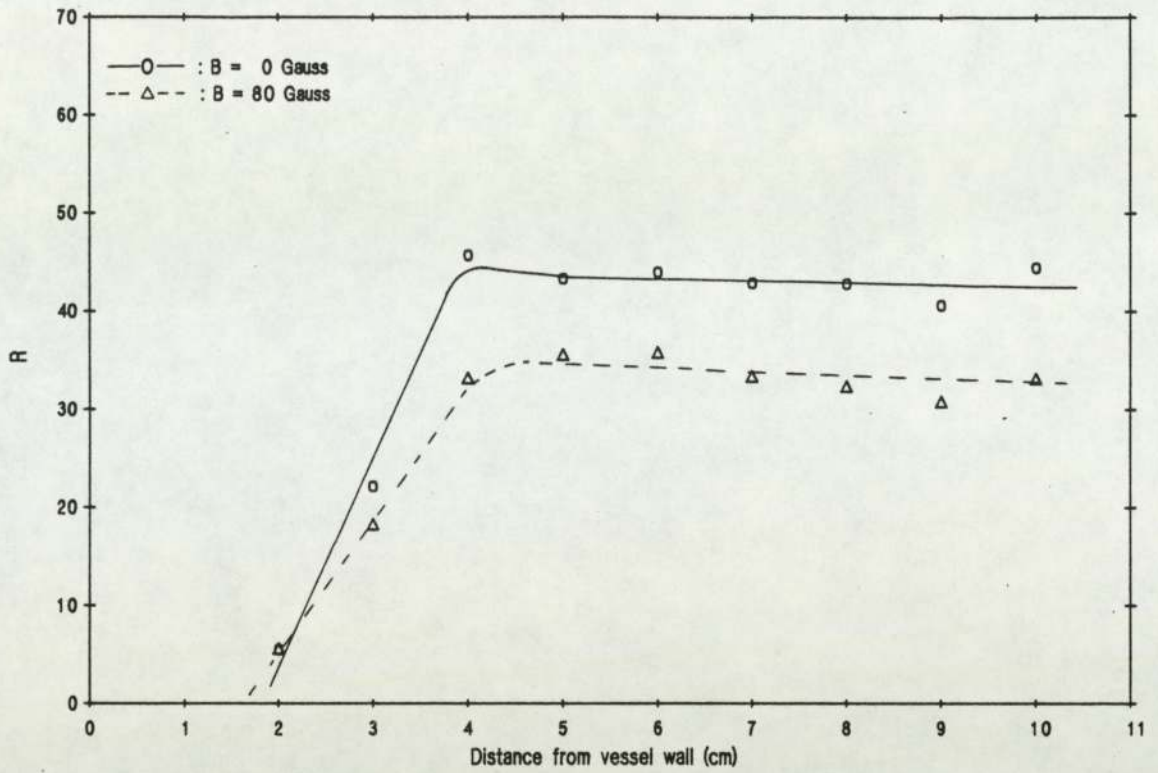


Figure 5.25 Radial variation of probe ratio
 $I_{arc} = 5A$ $V_{arc} = 80v$ $Pres. = 3mT$

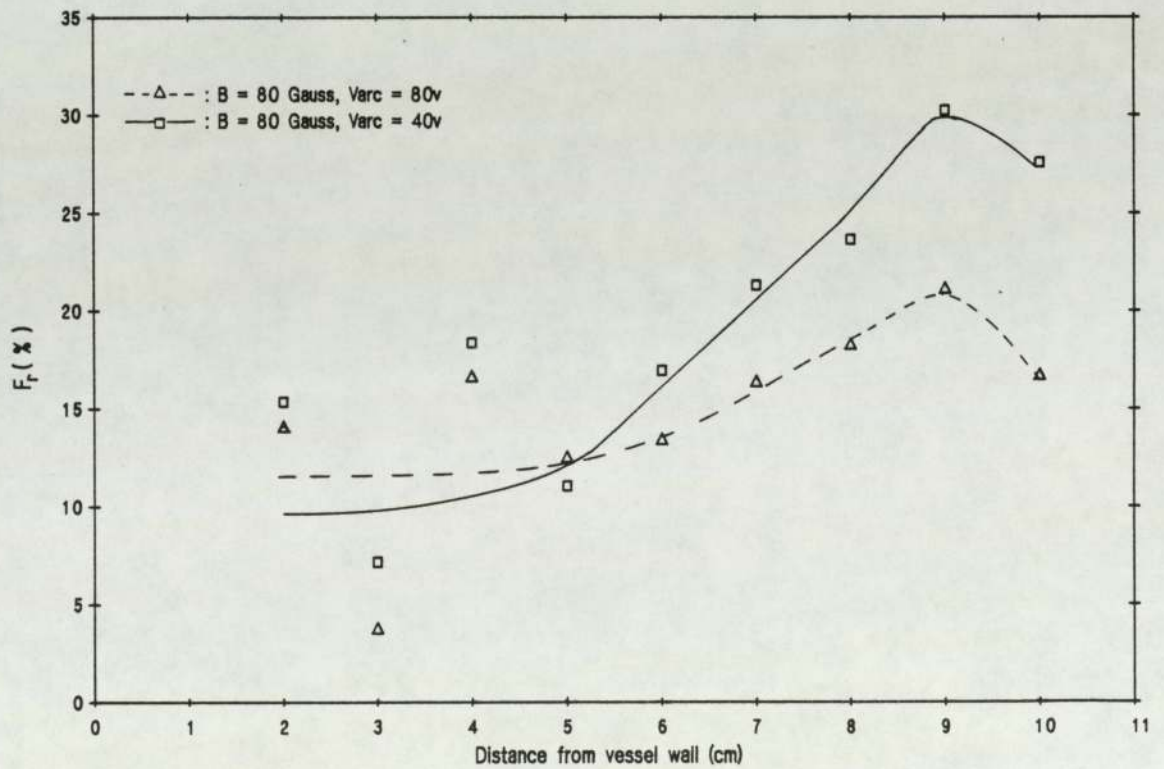


Figure 5.26 Radial variation of H^- ion fraction
 $I_{arc} = 5A$ $Pres. = 3mT$

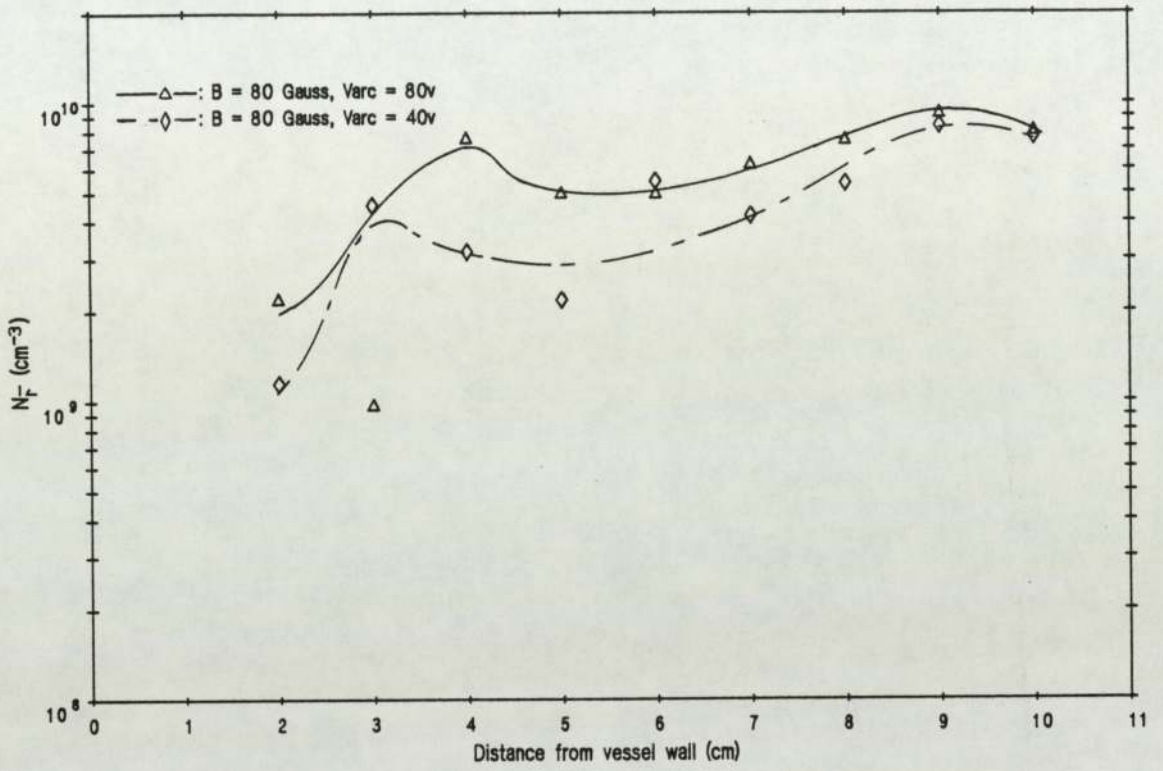


Figure 5.2.7 Radial variation of H^- ion density
 Iarc = 5A Pres. = 3mT

to the wall, the active-filter curve is nearly identical to that of the inactive-filter. Away from the wall, a constant 20% difference between the curves exists. Figure (5.2.6) shows the calculated H^- fraction for these results. Ignoring the region close to the wall, the $V_{arc} = 80v$ case shows a rapid increase in F_r from the edge of the confinement field to the axis. A small peak of $F_r = 0.2$ exists near the axis of the source, falling to 0.12 at 4cm from the wall. Once again, the data obtained in the wall-field region ($< 4cm$) must be ignored. Data taken at half the arc voltage produces an identical curve with a definite increase in F_r of $\sim 50\%$. The radial negative ion distribution resulting from this is shown in figure (5.2.7). As may be seen, N_{-r} shows a shallow fall of 50% from the source axis to the edge of the confinement field for both voltages. Absolute values of N_{-r} in the 40v case are $\sim 70\%$ of those at 80V, despite the larger F_r value.

Summary - spatial N_{-r} variation

The principal observations made in this section are as follows:

1. The axial variation in F_r shows the dramatic rise caused by the filter field. The maximum value of F_r is not reached until after the peak of the filter field at 10.5cm from the BFE. However, the axial variation of N_{-r} peaks at ~ 11 cm from the BFE, 2cm inside the

30-gauss contour of the field closest to the driver. The variation in F_r shows an approximate plateau once past the filter, whereas the N_{-r} variation falls in a shallow exponential. The axial N_{-r} variation shows a peak value of N_{-r} in the 3mT discharge of $4.5 \times 10^9 \text{ cm}^{-3}$. A value of $N_{-r} = 3 \times 10^9 \text{ cm}^{-3}$ appears in the driver region. This is due mainly to the effect of the high driver density and ratio scatter on the diagnostic technique, the fractional density of H^- ions in this region probably being insignificant.

2. The transverse variation of F_r is constant from the confinement field edge to the axis. The axial N_{-r} variation shows N_{-r} doubling over the same distance. A lower arc voltage increases F_r , but the corresponding N_{-r} curve is actually lower.

5.2.1.2 Arc parameter variation

This subsection covers the variation in negative ion density as a function of the arc parameters. Experimental conditions and methods correspond to those described in section 5.1.2.

5.2.1.2.1 Arc current variation

Figure (5.2.8) shows the ratio R as a function of I_{arc} in the driver and extraction regions of the variable-filter source. As may be seen, R is invariant with arc current over the measured range in both regions, despite the scatter around the low-current area. The extraction region values are some 70% of those in the driver region. Figure (5.2.9) shows the variation of F_r obtained from this data, F_r displaying no dependence on I_{arc} . The extraction region yields a value for F_r of ~ 0.2 . The H^- ion density variation in the extraction region corresponding to this is shown in figure (5.2.10). This shows a linear increase of over an order of magnitude in N_{-r} with I_{arc} over this range.

5.2.1.2.2 Arc voltage variation

Figure (5.2.11) shows R as a function of arc voltage at four positions within the variable-filter source. In the driver region, R falls slightly when $V_{arc} > 80v$. Elsewhere, a very slight linear increase in R with V_{arc} is visible. The fractional density variation resulting from this is shown in figure (5.2.12). The results show values of $F_r \sim 0.05, 0.07$

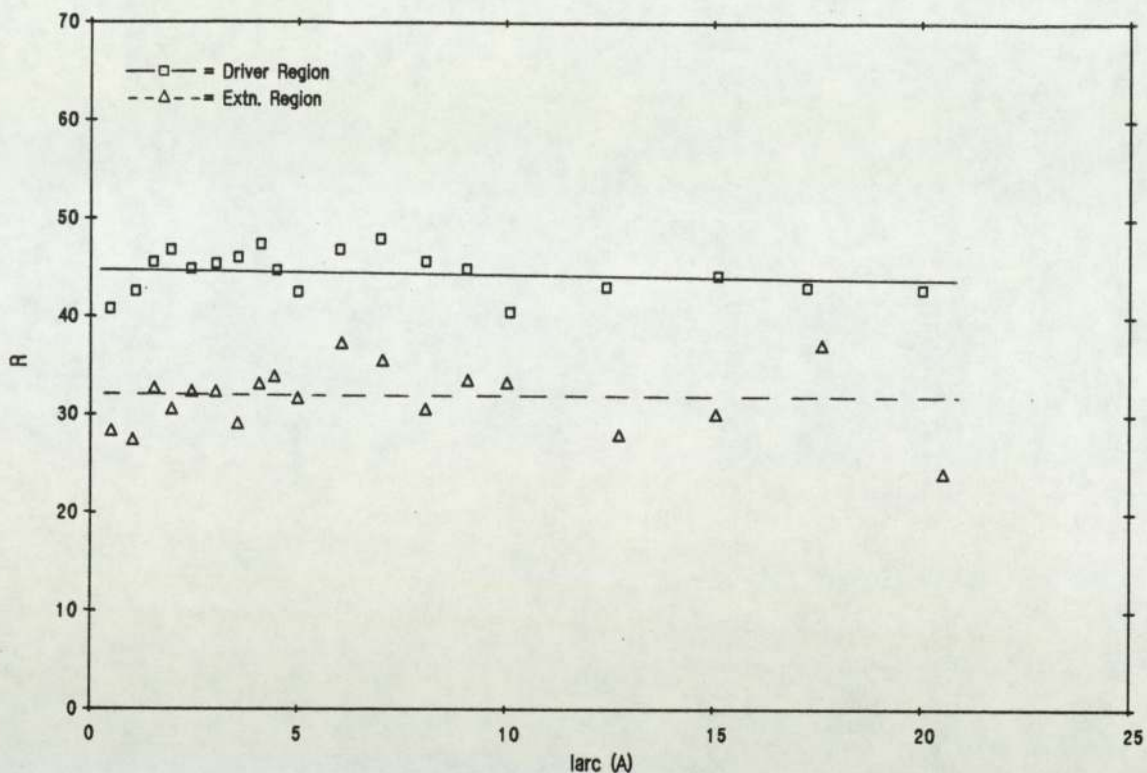


Figure 5.2.8 Variation of probe ratio with arc current
 Varc = 60v Pres. = 3mT B = 80 gauss

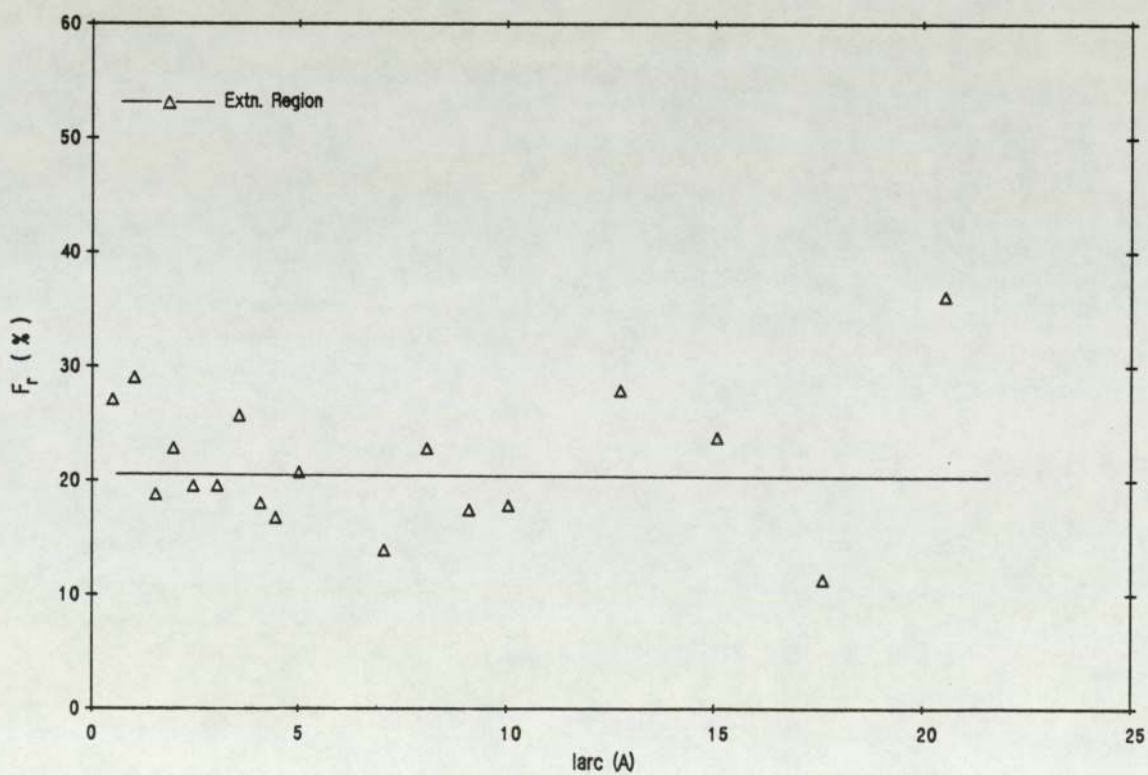


Figure 5.2.9 Variation of H⁻ ion fraction with arc current
 Varc = 60v Pres. = 3mT B = 80 Gauss

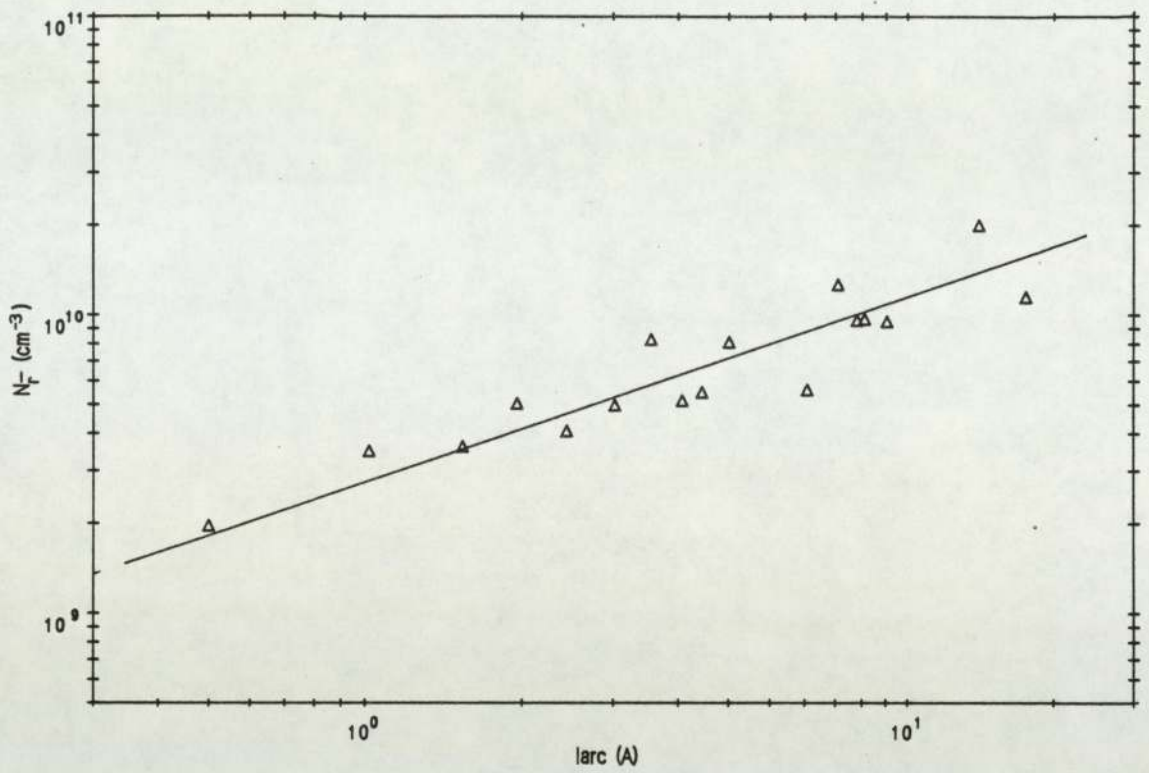


Figure 5.2.10 Variation of H^- ion density with arc current
 $V_{arc} = 60v$ Pres. = 3mT B = 80 Gauss

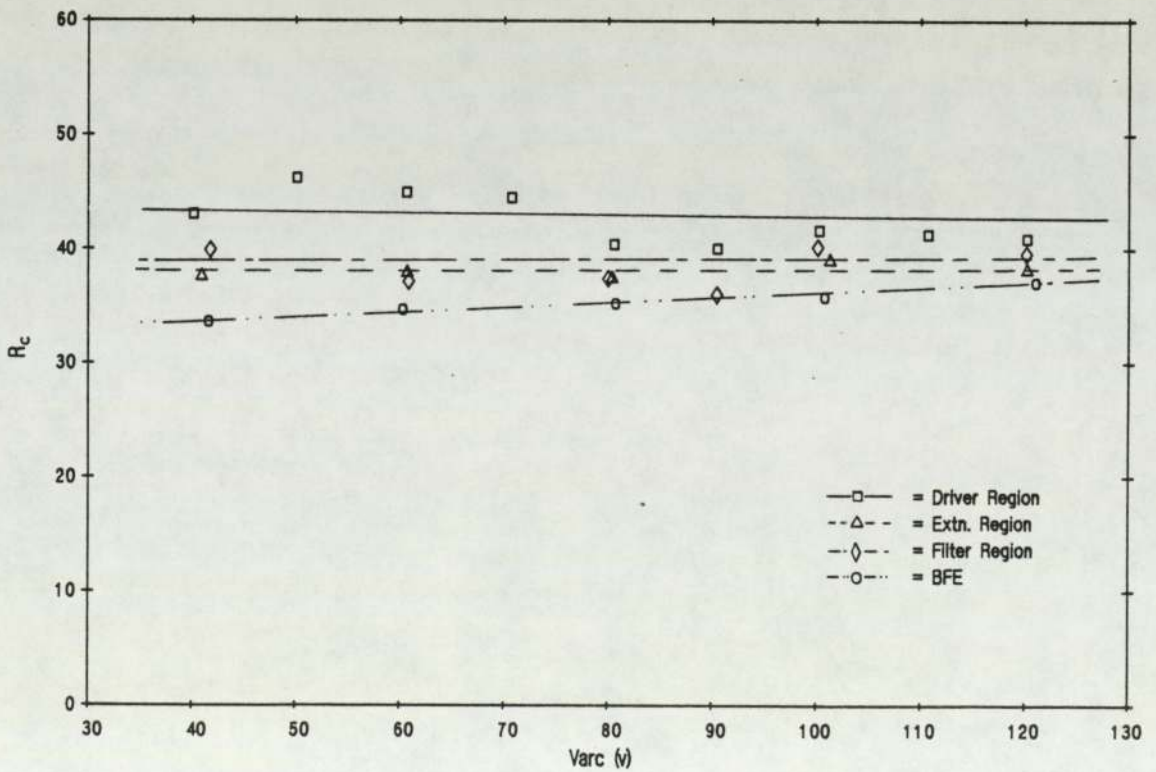


Figure 5.2.11 Variation of probe ratio with arc voltage
 $I_{arc} = 5A$ Pres. = 3mT B = 80 Gauss

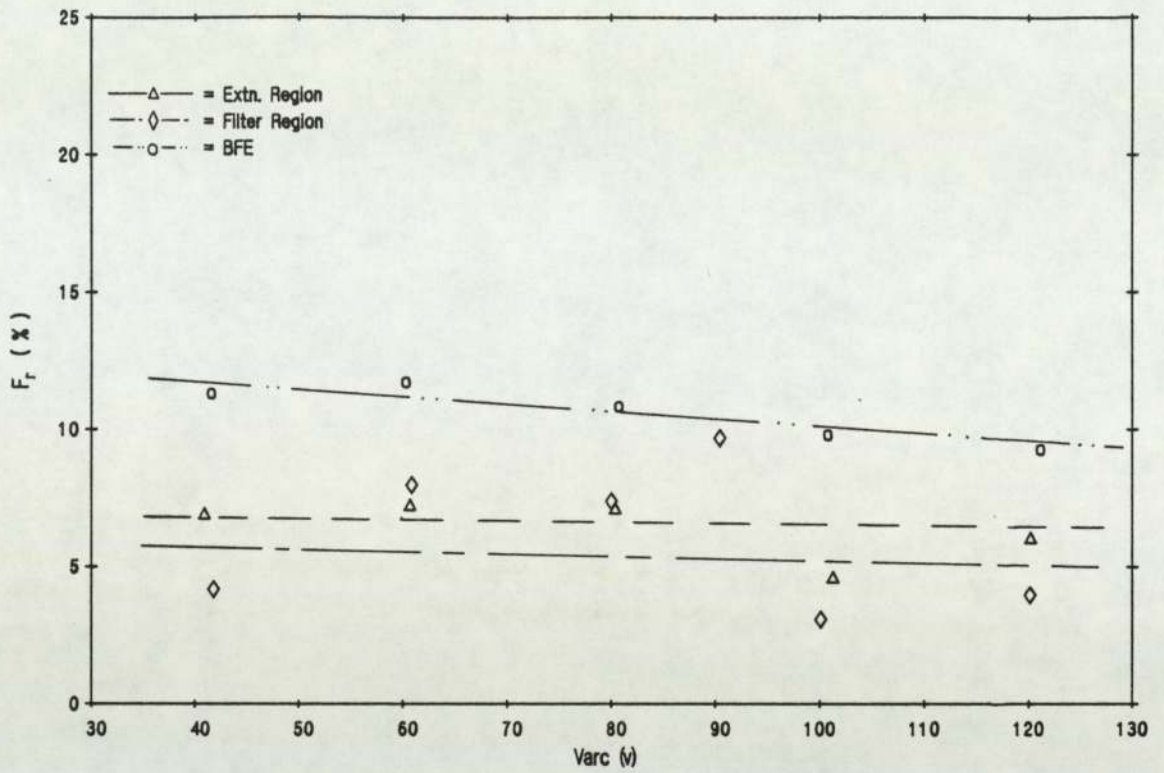


Figure 5.2.12 Variation of H⁻ ion fraction with arc voltage
I_{arc} = 5A Pres. = 3mT B = 80 Gauss

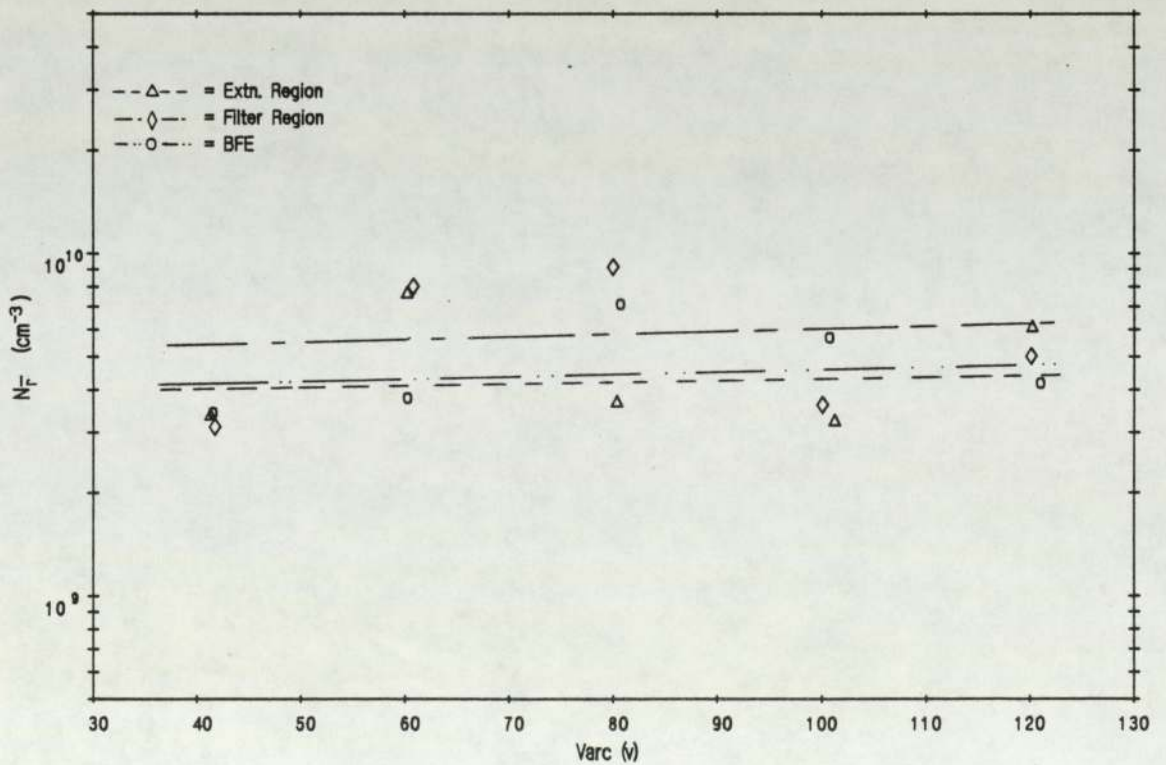


Figure 5.2.13 Variation of H⁻ ion density with arc voltage
I_{arc} = 5A Pres. = 3mT B = 80 gauss

and 0.11 respectively. These are approximately invariant with V_{arc} . The corresponding variation in N_{-r} is shown in figure (5.2.13). N_{-r} appears to be approximately invariant with V_{arc} over the measured range.

5.2.1.2.3 Pressure variation

Figure (5.2.14) shows the ratio R as a function of source filling pressure. Results from the driver region of the variable-filter source show no variation with pressure. The filter region shows a slight but steady fall $\sim 15\%$ below the driver region curve. The extraction region also shows a fall. The fractional densities calculated from these results are shown in figure (5.2.15). In the filter region of the variable filter source F_r increases with pressure from 0.07 to 0.1 in a linear fashion. In the extraction region, F_r shows a slight increase up to $\sim 7mT$, followed by a gradual fall. The N_{-r} variation corresponding to this data can be seen in figure (5.2.16). In both the extraction and filter region cases N_{-r} increases with pressure in a saturation-type curve. This is most easily seen in the filter region where a 3-fold increase in N_{-r} occurs over the initial $5mT$ increase in pressure.

5.2.1.2.4 Filter field variation

The variation in R at four positions in the variable-filter source is shown in figure (5.2.17). In the driver region, R is invariant with B over the entire range.

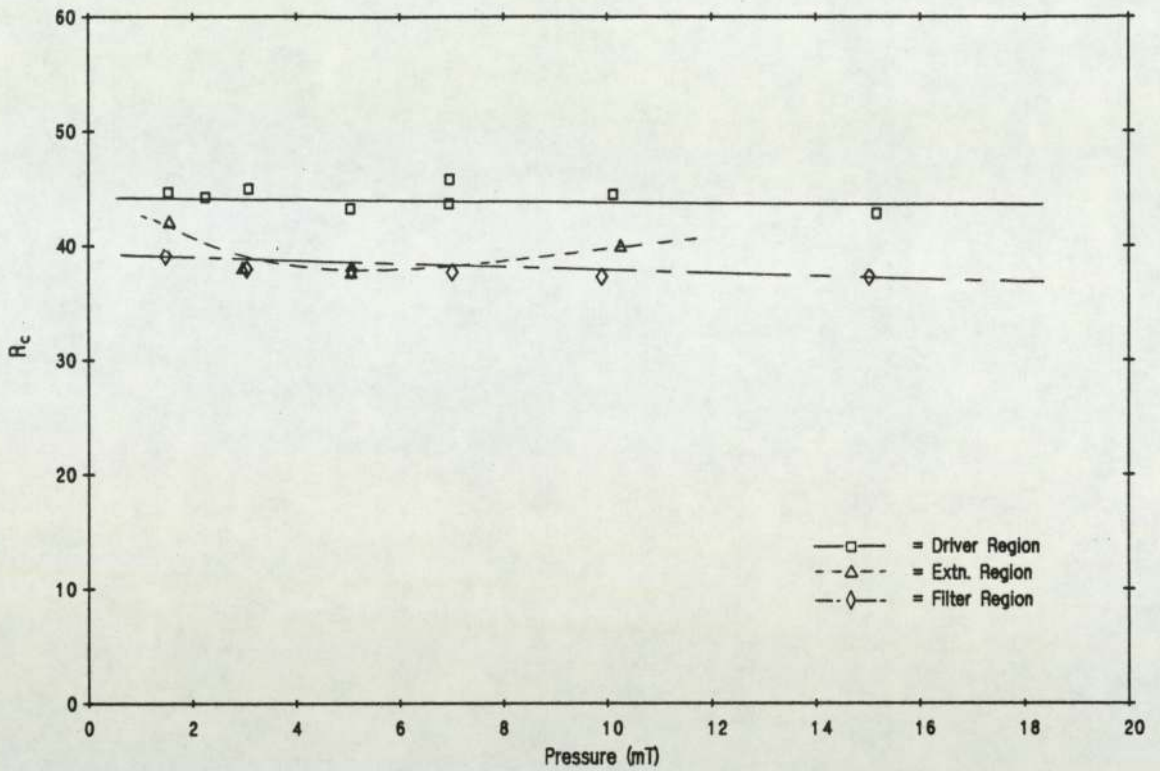


Figure 5.2.14 Variation of probe ratio with pressure
 Iarc = 5A Varc = 60v B = 80 Gauss

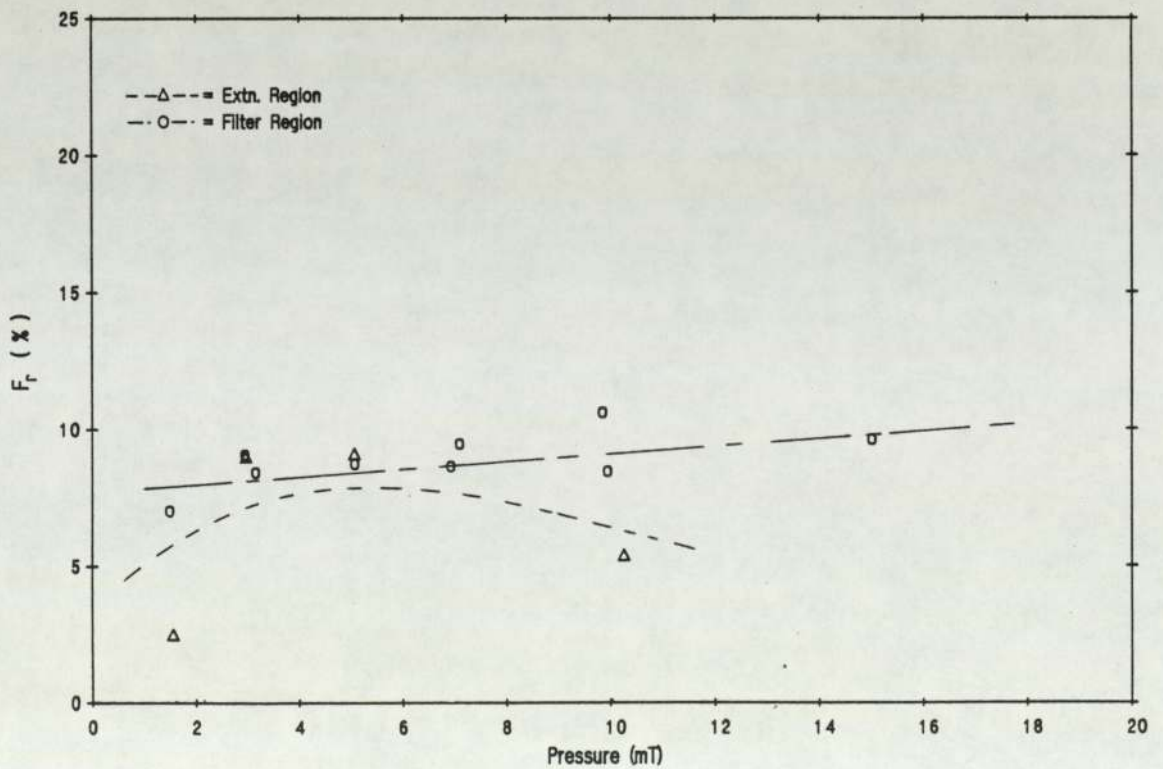


Figure 5.2.15 Variation of H⁻ fraction with pressure
 Iarc = 5A Varc = 60v B = 80 Gauss

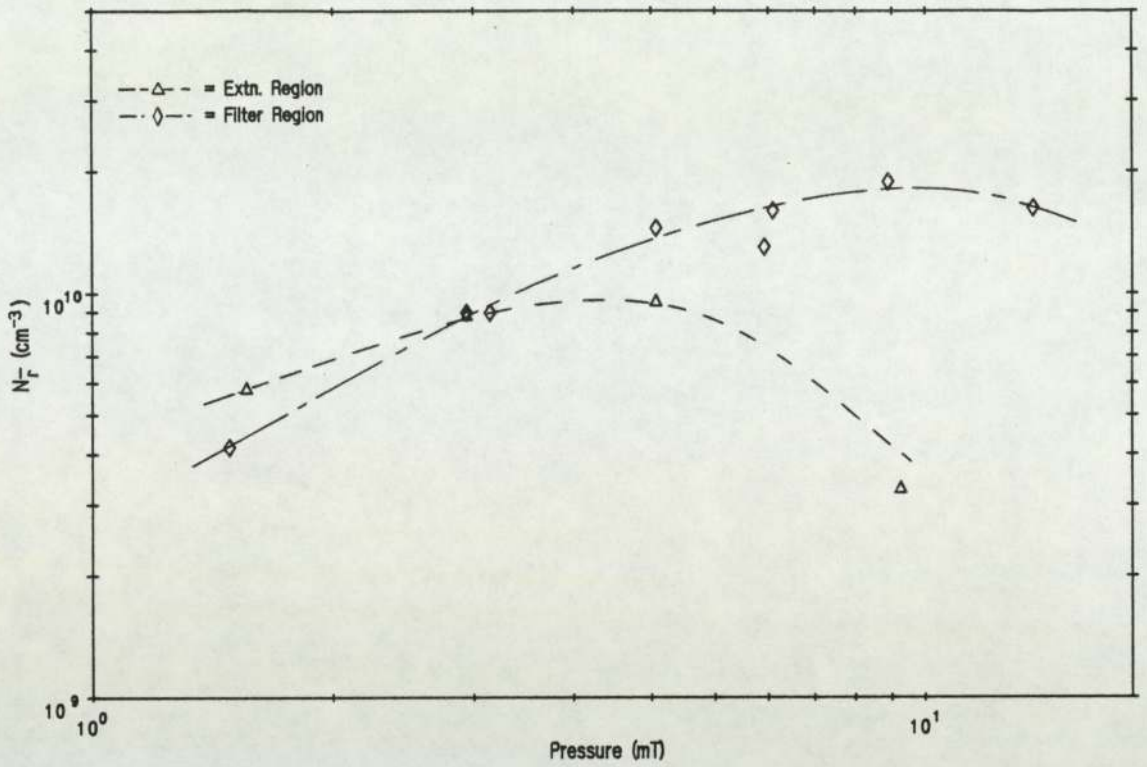


Figure 5.2.16 Variation of H^- ion density with pressure
 $I_{arc} = 5A$ $V_{arc} = 60v$ $B = 80$ Gauss

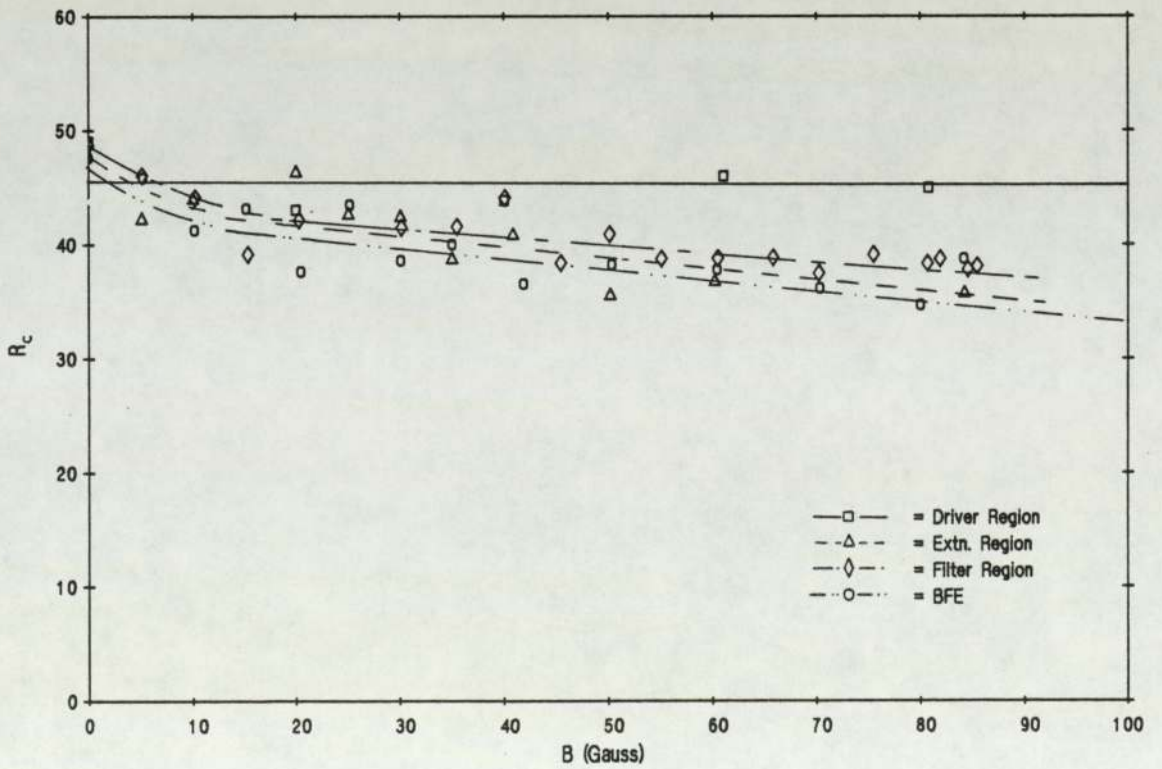


Figure 5.2.17 Variation of probe ratio with filter intensity
 $I_{arc} = 5A$ $V_{arc} = 60v$ $Pres = 3mT$

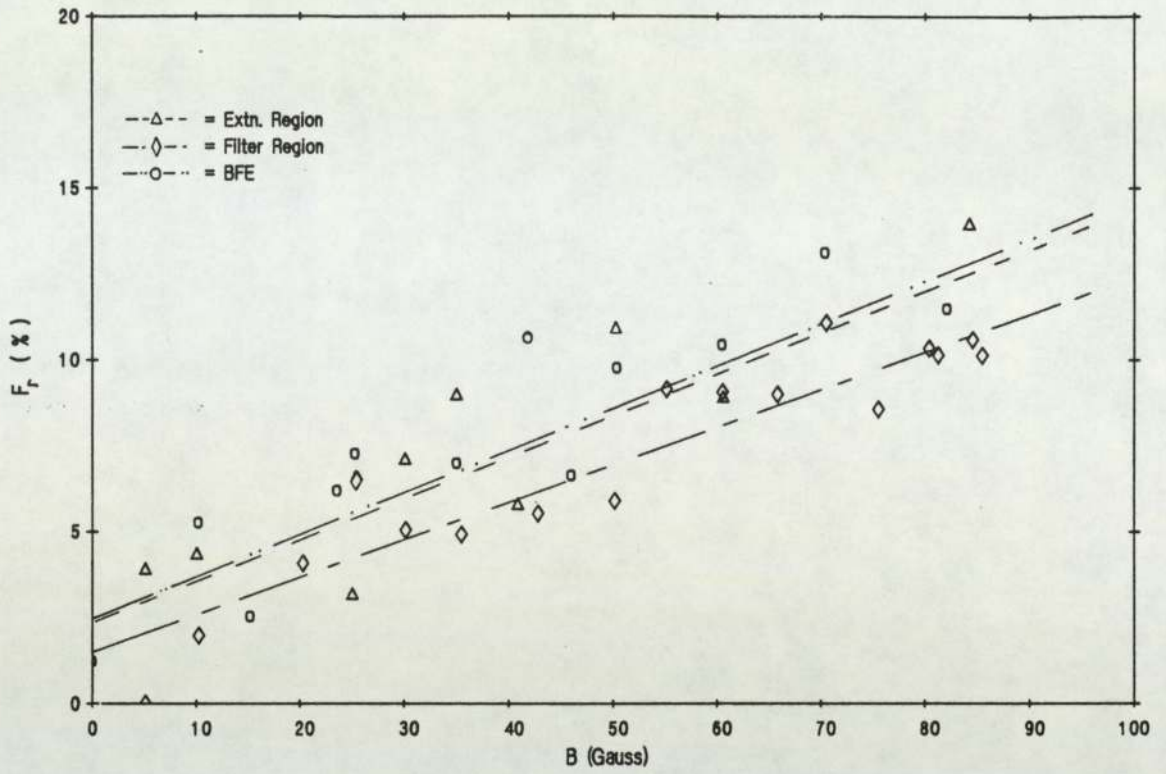


Figure 5.2.18 Variation of H^- ion fraction with filter intensity
Iarc = 5A Varc = 60v Pres = 3mT

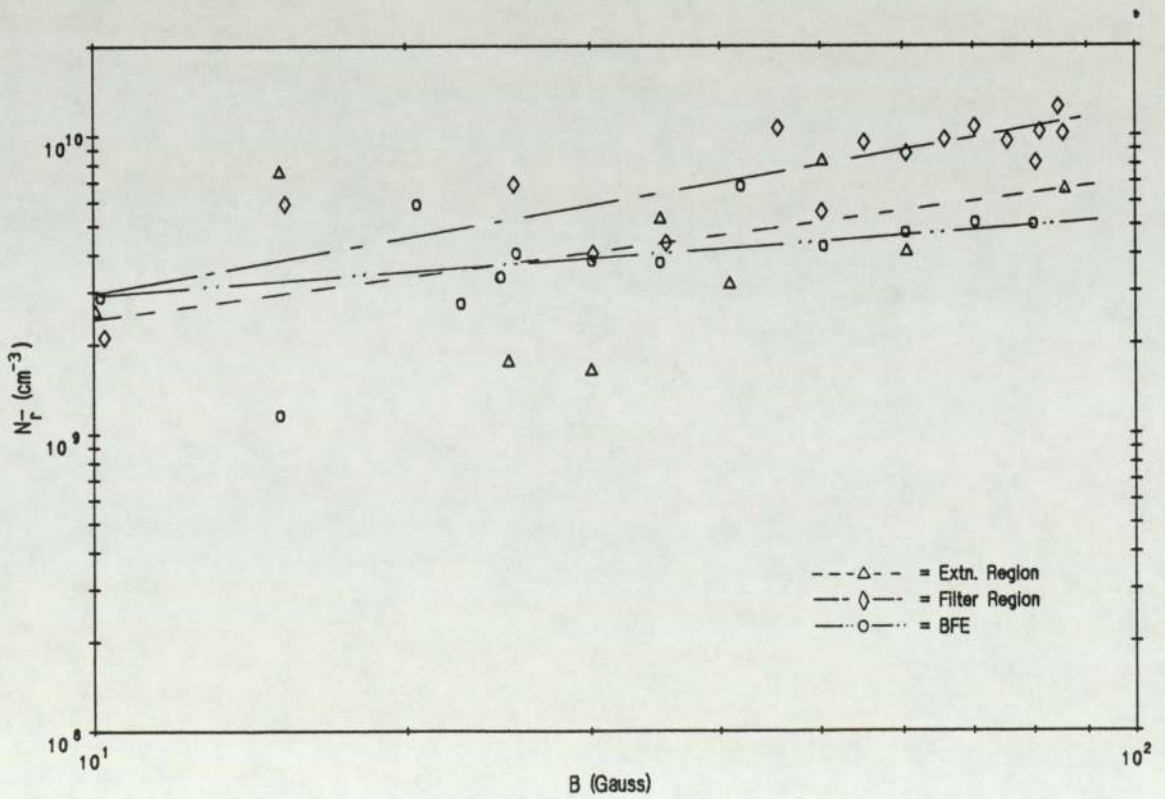


Figure 5.2.19 Variation of H^- ion density with filter intensity
Iarc = 5A Varc = 60v Pres = 3mT

In all the other three regions, R shows a slow linear fall with B, reaching a value ~18% below that in the driver region. The F_r values calculated from this are shown in fig. (5.2.18). All of the non-driver results exhibit a linear increase with B, to a value of ~ 0.1 at 80 gauss. In figure (5.2.19) the corresponding N_{-r} variation may be seen. In all regions except the driver, N_{-r} shows a slow linear increase with B. The gradient of this line is largest at the filter.

5.2.1.2.5 Summary - arc parameter variation

The main observations of H^- behavior outside the driver region from these experiments may be summarized as follows;

1. F_r is invariant with I_{arc} . N_{-r} increases in a linear fashion with I_{arc} .

$$N_{-r} \propto I_{arc} \quad \dots (5.2.1)$$

2. Both F_r and N_{-r} are approximately invariant with V_{arc} . There is some evidence of a slight fall in both when $V_{arc} > 80v$.

3. F_r and N_{-r} increase with pressure, N_{-r} in a saturation curve. The degree of saturation varies with arc conditions.

$$N_{-r} \propto P^\eta, \quad \eta < 1 \quad \dots (5.2.2)$$

4. F_r and N_{-r} increase in a linear fashion with B

$$N_{-r} \propto B \quad \dots(5.2.3)$$

5.2.1.3 Bias potential variation

This subsection covers N_{-r} data obtained by varying the bias potential of the BFE. Experimental conditions correspond to those of section 5.1.3.

Figure (5.2.20) shows the variation of R as a function of bias voltage at two positions within the variable-filter source. In the driver region, R is invariant at ~ 45 with V_{bias} , save for a fall at highly-negative potential. In the extraction region, R falls sharply with V_{bias} from its zero-bias value of 35 to a minimum of 15 at +5v. R also falls with negative bias, although the magnitude of the fall is much smaller. At the BFE, this behavior is repeated to a slightly greater extent. The variation in F_r calculated from this data may be seen in figure (5.2.21). F_r shows a very rapid increase with positive bias, from ~ 0.16 to ~ 0.6 in the case of the extraction region. This appears to saturate quite sharply at $V_{bias} = +2$ volts. Negative bias produces a smaller linear rise in F_r , doubling at $V_{bias} = -20v$. Figure (5.2.22) shows the corresponding N_{-r} variation. N_{-r} appears to fall with + V_{bias} to slightly less than half the zero-bias value over the range 0 - +2v. N_{-r} shows a gradual increase with negative bias, doubling over the range 0 to -25v.

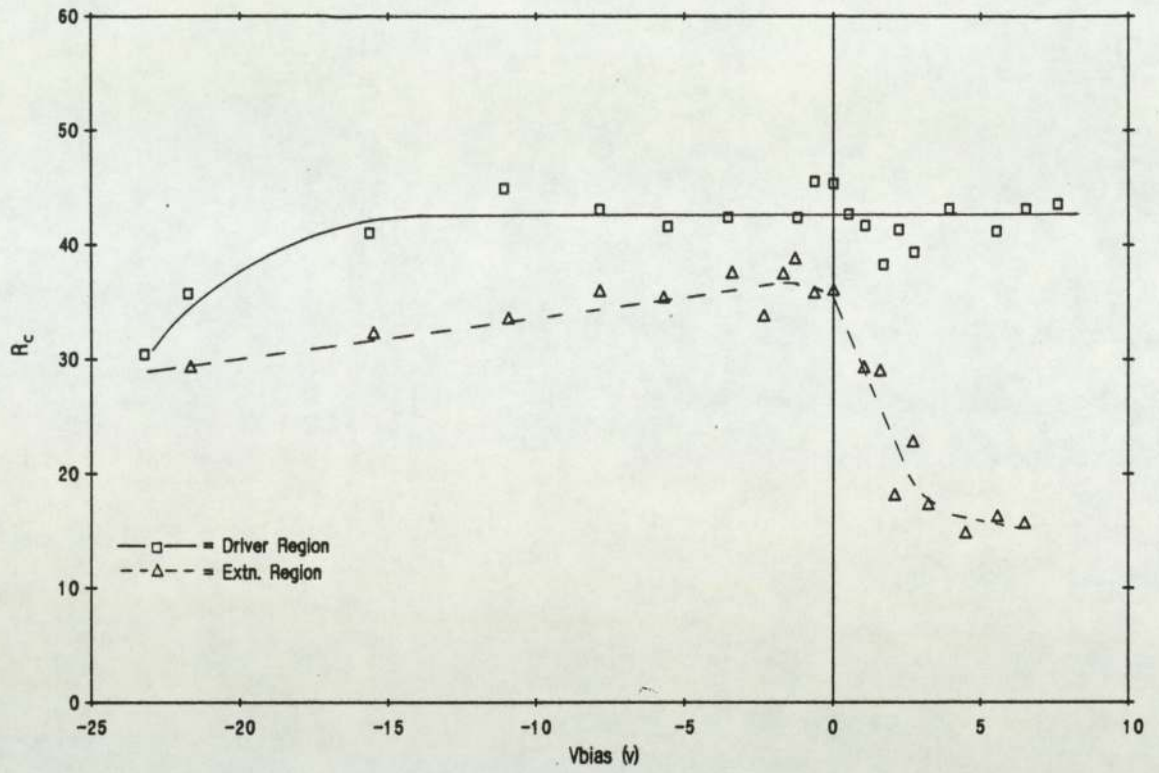


Figure 5.220 Variation of probe ratio with bias voltage
 I_{arc} = 5A V_{arc} = 60v Pres = 3mT B = 80 Gauss

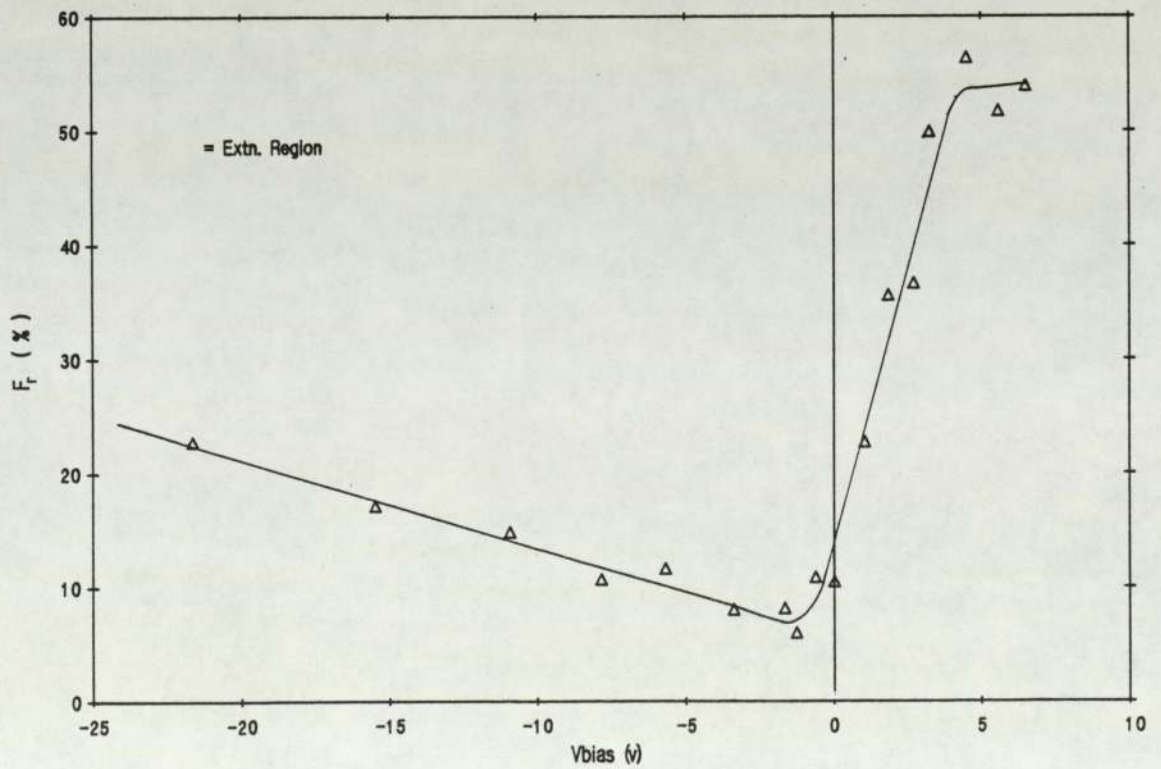


Figure 5.221 Variation of H⁻ ion fraction with bias voltage
 I_{arc} = 5A V_{arc} = 60v Pres = 3mT B = 80 Gauss

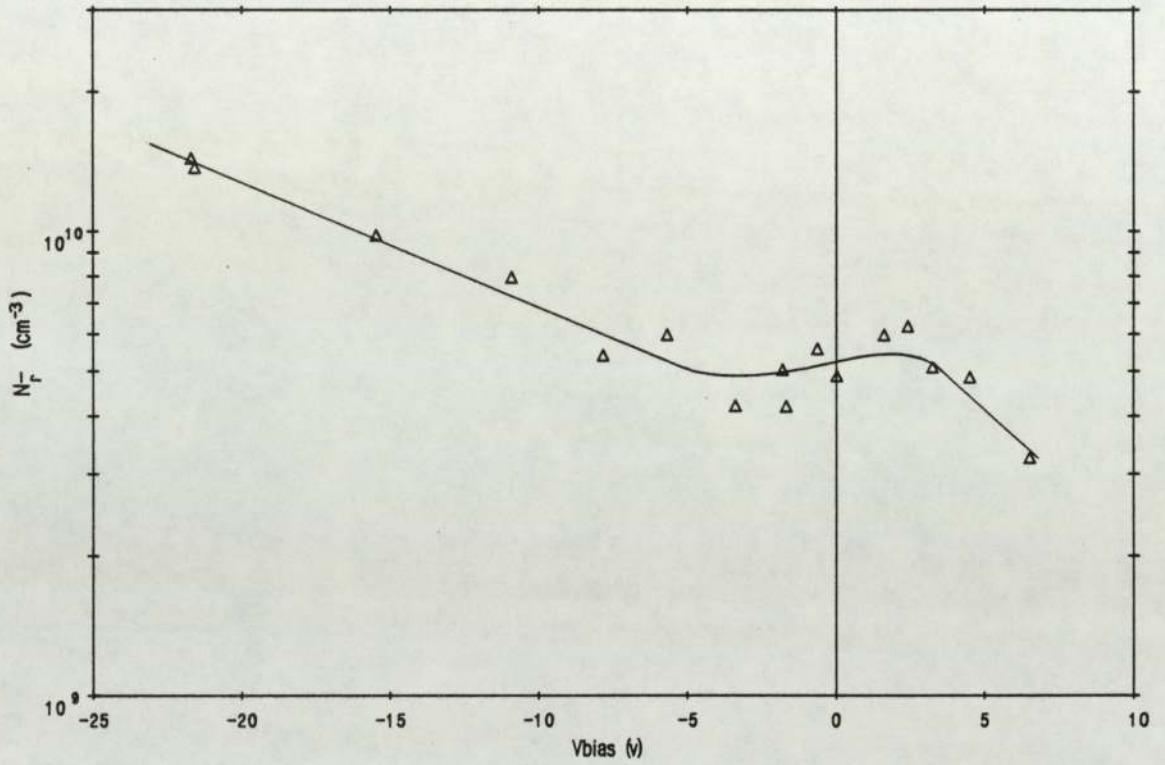
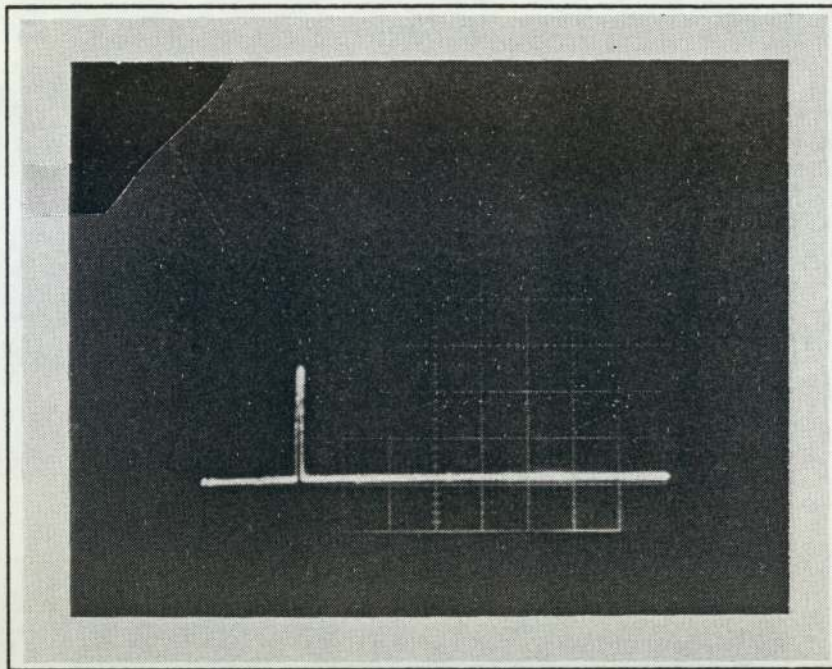


Figure 5.2.22 Variation of H^- ion density with bias voltage
 $I_{arc} = 5A$ $V_{arc} = 60v$ $P_{res} = 3mT$ $B = 80$ Gauss

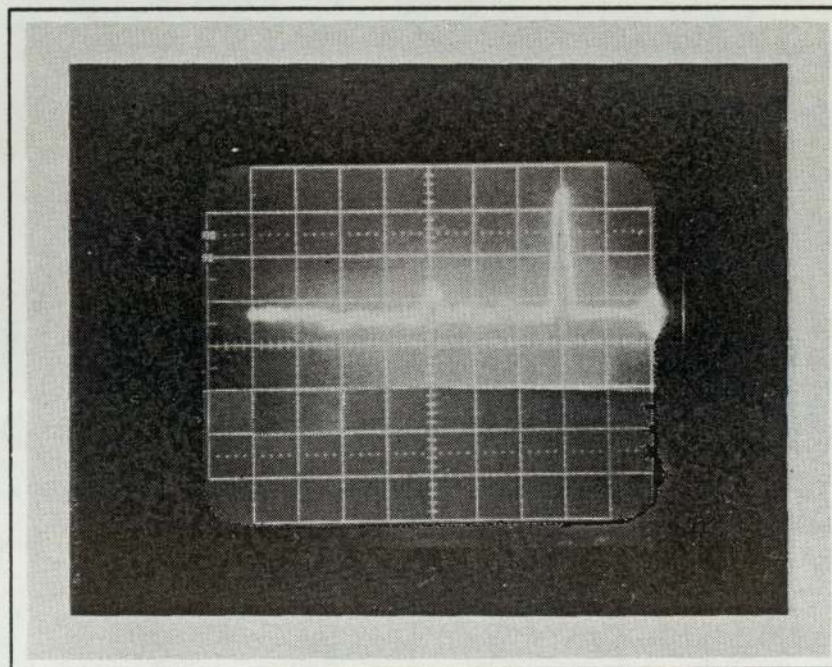
5.2.2 Beam-extraction data

This section presents measurements of J_- and J_e obtained by beam extraction from the fixed-filter source using the Culham 30kV accelerator and beamline. The beam of negative ions thus obtained was directed so as to strike the calorimeter assembly at the end of the beamline. As mentioned in section 3.2.2, this could be used either as a set of Faraday plates or the watercooled centre sections could be used as true power calorimeters, with a long (~ 40 sec) response time. Due to the stripping of H^- ions in collisions with gas molecules in the beamline, and the thermal limit on continuous source operation at high power it proved necessary to use both functions. At low arc currents, the Faraday plates were used in conjunction with the power calorimeter to obtain a correction factor for the degree of stripping as a function of source and tank pressures. This enabled the use of the fast-response Faraday plate system at higher pressures, up to a maximum of $\sim 19mT$ determined by the errors caused by the stripping factor.

Secondary electron emission from the plates was avoided by biasing the assembly $\sim 20v$ positive with respect to the tank. The collection of plasma formed in the beamline by the extracted beam was prevented by applying a 20-gauss magnetic field across the calorimeter assembly using the Helmholtz coils shown in figure (3.2.4). Mass analysis of a beamlet allowed to pass beyond the calorimeter produced no trace of an electron peak, as shown in figure (5.2.23). The H^- peak



(a) Trace obtained from negative ion beam
1.0A 90V 7.8mT discharge, $V = 27$ kV



(b) Trace obtained from positive ion beam
1.0A 90V 5mT discharge, $V = 16.8$ kV

Figure 5.2.23 Mass analysis of the extracted beam

can clearly be seen here, proving that the beam reaching the calorimeter is for all practical purposes composed entirely of H^- ions. No sign of an impurity peak is visible. Variation of the magnetic field across the calorimeter assembly produced no variation in collected current, confirming the absence of a full-energy electron beam at the calorimeter. The results of mass analysis of a positive ion beam extracted from the same system may also be seen in figure (5.2.23). Despite the truly appalling beam quality obtained from the extraction system, the dominance of H_3^+ ions in the fixed-filter source may be easily seen.

The H^- current densities presented in the following section are those obtained from Faraday-plate measurements corrected for stripping using the correction factor described above. The electron current densities are obtained from the drain current of the second grid supply, and represent the fraction of the electron current extracted from the source striking the second grid, estimated to be $\sim 90\%$ of the total extracted electron current. Current densities are presented as such, rather than particle number densities, as the relationship between the two is indeterminate; the collection of negative particles is certainly not random as in the case of probes, and no data is available regarding the negative ion velocity in the small Culham sources. v_- data from the large Culham H^- source [100] obtained from simultaneous probe and extraction measurements is of little help, as a strong dependence of v_- on arc current is suggested by this for Iarc

< 300A, but no data is available in this region.

5.2.2.1 Spatial variation

Due to the nature of the experimental assembly, spatially resolved data obtained by beam extraction from the fixed filter source is very limited. As mentioned in section 2.2.2, the position of the extraction aperture within the source could be adjusted, with some effort, by the reassembly of the accelerator stack with enlarged spacing modules. In effect, due to the size of the electrodes, this shifted the position of the entire beam-forming electrode. As a non-invasive diagnostic technique, this procedure left something to be desired. However, by this means, the axial position of the extraction aperture was altered to 12.5 cm from the backplate, 7.5cm closer than previously and just beyond the filter position. Data is thus available for two positions on the axis. This shows that the extracted H^- current density (J_-) increases by $\sim 50\%$ over this distance, and the extracted electron flux (J_e) by a factor of 2.

5.2.2.2 Arc parameter variation

Arc parameters were adjusted in the same fashion as for the probe experiments described in section 5.2.1. The results are presented in sections 5.2.2.2.1 through 5.2.2.2.4

5.2.2.2.1 Arc current variation

Figure (5.2.24) shows J_- as a function of I_{arc} for several different pressures. As may be seen, J_- follows a saturation curve in all cases. The exact shape depends upon the operating pressure, higher pressures reducing the degree of saturation and increasing the arc current at which saturation begins. This onset value is a linear function of pressure. It should be noted that for $I_{arc} \leq 20A$ (typical in the variable-filter source) the onset of saturation is just visible only at the lowest pressure, and J_- has a similar value at all pressures. Figure (5.2.25) shows the corresponding electron current density as a function of arc current. I_e increases rapidly with I_{arc} , the rate of increase being a strong inverse function of pressure.

5.2.2.2.2 Arc voltage variation

Figure (5.2.26) shows J_- as a function of V_{arc} . A strong increase is apparent, up to ~ 100 volts. Beyond this, J_- begins to saturate. The corresponding I_e curve is shown in figure (5.2.27). I_e appears to increase in a much greater than linear fashion with V_{arc} , and shows no signs of saturation.

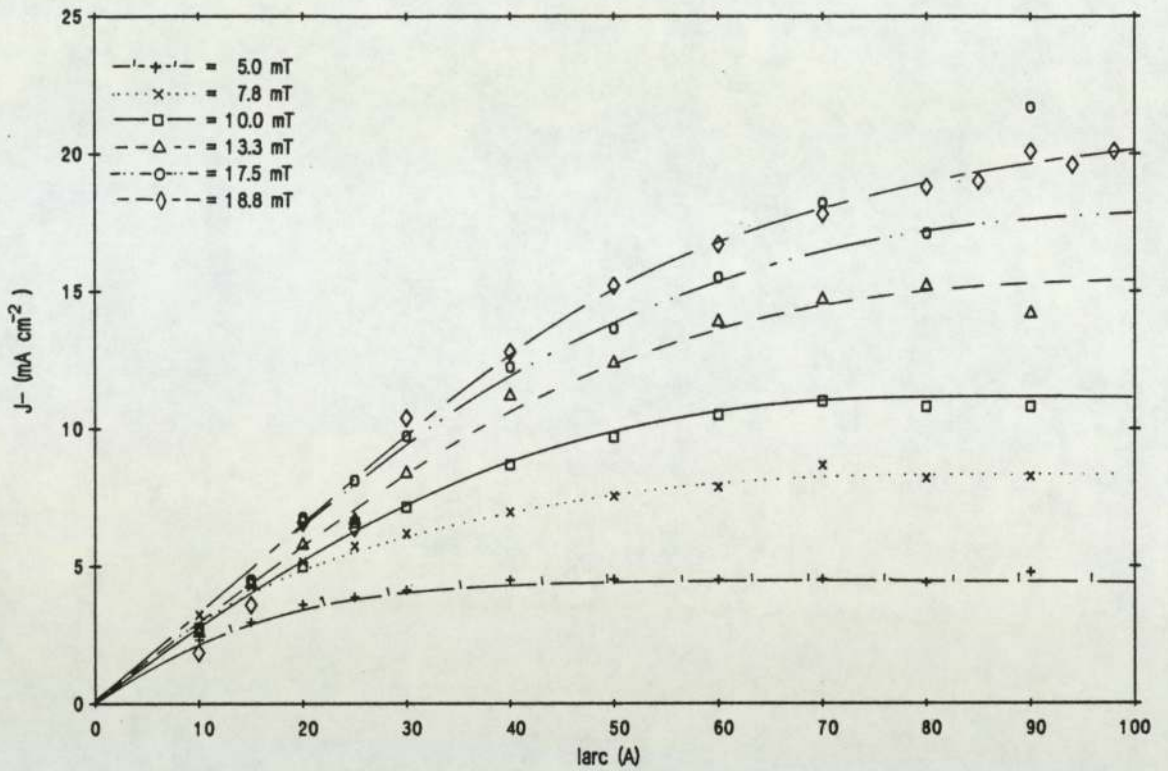


Figure 5.2.24 Variation of extracted H^- current density with larc

$V_{arc} = 90v$ $V_x = 27kV$ $V_{bias} = 0v$

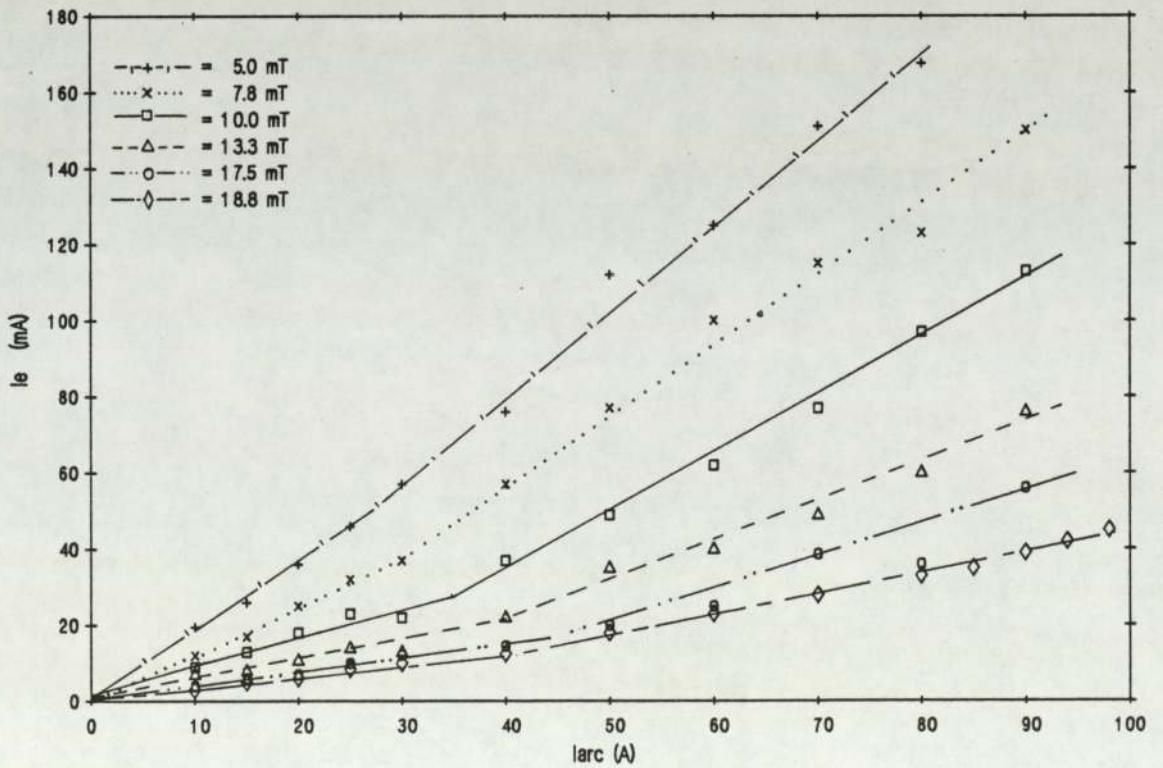


Figure 5.2.25 Variation of extracted electron current with larc

$V_{arc} = 90v$ $V_x = 27kV$ $V_{bias} = 0v$

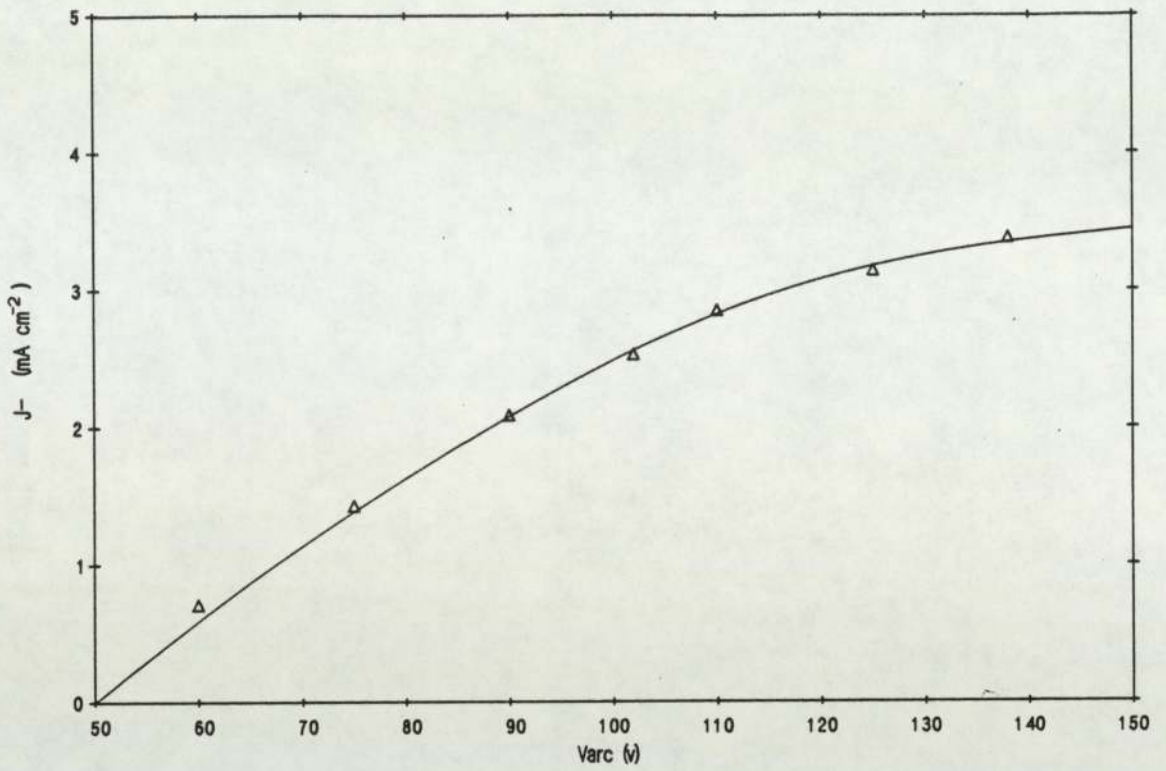


Figure 5.2.26 Variation of extracted H⁻ current density with arc voltage
 I_{arc} = 15 A Pres. = 18.8mT V_x = 27kV V_{bias} = 0v

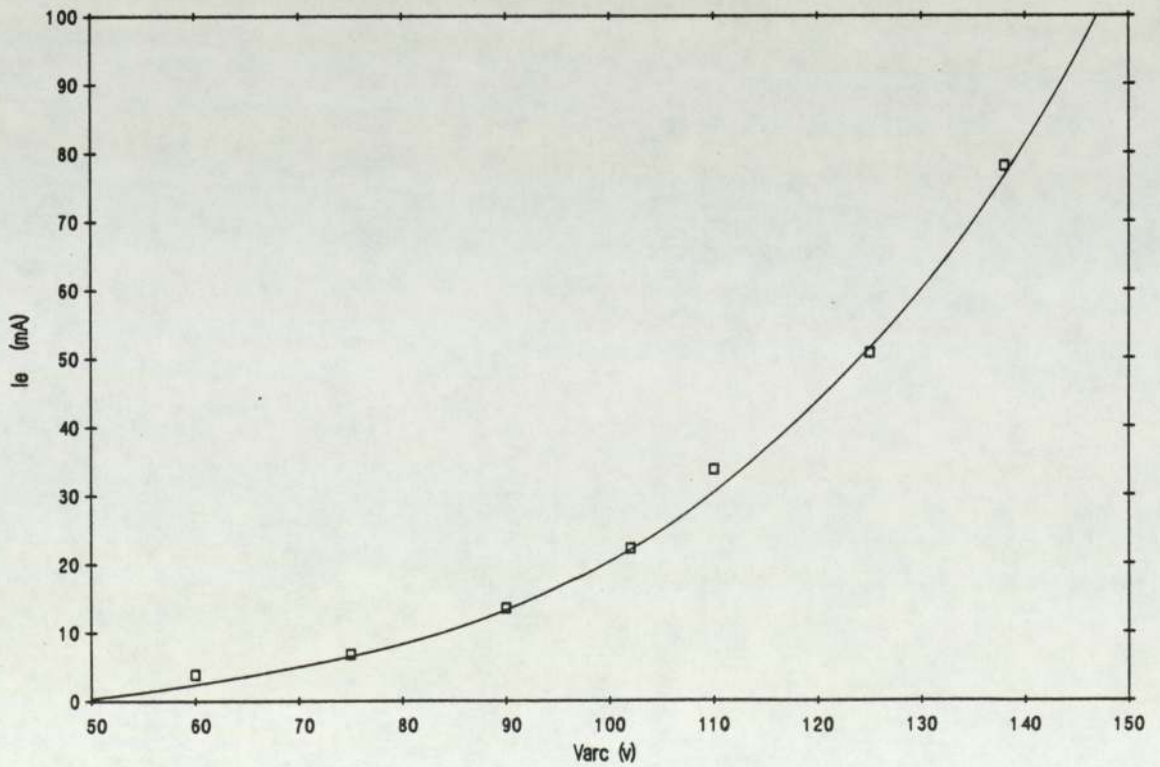


Figure 5.2.27 Variation of extracted electron current with arc voltage
 I_{arc} = 15 A Pres. = 18.8mT V_x = 27kV V_{bias} = 0v

5.2.2.2.3 Source pressure variation

The variation of J_- with pressure is shown in figure (5.2.28) for both the saturated ($I_{arc} = 80A$) and non-saturated ($I_{arc} = 20A$) arc current regimes. As may be seen, the rate of increase with pressure is much greater for the 80A case, the dependence being approximately linear. In the 20A case J_- saturates very quickly, becoming invariant with pressure at around 6mT. The corresponding electron currents are shown in figure (5.2.29). A rapid fall of I_e with pressure is obvious in both cases. Although the 20A values are understandably lower, the variation with pressure appears to be the same in both cases. Note that at the highest pressure, the extracted ion-electron ratio at 20A is approximately unity, falling to ~ 0.5 at 80A.

5.2.2.2.4 Filter field intensity variation

The strength of the filter-field could be varied somewhat even in the fixed-filter source by the addition of more external filter-position magnets on top of the first set. The increase in field obtained is shown in figure (3.2.2). With the extraction aperture in the extended position, the extracted negative ion and electron currents were measured using the calorimeter assembly for 0, 1, and 2 sets of extra filter magnets. The Helmholtz coils were active at 20 gauss for this experiment. The results are shown in figures (5.2.30) and (5.2.31). As may be seen,

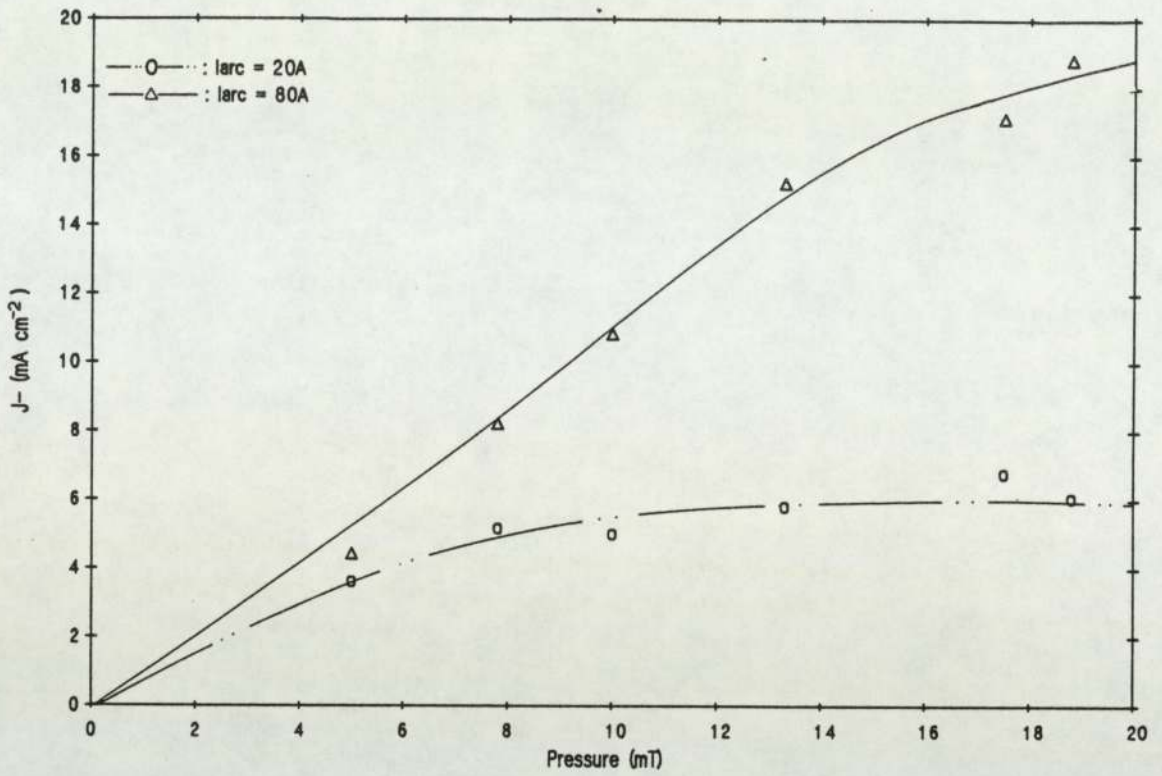


Figure 5.2.28 Variation of extracted H^- current density with pressure
 $V_{arc} = 90V$ $V_x = 27kV$ $V_{bias} = 0V$

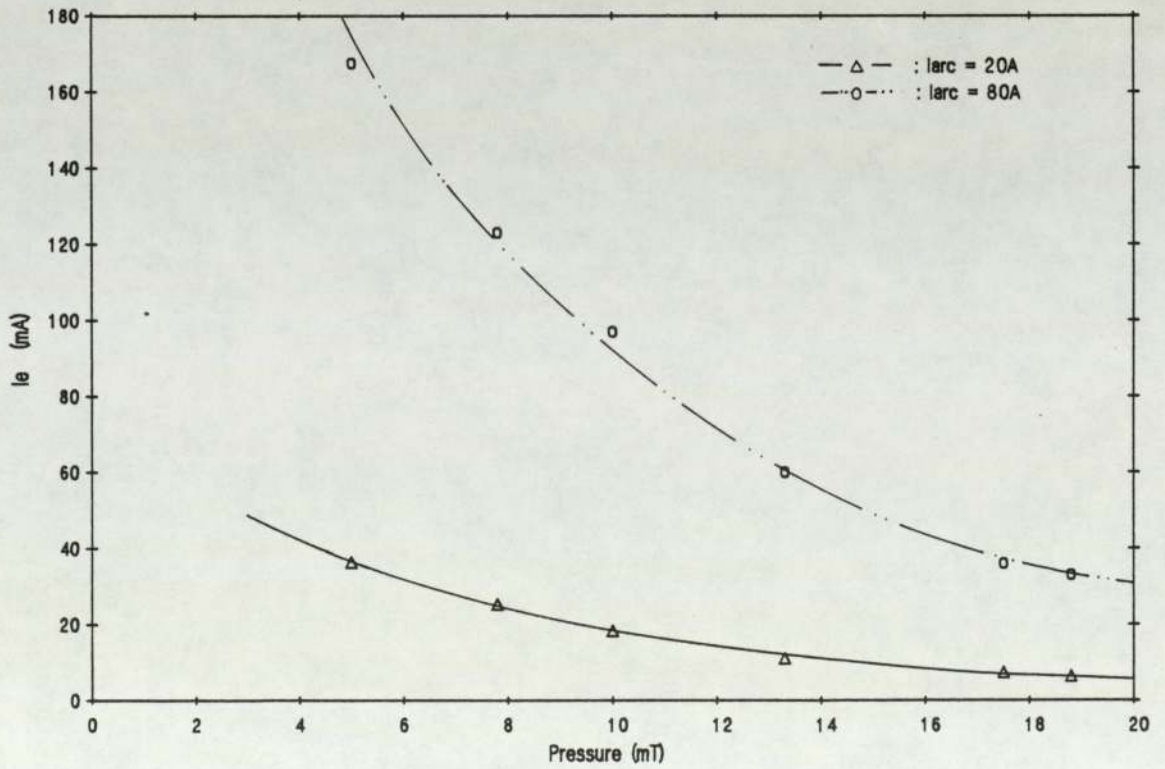


Figure 5.2.29 Variation of extracted electron current with pressure
 $V_{arc} = 90V$ $V_x = 27kV$ $V_{bias} = 0V$

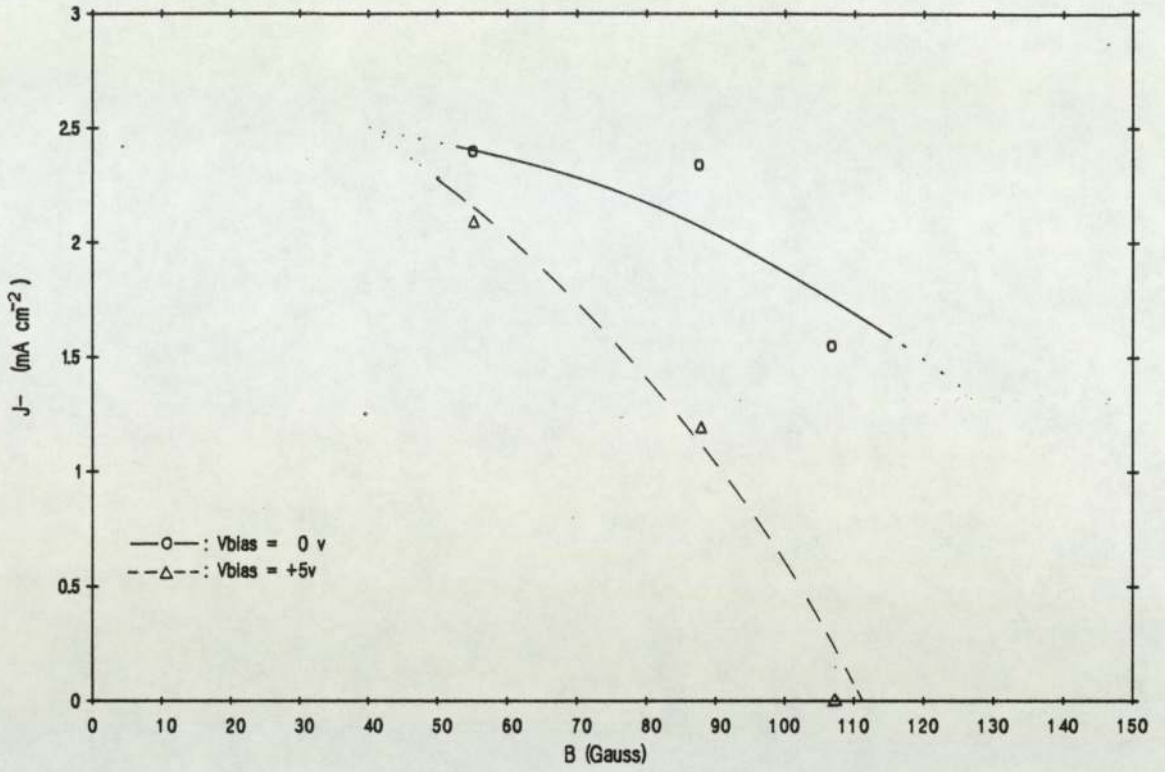


Figure 5.230 Variation of extracted H⁻ current density with filter intensity.
I_{arc} = 15A V_{arc} = 90v Pres. = 4mT V_x = 25kV

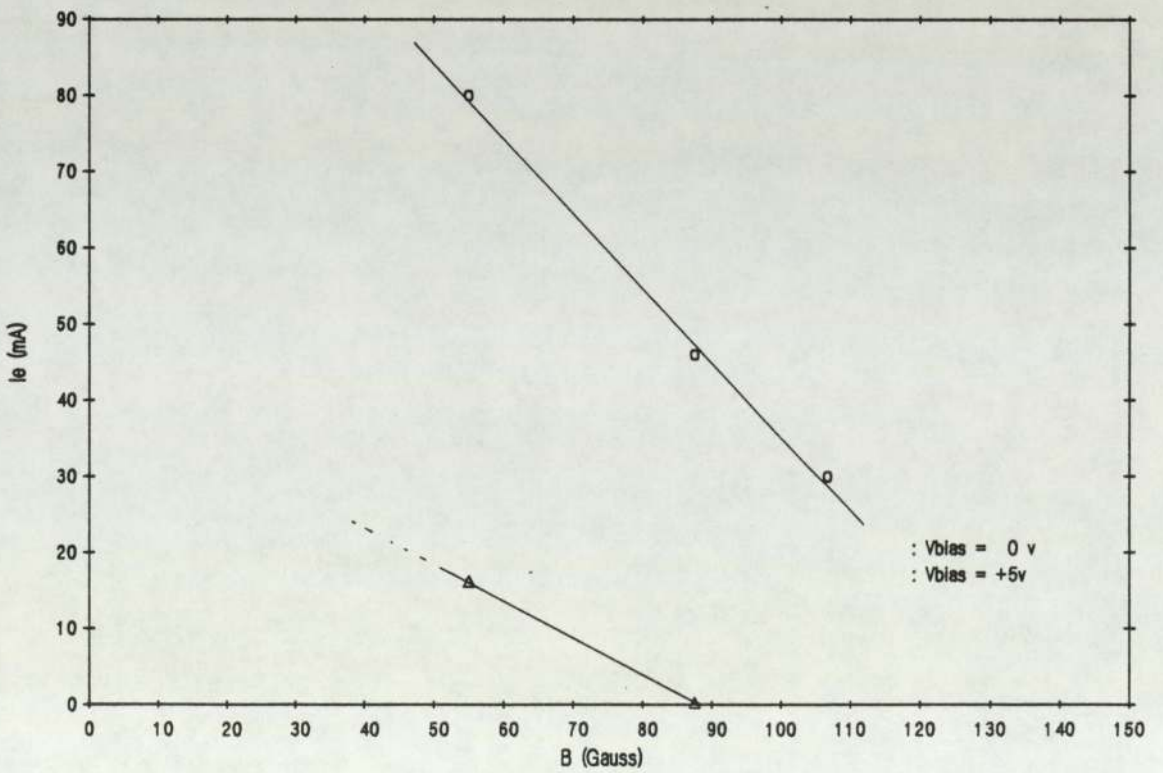


Figure 5.231 Variation of extracted electron current with filter intensity.
I_{arc} = 15A V_{arc} = 90v Pres. = 4mT V_x = 25kV

increasing the filter strength causes both the electron current and H^- ion current density to fall, I_e more rapidly than J_- . The first increment in B appears to provide a large fall in J_e for a small J_- penalty. The same experiment performed with a positive bias voltage of 5v on the BFE shows J_- falls much more rapidly with B than in the zero bias case, and conversely that V_{bias} has a larger effect on J_- at a higher filter strength.

5.2.2.2.5 Summary

Varying the arc parameters has the following effects:

1. The extracted J_- increases in a saturation curve with I_{arc} , saturation level being determined by pressure.

$$J_- \propto (I_{arc})^\eta, \quad \eta < 1 \quad \dots(5.2.4)$$

Electron current increases in a greater than linear fashion, and does not saturate.

2. J_- increases with V_{arc} in a saturation curve.

$$J_- \propto (V_{arc})^\eta, \quad \eta < 1 \quad \dots(5.2.5)$$

I_e increases at a much greater (almost cubic) rate, and shows no signs of saturation.

3. J_- increases linearly with pressure provided I_{arc} is set so that the source operates in the arc-current saturated region. At lower I_{arc} the pressure variation is very slight, and is itself saturated. I_e falls in a greater than linear fashion with pressure regardless of the I_{arc} value

4. Both J_- and J_e fall with increasing filter field, J_e faster than J_- . However, increasing the field causes J_- to be attenuated faster with increasing bias voltage.

$$J_- \propto -B \quad \dots(5.2.6)$$

5.2.2.3 Bias potential variation

Figure (5.2.32) shows I_- (here the extracted H^- ion current) and I_e as a function of positive bias potential. As can be seen, the electron flux is attenuated far more rapidly than the negative ion flux; at +1v the difference in attenuation factor is eight-fold, producing an order of magnitude fall in J_e for a 20% fall in I_- . In general, I_- falls slowly with bias potential in the range 0 to +2v. The extracted electron current falls exponentially over this range, although the rate reduces when $V_{bias} > 1.5v$.

Increasing I_{arc} requires an increase in V_{bias} to maintain the same attenuation factor. As noted above, an increase in the fractional H_- density reduces the useful preferential attenuation of the electron flux.

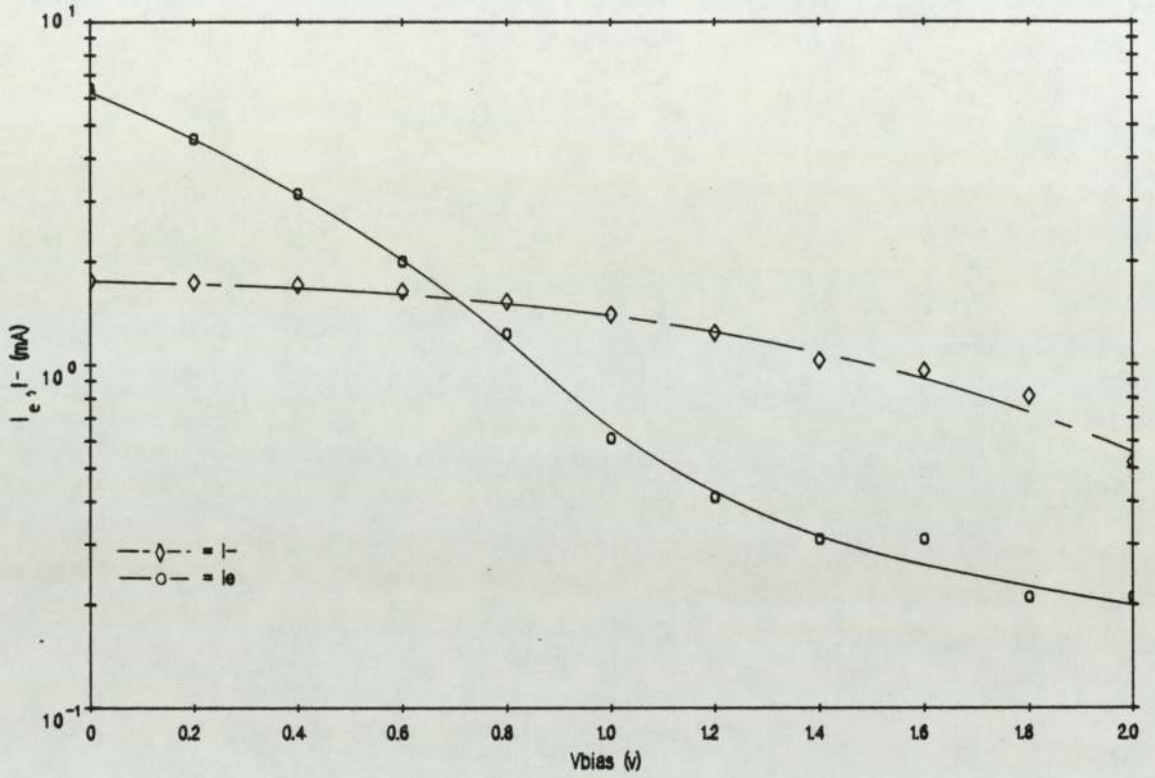


Figure 5.2.32 Variation of I_c and I_e with bias voltage
 $I_{arc} = 10A$ $V_{arc} = 90v$ $Pres. = 10mT$ $V_x = 27kV$

5.3 Results from the mass-analyser probe

Results obtained from this diagnostic are limited to tests of the probe itself. No useful data about the source plasma was obtained, as the origins of the "mass spectra" produced by the probe were ambiguous.

5.3.1 Tests on the extraction system

Since the extraction system of the probe consisted only of a beam forming aperture and final electrode, it was not possible to focus the beam with a middle grid potential, as in the large 30kV accelerator stack. However, the extraction system did exhibit an electrostatic focusing effect, as shown in figure (5.3.1). The voltage at which the focus occurs varies with the arc current, higher voltages being required as V_{arc} is increased. This indicates that some type of "perveance matching" was occurring in the same fashion as the large accelerator, but this could not be controlled independently of the extraction potential. It proved impossible to extract any measurable current of positive ions. This may be due to the difficulty of manufacturing and aligning the electrode apertures, resulting in poor electron and ion optical properties. In fact, the stainless-steel aperture plates were found on examination to have melted slightly due to the thermal loading, and had to be replaced with tungsten, which was unfortunately even harder to machine accurately.

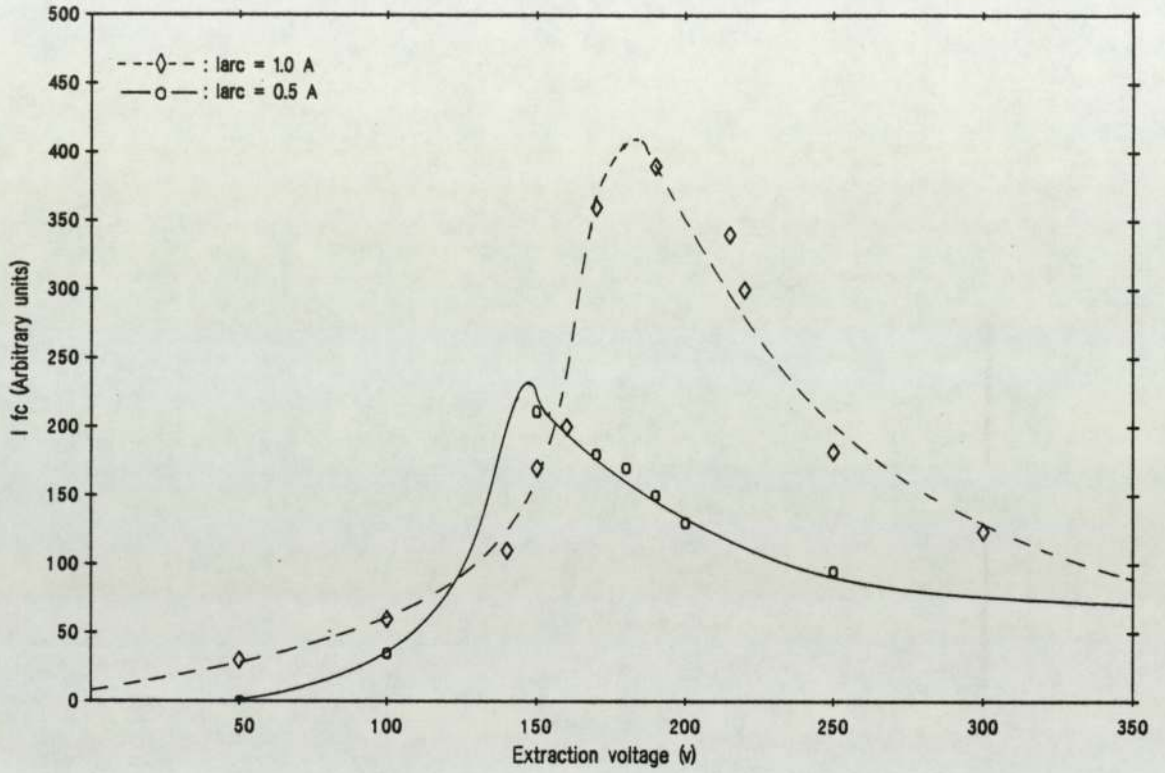
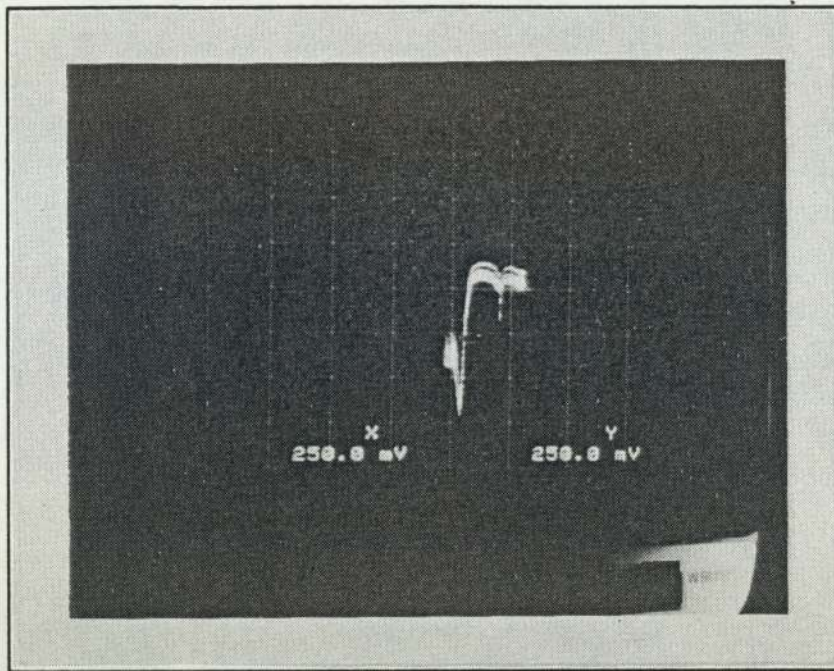


Figure 5.3.1 Variation of Faraday cup current with extraction voltage
 $V_{arc} = 90\text{v}$ Pres. = 12.3mT Driver region

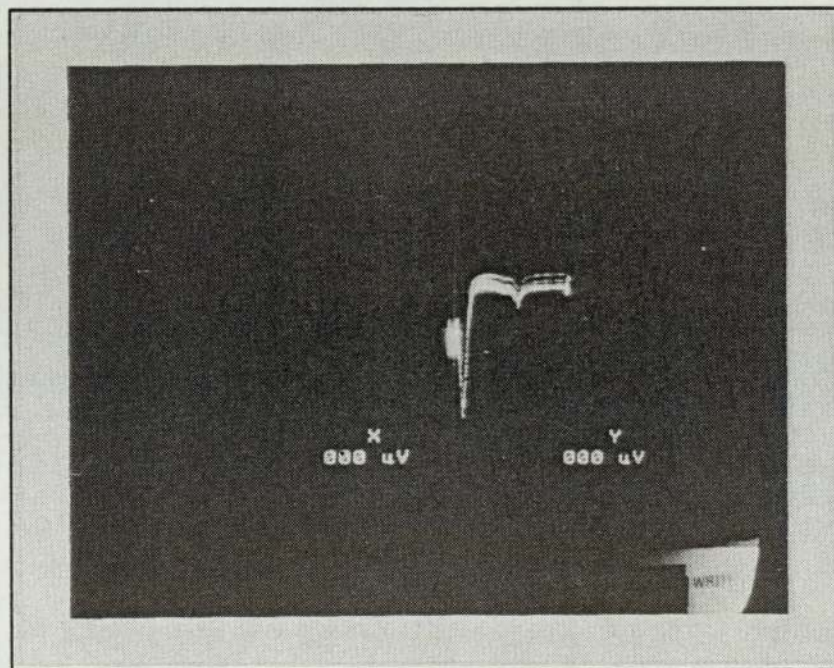
5.3.2 Test spectra

Having established the existence of at least a negative particle extracted beam, attempts were made to obtain a mass-spectrum. The acceleration voltage was set to the perveance match determined above and the magnetic lens activated with the battery circuit. The lens current was swept to 1A in ~ 2 sec. The resultant spectra may be seen in fig (5.3.2). Two peaks are evident in the spectrum. The larger of these occurs at a low lens excitation current, ~ 35 mA. This agrees well with the 30mA predicted by lens theory for electron focus. The increase in coil current required to obtain the peak at higher voltage also agrees with the 27% predicted by theory. The smaller peak is broader, and occurs at ~ 260 mA. This is only 25% of the value predicted by lens theory for H^- ion focus, which suggests that this peak may not be due to H^- ions. However, no particle of the requisite mass exists.

The comparative scaling of the two peaks under different conditions in the variable filter source was then investigated. Spectra obtained in the driver and extraction regions are shown in fig (5.3.3). Despite the considerable amount of noise, it is possible to see a 20% rise in the ratio of the small to large peak, from 0.25 to 0.3. Signal level falls by the expected order-of-magnitude. An H^- fractional density of this magnitude in the driver region would be much greater than that determined by probe measurements. This could possibly be explained by the very



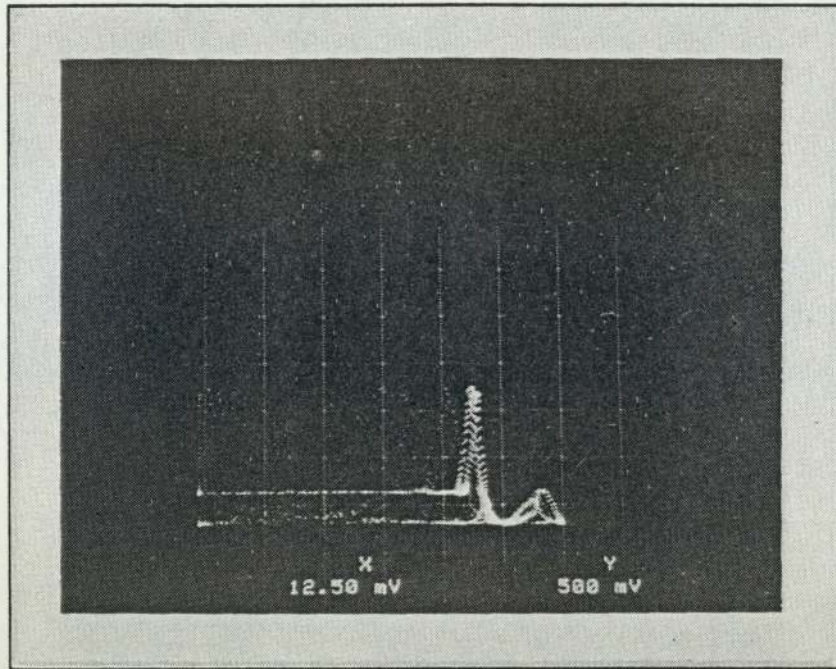
(a) $V = 130\text{v}$ $V = +10\text{v}$
 1A 60v 3mT extraction region discharge



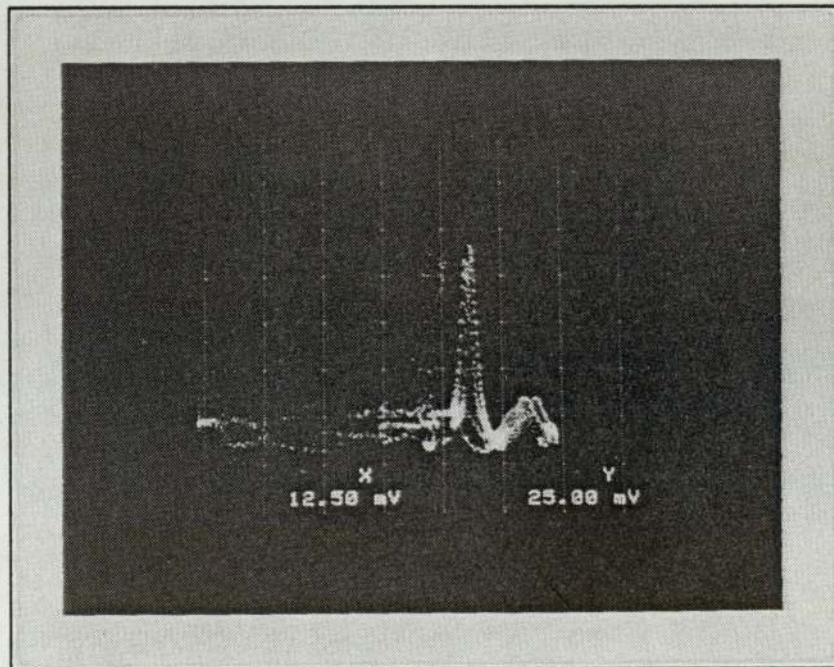
(b) $V = 205\text{v}$ $V = +10\text{v}$
 1A 60v 3mT extraction region discharge

(The polarity of the signal is reversed in these spectra)

Figure 5.3.2 MAP spectra obtained at varying extraction potentials



(a) Driver region
2A 3mT 60v 80 gauss discharge



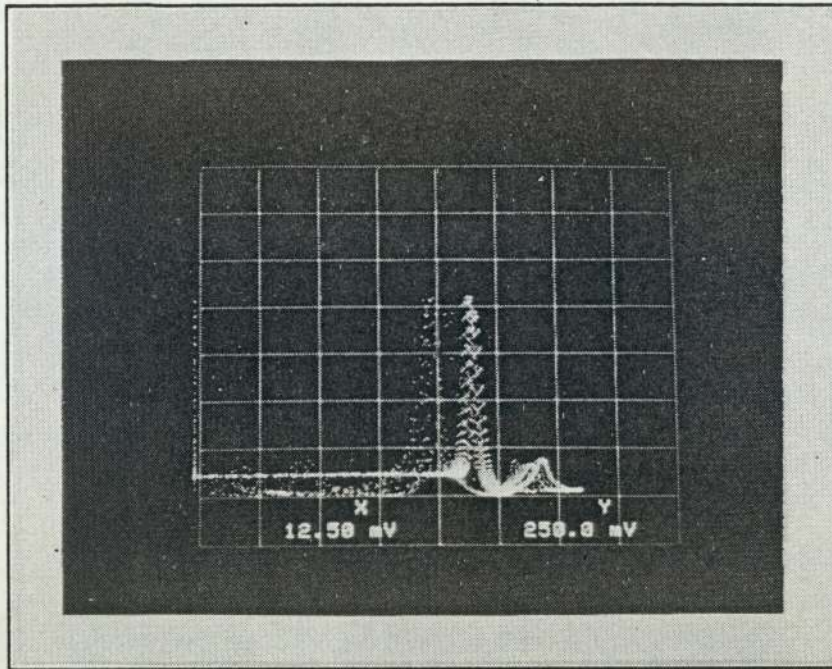
(b) Extraction region
2A 3mT 60v 80 gauss discharge

In both cases, $V = 200v$ $V = +10v$

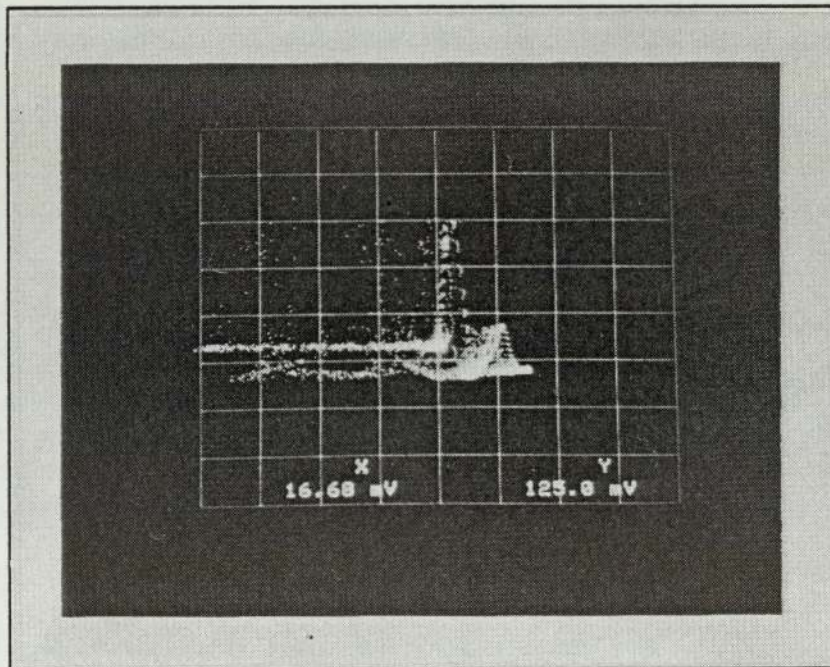
Figure 5.3.3 MAP spectra obtained from the two regions

low arc current, and therefore primary electron population, in this regime. Figure (5.3.4) shows spectra obtained at the peak of the filter field, with the filter inactive in (a) and active in (b). The ratio of the smaller to the larger peak doubles in the presence of the filter field, from 0.17 to 0.33. Although the effect of the filter field on electrons entering the accelerator gap is not negligible at this point, if the second peak were due to electrons as well as the first it would be reasonable to expect both peaks to scale in the same manner with the filter field intensity.

The effect of varying the pressure on the spectra in the driver and extraction regions was then investigated. Figure (5.3.5a) shows a spectrum obtained at a pressure of 1mT in the driver region. Despite a low signal level and a great deal of noise, it is possible to obtain a peak-ratio of 0.11. Comparing this with figure (5.3.3a), it is seen that the ratio is approximately halved by the reduced pressure. A similar comparison can be made between figure (5.3.5b), obtained at 10mT in the extraction region, and (5.3.3b), obtained at 3mT under similar conditions. An 80% rise in peak-ratio, from 0.25 to 0.45, is seen.



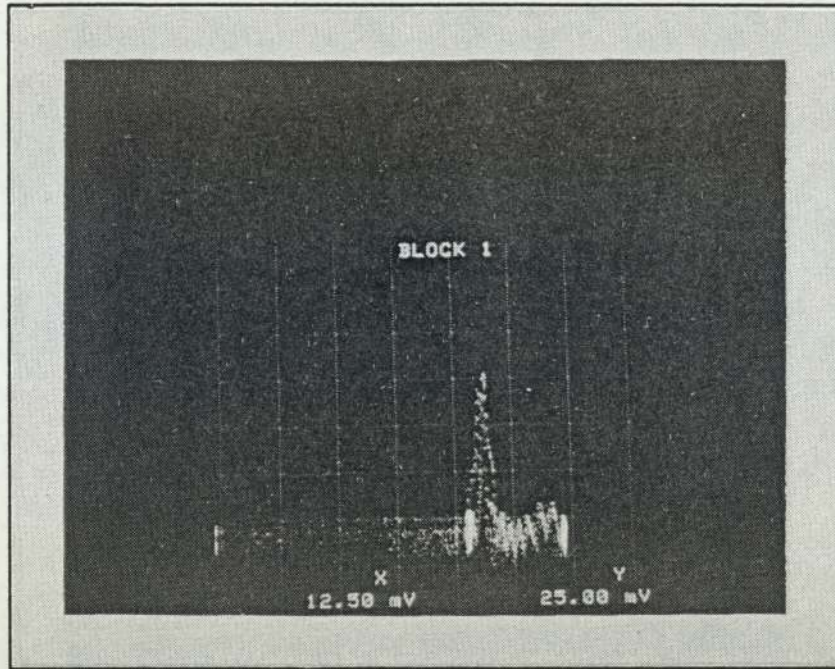
(a) $B = 0$ gauss
 3mT 2A 60v discharge at filter peak



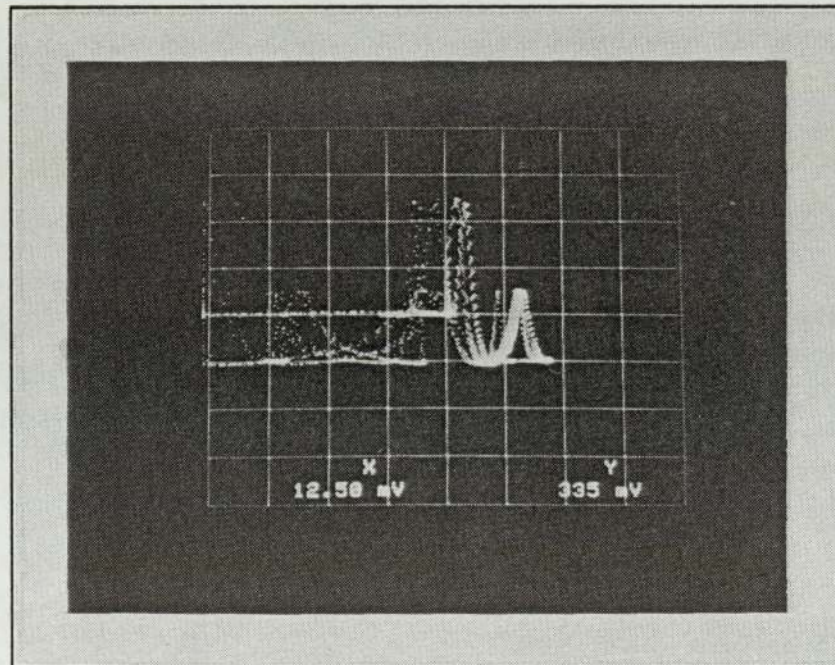
(b) $B = 80$ gauss
 3mT 2A 60v discharge at filter peak

In both cases, $V = 200v$, $V = +10v$

Figure 5.3.4 MAP spectra obtained at varying filter intensity



(a) 1mT 2A 60v 80 gauss driver region discharge
c/f figure 5.3.3a



(b) 1.0mT 5A 60v 0 gauss extraction region discharge
c/f figure 5.3.3b

In both cases, $V = 200v$ $V = +1.0v$

Figure 5.3.5 MAP spectra obtained at varying pressures

5.3.3 Summary

Results of the tests on the mass-analyser probe may be summarized as follows;

1. The probe extraction system proved capable of extracting a beam of negative particles through to the Faraday cup. Electrostatic focus of the beam by the accelerating potential occurred, the focus voltage increasing with current density as required by the Child-Langmuir law. Extraction of positive ions proved impossible.
2. Two peaks in the collected current were obtained by sweeping the lens excitation current. The larger of these peaks occurred at the current predicted by lens theory for electron focus. The smaller occurred at less than 25% of the excitation current predicted by lens theory as being necessary to focus H^- ions.
3. The ratio of the smaller to the larger peak was greater in the extraction region than in the driver, but not by much. This ratio increased with pressure and filter field intensity in the manner that would be expected if it were due to H^- ions. In general, the ratio was greater than that obtained from probe and extraction measurements made under the same conditions.

Given the above observations, it is not possible to

conclude unequivocally that H^- ions have been successfully observed with this device.

CHAPTER 6

Discussion

This chapter discusses the experimental results presented in chapter 5. Where appropriate, these are compared to the theoretical models of the source and atomic physics presented in chapter 2. Section 6.1 considers the behavior of the basic plasma parameters, and 6.2 that of the negative ion density. Each of these is further subdivided in the same way as the corresponding section in chapter 5. However, the internal division by arc parameter of section 5.1.2 is not repeated in section 6.1.2, as the interdependencies of plasma parameters are such that the results may be more sensibly discussed in terms of these, rather than the alterable arc parameters.

6.1 Plasma parameters

6.1.1 Spatial dependence

The axial variation of the primary electron temperature and density suggest that inelastic interactions between primaries and neutrals are only likely in the volume immediately surrounding the filament. Since ionization is an inelastic process, this in turn suggests that plasma is generated only in the filament region, and diffuses from there to the rest of the source. This interpretation is

supported by other evidence; In the absence of the filter field, the energy density falls off exponentially with distance from the filament region. This behavior is that which might be expected from an axial variation governed by diffusion of plasma from the driver. If the energy density is represented as P and the drift velocity of a volume of plasma energy by v_d , then the axial (z) variation in the absence of the filter field should be governed by

$$P v_d = -D \frac{dP}{dz} \quad \dots(6.1.1)$$

where D is the appropriate diffusion coefficient. This has a solution

$$P = P_o e^{-\left(\frac{v_d}{D}\right)z}$$

which is of the form observed. In the case of diffusion being governed by neutral gas collisions with the thermal plasma, this becomes

$$P = P_o e^{-3N_o \sigma \left(\frac{v_d}{v_e}\right)z} \quad \dots(6.1.2)$$

implying that the attenuation of P should increase with neutral gas density. This is also the case, as may be seen in figure (6.1.1). The presence of the filter field will affect the rate of diffusion through the velocity terms in

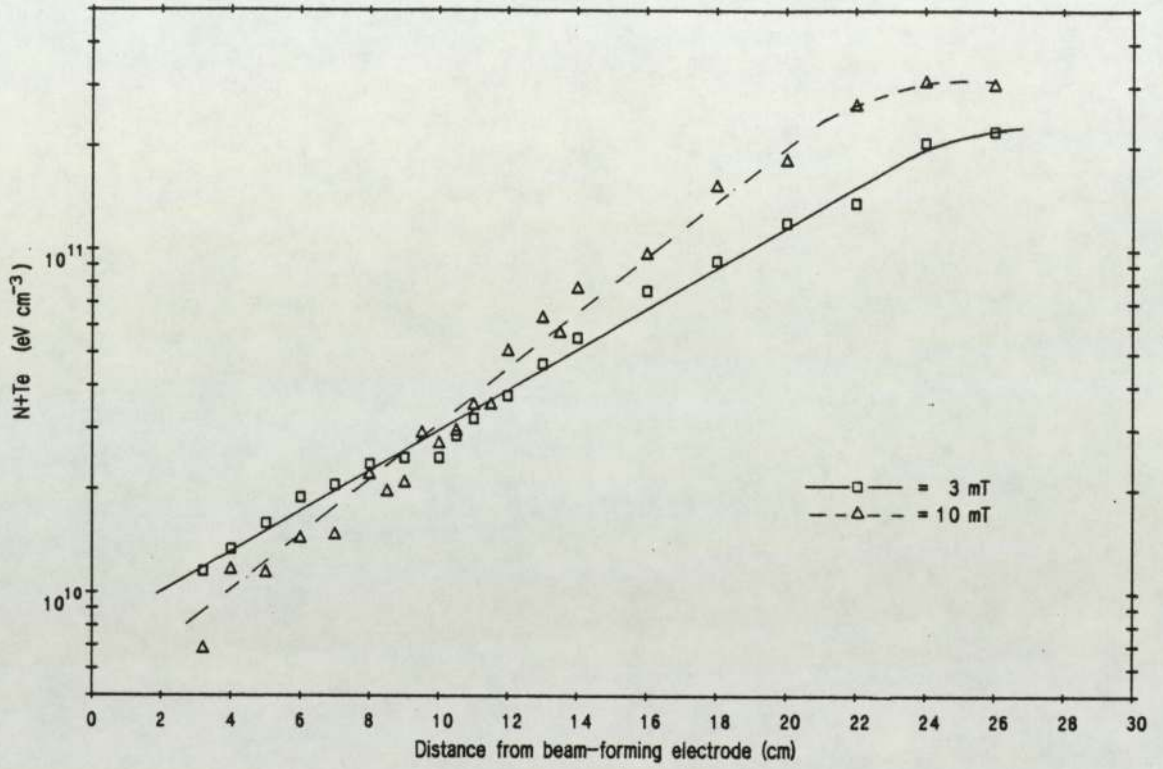


Figure 6.1.1 Exponential attenuation of N+Te with distance for two pressures
 I_{arc} = 5A V_{arc} = 60v B = 0 Gauss

the exponent, producing the structure seen in figure (5.1.3) for the active filter.

The presence of the filter field helps to confine primaries to the driver region, and therefore increases both primary and plasma density there. Naturally, the opposite is true of the extraction region. The field attenuates primaries much more rapidly than thermal electrons, as the colder species is more likely to collide and thus diffuse randomly across the fieldlines. Consequently, the density of primaries in the extraction region is a smaller fraction of the total density than in the driver, both in number and energy terms. The minimum field required to produce significant attenuation appears to be ~ 30 gauss.

The main feature of the radial variation is the attenuation of the otherwise uniform plasma at ~ 3 cm from the walls. This distance corresponds to the range of the strong (> 1000 gauss) cusp fields generated by the confinement magnets on the walls of the extraction region (see figure (3.1.1a)), and it would seem obvious that these are the cause of the attenuation. The enlargement of the plasma as defined by N_+ is due to the reduction in T_e by the field increasing the collisionality of the thermal plasma, and thereby increasing diffusion across the fieldlines. This effect is seen because the horizontal probe is mounted so that it passes through the field between two cusps.

6.1.2 Parametric dependence

From the results of the previous section, it may be seen that the parametric variation of the plasma parameters throughout the source will be determined largely by events in the driver region. With this in mind, therefore, parametric behavior is examined primarily for the driver region, and other regions discussed with reference to this.

6.1.2.1 Primary electrons

The behavior of a fast electron group can have a large effect on that of the plasma as a whole. However, it is important to note that here the term "primary" electron refers to those electrons apparently forming the second Maxwellian group visible on the Langmuir probe traces, the exact identity and distribution function of which is still a matter for debate.

The production and loss of primaries is described by eqn. (2.1.1). The variation of N_p with arc current obeys this to a high degree of correlation, I_{arc} representing the rate of injection of primaries into the plasma. The fraction of primaries as a percentage of the plasma density increases in a linear fashion from 5 to 10% over the measured range of I_{arc} , as shown in figure (6.1.2). Results from the large Culham multipole source [43] show that N_p is a similar fraction of N_+ at very high discharge currents ($> 1000A$) indicating that the primary fraction does not increase continuously at the rate observed here.

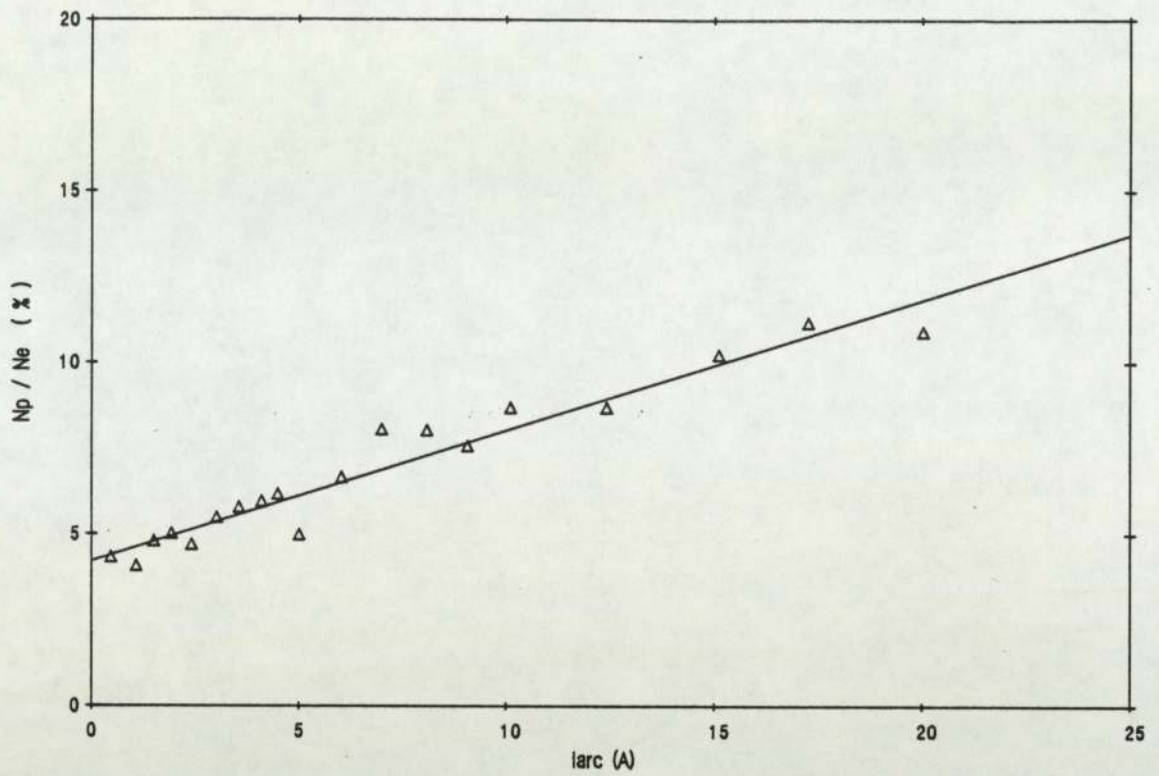


Figure 6.1.2 Variation of primary electron fraction with arc current
 Varc = 60v Pres = 3mT B = 80 Gauss

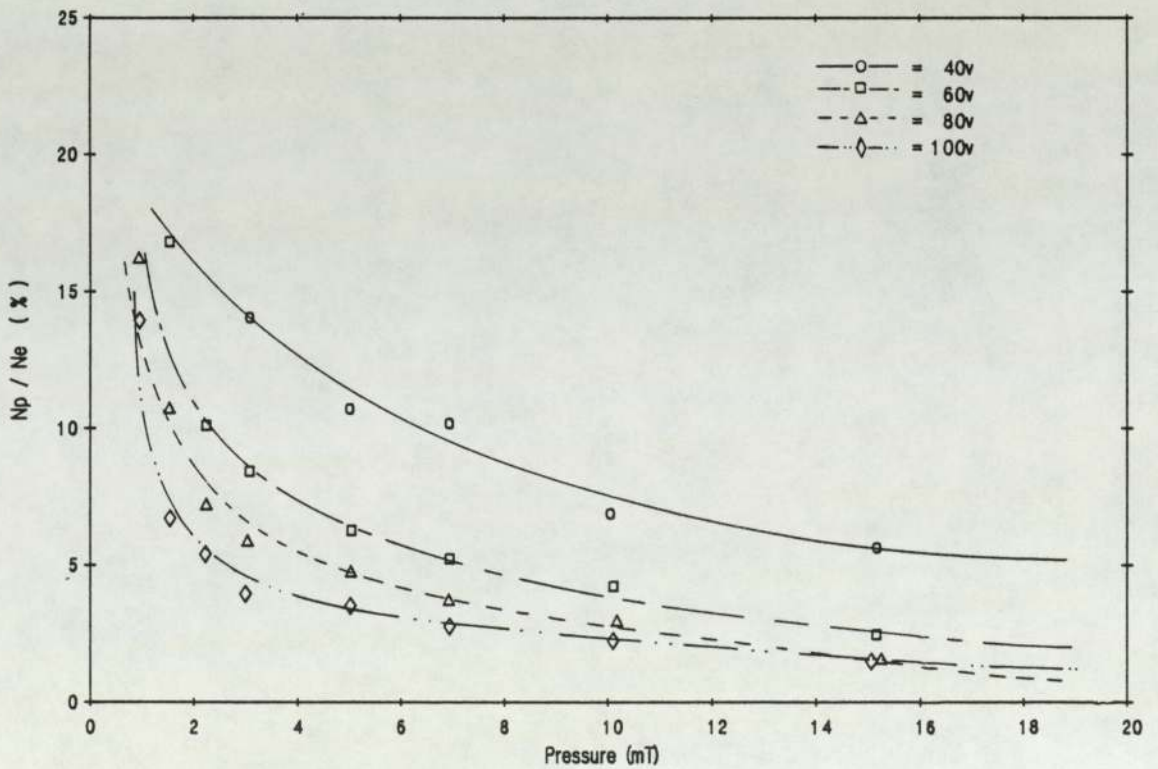


Figure 6.1.3 Variation of primary electron fraction with pressure
 Iarc = 5A Varc = 60v B = 80 Gauss

The primary electron temperature T_p appears independent of Iarc, indicating that the process degrading the energy spectrum of the primaries is not a strong function of plasma density. This is not predicted explicitly from the model, but agrees with the invariance found in calculated distribution functions [84].

The way primaries are lost to the discharge affects the dependence of the primary density, through the loss terms in eqn. (2.1.1). These terms govern the pressure and voltage dependencies of N_p and T_p . The behavior of N_p with these parameters indicates that in the variable-filter source, the loss mechanisms may differ from those observed in other multipole sources. Eqn. (2.1.1) contains two loss terms, describing the destruction of primaries by impact with the wall, and by inelastic collisions with neutrals which act to "thermalize" the primaries. If the neutrals were the dominant loss channel, eqn. (6.1.1) predicts the inverse dependence of N_p on pressure seen in [44]. This is not observed in the variable filter source, figs (5.1.32) and (5.1.33) showing N_p to be virtually independent of pressure over this range, for several arc voltages. It should be noted that the fraction of primaries as a percentage of the plasma density does vary inversely with pressure, as shown in figure (6.1.3). The weak inverse relationship of T_p with pressure indicates the primary energy spectrum is degraded at least partly by gas collisions, an obvious statement since some ions must be being made in the discharge!. However,

this loss mechanism does not appear to cause a major drop in N_p .

Since primaries do not appear to be lost principally through gas collisions, they must leave either the primary group or the discharge itself via some other means. This leaves the wall-loss term. An expression for primary loss to a magnetically-shielded wall may be obtained by substituting eqn. (2.1.6) into eqn. (2.1.1) and rearranging to give N_p ;

$$N_p = \frac{I_{arc}}{eV(V_{arc}(\alpha_1 E \phi_1)^{-1} + N_o(ILP))} \dots(6.1.3)$$

Thus if primaries are lost principally to the cusps of a magnetically-screened anode wall, the pressure-dependent term may be assumed negligible and the primary density should vary inversely with primary electron temperature, or arc voltage if T_p may be expressed as a linear function of this. This is indeed the case, as may be seen in figure (5.1.26). Figure (6.1.4) shows $\ln(N_p)$ as a function of $\ln(T_p)$ for two pressures. A gradient ~ -1 is obtained in both cases with a high statistical correlation. This implies that under the conditions obtaining in the driver region of the variable filter source, losses of primaries to the wall occur more often than those due to gas collisions. The theoretical importance of wall losses for primaries in the energy range observed here is illustrated by the work of Bretagne et al [84]. The model they used showed that a difference in N_p of

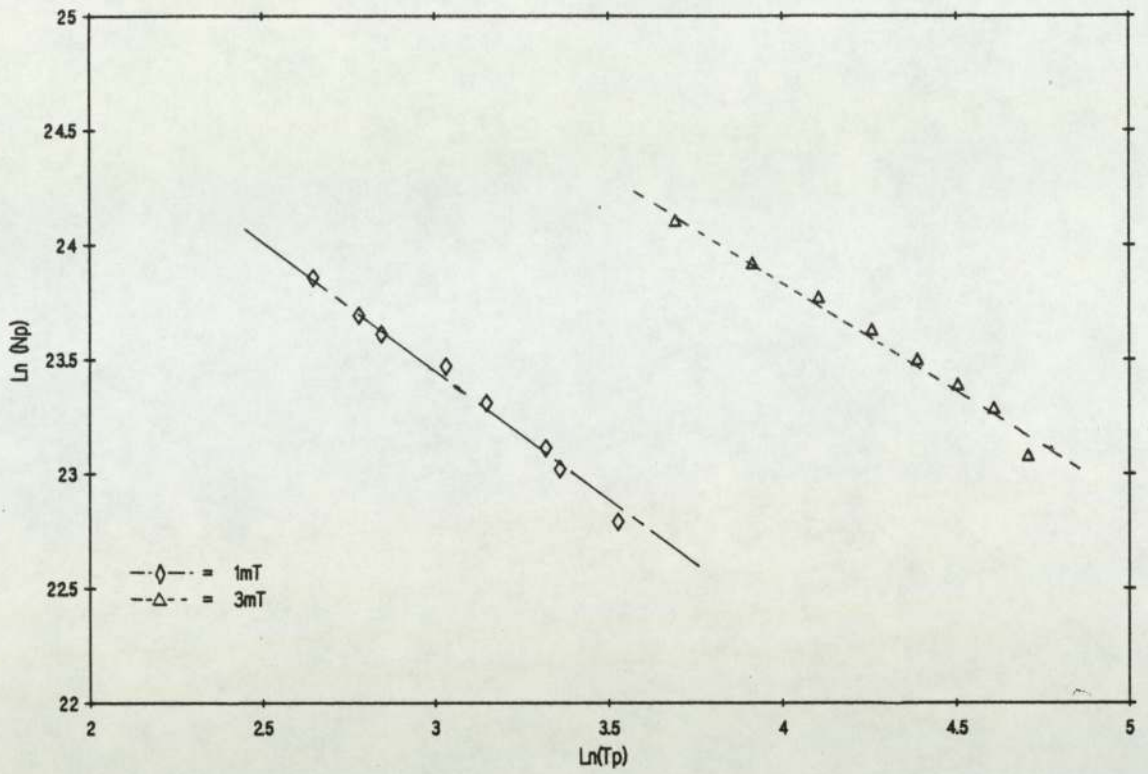


Figure 6.1.4 Inverse dependence of Ln (Np) on Ln (Tp)
 Iarc = 5A Varc = 60v Pres. = 3mT B = 80 Gauss Driver region

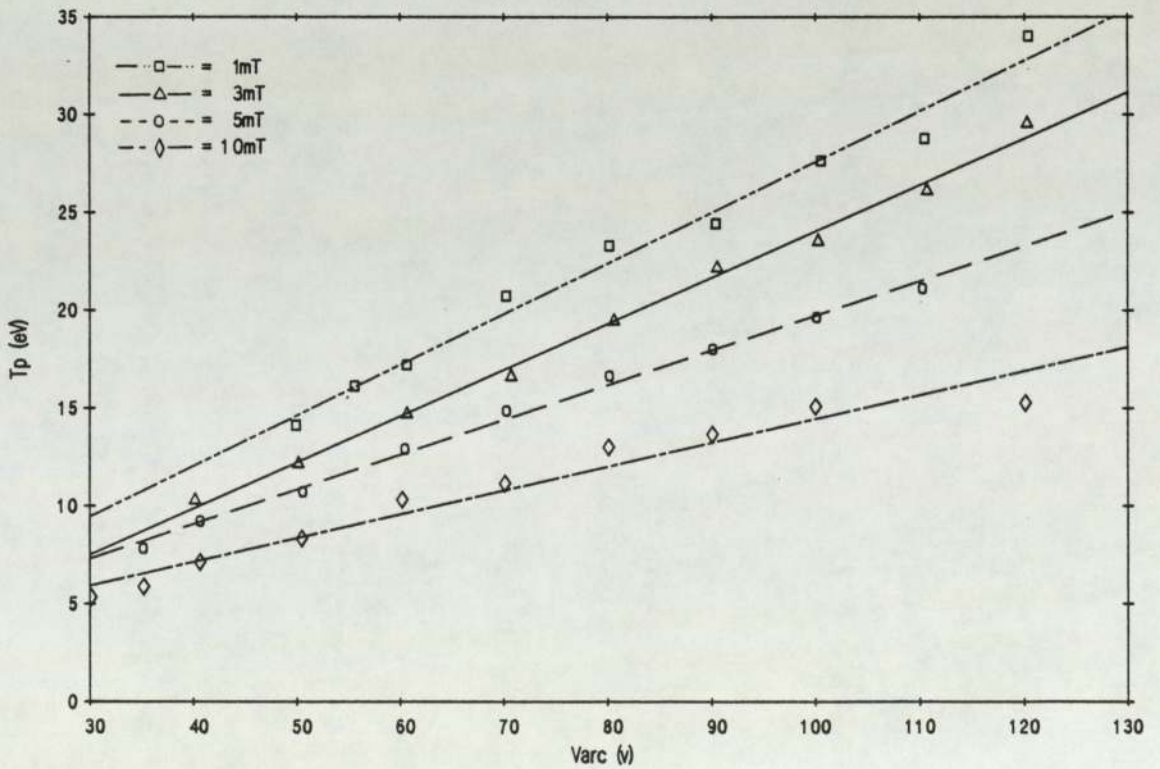


Fig 6.1.5 Effects of inelastic primary energy loss on the Tp/Varc line
 Iarc = 5A B = 80 Gauss

an order of magnitude over this energy range existed between the distribution functions calculated with and without wall losses for a 4mT multipole discharge. Even at pressures of 40mT the wall loss term remained significant. The axial scan data indicates that the plasma production region may be restricted to the volume surrounding the filament, implying that the magnetic shielding of the anode in this region only is responsible for the observed wall-loss behavior.

The linear increase in T_p with arc voltage shown in fig. (5.1.27) is expected, as V_{arc} represents the energy with which the primaries enter the discharge. T_p appears to represent a constant fraction of V_{arc} , in this case ~ 0.25 . This relationship has been noted before [44], with the fraction closer to 0.3. The value of this fraction deserves a closer investigation. In the case of the variable filter source, from the above reasoning the major loss of primary energy is to the walls. Thus eqn. (2.1.1) reduces to

$$\frac{I_{arc}}{eV} = \frac{N_p}{\tau_p} \quad \dots(6.1.4)$$

However the energy balance, rather than the particle balance, is required. This may be obtained by comparing the power input with the power leakage, such that

$$\frac{I_{arc} V_{arc}}{eV} = \frac{\phi T_p N_p}{\tau_p} \quad \dots(6.1.5)$$

where ϕ is the energy in eV carried out of the plasma by a single primary electron. Replacing I_{arc} in eqn. (6.1.5) using eqn. (6.1.4), and expressing τ_p in terms of the primary velocity v_p , driver volume V and loss area A_p , the relationship

$$V_{arc} \frac{N_p A v_p}{4V} = \phi T_p \frac{N_p A v_p}{4V} \quad \dots(6.1.6)$$

is generated. A simple cancellation then leads to

$$V_{arc} = \phi T_p \quad \dots(6.1.7)$$

which is of the form observed experimentally. The value of ϕT_p should be given by the average energy of a primary electron in the plasma, obtained from the textbook integral over the assumed Maxwellian distribution function as $\phi = 3/2 T_p$. However, this yields $T_p = 0.66 V_{arc}$, more than double that observed. Obviously, a primary electron leaving the discharge must on average carry more energy than $3/2 T_p$.

In the case of wall-loss dominance, the physical reason for this lies in the temperature-dependent cusp lines, which determine the area of anode "seen" by the electrons. This area is larger for hotter particles, and therefore preferentially leaks hotter electrons to the wall. This "Maxwell's demon" therefore has the effect of skewing the primary velocity distribution at the wall in favour of the

faster electrons. Mathematically, this may be seen by returning to eqn. (6.1.6), collecting the velocity terms on each side and integrating the resultant velocity-dependent energy input and energy loss terms, as entities, over the distribution function. The cusp area is given by eqn.

(2.1.2), so replacing T_p by $\frac{1}{2}M_e v_p^2$, eqn. (6.1.6) becomes:

$$V_{arc} \frac{2N_p \theta L M_e v_p^2}{4V_e B} = \phi \frac{M_e v_p^2}{2} \frac{2N_p \theta L M_e v_p^2}{4V_e B} \dots (6.1.8)$$

where θ is the primary cusp half-width in Larmor radii.

Cancelling the constant terms, the expression in terms of average velocity becomes:

$$V_{arc} \langle v_p^2 \rangle = \frac{\phi M_e}{2} \langle v_p^4 \rangle \dots (6.1.9)$$

Where $\langle \rangle$ represents, as usual, an average over the velocity distribution. The average of v_p is given for a Maxwellian distribution by

$$\langle v_p \rangle = \frac{1}{N} \int_0^\infty v_p \frac{dN}{dv_p} \cdot dv_p = 4\pi \left(\frac{M_e}{2\pi kT} \right)^{\frac{3}{2}} \int_0^\infty v_p^3 e^{-\frac{M_e v_p^2}{2kT}} \cdot dv_p$$

so eqn. (6.1.9) becomes

$$V_{arc} \int_0^\infty v_p^4 e^{-\frac{M_e v_p^2}{2kT}} \cdot dv_p = \frac{\phi M_e}{2} \int_0^\infty v_p^6 e^{-\frac{M_e v_p^2}{2kT}} \cdot dv_p$$

since normalization factors cancel both sides. Using standard formulae for the integrals, this yields

$$V_{arc} = 2.5 \phi T_p \quad \dots(6.1.10)$$

Thus the temperature-dependent leak effectively multiplies ϕ by a factor of 2.5, giving a T_p / V_{arc} fraction ($= \phi_1$) of 0.266, very close indeed to that observed. It is interesting to note that with N_p inversely dependent on V_{arc} , the primary energy density should be approximately invariant with V_{arc} . This is indeed the case, as shown in figure (5.1.28).

It was noted at the start of this calculation that the observed T_p / V_{arc} fraction was similar in the inelastic-collision dominated case of a fixed-filter type source with efficient magnetic screening [44]. The same reasoning may be applied in this situation. In this case, however, the Maxwellian demon manifests itself in the form of the reaction rates for inelastic energy loss, which according to Hiskes [68] are a function of T_p over the range encountered here. This may be the cause of one other effect noted in the variable-filter source; namely, the fall in ϕ_1 with pressure shown in figure (6.1.5). This indicates that inelastic gas collisions cause losses of primary energy even when losses of primary electrons are dominated by wall collisions.

The chief effects of the filter field on the primary electron population are seen outside of the driver region.

In the driver, N_p increases slowly with field intensity, due to the increase in confinement time obtained from magnetic shielding of the filter rods. Outside the driver region, if $B > 30$ gauss, the characteristic dependencies of N_p and T_p discussed above no longer hold; N_p shows no variation with V_{arc} and T_p shows a negligibly small increase with V_{arc} . The arc current dependency of N_p does hold. The explanation of these non-dependencies is indicated by the filter field variation of N_p . Increasing B beyond ~ 30 gauss essentially eliminates primaries from the extraction region, the temperature falling to a level at which the assumption that they behave as an independent Maxwellian population of fast electrons is probably no longer valid.

6.1.2.2 Ions and thermal electrons

The parametric behavior of the plasma density in the case of a magnetically-confined plasma is given by eqn.

(2.1.8). Rearranging this yields the bulk energy density

$N_+ T_e$:

$$N_+ T_e = \frac{N_o \langle ION \rangle E \alpha_2 I_{arc}}{eV \left(V_{arc} (\alpha_1 E \phi_1)^{-1} + N_o \langle ILP \rangle \right)} \quad \dots(6.1.11)$$

Thus the variation of $N_+ T_e$ with I_{arc} should be linear, regardless of the primary loss mechanism. As may be seen, results from the variable filter source, shown in figure

(5.1.18), and from the fixed filter source (fig. (5.1.19)) prove that this is indeed the case. This applies in all regions of the source. It should also be noted that T_e increases with I_{arc} , indicating that heating of the thermal electrons by electron-electron (Coulomb) collisions may be significant. The index of this dependence is ~ 0.5

The observed density variation with arc voltage also agrees with eqn. (2.1.8). Although this expression appears to suggest an inverse dependence of N_+ on V_{arc} , the ionization rate coefficient $\langle ION \rangle$ may be seen from [75] to be a strong non-linear function of T_p in this range, becoming weaker as T_p increases. The results of section 6.1.2.1 show that T_p may be expressed as a linear function of V_{arc} . In the case of a source dominated by primary wall-losses, therefore, $N_+ T_e$ should vary in a saturation curve with V_{arc} as the rapid but saturating $\langle ION \rangle$ term in the numerator is overcome by the slower but linear wall-loss term in the denominator. As shown in figure (6.1.6), this is the case. $N_+ T_e$ has a maximum with V_{arc} at all pressures.

The same equation predicts that N_+ and $N_+ T_e$ should increase with pressure, gradually saturating as the gas-loss term increases in relation to the wall losses. Both N_+ (figure (5.1.30)) and $N_+ T_e$ increase with pressure in the driver region, and both fail to completely saturate. In the extraction region, saturation appears to be more complete. However, there are two other effects which could also explain this departure from linearity, both depending on a fall in

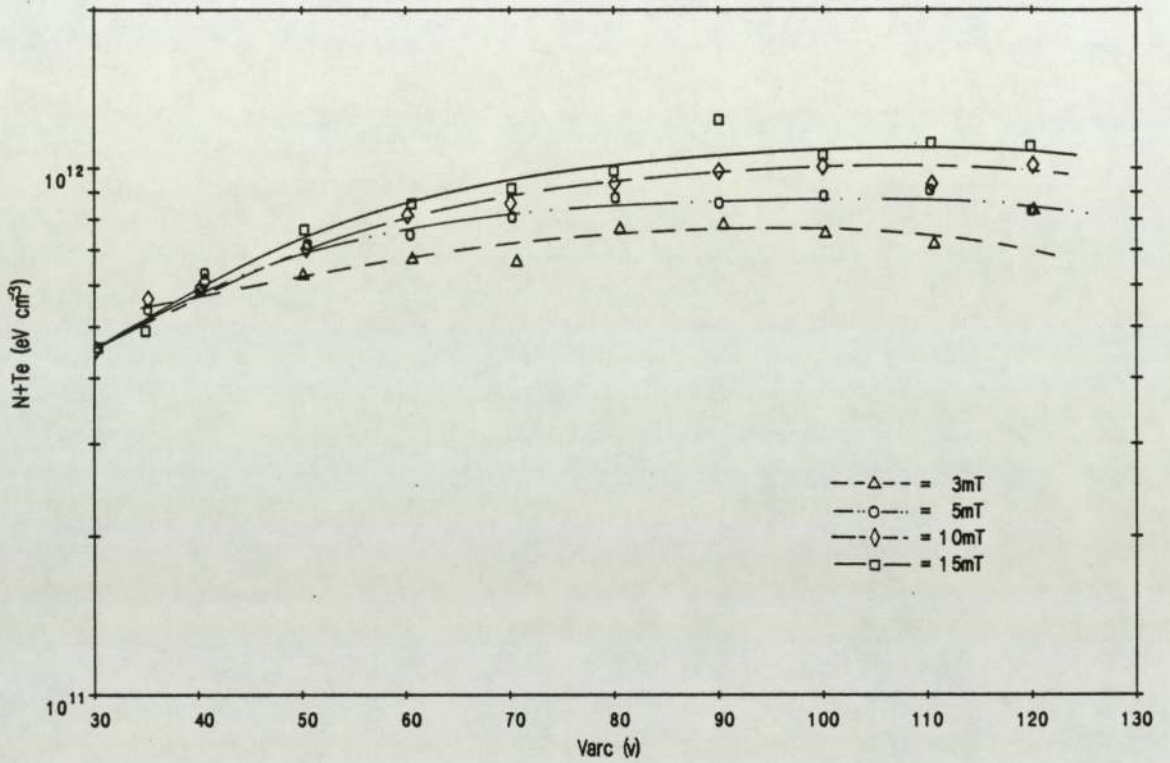


Figure 6.1.6 Saturation of N+Te with Varc at various pressures
Iarc = 5A B = 80 Gauss

T_e . T_e falls slowly with pressure (eqn. (5.1.5)), and in the extraction region with filter intensity (eqn. (5.1.9b)). The first possibility is an increase in the rate of collisional diffusion of thermal electrons across the the fieldlines of the confinement magnets. This has the effect of increasing the loss of plasma to the intercusp regions, thereby reducing the effectiveness of the confinement magnets. This effect is well-known, having been documented by Limpaecher and MacKenzie [24] for the first multipole source at pressures $> 10\text{mT}$. The other possible mechanism is that mentioned in [44], the increase in the probability of ion-electron recombination as the temperature falls. Both of these effects would increase with pressure and be enhanced still further in the extraction region, providing an additional N_+ loss at higher pressures. In actual fact, the fall off in the rate of increase of N_+ with pressure is probably due to a combination of both these effects, plus some saturation of eqn. (2.1.8).

The behavior of the thermal electron temperature in the source is useful, as the $\langle\text{DA}\rangle$ reaction requires a high density of cold electrons for optimum H^- production. Knowledge of the sources and sinks of thermal electron energy would therefore be useful. The increase of T_e with arc current means that the process heating T_e is a function of arc current, and therefore of N_e . The invariance of T_e with V_{arc} observed in figure (5.1.24) implies that this process cannot be a function of primary electron energy. This

invariance is predicted from the model of Bretagne et al [84], which shows little change in the low-temperature end of the calculated electron distribution function with varying arc voltage. T_e has a weak inverse dependence on pressure. This implies that the process heating the thermals is also inversely dependent on pressure, as the threshold energy for inelastic interactions with hydrogen is approximately 10 eV, much greater than T_e . These results have some bearing on the structure of the thermal electron energy balance in the source. Thermal electrons are produced mainly as a product of ionization. Energy may be transferred directly from the primaries to the thermals by Coulomb collisions. This process also acts to redistribute energy within the thermal group, calculations by Hiskes et al [74] suggesting that this process is dominant in the range 0.2-3eV. Energy may also be gained from Coulomb collisions with intermediate energy electrons generated from inelastic collisions with neutrals, "pulling" the intermediate electrons into the thermal group and thereby raising the average energy.

Considering the first process, T_e is a slow function of I_{arc} , indicating Coulomb effects play some part in heating the thermals. The invariance of T_p with I_{arc} suggests little energy is lost from the primary group via direct Coulomb collisions. However, the ratio of T_e to T_p is large, so a small fraction of the primary energy might produce a significant change in T_e , despite the difference in number density. The fall in T_p with pressure might then be possibly

explained as an increase in the probability of primary energy producing excited neutrals, rather than being transferred to the thermals. The invariance of T_e with V_{arc} might then be explained in terms of the increase in the energy of the primaries involved in the Coulomb process being balanced by a fall in the collision cross-section.

Evidence for the second process is also present. Energy is undoubtedly lost from the primary group via inelastic processes, the T_p /pressure curve of figure (5.1.34) flattening out at the level of the inelastic threshold. In addition, the variation of T_p with I_{arc} in the extraction region (fig. (5.1.21)) clearly shows the intermediate ($\sim 5eV$) electrons present there at low arc current vanishing, presumably due to Coulomb thermalization, as I_{arc} is increased. However, heating of the thermal group by intermediate-energy "superthermal" electrons implies some dependence of the heating rate on the density of primary electrons, and none of the N_p dependencies discussed in the previous section are reflected in T_e . It is possible that the N_p/V_{arc} variation is balanced out by an increase in the cross sections governing production of superthermals. The thermal electron energy balance is a complex problem!

The effects of the filter field are once again largest in the extraction region. In the driver, the slow linear increase in N_+ and $N_+ T_e$ with field intensity may be attributed to the reduced diffusion through the field of electrons, especially primary electrons, together with the

reduction in primary wall losses as the unshielded filter rods are screened by the filter. In the extraction region, reduced diffusion produces a linear fall in density, but the field has a larger effect on temperatures. Both T_e and T_p are reduced rapidly here as the electrons with the lowest collisionality are reflected back into the driver. Beyond 30 gauss, T_e and T_p are constant with B.

6.1.2.3 Plasma potential

The variation of plasma potential in the source is important for two reasons. Firstly, the existence of a large differential between driver and extraction regions can make H^- ion extraction difficult, and possibly cause the ions to be heated by Coulomb collisions with protons accelerated across the electric field. Secondly, the existence of a low or negative V_p can allow a significant proportion of H^- to reach the walls, where it is lost. Knowledge of the variation of V_p is therefore useful.

In general, the variation of V_p should follow that of the thermal electron temperature, as electrons determine the wall-sheath characteristics. This is true of most, but not all of the parametric results. The arc current variation shows V_p increasing with T_e in the driver and remaining constant in the extraction region, thereby increasing the axial potential difference (ΔV_p). In the driver region T_e is independent of V_{arc} , but V_p increases very slightly. This is due to the increased energy of the small fraction of

primaries which contribute to sheath formation. The pressure dependence of V_p follows that of T_e exactly in all regions, and no alteration of ΔV_p occurs. The exception to the rule is the filter intensity variation. V_p appears independent of B in all regions, whereas in the extraction region, T_e shows the rapid fall for $0 < B < 30$ gauss discussed above. This may possibly be explained by the increased collisionality of the cooler electrons making the wall-fields less effective. The independence of ΔV_p from the filter field is one of the stranger aspects of the source.

6.1.3 Bias variation

The exponential decrease in N_+ with positive bias implies a rapid depletion of electrons by the BFE in the region sampled by the probe. The corresponding T_e variation shows a rapid linear increase in T_e with positive bias potential. A possible explanation for this would be that the probe lay in the BFE sheath region. However, the spatially-resolved data of figure (5.1.50) shows that N_+ is depleted by a similar factor for a given bias voltage throughout the extraction region. A simple explanation for the ion density depletion might be as follows: The positive plasma potential normally retards electrons from leaving the plasma. Ions are not so retarded. A positive bias on the BFE helps reduce the potential barrier for electrons, and thus large numbers leave the plasma. Quasineutrality then forces similar numbers of ions to leave the plasma. The exponential fall in N_e and N_+

results from reduction of the original Boltzmann attenuation of the electron flux to the BFE as the bias voltage reduces the plasma potential. The temperature increase could be attributed to the addition of a BFE-directed drift velocity to the random electron velocity. The magnitude of this drift would, however, need to be comparable with the thermal velocity. An alternative explanation may be obtained by treating the BFE as a large probe, although a drift-velocity must be assumed. The electron current collected by the BFE saturates when $V_{\text{bias}} > V_p$, as the edges of the BFE presheath are defined by the source and sheath-expansion is therefore not possible. The total current density entering the sheath is thus almost constant with bias voltage for a given set of arc conditions. If the drift velocity continues to increase with V_{bias} , from simple probe theory for constant J_e , if \bar{v}_e increases, N_e (and therefore N_+) must decrease.

The increase in N_p with V_{bias} , together with the independence of T_p , are curious given the previous discussion. The increase in N_p may be due to the attraction of the highest-energy electrons from the extraction region by the BFE, their energy being high enough to overcome any ionic sheath. The drift velocity provided by the BFE in this case would be small in comparison with the thermal velocity, hence the independence of T_p . The variation of N_p at zero gauss in the driver region shows the BFE can draw primaries from the driver in the absence of a filter field. It should be noted here, however, that these measurements are at the extreme

lower limit of the sensitivity of the probe system, and must be interpreted with caution. In addition, the points raised in section 5.1.1 about the nature of the "primary" electrons detected in the extraction region must be considered.

The variation of V_p with V_{bias} at the BFE and in the extraction region corresponds closely to the applied bias, provided this is not very negative. This variation penetrates in an attenuated form through the filter to the driver region. This again reflects the relative unimportance of the filter where ΔV_p is concerned. A positive bias reduces ΔV_p , thus reducing heating of the negative ions and possibly improving the beam quality. Thus a positive bias may have an additional beneficial effect on the operation of an H^- ion source.

6.2 Negative ions

In this section, measurements of H^- ion density are discussed. Comparisons are made both with theory and between results obtained using beam extraction and Langmuir probes. The latter comparison is made difficult by the fact that the extraction data consists of current density measurements, related to number densities through the negative ion velocity v_- . In the case of the probes, this is assumed to be random, and described by a Maxwellian temperature T_- . The extraction system is thought to alter this random velocity [103], but it is not known exactly how, or to what degree. Comparing the two sets of results is useful nevertheless, as any large-scale variation of N_- will obviously still be reflected in J_- . In addition, differences exist in the conditions obtaining in the two sources. Unfortunately, these together with the design differences rule out a direct check on probe measurements of H^- , and the existence of the electron-suppressor magnets in the BFE make even comparison of the ion-electron ratio between the two sources meaningless. However, the probe technique itself has been verified elsewhere [43], and as will be seen, the results obtained do not appear unreasonable.

6.2.1 Numerical estimate of N_-

An immediate check on the assumptions made about the atomic processes governing H^- production is possible. The numerical estimate of the H^- ion density of $5.4 \times 10^9 \text{ cm}^{-3}$ at

the filter peak of the variable filter source obtained in chapter 2.2 is within $\sim 20\%$ of the measured peak value of $N_{-r} = 4.5 \times 10^9 \text{ cm}^{-3}$. This indicates that the production and loss mechanisms described in chapter 2.2 are very probably the ones responsible for H^- production.

6.2.2 Spatial dependence

Probe data shows the negative ion density peaking just inside the 30-gauss contour of the filter field and falling rapidly as the BFE is approached, whereas the negative ion fraction peaks at the centre of the filter and remains constant. These results indicate an increase of N_- between extraction region and filter peak of between three and four times, a figure noted in similar studies of other sources [38,79]. However, the increase in J_- obtained by moving the extraction aperture to the peak of the fixed-filter source is only some 50%. The doubling of extracted electron current is also less than expected from the probe data. As mentioned previously, moving the aperture entailed the repositioning of the entire BFE assembly, altering drastically the plasma density and potential profiles across the filter. The discrepancy between expected and measured J_- values could either be due to a fall in N_+ and N_e as discussed below, or some alteration of the negative ion velocity by the modified electric fields.

The variation in N_{-r} with distance beyond the filter in the variable filter source is interesting. The instinctive

solution is to attribute the fall in H^- density to the fall in plasma and thermal electron density due to the filter. However, the model presented in chapter 2.3 explicitly excludes a dependence of N_- on the extraction-region plasma density over the range of conditions studied here. In addition, the H^- fraction F_r appears to be approximately constant with distance beyond the filter. Another explanation for the fall must therefore be found. Two possibilities exist: Firstly, the loss of H^- may become dominated by a process whose rate is independent of plasma density, thus introducing a dependence of N_- on N_e and N_+ . Secondly, the density of vibrationally-excited molecules (N_v) may not, as has been assumed, be spatially invariant.

Considering the N_e dependence first, the density independent loss process need only be partially dominant, as the fall in N_e ($\sim N_+$) from filter to extraction region is large. Examining eqn. (2.2.2), the only truly density-independent loss process is that due to wall collisions. However, although the $\langle AD \rangle$ process has a dependency on N_+ through the dissociation reaction (as explained in chapter 2.3) this N_+ is the ion density in the driver region. For fixed arc conditions this is constant, and the assumption that the N_e and N_+ dependencies cancel is therefore no longer valid. The relative magnitudes of the two processes may be seen in eqn. (2.2.5).

This theory may now be tested against the axial variation of N_{-r} shown in figure (5.2.4). The fall in the

3mT N_{-r} curve from the filter peak to the extraction region, 7cm from the BFE, will be examined using data from section 5.1.1. At the filter peak, N_+ is high enough to ensure the $\langle MN \rangle$ process dominates over $\langle AD \rangle$ and $\langle WALL \rangle$ by one and two orders of magnitude respectively. At 7cm from the BFE, N_+ has fallen by a factor of ~ 5 . Due to the fall in T_e from 0.73eV to 0.35eV, $\langle MN \rangle$ increases by $\sim 42\%$, according to the Hickman [65] formula. The rate for the $\langle AD \rangle$ process remains constant, whilst the wall loss rate increases by a factor of 17 due to the fall in V_p from +1.75v to +0.9v increasing the Boltzmann factor. Temporarily, N_v is assumed constant. The total H^- loss rates may now be calculated, and combined with the 5-fold fall in N_e to give a parameter indicating the relative increase in H^- loss compared with production experienced in moving 5cm down the axis toward the BFE:

$$\frac{\text{peak loss}}{\text{peak prod.}} = \frac{5 \times 10^{10} \langle 6.5 \times 10^{-8} \rangle + 2 \times 10^{11} \langle 1.3 \times 10^{-9} \rangle + 39}{N_v 5 \times 10^{10} \langle 1.6 \times 10^{-8} \rangle}$$

$$= 4.4 N_v^{-1}$$

$$\frac{\text{ext. loss}}{\text{ext. prod.}} = \frac{10^{10} \langle 9.4 \times 10^{-8} \rangle + 2 \times 10^{11} \langle 1.3 \times 10^{-9} \rangle + 654}{N_v 10^{10} \langle 1.6 \times 10^{-8} \rangle}$$

$$= 11.6 N_v^{-1}$$

...(6.2.1)

the relative loss increases by a factor of 2.6, less than the observed reduction factor for N_{-r} over this distance of 3.75. Both T_- and N_v have been assumed to be spatially invariant. Note the rapid increase of the wall loss term for a relatively minor fall in V_p . One problem is that the fall in N_{-r} appears to be roughly constant between filter and extraction region, whereas that of N_e and N_+ is bilinear, being more rapid in the filter region. This may be offset by the variation of the $\langle DA \rangle$ rate coefficient. This has a peak at $\sim 0.5\text{eV}$, straddled by the two T_e values considered here, which is also the reason for the constancy of $\langle DA \rangle$ in the above calculations. The fall in T_e through the filter causes $\langle DA \rangle$ to peak at about the position of the dip in N_e expected from the bilinear N_e variation.

A spatial variation of N_v is possible. Since there are effectively no primaries in the extraction region, there is no source mechanism to replace those $H_2(v)$ molecules lost to $\langle DA \rangle$ and other reactions. Since all $H_2(v)$ feed thus comes from the driver, it would seem reasonable to expect that some attenuation of N_v will occur as the distance from the driver increases. As already mentioned in chapter 2.2, $H_2(v)$ may be destroyed by a number of processes, but outside of the driver region the wall loss rate is probably dominant. Assuming this is true makes it possible to estimate the attenuation of N_v with distance. The standard expression under these circumstances is that of exponential attenuation with

distance z ,

$$N_v = N_{v0} e^{-n\sigma z} = N_{v0} e^{-\frac{z}{\lambda}}$$

Thus a value for the mean free path of $H_2(v)$ is required:

Since wall losses are assumed to be dominant, this is given geometrically by

$$\lambda_v = \frac{4V}{A} = 15.2 \text{ cm}$$

where V and A in this case are the volume and surface area of the extraction region. Defining 12 cm from the BFE as the reference point (as this is where the rapid attenuation of primaries begins), moving 5 cm into the extraction region will produce an attenuated N_v flux from the driver of

$$N_v = N_{v0} e^{-\frac{5}{15.2}} = 0.72 N_{v0}$$

where N_{v0} is the $H_2(v)$ density at 12 cm from the BFE. Thus the N_v flux suffers a drop of $\sim 28\%$. Substituting this into eqn. (6.2.1), the calculated relative loss factor is increased from 2.6 to 3.5, much nearer the observed result.

The fall in N_v with distance may therefore be explained in terms of a combination of effects. In order of decreasing magnitude, these are the relative increase in the importance of density-independent loss processes as the $\langle MN \rangle$ rate falls,

together with the attenuation of the $H_2(v)$ flux from the driver.

6.2.3 Parametric dependence

The model discussed in chapter 2.2 is the general expression, and includes terms for wall losses of H^- , $H_2(v)$ and primary electrons. Some of these terms may be considered insignificant, depending upon the source being modelled.

For the fixed filter source, other work [44] suggests that losses of primary electrons are dominated by inelastic gas collisions. Thus the wall loss term may be removed from eqn. (2.3.3), and eqn. (2.3.4) becomes

$$N_- = \frac{N_e N_o I_{arc} \langle E - V \rangle \langle DA \rangle}{e V N_+ N_o \langle ILP \rangle} \times \frac{1}{\left[\langle MN \rangle + \frac{3 \times 10^{-4} \langle ND \rangle \langle AD \rangle}{\tau_+ \langle ION \rangle} \right] \left[\frac{I_{arc} \langle PE \rangle}{e V N_o \langle ILP \rangle} + \tau_v^{-1} \right]} \dots(6.2.2)$$

The dual-regime behavior with I_{arc} described in chapter 2.3 arises as the $H_2(v)$ loss term changes from wall loss at lower primary density to primary over-excitation at higher N_p . Thus saturation-type behavior is predicted for N_- with I_{arc} and pressure in the fixed-filter source. N_- is a function of I_{arc} until saturation and one of pressure alone thereafter. Notwithstanding any alteration of the negative ion velocity

with I_{arc} , the extracted J_- data of figure (5.2.25) appears to fit this theory well. Eqn. (6.2.2) also predicts that N_- should be invariant with pressure below saturation, and directly proportional afterwards. Figure (5.2.28) shows this to be true for J_- . Above saturation, J_- increases directly with pressure; below saturation, J_- is approximately independent of pressure, as predicted.

In the case of the variable-filter source, the wall collision term dominates primary electron loss, and the inelastic term may be removed from eqn. (2.3.3). In this case, eqn. (2.3.4) becomes:

$$N_- = \frac{N_e N_o I_{arc} \langle E - V \rangle \langle DA \rangle (\alpha_1 E \phi_1)}{eV N_+ V_{arc}}$$

$$\times \frac{1}{\left[\langle MN \rangle + \frac{3 \times 10^{-4} \langle ND \rangle \langle AD \rangle}{\tau_+(ION)} \right] \left[\frac{I_{arc} \langle PE \rangle (\alpha_1 E \phi_1)}{eV V_{arc}} + \tau_v^{-1} \right]}$$

...(6.2.3)

This again predicts a dual-regime behavior with I_{arc} . However in this case, in the non-saturated I_{arc} regime, N_- has a pressure-dependence due to the pressure-independence of the primary loss rate. Experimentally, the probe data of figure (5.2.10) shows N_{-r} increasing in a linear fashion with I_{arc} , indicating that the variable filter source is operating in the unsaturated I_{arc} regime. Confirming this, N_{-r} varies with pressure as described by eqn. (6.2.3), this being shown

in figure (5.2.16). The saturation of this pressure curve is probably due to the increasing importance of inelastic collisions as a primary loss mechanism at higher pressures, as discussed in section 6.1.2.1.

No explicit dependence of N_- on V_{arc} is predicted for the fixed-filter source. The extracted negative ion current density shows a strong increase of J_- with V_{arc} , which begins to saturate at the highest voltages (figure (5.2.26)). The variable-filter source equation (6.2.3) predicts an explicit inverse dependence of N_- on V_{arc} through the primary wall loss term. Although the probe data suffers from scatter, it is possible to see from figure (5.2.13) that no such variation exists, N_{-r} being very nearly invariant with arc voltage across the entire measured range. Assuming that the negative ion velocity does not alter very much with V_{arc} , it is possible to infer from this that the combined rate coefficients in both equations introduce a direct dependence of N_- on V_{arc} , which is cancelled in the case of the variable filter source by the primary loss term. One point of agreement between the two result sets is the fall in the ion-electron ratio; the electrons increase faster with V_{arc} .

The probe data of figure (5.2.19) shows that both F_r and N_{-r} increase in a slow linear fashion with B . Figure (5.2.30), however, shows that although the ratio of extracted ion to electron current densities increases with B , J_- falls. There are two possible reasons for this: Firstly the

maximum field intensity in the extraction experiment is roughly double that in the probe experiment, and the axial line-integral is greater, so the extraction results may be obtained from an entirely different B regime. Secondly, B (or something dependent upon B) might affect extraction so as to reduce the negative ion drift velocity. This cannot be the plasma potential, as figure (5.1.47) shows this to be invariant with B. One interesting point to emerge from the extraction data is that increasing the fraction of negative ions by increasing B imposes a limit on the benefits of applied BFE bias. A positive bias voltage will deplete the negative current-carrier concentration regardless of its type. If the H^- ions comprise a significant proportion of the negative charge carriers, they are simply attenuated in place of the electrons. Since increasing B appears to reduce the extracted J_- , an optimum B and V_{bias} must exist where the reduction in power used by the bias system is balanced by the increased discharge power required to generate a given J_- .

The bias voltage, like the axial distance in the probe experiments discussed in section 6.2.2, causes the plasma density to vary without affecting the generating terms in the driver region. The same mechanisms for the reduction of N_- will therefore occur when V_{bias} is varied. The extracted J_- shows a slow fall with positive bias, J_- halving over the first 2v in figure (5.2.32). The extracted electron current falls by over an order of magnitude, causing the negative ion fraction to increase six-fold. This behavior is repeated in

the probe experiments, the relative values being almost exactly the same in figure (5.2.22). This agreement implies that variations in N_- may have more importance in determining the bias dependence of J_- than variations in v_- do, as the application of a positive bias potential almost certainly adds a drift velocity in the direction of the BFE to the negative ions. The induced increase in the negative ion fraction limits the usefulness of the bias potential, as mentioned above.

The differential effect of bias on electrons and H^- ions may be explained in terms of wall losses. The $\sim 30\%$ fall in N_- with positive bias is relatively small considering the magnitude of the variation of V_{bias} and its potential effect on the Boltzmann wall-loss factor for H^- ions. A massive fall in N_- is avoided as the plasma potential adjusts itself to screen out the applied BFE bias. This screening is not perfect, and the consequent slight reduction in the potential between plasma and BFE causes the wall loss factor to increase, reducing N_- . The doubling of N_- for a 20v negative bias may be attributed to the almost total elimination of wall losses by the reduction in the Boltzmann factor. In the case of electrons, the above comments also apply, but the higher electron temperature means that V_{bias} will have a larger effect on N_e than N_- .

As a final comment on the H^- formation processes, it has been shown [43] that results from the large Culham multipole H^- source also fit the parametric model described above. The

positive ion population of this source is dominated by protons. Since the smaller sources are H_3^+ dominated, it would therefore seem that the presence or absence of H_3^+ ions in the discharge has little overall effect on the mechanisms governing the production and loss of H^- ions.

CHAPTER 7

Conclusions

7.1 Plasma parameters

The basic plasma in the source appears to originate entirely in the driver region, being generated in the volume immediately surrounding the filament. The plasma diffuses toward the BFE, and is attenuated in the manner expected of a flux diffusing classically through a target material. The spatial form of this attenuation is modified by the filter field, the major part of the attenuation being restricted to the filter region. The amount by which the overall attenuation of a parameter is increased by the field depends on the parameter; at one extreme, primary electrons are very strongly attenuated by the field; at the other, the plasma potential is hardly affected at all. A minimum field of ~ 30 gauss appears necessary in most cases to produce significant attenuation.

Confirming the above, most of the dependencies observed in the driver region are repeated in an attenuated form beyond the filter. The main exception to this is the primary electron population; the filter field appears to attenuate both the primary temperature and density to a level at which the dependencies observed in the driver are no longer observed. For all practical purposes, therefore, primaries do not exist outside the driver region, provided the field is

greater than 30 gauss.

The majority of the arc-parametric dependencies of the plasma observed in the variable filter source may be explained in terms of existing models of a standard (H^- -free) multipole discharge, given one assumption. This is that losses of primary electrons to the magnetically-screened anode walls in the plasma production volume dominate over losses to thermalization by gas collisions. Most other sources have a more efficient magnetic confinement geometry, ensuring primary loss is dominated by gas collisions. The agreement of experimental results from both types of source with the models provides a useful test of their validity. Despite the uneven confinement fields in the source, both the primaries and the bulk plasma appear to be magnetically confined, albeit poorly in comparison to other multipole devices.

The behavior of primary electron temperature may be adequately explained in terms of a skewing of the velocity distribution at the wall by the loss processes already mentioned, causing an increase in primary energy loss to the wall. The thermal electron temperature variation is harder to understand, although many features agree with published theoretical models of the energy distribution. The variation of the plasma potential may be explained in terms of the electron temperature, except for the filter-intensity invariance. The contention that the majority of primary electrons are lost to the wall begs the question of why they

obey a Maxwellian distribution at all. Some process must be acting to re-distribute the energy of the primaries left in the plasma. As indicated in chapter 6.1.2, inelastic collisions must play some part in this. The second possibility is that mentioned by Green et al. [103], where non-linear oscillations are induced in the plasma by the impact of the injected electrons, the consequent potential variation transferring primary energy to the plasma. The use of a diagnostic technique which presupposes the form of the energy distribution prevents any valid judgment on this matter, which must be left to more detailed studies.

A positive bias on the BFE depletes negative current carriers throughout the extraction region, causing a fall in plasma density. This fall extends to the 30-gauss contour of the filter, but not beyond, and may be explained by an increase in carrier drift velocity toward the BFE.

7.2 Negative ions

The numerical estimate of the H^- density obtained from the balance of atomic processes compiled in chapter 2 is within $\sim 20\%$ of the measured value, indicating that the atomic reaction paths discussed are most probably those responsible for H^- production.

The axial variation of N_{-r} points to the filter peak as providing the highest density of H^- ions together with the lowest electron density, and therefore the ideal location for the extraction aperture. However, experiments show that

shifting the extraction apparatus to this position alters the discharge, so the increase in extracted J_{-} obtained is less than probe measurements suggest. This would obviously not be improved by the full-scale extraction grid of a neutral injector. The electron current extracted at this position is also greater, although the design of the extraction system may be adjusted to compensate for this. The axial attenuation of N_{-r} in the extraction region may be explained in terms of two effects; the increasing importance of density-independent H^{-} loss processes as the plasma density falls, and the simultaneous attenuation of the flux of vibrationally-excited molecules from the driver. The radial variation of N_{-r} across the extraction region appears approximately uniform outside the range of the confinement magnets, a useful characteristic if multiple-aperture extraction is desired.

The variation with I_{arc} and pressure of both the J_{-} values extracted from the fixed filter source and the N_{-r} results obtained with the probes can be seen to fit the model described in chapter 2.3. The adherence of J_{-} is somewhat surprising, given that both the discharge conditions and the extraction process itself probably affect \bar{v}_{-} . It is possible that the variation in N_{-} is so large as to render any changes in \bar{v}_{-} insignificant in comparison. This theory is supported by the fact that comparison of results from the two sources suggests the variation of J_{-} with V_{bias} may be explained completely by the depletion of N_{-r} . Given this to be true,

the variation of N_- with V_{arc} in the two sources implies a linear dependence of N_- on V_{arc} is introduced through the rate coefficients of eqn. (2.3.4). Increasing the filter field is seen to increase N_{-r} but decrease the extracted J_- . This could be due to the differences in field geometry and intensity between the sources, or a \bar{v}_- effect.

Maintaining a bias potential on the BFE to remove electrons is useful when electrons predominate. For a plasma with a very high negative ion fraction this may be less useful. The preferential depletion of electrons may be explained in terms of the higher electron temperature.

7.3 General conclusions and suggestions

The object of this study was to obtain spatially resolved data from a filtered magnetic multipole source, and relate this to the generation of H^- ions in the plasma volume. This has been achieved, and the conclusions appear to support many of the theories about the mechanisms of H^- production in such a source.

The basic plasma has been investigated in detail, and shown to originate entirely in the driver region, events here causing the parametric variations observed throughout the source. The effects of the filter field on the diffusion of plasma have been assessed. The particle and energy confinement of primaries has been studied, and explained in terms of anode loss. The variation of the other plasma parameters has been explained principally in terms of the

primary electron behavior and magnetic field geometry. However, a more detailed understanding of the transfer of energy from the injected electrons to the very cold thermals is necessary, probably best tackled by another study aimed at examining the parametric variation of the primary electron distribution function. A more rigid definition of a "primary electron" would be useful in this respect. Since inelastic processes appear to feature so greatly in models of the primary distribution function, perhaps this should read "any electron with sufficient energy to interact inelastically with the background gas". This would, however, imply the existence of a third group of "superthermal" electrons.

The parametric dependence of J_{-} and N_{-} have been shown to fit modifications of existing simple models, obtained by combining the plasma physics of the basic multipole discharge with atomic equilibria. This implies that the atomic processes considered are in fact those mainly responsible for the production of H^{-} ions. A rough numerical estimate using data from the probes supports this. The major unknowns now appear to lie in the channels exciting and de-exciting the necessary vibrational states of hydrogen. The balance of loss processes has been shown to be capable of explaining the spatial variation of N_{-} , although a more detailed picture of the axial attenuation of vibrationally-excited molecules would be useful.

Relating J_{-} to N_{-} is a problem. Models based on atomic processes must by their nature deal in number densities, but

the most reliable measurements of H_- are obtained from extraction studies, where J_- is measured. Although in many cases agreement between N_- and J_- data suggests the variation of the H^- velocity is comparatively small, a detailed investigation of the magnitude and parametric dependence of \bar{v}_- is required, both within the source and entering the extraction system. A comparative study using probes and an extraction system might provide this.

In the course of this study, an advanced Langmuir probe system allowing rapid trace capture and analysis has been developed, together with the theoretical apparatus allowing it's use in certain types of magnetized plasma. A further theory allowing compensation for the effects of ionic sheath-expansion has also been developed. This system would benefit from a new probe measurement circuit incorporating optically-isolated transducers for the probe signals. A higher voltage sweep or voltage offset device would improve the ion-trace at high arc voltages. A more detailed algorithm for analysing the primary electron region of the characteristic is necessary, although this requirement might be better served by a dedicated diagnostic.

The results obtained from the mass-analyser probe showed that extraction and focusing a plasma beamlet using an electron lens within the plasma is practicable, but it was not possible to conclude that negative ions were detected. A new isolated driver circuit with a high bandwidth, together with an improved extraction system design would hopefully

make this a useful diagnostic tool.

Finally, some of the implications of the model of the H^- parametric dependency are disturbing, in that in order to avoid arc current saturation, relatively high source pressures must be used. In an NBI situation, this means a high gas throughput, requiring much pumping equipment to maintain the pressure differential between source and torus. Although the smaller apertures required by H^- beams would help to reduce this, further optimization with the aim of reducing the source operating pressure is desirable.

APPENDIX A

Langmuir probe theory

A.1 Basic probe theory

Langmuir probes formed the principal diagnostic system in the study. They are practically very simple devices, but the theory required to analyse them is more complex. The theories used by the LPA system were reviewed in chapter 4, but many of the details and assumptions made to allow their use were omitted. The purpose of this appendix is to remedy these omissions. This is done by way of a brief review of the Langmuir probe and the principles by which it operates.

At it's most basic, the Langmuir probe consists of conductor of known area inserted into the plasma, and biased relative to a reference electrode using a voltage source. In the simplest case, the area of the reference electrode is large compared with that of the probe, allowing it to balance any current drawn from the plasma by the probe. In a multipole source, this reference is usually the anode or BFE. As the probe is biased, the current drawn by it from the plasma is recorded as a function of bias voltage, generating an I-V characteristic. The shape of this characteristic is determined by the number density and velocity of charged particles in the plasma. Given knowledge of the velocity distributions, an analysis of the characteristic can therefore yield information about these parameters.

This simplicity of experimental technique is one of the two advantages that Langmuir probes have over other plasma diagnostics. The other is their ability to make spatially resolved measurements, possible as the plasma sampled by the probe is restricted to a very small volume around the collection area. The latter is due to the Debye screening of the applied probe potential by the plasma, the probe becoming surrounded by sheath of charge carriers opposed to the probe potential. This sheath is also the cause of the experimental complexity referred to above, as it forms a boundary to the plasma, and the equations governing particle transport within the plasma may not therefore be used at the probe. As discussed in chapter 4.1.2, changes in the size of this sheath or processes occurring within it can perturb the probe results. Prior to discussing a typical characteristic, the following assumptions about the probe and plasma are made to enable the use of Langmuir's theory and its modifications:

1. The dimensions of the probe are \ll the mean free path of an ion or electron, so that no collisions occur within the sheath.
2. The Debye length of the plasma is \ll than the dimensions of the probe, so that the area of the sheath can be assumed to be that of the probe face.

3. The values of the plasma parameters at the sheath edge are those obtaining in the body of the plasma.
4. The probe face is perfectly absorbing, and charges are neutralized on impact.
5. The effects of magnetic fields, ionization and the emission of secondary electrons from the probe are ignored.
6. The ion temperature is negligible compared to the electron temperature.
7. The velocity distributions of ions and electrons are Maxwellian about their respective temperatures.

A typical planar probe characteristic is shown in fig. (A.1.1), and may be divided for convenience into three regions.

1. Electron saturation region

If V_{probe} is at the same potential with respect to the reference electrode as the plasma (the plasma potential, V_p), then no sheath exists, and all particles striking the probe do so as a result of random motion. Since electrons have a smaller mass and thus move faster, they dominate the current flowing to the probe. If the probe is made more positive

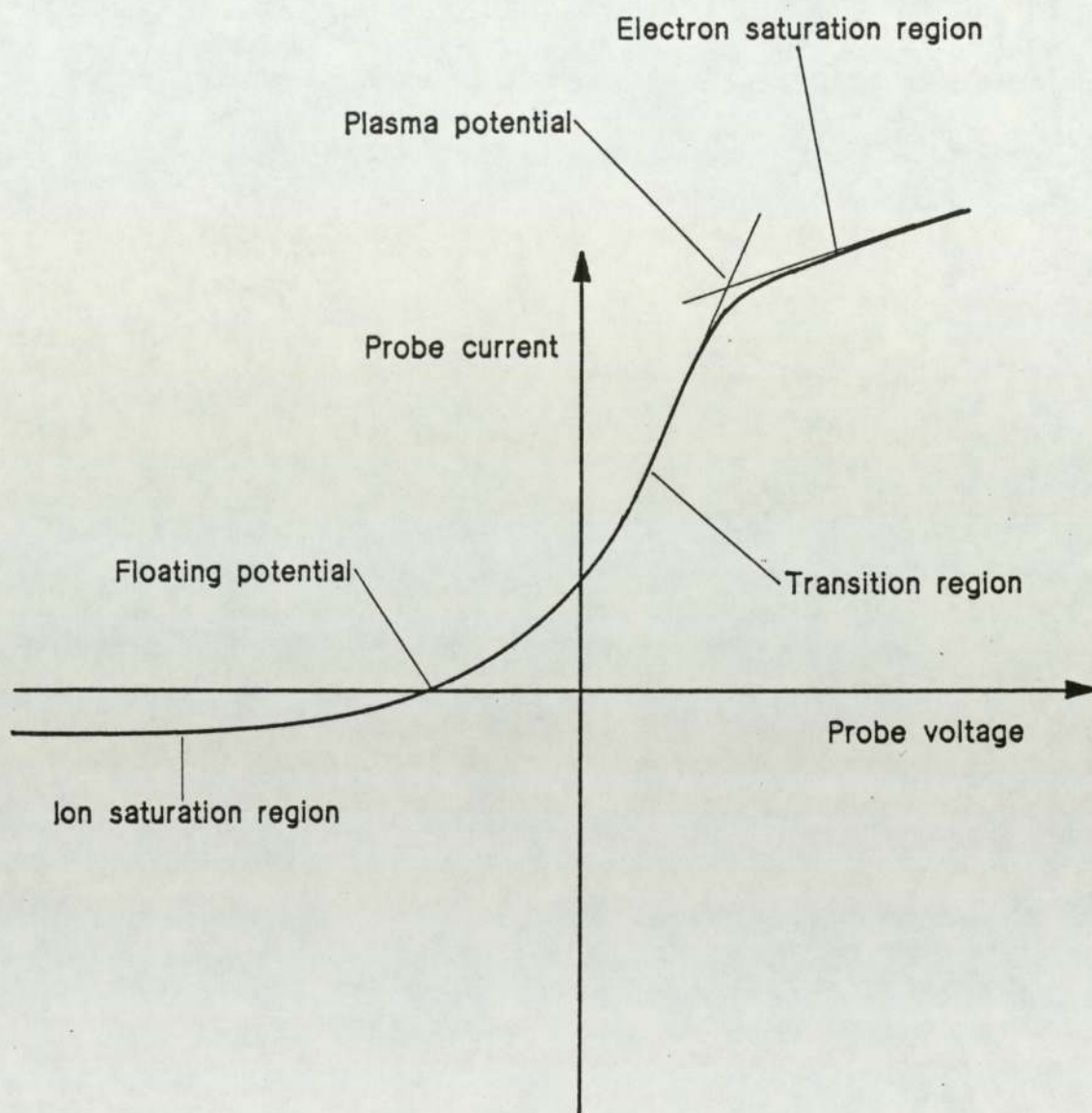


Figure A.1.1 A typical planar Langmuir probe characteristic

than V_p , electrons are accelerated to the probe, and ions retarded. The excess negative charge attracted to the probe thus forms an electron sheath, which cancels out the accelerating potential within a short distance. The current to the probe is then determined by the number of electrons entering the sheath due to random motion, which from conditions 2 and 7 is given by

$$I_e = \frac{e A_p N_e \bar{v}_e}{4} = e A_p N_e \sqrt{\frac{kT_e}{2\pi M_e}} \dots (A.1.1)$$

Ideally, this is determined by the current density alone, and is independent of V_{probe} . However, sheath expansion causes I_e to increase. I_e is thus measured at the plasma potential.

2. Transition region

When $V_{probe} < V_p$ electrons start to be repelled. This repulsion is energy-dependent, so low energy electrons are retarded first. The shape of this transition region may therefore be used to deduce the energy of the electrons. Assuming that condition 7 applies, eqn. (A.1.1) is modified by the attenuation of N_e by the Boltzmann factor, so for $V < V_p$;

$$I_e = e A_p N_e e^{-\left(\frac{eV}{kT_e}\right)} \sqrt{\frac{kT_e}{2\pi M_e}} \dots (A.1.2)$$

Thus in this region, a plot of $\ln(I_e)$ vs. V_{probe} will yield a

line with gradient = e/kT_e , enabling the electron temperature to be found. For the case of two Maxwellian populations, each in a separate internal thermodynamic equilibrium, this plot is bilinear.

As V_{probe} falls further, the voltage at which electron flux is exactly balanced by ion flux is reached, and no current flows in the probe circuit. This is known as the floating potential.

3. Ion saturation region

Finally, at high negative values of V_{probe} , even the most energetic electrons are repelled, and the current reaching the probe is entirely due to accelerated ions. Under these conditions, an ion sheath forms. In the original theory developed by Langmuir [81], ion collection was assumed to obey the ionic equivalent of eqn. (A.1.1). This does not agree with observed experimental results, a fact noted by Langmuir himself [104]. In fact, in the usual case where condition 6 is true, ion collection is not random. The problem lies with the assumption of perfect Debye screening of the probe potential. This is not actually the case. Bohm [87] has shown that a stable solution of Poisson's equation for the case of sheath formation during cold ion collection requires that ions enter the sheath with a minimum energy

$$eV_s \geq \frac{kT_e}{2}$$

where V_s is the potential of the region close to the sheath. This condition, known as the Bohm sheath criterion, is satisfied as the sheath allows a small potential $\sim kT_e/2$ to leak into the pre-sheath region, accelerating ions into the probe. The Bohm expression was derived for monoenergetic ions. The theory has been extended by Boyd and Thompson [82], who produced a more concise restriction on the average of the energy distribution associated with the probe-directed component of the ion velocity, W_+ ,

$$\left\langle \frac{1}{W_x} \right\rangle^{-1} \geq \frac{kT_e}{2}$$

which also imposes an additional restriction on the presheath potential:

$$N_+ = N_{+0} e^{\left(\frac{eV}{kT_e}\right)}$$

for $V < 0$, at any point in the presheath. When these conditions are met, the ionic velocity at the sheath edge is given by

$$v_{+s} = \sqrt{\frac{kT_e}{M_+}}$$

and the ion density just inside the sheath is smaller than

that in the plasma volume by a factor

$$e^{\left(\frac{eV_s}{kT_e}\right)} \sim e^{\frac{1}{2}} \sim 0.6$$

Thus the collected ion current is finally given by

$$I_+ = eA_p N_+ C_s = 0.6 e A_p N_+ \sqrt{\frac{kT_e}{M_+}} \dots (\text{A.1.3})$$

The fact that the formation of the ionic sheath is independent of the ion temperature precludes any measurement of T_+ using Langmuir probes.

A.2 Collection of electrons in a magnetic field

This section discusses the results obtained by Bohm et al [87] describing the collection of electrons by a probe in a magnetic field. As stated in chapter 4, this is achieved by integrating the electron flux entering a surface around the probe. This surface is defined by the point at which electrons suffer their last collision before entering the probe, so free motion occurs within the enclosed volume. The surface is shown in figure (4.1.3), being r_e from the probe perpendicular to the field and $\sim \lambda$ parallel. Expressing the current in terms of the density just outside the surface, N_λ ,

$$I_e = \frac{A_p N_\lambda e \bar{v}_e}{4K}$$

the problem is to find N_λ in terms of the plasma volume density N_e , for a magnetic field B directed along the z direction. The current density outside the surface A_λ is given by the diffusion relation;

$$J_e = -D \cdot \nabla N_\lambda$$

where

$$D = \begin{pmatrix} D_\perp & 0 & 0 \\ 0 & D_\perp & 0 \\ 0 & 0 & D_\parallel \end{pmatrix}$$

It is then possible to obtain an expression for the total

current entering the surface by integrating J_e over A_λ . This Bohm achieves by transforming the relationships to a space contracted in the z direction by a factor $\sqrt{\Omega}$, where

$$\sqrt{\Omega} = \frac{1}{1 + \omega^2 \tau^2} \sim \frac{r_e}{\lambda} \quad \dots(\text{A.2.1})$$

Assuming D is constant, I is given by

$$I_e = D\sqrt{\Omega} \oint_{A_\lambda} \nabla' \cdot N_\lambda \cdot dS'$$

where primes indicate transformed entities. This integral is obtained with the aid of the following formal analogy with the capacitance of the surface A_λ relative to infinity:

Outside A_λ , J_e is conserved, so

$$-\nabla \cdot J_e = D^2 \nabla N_\lambda = D_\perp^2 N_\lambda + D_\parallel \frac{\delta^2 N_\lambda}{\delta Z^2}$$

This has the same form as Laplace's equation outside a hollow conductor of area A_λ , for a potential V . Integrating Poisson's equation over the internal volume of A_λ ;

$$\nabla^2 \cdot V = -4\pi\rho$$

where ρ is the volumetric charge density.

The analogy is made between (N, I_e) and (V, q) , so since

$$q = C(V_\lambda - V_\infty)$$

the analogy allows

$$I_e = 4CD\sqrt{\Omega}(N_e - N_\lambda) \quad \dots(\text{A.2.2})$$

comparing this with eqn. (4.1.7), the density just outside the area A_λ is then given by

$$N_\lambda = N_e \left(1 + \frac{A_p \bar{v}_e}{16K\sqrt{\Omega CD}} \right)^{-1} \quad \dots(\text{A.2.3})$$

I_e is then given by

$$I_e = I_{e0} \left(K + \frac{6a}{16r_e} \right)^{-1} \quad \dots(\text{A.2.4})$$

as used in chapter 4. In the case of the 0.15cm radius probe used in the axial scan, at $B = 30$ gauss and $T_e \sim 0.5\text{eV}$, the second term becomes

$$\frac{6 \times 0.15 \times 30}{16 \times 3.8 \times \sqrt{0.5}} \quad \sim \quad 0.63$$

and thus begins to dominate over K (~ 0.5). So for sufficiently large value of B , the K term may be neglected.

Substituting in the classical value of D under these circumstances

$$D = \frac{\lambda \bar{v}_e}{3}$$

the attenuated current to the probe is given by

$$I_e = \frac{4}{3} \pi N_e \bar{v}_e \sqrt{\Omega} C \lambda e$$

and thus depends on the capacitance of the area A_λ in the transformed space.

A.3 Lea theory

This section briefly describes the derivation by Lea [93] of the theory allowing calculation of N_- values from measurements of R . As stated in chapter 4, negative ions modify the pre-sheath potential V_s for a negatively-biased probe, altering v_+ and N_+ at the sheath edge to v_{+s} and N_{+s} . This alters I_+ , and hence R . V_s is needed to find N_- and N_- to find V_s , so the calculation is iterative. Lea assumes quasineutrality of the plasma holds both in and out of the sheath, and so for potential $V = 0$ at the edge, the following is true just inside the sheath:

$$\frac{dN_+}{dV} = \frac{d}{dV}(N_e + N_-) \quad \dots(\text{A.3.1})$$

All positive ions entering the sheath are assumed to reach the probe, so

$$N_+ v_+ = N_{+s} v_{+s}$$

and their energy is also conserved, so

$$\frac{1}{2} M_+ v_+^2 = \frac{1}{2} M_+ v_{+s}^2 - eV$$

$$\frac{1}{2} M_+ v_{+s}^2 = -eV_s$$

giving for the ion density

$$N_+ = \frac{N_{+s}}{\left(1 + \frac{V}{V_s}\right)^{\frac{1}{2}}} \quad \dots(A.3.2)$$

N_{es} is given by the Boltzmann relation (eqn. 4.1.19a). V_s may be found by differentiation of these expressions, and an appropriate expression for N_{-s} in terms of N_- . Substituting these into (A.3.1) and taking the value as $V \rightarrow 0$, yields the required expression for V_s .

For N_- diffusing from the plasma body, N_{-s} is given by the Boltzmann eqn. (4.1.19b), and quasineutrality is used to give N_{+s} as a function of N_+ and N_e to yield eqn. (4.1.20). The case of locally-produced N_- is more complex. With N_{-s} given by (4.1.21), the negative ion density is given by

$$N_- = \frac{N_{es} e^{\left(\frac{eV}{kT_e}\right)} N_v \langle DA \rangle}{N_{+s} \left(1 - \frac{V}{V_s}\right)^{\frac{1}{2}} \langle MN \rangle + N_{es} e^{\left(\frac{eV}{kT_e}\right)} \langle ED \rangle} \quad \dots(A.3.3)$$

The differentials of (A.3.2), (A.3.3) and (4.1.19a) are substituted into (A.3.1). In the limit $V \rightarrow 0$, this gives

$$-\frac{1}{2} V_s \frac{N_{+s}}{N_{es}} = \frac{e}{kT_e} + \frac{\frac{N_v}{N_e} \langle DA \rangle \left(\frac{N_{+s}}{N_{es}} \langle MN \rangle \left(\frac{e}{kT_e} + \frac{1}{2V_s} \right) \right)}{\left(\frac{N_{+s}}{N_{es}} \langle MN \rangle + \langle ED \rangle \right)^2}$$

Assuming N_v is spatially invariant, V_s is thus given by eqn. (4.1.22). To solve this, the sheath-edge densities may be obtained once again from quasineutrality. This yields a pair of simultaneous equations involving $\frac{N_-}{N_e}$ and $\frac{N_{-s}}{N_{es}}$:

$$\frac{N_-}{N_e} = X = \frac{\frac{N_v}{N_e} \langle DA \rangle}{\langle MN \rangle + \langle ED \rangle + \frac{N_-}{N_e} \langle MN \rangle} \quad \dots(\text{A.3.4a})$$

$$\frac{N_{-s}}{N_{es}} = Y = \frac{\frac{N_v}{N_{es}} \langle DA \rangle}{\langle MN \rangle + \langle ED \rangle + \frac{N_{-s}}{N_{es}} \langle MN \rangle} \quad \dots(\text{A.3.4b})$$

Given the spatial invariance of N_v and eqn. (4.1.19a), these yield a quadratic in Y:

$$\begin{aligned} \langle MN \rangle e^{\left(\frac{eV_s}{kT_e}\right)} Y^2 + (\langle MN \rangle + \langle ED \rangle) e^{\left(\frac{eV_s}{kT_e}\right)} Y \\ - X(\langle MN \rangle + \langle ED \rangle + X \langle MN \rangle) = 0 \end{aligned} \quad \dots(\text{A.3.5})$$

and since

$$\frac{N_{+s}}{N_{-s}} = 1 + \frac{N_{es}}{N_{-s}}$$

iterative solutions of (A.3.5) and (4.1.22) are possible.

APPENDIX B

Details of the LPA probe analysis system

As described in chapter 4, during this investigation a computerized Langmuir probe analysis system was designed and constructed. This appendix describes the functioning of the system in more detail.

B.1 Hardware

The LPA circuit is as shown in figure (4.1.21). Here, the purpose and operation of the major elements is clarified.

B.1.1 The computer and interface unit

The computer used was an IBM PC XT, fitted with a 10 Mbyte fixed disc, a floppy drive, a graphics display and 640 kbytes of memory, running under the disk operating system PC-DOS v2.1. This machine is fitted with an internal 1MHz "expansion bus", allowing direct connection of the dataports on the Intel 8088 microprocessor in the PC XT to external devices. A board inserted into this bus was used to link the computer with an interface rack manufactured by 3D Ltd. The rack contained an Analog Devices AD572 12-bit successive approximation ADC chip, able to sample data at $\sim 5\text{kHz}$. Also fitted were an 8-channel differential-input multiplexer, through which the ADC was addressed, and a 12-bit 4-channel

DAC card.

The maximum common-mode input voltage for the ADC was ~ 2 volts, and the reference electrode for the system (the BFE of the ion source) had to be earth. Since the probe was swept to negative voltages $> 100\text{v}$, the current-sensing resistor had to be placed in the earth-return line of the probe circuit rather than the probe supply line, and the amplifier chassis had therefore to float relative to earth to avoid bypassing the resistor.

B.1.2 The amplifier and drive circuitry

The amplifier used was a bipolar class AB type twin channel device, model A400, developed by Analogue Associates from the HH S500D stereo PA amplifier common in the entertainments industry. Output power in bridge (mono) mode was 1kW. This device had two major advantages over more modern designs employing MOSFET devices. Firstly the bipolar circuitry was capable of DC operation, enabling low-frequency scanning of the probe. Secondly the chassis could be safely floated relative to earth as it was totally enclosed, avoiding the common-mode problem. The latter also conferred another advantage; the semiconductors used in power amplifiers will withstand only a limited potential difference, in the case of the A400 ~ 65 volts. With the amplifier chassis linked to earth, the maximum sweep voltage range would be $-65\text{v} < V_p < 65\text{v}$, insufficient to retard primary electrons at all but the lowest arc voltages. With

the chassis floating, however, the amplifier used in bridge mode "saw" the probe voltage across the output terminals of both channels. Since this voltage was therefore divided across two transistors in series, the maximum voltage sweep was doubled to $-130\text{v} < V_p < 130\text{v}$, satisfactory for most discharges.

Floating the chassis required isolation of the amplifier input. This was achieved using a small opto-isolator / amplifier chip to break the galvanic connection. This device (ISO 100AP, manufactured by Burr Brown) consisted of an encapsulated matched set of infra-red transmitter and receiver, providing insulation of $\sim 1\text{kV}$ with a bandwidth of $\sim 1\text{kHz}$, and was adequate for this task. The circuit employed for this isolation is shown in figure (B.1.1).

Unfortunately, despite much effort, the device proved unsatisfactory for transmitting probe current signals from a resistor in the probe line to ground, due to a low signal to noise ratio. The amplifier earthing through the sensing resistor generated some noise, but this was surmountable by careful data handling.

B.1.3 The probe relay

The relay was required to isolate the probe due to the logic of the DAC card. When deselected (i.e. not in use) this set itself to minimum output. However, since the ADC and DAC were both run in bipolar mode, this generated full negative volts. Attempts to control the input signal or the

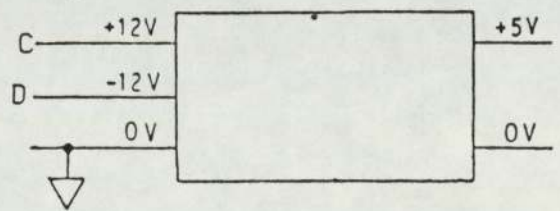
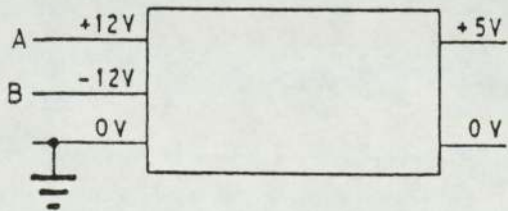
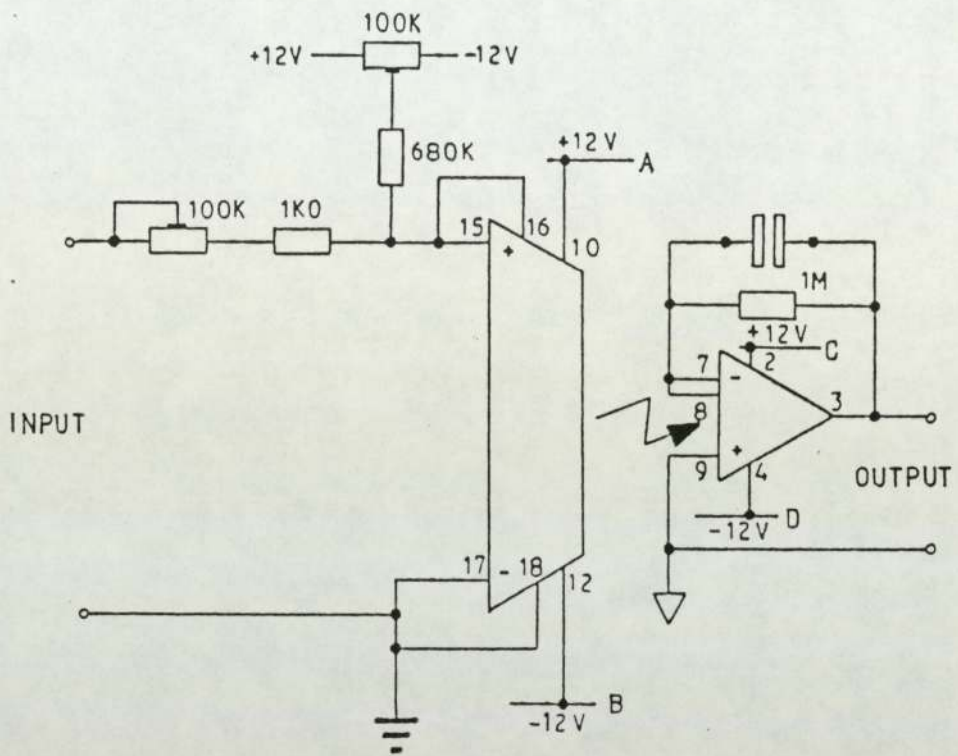


Figure B.1.1 ISO 100 optoisolator used by LPA and MAP systems

power supply to the amplifier led to induced oscillations when the relay operated. The positioning of the relay in the probe line had the advantage of completely isolating the probe between shots.

B.2 Software

In chapter 4, the LPA software was described and the data acquisition and analysis (DAA) segment briefly outlined. In this section, the design of the complete LPA system is described. The functioning of the aforementioned segment is explained in more detail, and it's position in the total LPA system defined.

B.2.1 The complete LPA system

As stated in chapter 4, the compiled object code totalled about 130 kBytes. The TurboPascal compiler used to write LPA set a limit of 64 kbytes on the maximum code size of an executable program, with a separate 64 kbytes for data. Consequently, the overlay system described in chapter 4 had to be used. Since disk access slowed the program, the code run in overlay was that of the subsystems, which dealt in human rather than plasma response times!

Figure (B.2.1) shows a diagram of the complete LPA system, of which the DAA segment is the principal subsystem. The main control level was simply the selection menu from which subsystems are accessed. Most of these consist of

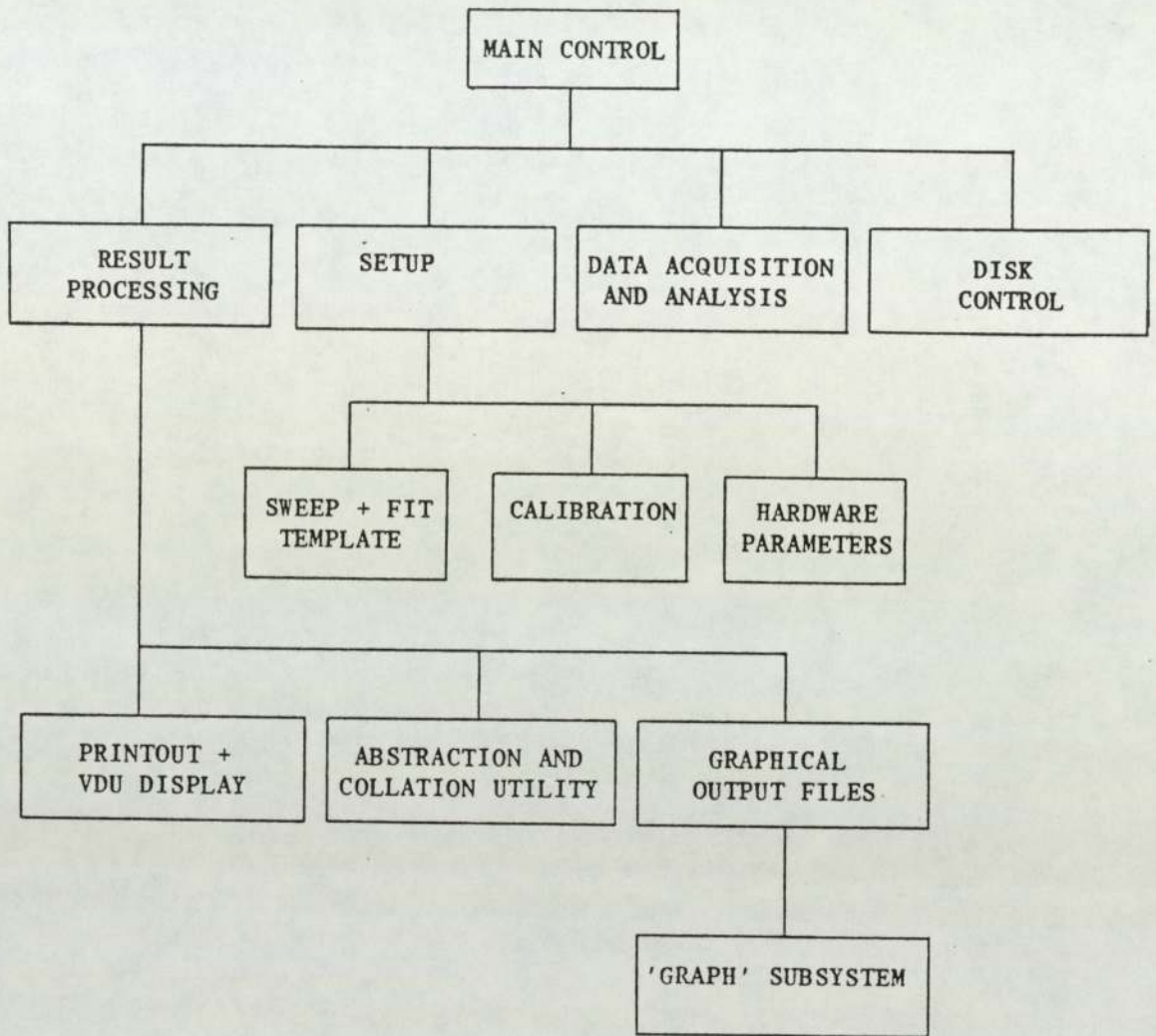


Figure B.2.1 Overall structure of the LPA system

nested levels of menus, allowing values to be set or operations to be executed. There were four main subsystems apart from the DAA segment:

1. The disk control segment, used to directly operate the computer's disk drives.
2. The SETUP segment. The main use of this was in defining the template that controls the DAA segment. This template contained details of the DAC and ADC channels, voltage resolutions, resistance, probe and point average to be used, as well as tolerances governing the fitting of the data. System profiles defined here could also be stored for future use. The ADC system could also be calibrated from SETUP.
3. The result processor. This segment allowed results stored by the DAA segment to be output in three ways; either as a printed list, as a plotfile readable by the GRAPH subsystem, or to external programs, e.g. discharge models. The other facility offered by this segment was the result abstraction and collation utility. This allowed the complete database of files of stored probe results to be searched for those obtained under a specified set of arc conditions. These results could then be collated into a new results file and output graphically, etc. In effect, the utility

comprised a primitive database management system.

4. The GRAPH subsystem. This allowed results from LPA to be directly plotted out on a pen-plotter, with the minimum of human intervention. All the graphs presented in the thesis were generated using GRAPH to plot results directly from stored resultfiles. Data from other sources could also be plotted, so GRAPH could be run separately from LPA if required.

The LPA system is presently being rebuilt with high-frequency low-noise optical transducers. When completed, it will be used as a principal diagnostic on the Culham plasma neutralizer experiment.

B.2.2 The data acquisition and analysis segment

This operates according to the outline presented in chapter 4. The stages mentioned in the outline are explained in further detail here.

Data acquisition

The arc parameter ADC channels were first scanned and the values held in memory. An enable pulse was then sent to close the main probe relay, and sweeping of the probe voltage by the D/A started with the most negative value in the sweep design. The voltage was swept in steps, of a resolution determined by the template, up to the most positive design

value, multiple reading and averaging of each step being performed as specified. During this period, the current flowing through the probe circuit was monitored by the ADC, as was the voltage between the probe and the reference electrode. On reaching the maximum design value, the ADC monitoring was halted, the sweep voltage was returned to the most negative value, and the main probe relay opened. The probe characteristic was then held in memory in two 1x4095 arrays, containing probe current and voltage. The acquisition section was completed by again scanning the parameter channels and averaging with those values held in RAM.

Normalization and smoothing

Probe data was index-sorted into order of increasing probe voltage, and corrected for a previously measured baseline. The data was then normalized to the range -2047 to 2047. Noise was filtered out with a smoothing algorithm according to parameters specified in the template.

Ion saturation region

A line was fitted to the ion saturation region between two voltage points specified in the template, to a voltage ordinate of $(V_{\text{probe}})^{0.75}$ as discussed in section 4.1.2.1. The ion saturation current was tested by extrapolation of this line back to V_p , (guessed at 0v in the first instance). The value of I_+ was then added to all datapoints for which

$V_{\text{probe}} > V_f$, and any remaining negative points discarded.
Natural logarithms of all I_{probe} values were then obtained.

Region location

In order to select the linear portions of the curve, the $\ln(I_{\text{probe}})$ data was numerically differentiated. If the probe was behaving in accordance with Langmuir's theory, the electron transition (retarding) region would be characterized by $d(\ln(I_{\text{probe}}))/dV = \text{constant}$. The upper and lower bounds of the thermal region were identified using $d(\ln(I_{\text{probe}}))/dV$ in conjunction with limiting values defined in the template. A line was then fitted to the data in this region, and extrapolated back towards V_f . Comparison of the data below the lower thermal bound with the extrapolated thermal line allowed the presence of a Maxwellian population of primary electrons to be tested for. If a significant difference existed between line and data, primaries were assumed present. $d(\ln(I_{\text{probe}}))/dV$ was then examined from the most positive voltage backwards towards V_f . An average of the most positive 10 points was taken, and the data tested for decreasing V_{probe} until a significant deviation from the average was found. The electron saturation region was defined between this point and the most positive voltage. The number of points in each region was then checked; if less than a set tolerance, an error was generated. If this or any of the other error traps was triggered, the option of a manual identification of the regions using a cursor on the graphic

display was offered.

Line fitting and result calculation

Least-squares lines were then fitted to the data in each region. The points in the thermal region were checked to see that they fell above an upward extrapolation of the primary electron line. If not, then the last point in the thermal region was discarded, the lower bound of the thermal region moved up one point and the test re-performed. If successful, the thermal data was corrected for the primary contribution and a new line fitted. The gradients and intercepts obtained from the fitted lines were then used to calculate the plasma parameters, in accordance with the theories in section (4.1.1). The option of an iterative calculation was then offered, in which the primary region line was used to subtract the primary electron contribution from the data. Data analysis recommenced with the fitting of the ion saturation line, using the recently calculated value for V_p .

APPENDIX C

Cross sections relevant to the volume production of H^- ions

This appendix contains the available data on cross sections relating to H^- production. Cross section and rate coefficient are given for each process for the following conditions:

<u>Extraction region</u>	$T_e = 0.4\text{eV}$	$T_p = 0.0\text{eV}$
<u>Driver region</u>	$T_e = 2\text{eV}$	$T_p = 20\text{eV}$

The appendix consists of four tables. The first two list known production and loss processes for H^- itself. Given the apparent dominance of dissociative attachment to $H_2(v)$ for H^- production, the third and fourth tables list processes populating and de-populating the relevant band of vibrational states.

Reactions involving $H_2(v)$ that participate directly in the dissociative attachment reaction are summed over the vibrational levels $6 \leq v \leq 9$. Processes used in the model in chapter 2 are marked *. In the driver region, the rate is given for either primary or thermal electrons, according to which yields the greater value. The exception to this is the <ED> process, where values are given for both primaries and thermals.

TABLE C.1 Processes producing H^-

PROCESS	DRIVER		EXTRACTION		REF
	σ cm ²	$\langle \sigma v \rangle$ cm ³ s ⁻¹	σ cm ²	$\langle \sigma v \rangle$ cm ³ s ⁻¹	
1. Dissociative attachment* $e^- + H_2(v) \rightarrow H_2^- \rightarrow H^- + H^*$	2×10^{-16}	1×10^{-8}	3×10^{-16}	1.6×10^{-8}	[52-53]
2. Dissociative attachment $e^- + H_2 c^3 \pi_\mu \rightarrow H^- + H^*$	3×10^{-18}	8×10^{-11}	5×10^{-18}	1×10^{-11}	[60]
3. Dissoc. recombination $e^- + H_2^+ \rightarrow H^- + H^*$	3×10^{-18}	1×10^{-10}	4×10^{-18}	8×10^{-11}	[61-63]
4. Dissoc. recombination $e^- + H_3^+ \rightarrow H^- + H_2^+$	1×10^{-19}	1×10^{-12}	$< 10^{-20}$	$< 10^{-12}$	[61-63]
5. Polar dissociation $e^- + H_2 \rightarrow H^- + H^*$	2×10^{-20}	4×10^{-12}	-	-	[16]
6. Radiative capture $e^- + H \rightarrow H^- + h\nu$	-	-	2×10^{-22}	1×10^{-14}	[106]

TABLE C.2 Processes destroying H^-

PROCESS	DRIVER		EXTRACTION		REF
	σ cm ²	$\langle \sigma v \rangle$ cm ³ s ⁻¹	σ cm ²	$\langle \sigma v \rangle$ cm ³ s ⁻¹	
1. Mutual neutralization* $H^- + H_n^+ \rightarrow H_n + H$	$\langle MN \rangle = (1.0416 \times 10^7 \sqrt{M.T.})^{-1} \text{ s}^{-1}$				[64-65]
2. Electron detachment* $e^- + H^- \rightarrow H + 2e^-$	3×10^{-15} 2×10^{-16}	1×10^{-6} 8×10^{-8}	$< 10^{-16}$	1×10^{-9}	[60]
3. Associative detachment* $H^- + H \rightarrow H_2(v) + e^-$	-	-	-	1.3×10^{-9}	[67-68]
4. Charge exchange $H^- + H_n \rightarrow H + H_n^-$	-	-	-	$< 10^{-9}$	[43]
5. Wall losses* $H^- + wall \rightarrow H + e^-$	$\langle WALL \rangle = 2.4 \times 10^4 \sqrt{T} e^{\frac{v_p}{T}} \text{ s}^{-1}$				Pg. 42

TABLE C.3 Processes populating $H_2(6 < v < 9)$

PROCESS	DRIVER		EXTRACTION		REF
	σ cm ²	$\langle \sigma v \rangle$ cm ³ s ⁻¹	σ cm ²	$\langle \sigma v \rangle$ cm ³ s ⁻¹	
1. E-V singlet excitation* $e^- + H_2 \rightarrow H_2^* \rightarrow H_2(v) + e^-$	1×10^{-17}	4×10^{-9}	-	-	[70]
2. Proton transfer $H_3^+(v) + H_2 \rightarrow H_2(v) + H_3^+(v)$	-	3×10^{-12}	-	3×10^{-12}	[43]
3. Wall recombination $H_2^+ + e^-(wall) \rightarrow H_2(v)$	rate = $6 \times 10^{-5} N \cdot \sqrt{\frac{kT}{M}} \sim 3.5 \times 10^{10} \text{ s}^{-1}$				[72-73]

TABLE C.4 Processes depopulating $H_2(6 < v < 9)$

PROCESS	DRIVER		EXTRACTION		REF
	σ cm ²	$\langle \sigma v \rangle$ cm ³ s ⁻¹	σ cm ²	$\langle \sigma v \rangle$ cm ³ s ⁻¹	
1. Dissociative attachment $e^- + H_2(v) \rightarrow H_2^- \rightarrow H^- + H^*$	2×10^{-16}	1×10^{-8}	3×10^{-16}	1.6×10^{-8}	[52-53]
2. Primary over-excitation* $e^- + H_2(v) \rightarrow H_2 + e^-$	6×10^{-16}	3×10^{-7}	-	-	[75]
3. Ionization* $e^- + H_2(v) \rightarrow H_2^+ + 2e^-$	3×10^{-17}	2×10^{-8}	-	-	[75]
4. V-T (gas) collisions $H_2 + H_2(v) \rightarrow H_2 + H_2(v-1)$	-	$< 10^{-12}$	-	$< 10^{-12}$	[68]
5. Atomic collisions $H + H_2(v) \rightarrow H + H_2(v-\Delta v)$	9×10^{-16}	2×10^{-10}	9×10^{-16}	2×10^{-10}	[68]
6. Wall losses* $H_2(v) + wall \rightarrow H_2$	$\langle W_{ALL_v} \rangle = \frac{A \bar{v}_v}{4V} \sim 3 \times 10^4 \text{ s}^{-1}$				[61-63]

APPENDIX D

Uncertainty in probe measurements of N_-

This appendix discusses the possible uncertainties inherent in the measurement of N_- using the local-production model of Lea's theory on Langmuir probe ratio data. Values of N_- obtained in this manner were the results of a three-stage process:

- (1) Measurement of the probe saturation current ratio R
($= I_-/I_+$).
- (2) Iterative calculation of R for F_r , a guessed value for F_r being adjusted until the measured R was obtained. Values for T_e , T_- , T_+ and M_+ were also required for this.
- (3) Multiplication of the value for N_+ obtained from the probe by F_r to obtain N_- .

There were thus three sources of error. The experimental measurement of R and the calculation of N_+ involved the usual random and systematic errors associated with experimental work. However, the principal source of error lay with the iterative calculation. Here, the problem lay with the accuracy of the additional temperature and mass values

required to perform the iteration:

- (a) T_e could be obtained from the probe characteristic with considerable reliability. Given the low values of T_e in these sources, and the small effect of varying T_e on the $R_c - F_r$ curve (as evidenced by fig. 4.1.16), this was not a major source of error.
- (b) T_- is an important parameter. Boyd and Thompson [82], pointed out that the collection of positive ions in a weakly-electronegative plasma is unaffected by the presence of negative ions under certain conditions, namely that $N_- / N_e < 2$ and $T_e / T_- > 30$, and if these conditions apply, N_- cannot be determined from R . In these sources, the first condition is certainly true. The second depends on T_- . In the relevant regions of these sources, T_e varies between 0.3 and 0.8 eV. This implies T_- must be > 0.03 eV for the theory to accurately apply, although the reduction in I_e due to the increase in average negative mass will still occur. The only experimental measurements of T_- available are those obtained from studies of the emittance of the extracted beam. These suggest values for T_- of between 0.2eV and 1eV, but must be considered subject to a large uncertainty due to the unknown effects of the extraction process itself on T_- . Hiskes and Karo [68] suggest values of between 0.2 and 0.45 eV from both observation

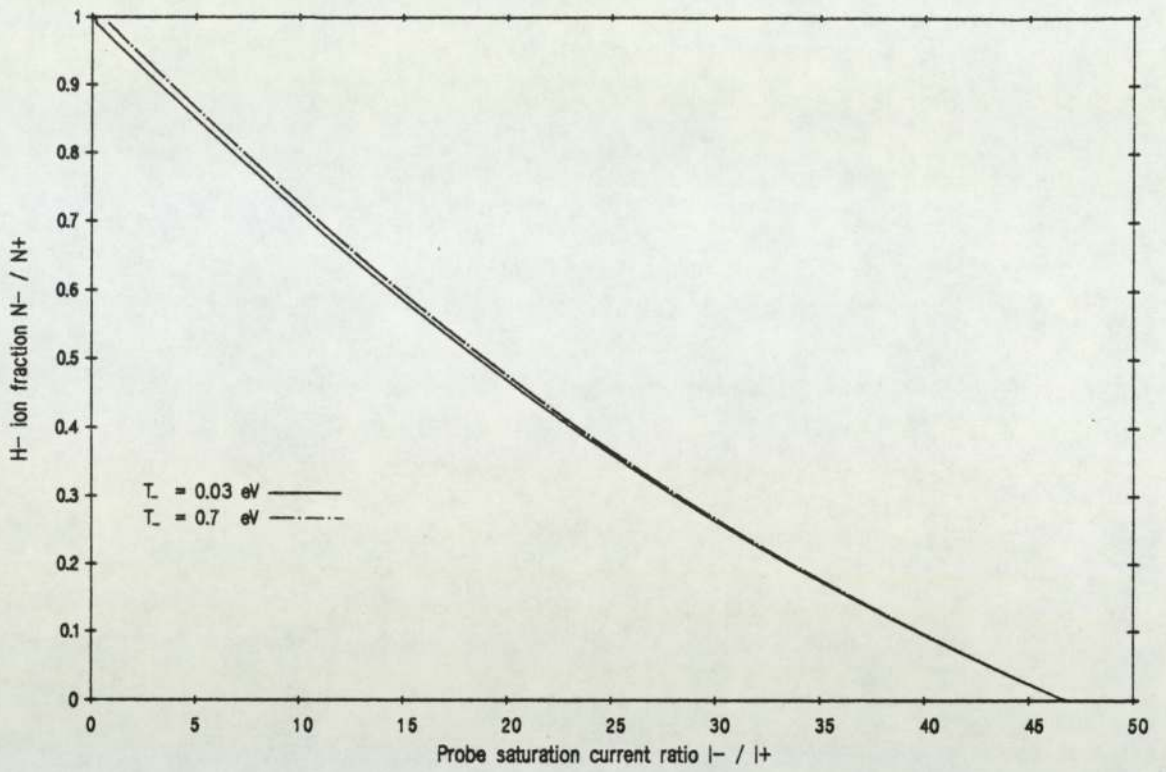


Figure D.1.1 Effect of variation in T_- on $R_C - F_r$ curve
 $M_+ = 2.8 \text{ amu}$ $T_e = 0.7 \text{ eV}$ $T_+ = 0.3 \text{ eV}$

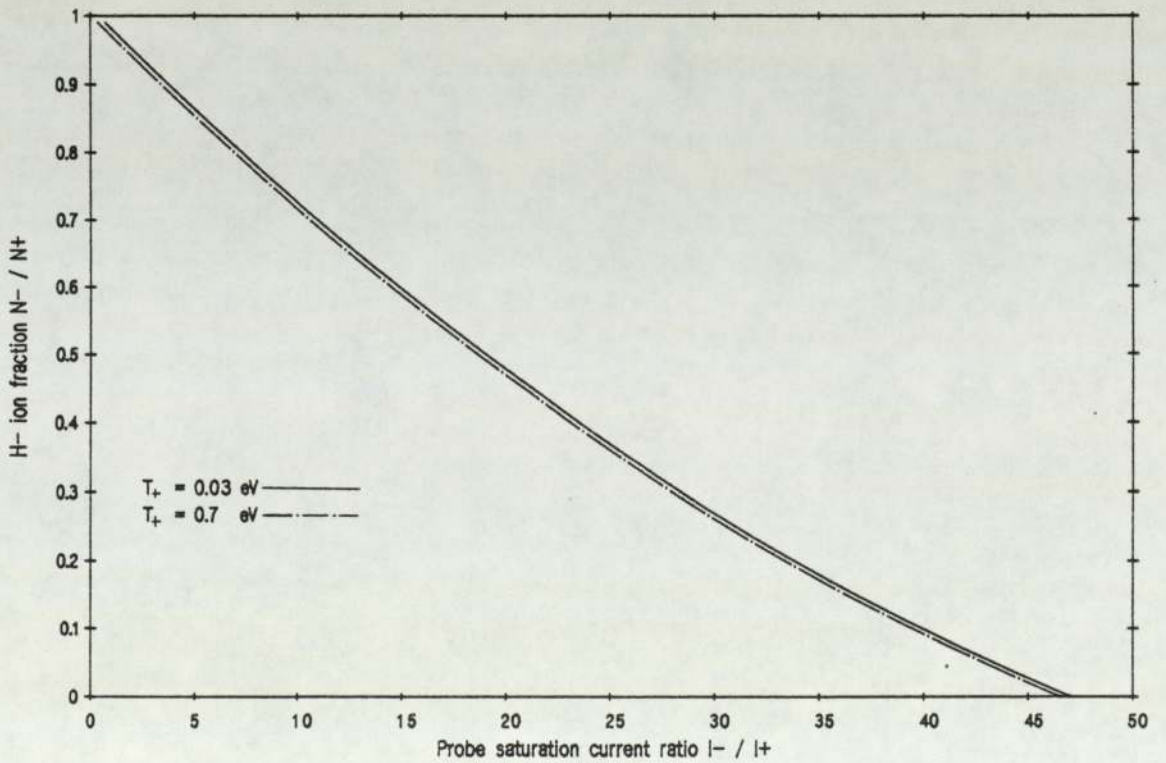


Figure D.1.2 Effect of variation in T_+ on $R_C - F_r$ curve
 $M_+ = 2.8 \text{ amu}$ $T_e = 0.7 \text{ eV}$ $T_- = 0.3 \text{ eV}$

and calculation. The estimate of 0.3 eV used here is probably close, and is easily enough to satisfy the minimum. Variational analysis (figure (D.1.1)) shows that errors in T_- induce only small errors in F_r , and thus N_- : an over-estimate of T_- leads to a small increase in F_r for a given R value.

(c) T_+ was estimated from plasma modelling [93] to be similar to T_- , as no experimental data at all is available for these sources. However, it has a less direct effect on the measurement of N_- . Variational analysis (figure (D.1.2)) shows that errors in T_+ have only a minor effect on F_r : an over-estimate of T_+ leads to a small reduction in F_r for a given R value. Note that this has the opposite effect to (b).

(d) M_+ values were available from mass-analysis studies of the extracted beam, yielding a value of 2.8 amu. Variation in M_+ can have a large effect on the calculated value of F_r (as discussed in chapter 4) especially when F_r and the associated reduction in R are small. Variational analysis (figure (D.1.3)) shows that an over-estimate of M_+ leads to a significant increase in F_r for a given R. Consequently, M_+ must be considered the largest source of uncertainty in the iterative calculation.

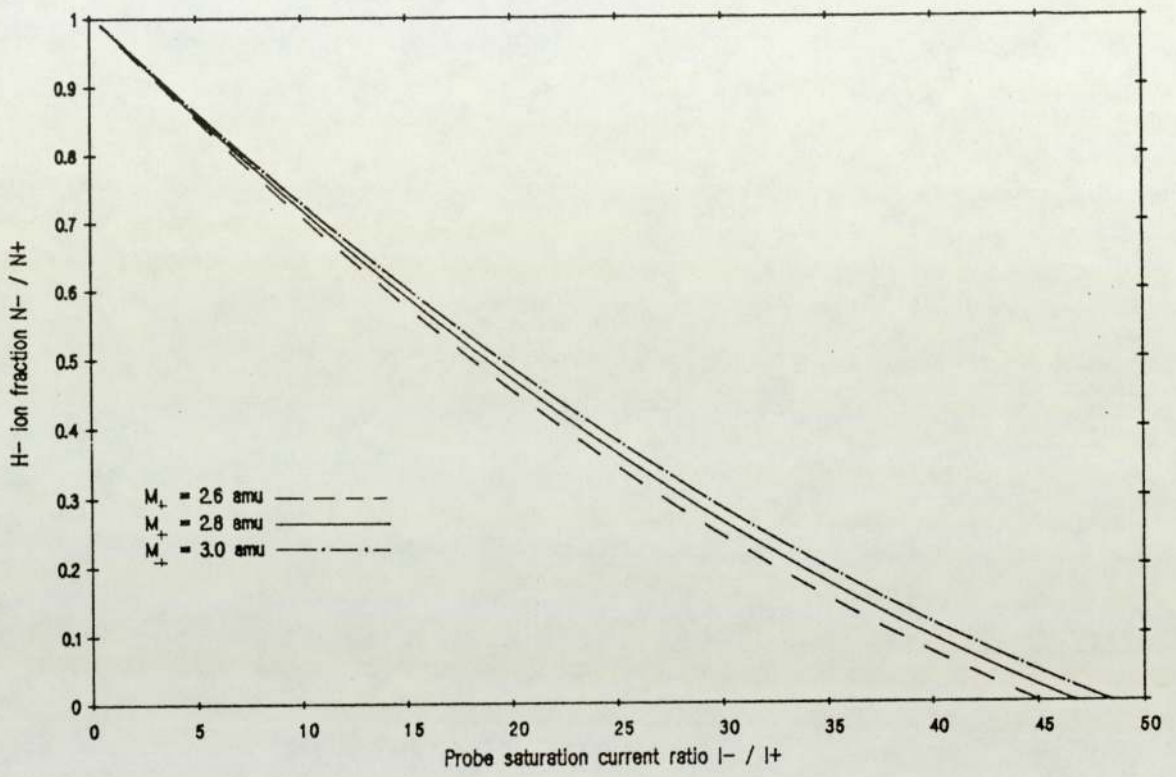


Figure D.1.3 Effect of variation in M_+ on $R_C - F_r$ curve
 $T_e = 0.7 \text{ eV}$ $T_- = 0.3 \text{ eV}$ $T_+ = 0.3 \text{ eV}$

Experimental uncertainties in measuring the saturation values of V_p , I_- and I_+ were small, and further reduced by repeated measurement. That of T_e was smaller still, given the statistical nature of the least-squares fit used. The uncertainties associated with measurements of R are thus estimated at $\sim 10\%$, and those in N_+ at $\sim 7\%$. Relative measurements of F_r and N_- are thus reasonably accurate. However, the effects of errors in the parameters discussed in (b), (c) and especially (d) imply that the maximum possible uncertainty in the measurement of absolute values of N_- using Langmuir probes may be large. The best single improvement in absolute accuracy would be to obtain a simultaneous mass spectrum for each probe trace, in order to accurately calculate the effective ion mass. However, if this were possible, mass spectrometry could also be employed to measure the H^- fraction!

APPENDIX E

Symbology

This appendix defines the more commonly used symbols in the thesis. It is not exclusive, some symbols being defined in the text. Here, the notation [symbol]_x indicates that the quantity relates to the species identified by the subscript. Subscripts are listed separately.

A	area of source anode
A _p	area of Langmuir probe face
a	probe radius
B	magnetic filter field intensity
b	"bounce" coefficient for H ₂ (v)
C	normalized capacitance (x 1/ε _o) relative to infinity
C _s	ionic sound speed
D	diffusion coefficient
E	"source efficiency" , =VB/L
e	electronic charge
F _r	negative ion fraction N ₋ /N ₊ obtained from probe data
G	constant related to H ⁻ wall loss rate
h	Planck constant
I _x	current of species x
I _{arc}	arc current (that flowing in arc discharge)
<ILP>	rate coefficient for inelastic primary collisions
<ION>	rate coefficient for ionization

J_x	current density of species x
K	coefficient of probe area anisotropy
k	Boltzmann constant
L	total length of unshielded cusps on anode
M_x	mass of species x
N_x	number density of species x
P	bulk thermal energy density ($= N_+ T_e$)
R	ratio of +ve to -ve probe saturation current
R_c	above ratio corrected for magnetic field screening
r_x	Larmor radius of species x
T_x	Maxwellian temperature of species x, ($= kT_x/e$)
V	source volume
Varc	arc voltage (anode-cathode arc potential)
V_s	presheath potential
V_f	floating potential
V_p	plasma potential
ΔV_p	differential plasma potential, driver to extraction
v	vibrational level
z	axial distance
α_1, α_2	constants related to source efficiency
β	constant related to ionic sheath expansion
γ	index of Debye sheath expansion
ϵ_0	permittivity of free space
θ	cusps half-width for primary electrons
μ	sheath thickness in Debye lengths
λ_x	mean free path of species x

λ_D	Debye length
μ_o	permeability of free space
σ	binary reaction cross section
τ_x	confinement time of species x
v_x	velocity of species x
\bar{v}_x	average velocity of species x over distribution
ϕ	average energy removed by a primary electron
ϕ_1	primary temperature as a fraction of arc voltage
ω	electron cyclotron frequency
Ω	magnetic coefficient of perpendicular diffusion

Species subscripts:

e	thermal electrons
H	atomic hydrogen
o	molecular hydrogen
p	primary electrons
v	vibrationally-excited hydrogen molecules
+	positive ions
-	H ⁻ ions
-r	H ⁻ ions measured with a probe

REFERENCES

- 1 Lawson J.D. "On the economics of thermonuclear reactors" A.E.R.E Harwell report GP/M 173, February 1955
- 2 Hunt S.E. "Fission, fusion and the energy crisis" 2nd ed. Pergamon press, Oxford 1980
- 3 Ohkawa T. "New methods of driving plasma current in fusion devices" Nucl. Fusion 10 (2) 1970 pp185-188
- 4 Cordley J.G. "A review of current drive by fast injection" Proc. of IAEA Technical Committee meeting on Non-inductive current drive in Tokamaks. Culham laboratory report CLM-CD (1983), April 1983 pp1-10
- 5 Goldston R.J. "Energy confinement scaling in Tokamaks - some implications of recent experiments with ohmic and strong auxiliary heating" Plasma Phys. and Cont. Fusion 26 1984 pp87-103
- 6 G. Duesing, with JET team "First results of neutral beam heating on JET" JET report JET-P (86) 20, March 1986
- 7 Rebut P.H., Lallia P. "JET: Evolution, status and prospects" JET report JET-P (86) 17, March 1986
- 8 Mikkelsen D.R., Singer C.E. "Optimization of Tokamak reactors with beam-driven current" Proc. of IAEA Technical Committee meeting on Non-inductive current drive in Tokamaks. Culham laboratory report CLM-CD (1983), April 1983 pp11-33
- 9 Ehlers K.W., Leung K.N. "Effect of a magnetic filter on hydrogen ion species in a multicusp ion source" Rev. Sci. Instrum. 52 (10) 1981 pp1452-1458
- 10 Ehlers K.W., Leung K.N. "Further study on a magnetic filtered multicusp ion source" Rev. Sci. Instrum. 53 (9) 1982 pp1423-1428
- 11 Ehlers K.W., Leung K.N. "Technique to increase the H⁺ fraction in a multicusp ion source" Rev. Sci. Instrum. 54 (10) 1983 pp1296-1299
- 12 Holmes, A.J.T. Nightingale M.P.S.N. "Design and operation of a 30kV accelerator for negative ion beams" Rev. Sci. Instrum. 57 (10) 1986 pp2402-2408
- 13 Proc. of IAEA Technical Committee meeting on Negative ions, Culham laboratory July 1987 (to be published)

- 14 Delaunay M., Geller R., Jacquot C., Ludwig P., Rocco J.C., Sermet P., Zadworny F., Bergstrom J., Hellblom G., Pauli R., Wilhelmsson H. "Large D^- source for energetic neutral beam" Int. Conf. on plasma physics, Gotebourg 1982 p47
- 15 Dimov G.I "Production of intense negative hydrogen ion beams" Controlled fusion and plasma physics: 10th European conf., Moscow 1981 Vol 2 pp35-41
- 16 Semashko N.N., Kusnetzov V.V., Krylov A.I. "Production of negative hydrogen ion beams by double charge-exchange" Proc. symp. on production and neutralization of negative hydrogen ions and beams, Brookhaven 1977 pp170-172
- 17 Hooper E.B., Poulsen P. "Prospects for negative ion systems based on charge-exchange" Proc. 2nd int. symp. on production and neutralization of negative hydrogen ions and beams, Brookhaven 1980 pp247-254
- 18 Bel'chenko Y. I., Dimov G.I., Dudnikov V.G. "A powerful injector of neutrals with a surface plasma source of negative ions" Nuc. Fus. 14 (1) 1974 pp113-114
- 19 Prelec K., Sluyters Th. "Formation of negative hydrogen ions in direct extraction sources" Rev. Sci. Instrum. 44 (10) 1973 pp1451-1463
- 20 Ehlers K.W., Leung K.N. "Multicusp negative ion source" Rev. Sci. Instrum. 51 (6) 1979 pp721-727
- 21 Ehlers K.W., Leung K.N. "Electron suppression in a multicusp negative ion source" App. Phys. Lett. 38 (4) 1981 pp287-289
- 22 Ehlers K.W., Leung K.N. " H^- formation from a surface conversion type ion source" J. App. Phys. 52 (6) 1981 pp3905-3911
- 23 Bacal M. "Volume generation of H^- ions in plasmas" Int. conf. on plasma physics, Goteburg 1982 Physica Scripta T2/2 1982 pp467-478.
- 24 Limpaecher R., MacKenzie K.R. "Magnetic multipole containment of large uniform collisionless quiescent plasmas" Rev. Sci. Instrum. 44 (6) 1973 pp726-731
- 25 Leung K.N., Samec T.K., Lamm A. "Optimization of permanent magnet plasma confinement" Phys. Lett. A 51 1975 pp490-492

- 26 Green T.S.G., Goble C., Inman M., Martin A.R. "The measurement of ionization rates in sources" 7th European conf. on Fusion and Plasma Physics, Lausanne 1975. Vol. 1 p93.
- 27 Bacal M, Nicolopoulou E, Doucet H.J. "Production of negative hydrogen ions in low-pressure hydrogen plasmas" Proc. symp. on production and neutralization of negative hydrogen ions and beams, Brookhaven 1977 pp26-34
- 28 Bacal M., Hamilton G.W. " H^- and D^- production in plasmas" Phys. Rev. Lett. 42 (23) 1979 pp1538-1540
- 29 Pealat M., Taran J-P.E., Taillet J., Bacal M., Bruneteau A.M. "Measurement of vibrational populations in low-pressure hydrogen plasma by coherent anti-Stokes Raman scattering" J. Appl. Phys. 52 (4) 1981 pp2687-2691
- 30 Green T.S.G., Holmes A.J.T., Walker A.R. "Measurements of negative hydrogen ion production rate by volume processes in a magnetic multipole ion source" 3rd neutral beam workshop on positive ion based systems, Gatlingburg 1981 pp277-292
- 31 Holmes A.J.T., Green T.S.G., Inman M., Walker A.R., Hampton N. "Formation of H^- ions by dissociative attachment in magnetic multipole sources" 3rd joint Varenna-Grenoble conference on heating in toroidal plasmas, Grenoble 1982 pp95-102
- 32 Leung K.N., Ehlers K.W., Bacal M. "Extraction of volume produced H^- ions from a multicusp source" Rev. Sci. Instrum. 54 (10) 1983 pp56-61
- 33 Holmes A.J.T., Dammertz G., Green T.S.G., Inman M., Walker A.R. "Extraction of H^- beams from a volume production source" Proc. int. ion engineering conference ISIPAT & IPAT, Kyoto 1983 pp71-76
- 34 Leung K.N., Bacal M. " H^- ion density measurement in a tandem multicusp discharge" Rev. Sci. Instrum. 55 (3) 1984 pp338-341
- 35 York R.L., Stevens R.R., Leung K.N., Ehlers K.W. "Extraction of H^- beams from a magnetically-filtered multicusp source" Rev. Sci. Instrum. 55 (5) 1984 pp681-686
- 36 Okumura Y., Ohara Y., Horiike H., Shibata T. "Development of a volume H^- source for neutral beam injector" Japanese atomic energy research institute report JAERI-M 84-098, 1984

- 37 Kendall K.R., McDonald M., Moss crop D.R., Schmor P.W., Yuan D. "Measurements on a DC volume H^- multicusp source for TRIUMF" Rev. Sci. Instrum. 57 (7) 1986 pp1277-1281
- 38 Leung K.N., Ehlers K.W., Pyle R.V. "Optimization of H^- production in a filtered magnetic multicusp source" Rev. Sci. Instrum. 56 (3) 1985 pp364-368
- 39 Leung K.N., Ehlers K.W., Pyle R.V. "Effect of wall material on H^- production in a multicusp source" App. Phys. Lett. 47 (3) 1985 pp227-228
- 40 Leung K.N., Ehlers K.W., Pyle R.V. "Effect of gas mixing on H^- production in a multicusp source" Rev. Sci. Instrum. 56 (11) 1985 pp2097-2100
- 41 Leung K.N., Ehlers K.W., Pyle R.V. "Enhancement of H^- production in a multicusp source by cold electron injection" Rev. Sci. Instrum. 57 (3) 1986 pp321-324
- 42 Trow J.R. " H^- production in a microwave multicusp plasma" (PhD thesis) LBL Report LBL-19136, Mar. 1985
- 43 Holmes A.J.T., Lea L.M., Newman A.F., Nightingale M.P.S. "Extraction of H^- and D^- ions from a large magnetic multipole source" Rev. Sci. Instrum. 58 (2) 1987 pp223-234
- 44 Hopkins M.B., Graham W.G. "Plasma parameter measurements in a tandem multipole hydrogen plasma" Vacuum 36 (11/12) 1986 pp873-876
- 45 Hershkowitz N., Leung K.N., MacKenzie K.R. "Plasma confinement by localized cusps" Phys. Fluids 19 (7) 1976 pp1045-1053
- 46 Christensen T., Hershkowitz N., Leung K.N. "Mass scaling of permanent magnet line cusp plasma leaks" IEEE Trans. on Plasma Science PS-5 (1) 1977 pp23-26
- 47 Sautter, J.M. (PhD thesis) Univ. de Grenoble, 1968 (in ref. 19)
- 48 Gabovitch M.D., Naida A.P., Isaev F.M. "Balance of negative ions in a plasma source of great intensity" Ukr. Phys. J. 15 1970 p667-671.
- 49 Kuchinskii V.V., Mishakov V.G., Tibilov A.S., Shukhtin A.M. "Luminescence of atomic lines under ion-ion recombination conditions and kinetics of formation of H^- ions" Opt. Spectrosc. 39 1975 pp598-601
- 50 Abroyen M.A., Golubev V.P., Komarov V.L., Tchemyakin G.V. Inst. D.V. Efremov Report OD-4, Leningrad 1974

- 51 Allen M., Wong S.F. "Effect of Vibrational and rotational excitation on dissociative attachment in hydrogen" Phys. Rev. Lett 41 (26) 1978 pp1791-1794
- 52 Wadehra J.M., Bardsley J.N. "Vibrational- and rotational- state dependence of dissociative attachment in e-H₂ collisions" Appl. Phys. Lett 35 (12) 1980 pp1795-1798
- 53 Wadehra J.M. "Dissociative attachment to rovibrationally excited H₂" Phys. Rev. (A) 29 (1) 1984 pp106-110
- 54 Bouchardy P., Gicquel P., Pealat M., Taran J.P.E., Bacal M. Proc. 8th Int. Conf. on Raman spectroscopy, Bordeaux 1982.
- 55 Pealat M., Taran J-P.E., Bacal M., Hillion F. "Rovibrational molecular populations, atoms, and negative ions in H⁻ and D⁻ magnetic multicusp discharges" J. Chem. Phys. 82 1985 pp4943-4953
- 56 Hiskes J.R., Karo A.M., Bacal M., Bruneteau A.M., Graham W.G. "Hydrogen vibrational population distributions and negative ion concentrations in a medium density hydrogen discharge" J. Appl. Phys. 53 (5) 1982 pp3469-3475
- 57 Hiskes J.R., Bacal M., Hamilton G.W. "Atomic reaction rates in H⁻ and D⁻ plasmas" Lawrence Livermore National Laboratory Report UCID-18031, Jan. 1979
- 58 Bacal M., Bruneteau A.M., Graham W.G., Hamilton G.W., Nachman M. "Pressure and electron temperature dependence of H⁻ density in a hydrogen plasma" J. Appl. Phys. 52 (3) 1981 pp1247-1254
- 59 Bonnie J.M., Eenshuistra P.J., Hopman H.J. "Measured densities and rotational temperatures of metastable H₂c³π_μ in a multicusp ion source" Phys. Rev. Lett. 57 (26) 1986 pp3265-3268
- 60 Bottcher C., Buckley B.D. "Dissociative electron attachment to the metastable c³π_μ state of molecular hydrogen" J. Phys B12 (16) 1979 ppL497-L500
- 61 Peart B., Dolder R.A. "Collisions between electrons and H₂⁺ ions VI. Measurements of cross sections for the simultaneous production of H⁺ and H⁻" J. Phys. B8 (9) 1975 pp1570-1574

- 62 Peart B., Forrest R.A., Dolder R.A. "Measured cross sections for the formation of H^- by collisions between H_3^+ ions and electrons" J. Phys. B12 (20) 1979 pp3441-3443
- 63 Kulander K.C., Guest M.F. "Excited electronic states of H_2 and their role in the dissociative recombination of H_3^+ " J. Phys B12 (16) 1979 ppL501-L504
- 64 Moseley J., Aberth W., Peterson J.R. " $H^- H^+$ mutual neutralization cross section obtained with superimposed beams" Phys. Rev. Lett. 24 1970 pp435-439
- 65 Hickman A.P. "Approximate scaling formula for ion-ion recombination rates" J. Chem Phys 70 (11) 1979 pp4872-4878
- 66 Walton D.S., Peart B., Dolder K.T. "A measurement of cross sections for detachment from H^- by a method employing inclined ion and electron beams" J. Phys. B4 (1971) pp1343-1348
- 67 Dalgarno A., Browne J.C. "The associative detachment of H^- and H_2 " Astrophys. J. 149 1967 pp231-232
- 68 Hiskes J.R., Karo A.M. "Generation of negative ions in tandem high-density hydrogen discharges" J. App.Phys. 56 (7) 84 pp1927-1938
- 69 Nightingale M.P.S., Holmes A.J.T., Forrest M.J., Burgess D.D. "Spectroscopic measurements of neutral hydrogen populations in a multipole plasma H^- source" J. Phys. D. Appl. Phys. 19 1986 pp1707-1722
- 70 Hiskes J.R. "Cross sections for the vibrational excitation of the $H_2(X^1\Sigma_g^-)$ singlet state via electron collisional excitation of the higher singlet states" J. Appl. Phys. 51 (9) 1980 pp4592-4594
- 71 Hiskes J.R., Karo A.M. "Generation of vibrationally excited H_2 molecules by H_3^+ wall collisions" Lawrence Livermore National Laboratory Report UCRL-89586, 1983
- 72 Hiskes J.R., Karo A.M. Hardy R.J. "Vibrational relaxation in H_2 molecules by wall collisions: applications to negative ion source processes" J. Vac. Sci. Tech. A3(3) 1985 pp1222-1228
- 73 Hiskes J.R., Karo A.M. Willmann P.A. "Hydrogen vibrational population distributions and negative ion generation in tandem high-density discharges" J. Vac. Sci. Tech. A3(3) 1985 pp1229-1233

- 74 Hiskes J.R., Karo A.M. "Electron Energy distributions, vibrational population distributions and negative ion concentrations in hydrogen discharges" Proc. NATO Advanced Study Institute on atomic & molecular processes, Palermo 1982 (LLNL report UCRL-87779)
- 75 Chan C.F. "Reaction cross sections and rate coefficients related to the production of positive hydrogen ions" Lawrence Berkley Laboratory report LBID-632, 1983
- 76 Holmes A.J.T., Hemsworth R.N. "Review of magnetic filters" Culham Laboratory ion source group, internal report, April 1983
- 77 Leung K.N. "Review of negative ion source technology" Lawrence Berkley Lab. Report LBL-17017, 1983 pp1709-1713
- 78 Graham W.G. "Wall material and wall temperature effects on negative ion production in a hydrogen plasma" J. Phys. D. 16 1983 pp1907-1915
- 79 Holmes A.J.T., Dammertz G., Green T.S. " H^- and electron production in a magnetic multipole source" Rev. Sci. Instrum. 56 (9) 1985 pp1697-1702
- 80 Holmes A.J.T., Nightingale M.P.S.N., Johnson J.D. "Negative hydrogen ion extraction and electron control in a multipole ion source" Rev. Sci. Instrum. 57 (10) 1986 pp2396-2401
- 81 Langmuir I., Mott-Smith H.M. Gen. Elec. Review 26 (1923) p731, 27 (1924) p449, in "Collected Works of Irving Langmuir" G. Suits (ed.) Pergamon Press, New York 1961.
- 82 Boyd R.L.F., Thompson J.B. "The operation of Langmuir probes in electronegative plasmas" Proc. Roy. Soc. A252 1959 pp102-119
- 83 Hopkins M.B., Graham W.G. "Fast electrons in a tandem multipole H^- source" Proc. 2nd European Workshop on production and application of light negative ions, Palaiseau 1986 pp69-74 also private communication
- 84 Bretagne J., Delouya G., Gorse C., Capitelli M., Bacal M. "Electron energy distribution functions in electron beam sustained discharges; application to magnetic multicusp hydrogen discharges" Preprint, Ecole Polytechnique 1978
- 85 Graham W.G., Hopkins M.B. "Langmuir probe and light emission measurements in a tandem multipole H^- source" Proc. 2nd European Workshop on production and application of light negative ions, Palaiseau 1986 pp61-67

- 86 Johnson J.D. "Probe measurements in a source with a variable magnetic filter" Proc. 2nd European Workshop on production and application of light negative ions, Palaiseau 1986 pp47-53
- 87 Bohm D., Burhop E.H.S., Massey H.S.W in "The characteristics of Electrical Discharges in Magnetic Fields" by Guthrie, A. and Wakerling, R.K. Mc.Graw-Hill, New York, 1949 pp13-86
- 88 Shotet J.L. in "The Plasma State" Academic Press, London 1971 p34
- 89 Chen F.F in "Plasma Diagnostic Techniques" by Huddleston R.H, and Leonard S.L. Academic Press, New York 1965 pp113-200
- 90 Holmes A.J.T. "Electron flow through transverse magnetic fields in magnetic Multipole arc discharges" Rev. Sci. Instrum. 53 (10) 1982 pp1517-1522.
- 91 Holmes A.J.T. "Electron cooling in magnetic multipole arc discharges" Rev. Sci. Instrum. 53 (10) 1982 pp1523-1526
- 92 Doucet H.J. "Production of a Quasi-Electron free plasma using electronic attachment" Phys. Lett. 33A (5) 1970 pp283-284
- 93 Lea L.M. "Measurement of H^- densities using Langmuir probes" - to be published. Also private communication.
- 94 Hopkins M.B, Graham W.G. "Langmuir probe technique for plasma parameter measurement in a medium density discharge" Rev. Sci. Instrum. 57 (9) 1986 pp2210-2217
- 95 Hopkins M.B., Graham W.G., Griffin T.G. "Automatic Langmuir probe plasma diagnostic" Rev. Sci. Instrum. 58 (3) 1987 pp475-476
- 96 Leung K.N., Guethlein G. "Small mass spectrometer probe for analysing hydrogen ion species" Rev. Sci. Instrum. 56 (7) 1985 pp1480-1481
- 97 Grivet P. "Electron Optics" part 2 (2nd ed.) Pergamon, Oxford 1972
- 98 Mulvey T. "The magnetic circuit in electron microscope lenses" Phys. Soc. Proc. B66 1953 pp441-447
- 99 Dugas J., Durandau P., Fert C. "Symmetric and asymmetric electromagnetic lenses" Rev. Opt. 40 1961 pp277-305

- 100 Nightingale M.P.S., Holmes A.J.T., Green T.S. "The dependence of extracted negative ion current density on discharge parameters in tandem volume sources" Proc. 2nd European workshop on the production and application of light negative ions, Palaiseau 1986 pp11-15
- 101 Kaneko O., Oka Y., Sakurai K., Kuroda T "Effect of the filament-induced magnetic field on the spatial distribution of primary electrons in a magnetic multicusp source" Rev. Sci. Instrum. 57 (1) Jan 1986 pp67-73
- 102 McAdams, R. Private communication.
- 103 Green T.S., Goede A.P.H, Singh B. "Measurement of electron energy distribution in a magnetic multipole ion source" J. Appl. Phys. 51 (4) 1980 pp1896-1899
- 104 Langmuir I., Tonks L. "A general theory of the plasma of an arc" Phys. Rev. 34 1929 pp876-922
- 105 Smythe W.R. "Static and Dynamic Electricity" McGraw-Hill, New York 1939. Also in [87]
- 106 Massey H.S.W., Burhop E.H.S. "Electronic and ionic impact phenomena" Clarendon press, Oxford 1952

Negative hydrogen ion extraction and electron control in a multipole ion source

M. P. S. Nightingale and A. J. T. Holmes

UKAEA Culham Laboratory, Abingdon, Oxfordshire, England (Euratom/UKAEA Fusion Association)

J. D. Johnson

Aston University, Birmingham, England

(Received 21 January 1986; accepted for publication 23 June 1986)

A dc negative ion facility has been built to study both the mechanisms controlling H^- production in multipole volume sources and the design of accelerators for negative ion beams. After a 7.5-cm movement of the extraction aperture position within the ion source, the arc current and source gas pressure were optimized, and an H^- current of 10 mA was extracted from a 0.5-cm² circular aperture in a 30-s pulse from a 100-A, 90-V discharge run at 18.8 mT. This is the first operation of such sources to provide a quasi-dc current of 20 mA cm⁻². The installation of an octupole electron trap in the beam forming electrode has lowered the electron current extracted simultaneously with the H^- beam by approximately a factor of 4, and this has led to a low H^- beam divergence. The application of a small bias voltage of up to 2 V between the beam forming electrode and the anode has reduced this electron current still further (by more than a factor of 10) while maintaining the extracted ion current. It is now possible to extract ion currents from such a source/accelerator configuration that are larger than the accompanying electron current.

INTRODUCTION

The production of H^- ions by collision processes within a discharge plasma volume is a promising technique for future neutral beam sources for fusion plasma heating. The production process occurs in two stages.^{1,2} First, vibrationally excited hydrogen molecules are produced by fast (≈ 20 -eV) electron impact with unexcited molecules, and secondly dissociative attachment collisions between these vibrationally excited molecules and cold electrons (0.5–1.5 eV) lead to H^- formation. Above 2 eV the cross section for H^- destruction by electron collisions becomes sufficiently large that it is impossible to maintain a high H^- density. It is, therefore, essential to separate the hot and cold electron populations by using a magnetic "filter" which is a sheet of unidirectional field, orthogonal to the beam axis.^{3,4}

The primary requirement for these sources is that they must provide sufficient beam current density. Present posi-

tive deuterium ion sources for use in neutral beam injection provide a current density of approximately 100 mA cm⁻² at energies above 150 kV which can be neutralized with 20% efficiency. Since gas neutralization of a negative ion beam should occur with an efficiency of around 60%, a negative ion current density of approximately 30 mA cm⁻² will be required if negative ion sources are to replace positive ion sources.

In the present work experiments on a magnetic multipole source of dimensions 20×20×24 cm³ are described which demonstrate the scaling of extractable H^- current with discharge parameters. We describe here improvements to the magnetic suppression filter and changes to the extraction aperture position compared with the source described in Ref. 1 which lead to higher H^- current densities and a reduction in the extracted electron flux relative to the H^- flux. This electron flux reduction is of particular importance for

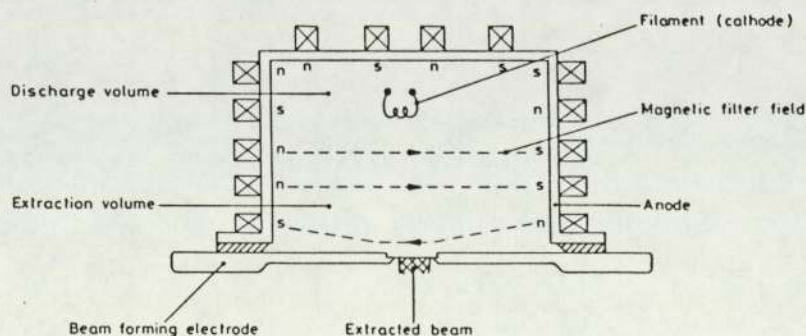


FIG. 1. Schematic design of the Culham Laboratory small volume H^- source.

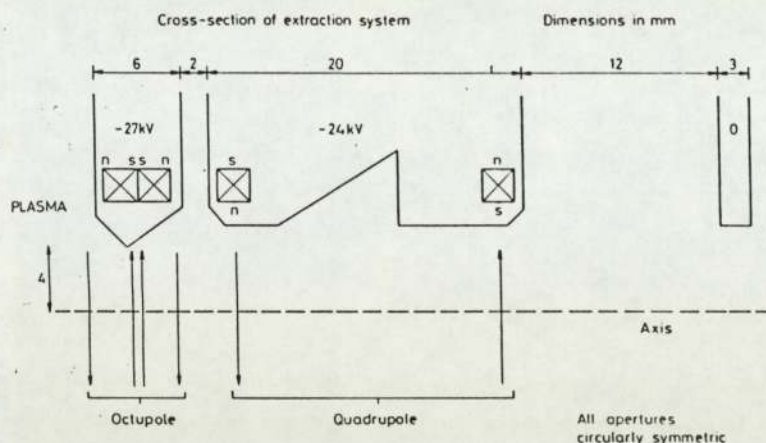


FIG. 2. Cross section of the Culham 30-kV negative ion accelerator.

the fusion application of H^- sources as it determines the overall efficiency of these ion sources.

I. SOURCE, ACCELERATOR, AND BEAM LINE

A negative ion test facility comprising a small volume source coupled to both a 40-kV optimized accelerator and a beam line equipped with current and calorimetric beam measurements has been constructed at Culham Laboratory. This is used to investigate:

- the basic physics controlling the extractable ion current densities from such sources and
- the suppression and control of the electrons simultaneously extracted.

In addition this facility is used to test negative ion accelerator designs and the properties of negative ion beams (Holmes and Nightingale⁸).

The source used in this present work is shown in Fig. 1 and is essentially that described previously¹ except that both

the operating arc current and pressure have been increased. During the measurements described here, the source was run dc at arc currents up to 15 A and run in a quasi-dc mode for between 30 s and 2 min at higher arc currents.

The accelerator used is shown in Fig. 2 and will be described in greater detail by Holmes and Nightingale.⁸ It is a triode accelerator operated in the present work at 27 kV and uses a quadrupole electron trap to prevent electrons penetrating beyond the second accelerator grid. At present 90% of the electrons extracted from the source are trapped on the second grid at approximately 10% of the full acceleration voltage, and all of the remainder are deflected onto the third grid (at full acceleration voltage) since no electron beam is observed to reach the end of the beam line. Since this trapping appears effective, the existing quadrupole trap has been maintained, and attention in this present work is turned to the suppression of electrons entering the accelerator.

The full beam line is shown in Fig. 3. After leaving the accelerator the beam travels 2.2 m to a combined Faraday cup and water calorimeter.

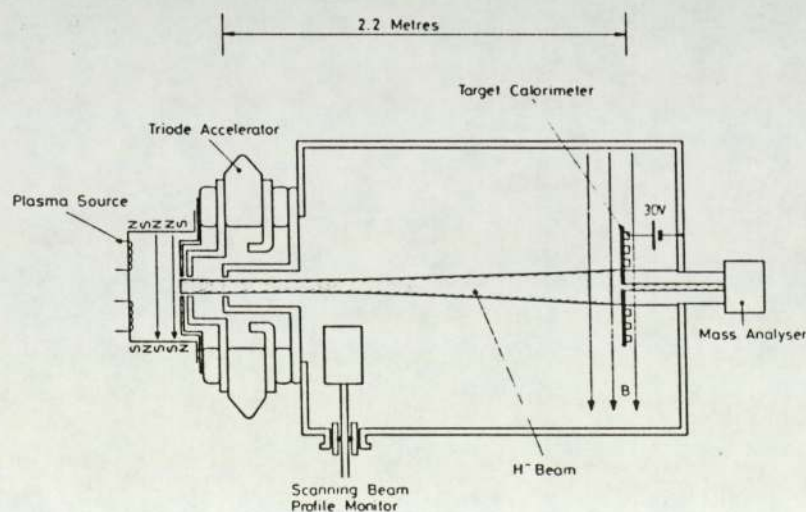


FIG. 3. Schematic plot of the beam line used for source and accelerator development.

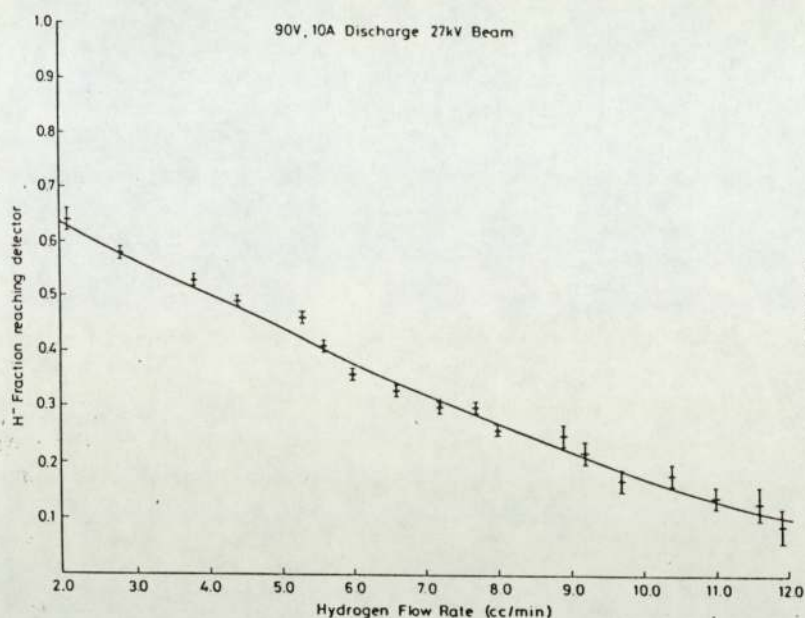


FIG. 4. Fraction of unstripped negative ion reaching the calorimeter (2.2 m from the accelerator) as a function of flow rate from the source.

central 2.75-cm-diam disk surrounded by two concentric rings of outer diameters 9.7 and 20.4 cm which allow beam focusing to be performed. The half-angle subtended by the Faraday cup current detector is 2.65° and the cup is biased positively with respect to the vacuum tank to prevent secondary electron emission, and a transverse magnetic field is applied to prevent the detection of beam plasma particles. The water calorimeter is fitted to the center disk and the inner ring. It is used at low arc currents (< 15 A) to determine the degree of stripping of the H^- beam in terms of the source flow rate (and hence beam-line pressure). The result is shown in Fig. 4. It should be noted that all the ion beam current densities quoted in this paper are those measured by the Faraday cup (after corrections for stripping), and these therefore represent the ion currents extracted, accelerated to full voltage, and focused onto a target which subtends an angle of 2.65° .

II. CHANGES TO THE ACCELERATOR FRONT GRID DESIGN

Although the majority of the accelerator design will not be discussed in this paper in detail, two recent changes have been made to the first electrode that directly affect either the extractable ion current or the electron control.

A. Movement of the extraction plane

It was suggested in previous work on this Culham source¹ that the previous position of the accelerator aperture at the edge of the discharge did not correspond to the position of maximum H^- density within the source which occurred some 5–10 cm closer to the virtual filter. Subsequently, Leung *et al.*⁵ have reported a factor of 3 gain in extracted ion current and lowering of a factor of 3 in the extracted

electron current by moving their filter 6 cm closer to the extraction aperture.

The extraction aperture used was, therefore, moved 7.5 cm closer to the filter (leaving the discharge volume unchanged). This resulted in a 50% increase in extracted ion current with a simultaneous doubling in extracted electron current compared with earlier results. Given the results obtained in previous probe measurements on this source, it would be expected that this new position of the accelerator should correspond approximately to the peak H^- density inside the source. Clearly, neither the factor of 3 increase in H^- current seen by Leung *et al.* nor the factor of 3 suggested by the previous probe measurements has been observed experimentally, although some increase does occur. It is presumed that this lack of gain in ion current occurs since the extraction aperture movement involves the repositioning of the entire beam forming electrode, which would require a threefold increase in positive ion current reaching the beam forming electrode if the density variation measured by probe was maintained. Since the discharge cannot supply such a high ion current increase, the particle densities must decrease. The conclusion is, therefore, that in a full-scale (multiple-aperture) source (where the entire beam forming aperture must move to reposition the extraction plane) some optimization of the extractable H^- current density can be obtained by moving the extraction plane, but that this may not be as high as earlier work has suggested.

B. Installation of an octupole filter in the extraction plane

Measurements of the negative ion beam profile made immediately after the change in accelerator position suggested that the H^- beam quality obtained deteriorated strongly with increasing arc discharge current up to arc of currents of

30 A. Adjustment of the source and accelerator magnetic field patterns showed that this decrease in beam quality was dependent not on the extracted H^- current, but on the electron current simultaneously extracted and trapped within the accelerator. As an example, removal of the quadrupole trap in the second accelerator grid resulted in a significant increase in beam quality, but also resulted in the extraction of a full-energy electron beam. This suggested that the decrease in beam quality arises from the nonplanar space charge resulting from the curved trajectories of the electrons deflected by the quadrupole filter onto the second grid. Since this filter must be maintained if electrons are not to be accelerated to full energy, it is clear that further electron suppression at the excitation plane is required.

In previous measurements on this source some suppression was achieved by the use of a dipole magnetic field placed inside the beam forming (extraction) grid. This, however, resulted in a deflection of the H^- beam by the dipole field leading to losses at the third accelerator grid. To overcome these problems an octupole filter was installed in the beam forming electrode, as shown in Fig. 2. This order of field produced neither deflection nor displacement of the H^- beam and also provided a strong suppressing field (peak of 120 G) for the electrons. This reduced the extracted electron current by approximately a factor of 4, resulting in increased ion beam quality. Some electrons do, however, pass through this filter, and so the quadrupole trap has been retained for the work described below.

III. BEAM MEASUREMENTS

Using both the new accelerator position and the octupole trap, the extracted ion and electron currents were measured as a function of arc current and pressure, at higher arc currents and filling pressures than previously attempted.

A. Extracted ion current density

The ion current density measured on the Faraday cup (after correction for gas stripping in the beam line) is shown in Fig. 5 as a function of arc current and gas flow rate. Note that the calculated conductance of the source pumping aperture is such that the flow rates used should be multiplied by approximately 1.66 to provide the cold filling pressure (in milli Torr). The drain current drawn from the 27-kV power supply was identical to within $\pm 10\%$ to the extracted H^- current, and it therefore appears likely that few electrons reached the third acceleration grid and that few H^- ions were stripped within the accelerator (and therefore collected on the third grid). In addition, variation of the magnetic field across the Faraday cup showed that no measurable electron beam reached the cup. The quadrupole trap does indeed then prevent electrons from escaping the accelerator. Several points arise from the measured ion current density:

(a) A current density of 20 mA cm^{-2} has now been extracted from this source at an arc current of approximately 95 A and an arc voltage of 90 V.

(b) It has proved necessary to raise the arc running pressure beyond that used previously to obtain higher current densities. The maximum usable flow rate was set by the errors involved in the correction for stripping to be 11.3 cc/min (corresponding to an estimated cold filling pressure of 18.8 mTorr). It was, therefore, impossible to attempt measurements at higher source pressures still to obtain the optimum H^- yield.

(c) At low arc currents the ion current density scales linearly with arc current as observed previously. At the higher arc currents now used, however, the ion current density appears to saturate with a value that increases linearly with pressure across the range of flow rates used.

A simple model explaining the general dependence of

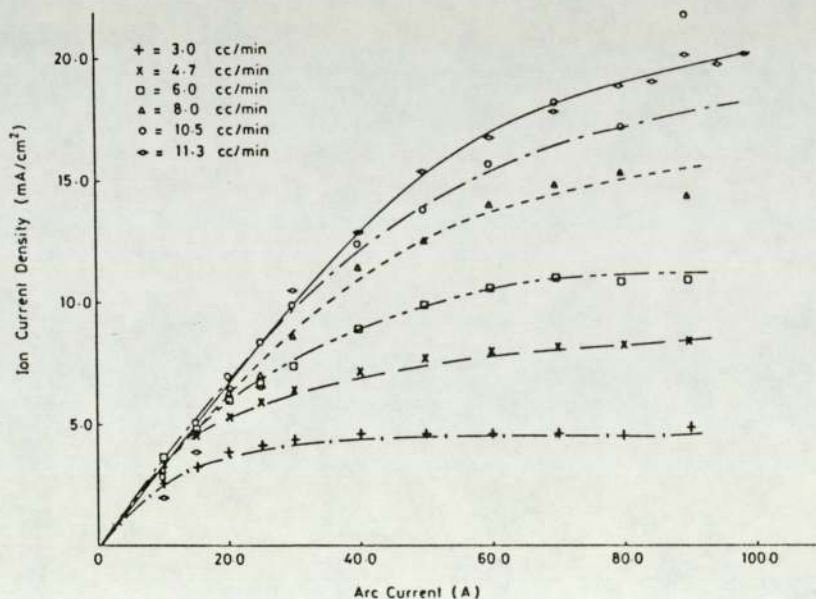


FIG. 5. Negative ion current density extracted from the source shown as a function of source current and flow rate.

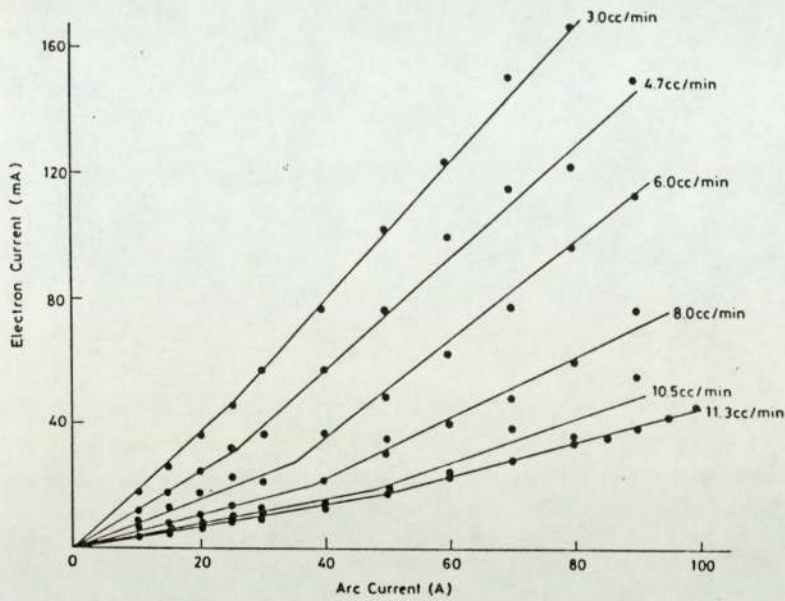


FIG. 6. Electron current extracted from the source shown as a function of source current and flow rate.

the extracted ion current on arc current and filling pressure will be published by Green *et al.*,⁶ which analyzes similar results obtained at Culham using a larger ion source (described in detail in another paper⁷).

B. Extracted electron current

The electron current simultaneously extracted and subsequently trapped inside the second accelerator grid is shown in Fig. 6 as a function of arc current and gas pressure.

The electron current increases with arc current at all pressures and decreases monotonically with increasing gas pressure. Raising the gas pressure, therefore, not only leads to an increase in extractable ion current, but lowers the accompanying electron current. Thus the peak extracted H^- current density of 20 mA cm^{-2} is accompanied by an electron current of 45 mA (90 mA cm^{-2}) reaching the second grid, with less than 10 mA/cm^2 reaching full energy.

It has been reported previously that the use of a positive bias voltage between the beam forming electrode and the

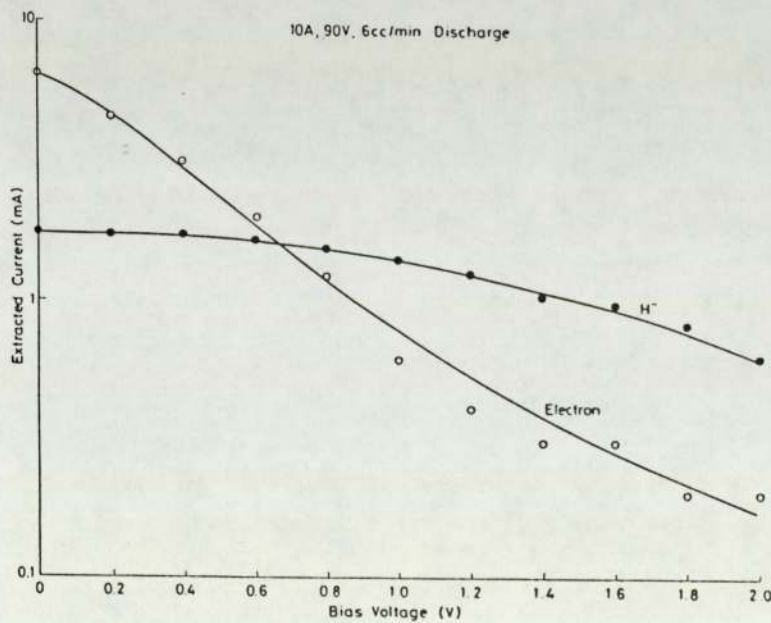


FIG. 7. Variation of the extracted negative ion and electron currents with bias voltage applied between the anode and the beam forming electrode.

anode can increase the extracted ion/electron current ratio.¹ Such a positive bias voltage has been used at low arc currents on the present source, and a typical result is shown in Fig. 7. With the application of 1 V of bias voltage the extracted electron current drops by one order of magnitude from its initial value, while the H⁻ currents drops by only 20%. The use of such a bias voltage can therefore considerably enhance the ion/electron current ratio without significantly perturbing the ion current density. The bias effect appears to be independent of arc current (although higher bias voltages seem to be required at higher arc currents) and so should allow similar reductions in extracted electron current to be obtained at high discharge powers. It therefore now appears feasible to extract ion beams of greater current than the accompanying electron beam for a small loss in extracted negative ion current.

IV. CONCLUSIONS

An existing negative ion facility has been modified to improve electron control and to extract the maximum possible H⁻ current density. Movement of the extraction plane within the source has not produced as large an increase in ion current as predicted, but the introduction of an octupole electron filter has successfully lowered the extracted electron current.

The extracted ion beam has been accelerated to 27 kV and focused to a target 2.2 m from the source. The resultant ion current increases with arc current but eventually satu-

rates at a value that increases with pressure. Such behavior is in reasonable agreement with an existing simple model of the processes controlling ion production and loss in volume sources.

The use of an octupole filter and the raising of the gas pressure in the source have reduced the electron fraction in the extracted beam. The application of a bias voltage has been shown to further reduce the electron current to a value where it may be smaller than the ion current.

The maximum ion current density extracted was 20 mA cm⁻² which is approximately that required for a future neutral beam injection system. It must be noted, however, that this current density was obtained using a high enough gas filling pressure that stripping of the H⁻ beam inside the accelerator may become a problem. In addition the ion current is close to saturation at these values. Optimization of the power and gas efficiencies within the source may, therefore, require source operation at lower arc currents.

- ¹A. J. T. Holmes, G. Dammertz, and T. S. Green, *Rev. Sci. Instrum.* **56**, 169 (1985).
²Y. Okumura, Y. Ohara, H. Horlike, and T. Shibata, JAERI Report No. 84-098, 1984.
³J. R. Hiskes and A. M. Karo, *J. Appl. Phys.* **56**, 1927 (1984).
⁴M. Bacal, A. M. Brunteau, W. G. Graham, G. W. Hamilton, and M. Nachman, *J. Appl. Phys.* **52**, 1247 (1981).
⁵K. N. Leung, K. W. Ehlers, and R. V. Pyle, *Rev. Sci. Instrum.* **56**, 364 (1984).
⁶T. S. Green, A. J. T. Holmes, and M. P. S. Nightingale (to be published).
⁷A. J. T. Holmes, L. M. Lea, A. F. Newman, and M. P. S. Nightingale (to be published).
⁸A. J. T. Holmes and M. P. S. Nightingale, *Rev. Sci. Instrum.* **57**, 2402 (1986).